Physics of Energy Conversion and Storage

Impact of Electrolyte Composition on Electrode Processes. Investigation Using Laser-Assisted, Electron Paramagnetic Resonance, and Impedance Techniques

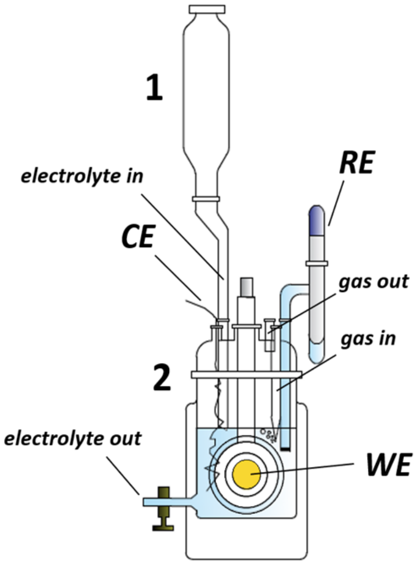

Dissertation

by

Theophilus Kobina Sarpey

Technische Universität München

TUM School of Natural Sciences

Impact of Electrolyte Composition on Electrode Processes. Investigation Using Laser-Assisted, Electron Paramagnetic Resonance, and Impedance Techniques

Theophilus Kobina Sarpey

Vollständiger Abdruck der von der TUM School of Natural Sciences der Technischen Universität München zur Erlangung des akademischen Grades eines

Doktors der Naturwissenschaften (Dr. rer. nat.)

genehmigten Dissertation.

Vorsitz:	Prof. Dr. David Egger
Prüfer der Dissertation:	1. Prof. Dr. Aliaksandr Bandarenka
	2. Prof. Dr. Heine Anton Hansen

Die Dissertation wurde am 28.07.2023 bei der Technischen Universität München eingereicht und durch die TUM School of Natural Sciences am 28.09.2023 angenommen.

This doctoral thesis is based on the following published (in preparation, submitted, and/or accepted) manuscripts and conference contributions:

List of Publications - Manuscripts

1. Ding, X., Garlyyev, B., Watzele, S. A., Sarpey, T. K., & Bandarenka, A. S., Spotlight on the Effect of Electrolyte Composition on the Potential of Maximum Entropy: Supporting Electrolytes are not Always Inert., ***Chemistry-A European Journal***, 2021, *27*, 39, 10016-10020.
2. Haid, R. W.,‡ Ding, X.,‡ Sarpey, T. K., Bandarenka, A. S., & Garlyyev, B., Exploration of the Electrical Double-Layer Structure: Influence of Electrolyte Components on the Double-Layer Capacitance and Potential of Maximum Entropy., ***Current Opinion in Electrochemistry***, 2021, 100882.
3. Ding, X.,‡ Sarpey, T. K.,‡ Hou, S., Garlyyev, B., Li, W., Fischer, R. A., & Bandarenka, A. S., Prospects of Using the Laser-Induced Temperature Jump Techniques for Characterisation of Electrochemical Systems., ***ChemElectroChem***, 2022, *9*, 4, e202101175.
4. Hou, S., Xu, L., Ding, X., Kluge, R. M., Sarpey, T. K., Haid, R. W., Garlyyev, B., Mukherjee, S., Warnan, J., Koch, M., Zhang, S., Li, W., Bandarenka, A. S., & Fischer, R. A., Dual In Situ Laser Techniques Underpin the Role of Cations in Impacting Electrocatalysts., ***Angewandte Chemie***, 2022, *134*, 24, e202201610.
5. Sarpey, T. K., Keleş, E., Gubanova, E. L., & Bandarenka, A. S., Probing the Electrified Solid-Liquid Interfaces with Laser-Induced Transient Techniques. In: Wandelt, K., and Bussetti, G. (Eds.) ***Encyclopedia of Solid-Liquid Interfaces***, Elsevier: Amsterdam, First Edition (Volume 1), 2024, 43-58.
6. Götz, R.,‡ Sarpey, T. K.,‡ Song, K. T ., Gubanova, E. L., & Bandarenka, A. S., *et al.*, *In-situ* Electron Paramagnetic Resonance Spectroscopy for Characterization of Electrified Solid/Solid and Solid/Liquid Interfaces. (In preparation)
7. Sarpey, T. K., Gubanova, E. L., & Bandarenka, A. S., *et al.*, Determination of the PME of Pd/Au Electrodes in $HClO_4$ media. (In preparation).
8. Sarpey, T. K., Gubanova, E. L., & Bandarenka, A. S., *et al.*, Determination of the PME of Au Electrodes in Mixed Na^+/K^+ electrolytes. (In preparation).

‡ Authors contributed equally to the publication.

Conference Contributions

Oral Presentation

- 71st Annual International Society of Electrochemistry (ISE) Meeting - Belgrade Online, "*Nanostructured* Pt_xM/C *(M = Cu, Co, Ni, Ir, Y) Alloy Electrocatalysts Synthesized via a novel Top-Down Route Towards the Enhancement of the ORR Activity*," Monday, August 31st to Friday, September 4th, 2020, ise200478, Symposium s17 (Electroactive Materials: Polymers, Inorganic Solids, Nanocomposites, and Hybrid Materials).

Poster Presentation

- 10th Energy Colloquium of the Munich School of Engineering (MSE) 2020, "*Nanostructured* Pt_xM/C *(M = Cu, Co, Ni, Ir, Y) Alloy Electrocatalysts Synthesized via a novel Top-Down Route Towards the Enhancement of the ORR Activity*," Munich/Garching Online, July 30th, 2020, Topics: Experimental, Fundamental, Fuel cell/Electrolysis.

Attendance

- 12th Energy Colloquium of the Munich School of Engineering (MSE) 2021, Garching - In person, Wednesday, July 27th, 2022.

- 7th RUHR-Symposium, Online, Wednesday, October 27th, 2021, Functional Magnetic Materials: Performance Enhancements for Electric Drives and Thermal Management.
- The SUNCAT Summer Institute: Catalysis for a Sustainable Future, Virtual meeting, 16 - 19 August 2021.
- 11th Energy Colloquium of the Munich School of Engineering (MSE) 2021, Munich/Garching Online, Wednesday, July 28th, 2021.

Abstract/Synopsis

In remedying the Earth from the overreliance on fossil fuels paradigm toward more sustainable and greener options, *i.e.*, renewable energy, there is no doubt an opportune place exists for electrochemical energy conversion and storage devices (electrolyzers, fuel cells, batteries, etc.). Electrocatalysis offers several solutions for efficient energy conversion and storage. In turn, the crucial role and significance of the electrified electrode/electrolyte interface in optimizing electrochemical systems must be emphasized. Therefore, grasping the processes, phenomena, and mechanisms occurring at the electrode/electrolyte interface is a prerequisite and significant for optimizing electrochemical systems. To this end, the advent of sub-microsecond laser pulses has paved the way and eased the investigations of the electrochemical interface (*e.g.*, electric double layer), which is problematic. Remarkably, the laser-induced current transient (LICT) technique has proven to be a valuable and unique tool for measuring critical parameters of the electrified interface, such as the potential of maximum entropy (PME) and the potential of zero charge (PZC). The knowledge of the PME is essential as the net orientation of dipoles and solvent layer structure at the electrode/electrolyte interface can immensely impact electrochemical processes such as the electrode catalytic activity and the charge and mass transfer.

In this dissertation, the theory behind the LICT technique is accentuated, laying the foundation for the relevant information about the experimental setup and design. Specific applications of the LICT methodology in probing the electrolyte (cation, anion, and pH) effects are studied using various electrodes and electrolytes. In general, the hypothesis that "*the closer the PME is to the thermodynamic equilibrium potential of a specific electrocatalytic reaction, the faster the kinetics of the reaction should be*" was further tested to conform with all the investigations performed. Notably, using a polycrystalline Au (Au_{pc}) electrode and 0.5 M Na_2SO_4 and K_2SO_4 solutions, pH, cation, and dissolved oxygen effects were probed. The PME of Au_{pc} shifts towards more positive potentials as the pH increases or O_2 is introduced. The PME exhibited a higher sensitivity to the pH in the presence of K^+ than Na^+. In this regard, the two alkali metal cations cannot be considered equal supporting electrolytes. A mixture of the two cations shifted the different PME values toward "an average" value significant for enhancing the oxygen reduction reaction (ORR) activity.

In another study, atomic layer deposition (ALD) deposited palladium (Pd) monolayers (MLs) on the Au electrodes were investigated. The system (electrode as mentioned earlier and electrolyte, *i.e.*, varying concentrations or pHs of perchloric acid solutions) was probed *via* the LICT, cyclic voltammetry (CV), and electrochemical impedance spectroscopy (EIS) methodologies. The PME and minimum double-layer capacitance correlated, with the latter drifting to more positive values, indicating the difference between the two parameters. At a higher pH of 2, the PME value was calculated as *ca*. 0.66 V *vs*. reversible hydrogen electrode (RHE). In comparison, the PME value increased to *ca*. 0.71 V *vs*. RHE at a lower pH of 0, suggesting that proton reduction in the electrolyte tremendously promotes the hydrogen evolution reaction (HER). The cation effect was probed using electrochemically deposited Pd MLs on an Au electrode and 0.1 M AMOH (AM = Li^+, Na^+, K^+, Cs^+). The obtained PME results show that Cs^+ is well suited to enhance the HER, whereas Li^+ promotes the ORR. Cation effect investigations on SURMOF electrodes revealed an exciting trend. Here, Cs^+ showed the best performance toward the oxygen evolution reaction (OER). For the NiHCF electrode, different sodium-based anions NaX (X = ClO_4^-, NO_3^-, Cl^-, SO_4^{2-}, CH_3COO^-) were deployed to probe the anion effect. Multiple PMEs were found, and the interpretation of the data became challenging, albeit the impact of anions in the degradation processes and toward the understanding of intercalation and deintercalation mechanisms were also observed. Stemming from these findings, one can infer that electrolyte components drastically influence electrode activity.

Moreover, specifically targeted and fastidious cell design makes it possible to simultaneously conduct electron paramagnetic resonance (EPR) spectroscopic and electrochemical measurements like CV. As such, the informative power of a single electrochemical experiment can be drastically increased with the detection of paramagnetic species at the electrochemical interfaces. As both EPR and electrochemical techniques have characteristic demands on the experimental setup, this study describes the challenges, design, and results for an exemplary electrochemical system. Within a solid/liquid system, adsorbed hydrogen atomic species were monitored at the surface of platinum (Pt) electrodes, attempting to detect and identify them using EPR spectroscopy. However, a functional *in-situ* EC-EPR cell was constructed and tested before that. The EPR signal reveals the dynamics of paramagnetic species at 0.25 V to 0.3 V *vs*. a palladium hydride (PdH) reference electrode. This work discusses the synergetic informative power of combined electrochemical and EPR experiments.

In a nutshell, within the framework of this dissertation, electrochemical reactions have been studied by combining a host of electrochemical methodologies, *i.e.*, cyclic voltammetry, *in-situ* laser-induced current transient technique, electrochemical impedance, and *in-situ* electrochemical electron paramagnetic resonance spectroscopic methods. Combining two or more electrochemical techniques enhances the electrochemical measurements' value, authenticity, and informative power.

Kurzfassung

Beim Übergang von einer übermäßigen Abhängigkeit von fossilen Brennstoffen zu nachhaltigeren und umweltfreundlicheren Optionen, *d.h.* erneuerbaren Energien, ist der Einsatz elektrochemischer Energieumwandlungs- und -speicherungssysteme (Elektrolyseure, Brennstoffzellen, Batterien usw.) zweifellos sinnvoll. Die Elektrokatalyse bietet mehrere Lösungen für eine effiziente Energieumwandlung und -speicherung. Im Gegenzug muss die entscheidende Rolle und Bedeutung der elektrifizierten Elektrode/Elektrolyt-Grenzfläche bei der Optimierung elektrochemischer Systeme hervorgehoben werden. Daher ist das Verständnis der Prozesse, Phänomene und Mechanismen, die an der Grenzfläche zwischen Elektrode und Elektrolyt ablaufen, eine Voraussetzung und von großer Bedeutung für die Optimierung elektrochemischer Systeme. Das Aufkommen von Submikrosekunden-Laserpulsen hat den Weg dafür geebnet und die Untersuchung problematischer elektrochemischer Grenzflächen (*z.B.* elektrische Doppelschichten) erleichtert. Bemerkenswerterweise hat sich die Technik der laserinduzierten Stromtransienten (LICT) als wertvolles und einzigartiges Werkzeug zur Messung kritischer Parameter der elektrifizierten Grenzfläche erwiesen, wie *z.B.* des Potentials der Maximalen Entropie (PME) und des Potentials der Nullladung (PZC). Die Kenntnis des PME ist von entscheidender Bedeutung, da die Nettoorientierung der Dipole und die Struktur der Lösungsmittelschicht an der Elektroden-Elektrolyt-Grenzfläche elektrochemische Prozesse wie die katalytische Aktivität der Elektrode und den Ladungs- und Stofftransport wesentlich beeinflussen können.

In dieser Dissertation wird die Theorie hinter der LICT-Methode erläutert, die die Grundlage für die relevanten Informationen über den Versuchsaufbau und die Versuchsplanung bildet. Spezifische Anwendungen der LICT-Methode zur Untersuchung von Elektrolyteffekten (Kationen, Anionen und pH-Wert) werden mit verschiedenen Elektroden und Elektrolyten untersucht. Im Allgemeinen wurde die Hypothese "*Je näher das PME am thermodynamischen Gleichgewichtspotential einer spezifischen elektrokatalytischen Reaktion liegt, desto schneller sollte die Reaktionskinetik sein*" weiter getestet, was mit allen durchgeführten Untersuchungen übereinstimmt. Unter Verwendung einer polykristallinen Au-Elektrode (Au_{pc}) und 0,5 M Na_2SO_4- und K_2SO_4-Lösungen wurde insbesondere der Einfluss von pH-Wert, Kationen und gelöstem Sauerstoff untersucht. Die PME der Au_{pc} verschiebt sich zu positiveren Potentialen, wenn der pH steigt oder O_2 hinzugefügt wird. In Gegenwart von K^+ reagiert die PME empfindlicher auf den pH-Wert als in Gegenwart von Na^+. In dieser Hinsicht können die beiden Alkalimetallkationen nicht als gleichwertige Stützelektrolyte angesehen werden. Eine

Mischung der beiden Kationen verschiebt die unterschiedlichen PME-Werte in Richtung eines "Mittelwertes", der für die Steigerung der Aktivität der Sauerstoffreduktionsreaktion (ORR) von Bedeutung ist.

In einer weiteren Studie wurden durch Atomlagenabscheidung (ALD) abgeschiedene Palladium-Monoschichten (MLs) auf Au-Elektroden untersucht. Das System (Elektrode wie oben beschrieben und Elektrolyt, *d.h.* verschiedene Konzentrationen oder pH-Werte von Perchlorsäurelösungen) wurde mittels LICT, zyklischer Voltammetrie (CV) und elektrochemischer Impedanzspektroskopie (EIS) untersucht. Die PME und die minimale Doppelschichtkapazität korrelierten miteinander, wobei letztere zu positiveren Werten driftete, was auf einen Unterschied zwischen den beiden Parametern hinweist. Bei einem höheren pH-Wert von 2 wurde der PME-Wert mit *ca.* 0,66 V gegen eine reversible Wasserstoff-Elektrode (RHE) berechnet. Im Vergleich dazu stieg der PME-Wert bei einem niedrigeren pH-Wert von 0 auf *ca.* 0,71 V gegen die RHE, was darauf hindeutet, dass die Protonenreduktion im Elektrolyten die Wasserstoffentwicklungsreaktion (HER) stark fördert. Der kationische Effekt wurde mit elektrochemisch abgeschiedenen Pd-MLs auf einer Au-Elektrode und 0,1 M AMOH (AM = Li^+, Na^+, K^+, Cs^+) untersucht. Die erhaltenen PME-Ergebnisse zeigen, dass Cs^+ gut geeignet ist, die HER zu verstärken, während Li^+ die ORR fördert. Untersuchungen des Kationeneffekts an SURMOF-Elektroden zeigten einen spannenden Trend. Hier zeigte Cs^+ die beste Leistung bei der Sauerstoffentwicklungsreaktion (OER). Für die NiHCF-Elektrode wurden verschiedene Natrium-basierte Anionen NaX (X = ClO_4^-, NO_3^-, Cl^-, SO_4^{2-}, CH_3COO^-) verwendet, um den Anionen-Effekt zu untersuchen. Es wurden mehrere PME gefunden, und die Interpretation der Daten erwies sich als schwierig, obwohl auch die Auswirkungen von Anionen auf die Degradationsprozesse und das Verständnis der Interkalations- und Deinterkalationsmechanismen beobachtet wurden. Aus den Ergebnissen lässt sich ableiten, dass die Elektrolytbestandteile die Elektrodenaktivität erheblich beeinflussen.

Darüber hinaus ermöglicht ein gezieltes und ausgeklügeltes Zelldesign die gleichzeitige Durchführung von Elektronen-Paramagnetischen-Resonanz-Messungen (EPR) und elektrochemischen Messungen wie CV. Dadurch kann die Aussagekraft eines einzelnen elektrochemischen Experiments durch den Nachweis paramagnetischer Spezies an elektrochemischen Grenzflächen drastisch erhöht werden. Da sowohl EPR als auch elektrochemische Techniken charakteristische Anforderungen an den experimentellen Aufbau stellen, werden in dieser Studie die Herausforderungen, der Aufbau und die Ergebnisse für ein beispielhaftes elektrochemisches System beschrieben. In einem Fest-Flüssig-System wurden

an der Oberfläche von Platin (Pt)-Elektroden adsorbierte Wasserstoffatomspezies überwacht und mittels EPR-Spektroskopie detektiert und identifiziert. Zuvor wurde jedoch eine funktionsfähige *in-situ* EC-EPR-Zelle gebaut und getestet. Das EPR-Signal zeigt die Dynamik der paramagnetischen Spezies bei 0,25 V bis 0,3 V in Bezug auf eine Palladiumhydrid (PdH)-Referenzelektrode. In dieser Arbeit wird die synergetische Aussagekraft von kombinierten elektrochemischen und EPR-Experimenten diskutiert.

Zusammenfassend lässt sich sagen, dass im Rahmen dieser Dissertation elektrochemische Reaktionen durch die Kombination verschiedener elektrochemischer Methoden untersucht wurden: zyklische Voltammetrie, laserinduzierte *in-situ* Stromtransiententechnik, elektrochemische Impedanz und elektrochemische *in-situ* Elektronenspinresonanzspektroskopie. Die Kombination von zwei oder mehr elektrochemischen Verfahren erhöht den Wert, die Authentizität und die Aussagekraft elektrochemischer Messungen.

Acknowledgments

Without any iota of doubt, the realization of this dissertation could not have been accomplished without the help and support of several colleagues and employees throughout my over four-year stay at the Physics of Energy Conversion and Storage (ECS) chair for my master's and doctoral studies, respectively. In this regard, I would like to unreservedly express my profound appreciation, respect, and gratitude to …

… **Prof. Dr. Aliaksandr S. Bandarenka** for the rare opportunity he offered me by accepting and supervising me, first as a master's student and afterward as a Ph. D. candidate in his chair. I must admit that the research topic really challenged me to work extra hard, making the entire work extremely exciting as I combined several intriguing techniques to merge physics and electrochemistry in a beautiful escapade. Let me hasten to add that I benefited greatly from his patient guidance, high research demands, critical scientific thinking, and adroit problem-solving skills. These values will undoubtedly stupendously enrich my life choices and ambitions.

… **Prof. Dr. Heine Anton Hansen** for accepting to be my doctoral dissertation's second examiner and reviewer. In this regard, I would like to express my most profound appreciation for his time, constructive criticisms, guidance, and warmest support.

I wish to single out **Dr. Elena L. Gubanova** for her exemplary guidance, unparalleled communication skills, constant push, motivation, pleasing scientific discussions, and supervision which led to the successful completion of my doctoral study through the publication of manuscripts and, finally, this dissertation. I am highly indebted to her for assisting me in realizing this feat.

Furthermore, I want to highlight the enormous contribution I received from **Dr. Sebastian A. Watzele**, **Dr. Johannes Fichtner**, and **Dr. Batyr Garlyyev** through scientific discussions from their rich expertise and background in electrochemistry, which guided and charted my research focus. Notably, I received excellent guidance from some of them when I started investigating the *in-situ* EC-EPR spectroscopy methodology, which has now been established in our chair.

Special thanks to **Dr. Xing Ding** for introducing me to the laser-induced current transient measurement technique and collaborating on several published manuscripts. Indeed, his unique personal relations and fruitful and intense scientific discussions were impeccable and will remain with me for a lifetime, as they left an indelible mark on me. Additionally, I wish to show my gratitude to **Rainer Götz** for his assistance with electron paramagnetic resonance spectroscopy. His insights on experimental measurements and data analysis came in handy for me during my research. Great appreciation to **Emre Keleş** for the partnership we established, leading to a book chapter and results from research work produced in **sections 5.3.4.2** and **6.6** of my dissertation.

Now, I appreciate other former and current members of the *ECS* group for the friendly relationship and pleasant working atmosphere throughout my stay at the chair. Specifically, **Dr. Shujin Hou**, **Dr. Richard Haid**, **Dr. Jeongsik Yun**, **Dr. Weijin Li**, **Xiaohan Sun**, **Philipp Marzak**, **Dr. Daniel Scieszka**, **Dr. Regina Kluge**, **Dr. Yunchang Liang**, **Dr. Rohit Ranganathan Gaddam**, **Maximilian Schart**, **Jongho Kim**, **Simon Helmer**, **Xiaoxin Ma**, **Muhamad Hilmi Aufa**, **Nina Thomsen**, **Omotayo Alexander Olanusi**, **Xaver Lamprecht**, **Leif Carstensen**, **Thorsten Schmidt**, **Kun-Ting Song**, **Göktug Yesilbas**, **Peter Schneider**, **Felix Haimerl**, **Yapeng Cheng**, **Raphael Streng**, **Christian Schott**, **Kais Sadraoui,** and **Iago Ungerer**. Moreover, I especially thank our secretaries, **Manuela Ritter** and **Susanne Tillich,** for their dedication and incredible, unbiased administrative support. Also, to our technical staff, **Siegfried Schreier,** for his spectacular work and the great conversations we usually had. I dare say that without his availability, generosity, and impressive suggestions, the accomplishment of this research work would have been impossible. Our master students, **Michael Kopp, Eduard Antics**, and **Adrian Himmelreich,** for their remarkable assistance under my guidance.

Next, I would like to profusely thank **Dr. Xing Ding** profusely, **Dr. Shujin Hou**, and **Dr. Richard Haid** for always lending a helping hand when I needed it and for allowing me to be part of some of their projects.

Deserving special commendations are my local church in Munich, notably **Katherine Wagner**, who helped me through proofreading, and the Ghanaian students' group, as they have been great pillars of support to me, especially during some challenging moments.

Finally, I would like to thank my mother, Madam **Grace Augustina Ewurafua Quansah,** for her constant encouragement and belief in me throughout my studies, particularly during my doctorate. I also appreciate my sister, **Henrietta Catherine Sarpey**, for single-handedly catering for our dear mother in my long absence. I am also aware of the enduring love and unconditional support I received from the entire family. Most importantly, the successful completion of this work would not have been possible without the grace, love, magnanimity, and endless and unwavering support I received from my wife, **Vivian Augusta Sarpey**, who has been an anchor and rock for me in the last years.

Glossary - Acronyms/Abbreviations

Symbol	**Description**
AIMD	Ab Initio Molecular Dynamics
AM	Alkali Metal
AFC	Alkaline Fuel Cell
AR	Assessment Report
ALD	Atomic Layer Deposition
BEV	Battery Electric Vehicle
CO_2	Carbon dioxide
C_{dl}	Capacitance of the double-layer/Double-layer capacitance
CL	Catalytic Layer
CMC	Charge of Maximum Capacitance
CME	Charge of Maximum Entropy
CES	Chemical Energy Storage
CA	ChronoAmperometry
CAES	Compressed Air Energy Storage
CE	Counter Electrode
CMIP	Coupled Model Intercomparison Project
CV	Cyclic Voltammogram/Cyclic Voltammetry
DFT	Density Functional Theory
DFTMD	Density Functional Theory Molecular Dynamics
DoD	Depth of Discharge
DHFC	Direct Hydrocarbon Fuel Cell
ESI	Earth Similarity Index
ESM	Earth System Model
EMIC	Earth System Models of Intermediate Complexity
EV	Electric Vehicle

EDL	Electric Double Layer
EES	Electrical Energy Storage
EEI	Electrified Electrode/Electrolyte Interface
EESS	Electrochemical Energy Storage System
ECSA	ElectroChemical active Surface Area
EIS	Electrochemical Impedance Spectroscopy
EC-EPR	ElectroChemical Electron Paramagnetic Resonance
Emf	ElectroMotive Force
EPR	Electron Paramagnetic Resonance
ESS	Energy Storage System
EEC	Equivalent Electric Circuit
FBESS	Flow Battery Energy Storage System
FES	Flywheel Energy Storage
FCEV	Fuel Cell Electric Vehicle
GDL	Gas Diffusion Layer
GMST	Global Mean Surface Temperature
GHG	GreenHouse Gas
HEV	Hybrid Electric Vehicle
HBE	Hydrogen Binding Energy
HESS	Hydrogen Electrode in the Same Solution
HER	Hydrogen Evolution Reaction
HOR	Hydrogen Oxidation Reaction
Hupd	Hydrogen UnderPotential Deposition
IHP	Inner Helmholtz Plane
IPCC	Intergovernmental Panel on Climate Change
ICE	Internal Combustion Engine
IEA	International Energy Agency
LiB	Lithium(Li)-ion Battery

LICT	Laser-Induced Current Transient
LIPT	Laser-Induced Potential Transient
LITJ	Laser-Induced Temperature Jump
LITT	Laser-Induced Transient Technique
LBL	Layer-By-Layer
LGR	Loop Gap Resonator
MES	Mechanical Energy Storage
MEA	Membrane Electrode Assembly
MMO	Mercury-Mercurous Oxide
MMS	Mercury-Mercurous Sulfate
MCFC	Molten Carbonate Fuel Cell
ML	MonoLayer
Nd:YAG	Neodymium-doped Yttrium Aluminum Garnet
n-EC-STM	noise ElectroChemical Scanning Tunneling Microscopy
NMR	Nuclear Magnetic Resonance
OHP	Outer Helmholtz Plane
OER	Oxygen Evolution Reaction
ORR	Oxygen Reduction Reaction
PdH	Palladium Hydride
PAFC	Phosphoric Acid Fuel Cell
PGM	Platinum Group Metal
PEM/PEMFC	Polymer Electrolyte (Proton Exchange) Membrane Fuel Cell
PSB	PolySulfide Bromide
PTFE	PolyTetraFluoroEthylene
PME	Potential of Maximum Entropy
PZC	Potential of Zero Charge
PZFC	Potential of Zero Free Charge
PZTC	Potential of Zero Total Charge

PZT	Potential of Zero Transient
PBA	Prussian Blue Analog
PHS	Pumped Hydroelectric Storage
QCM	Quartz Crystal Microbalance
RE	Reference Electrode
RCP	Representative Concentration Pathway
RHE	Reversible Hydrogen Electrode
SHINERS	SHell-Isolated Nanoparticle-Enhanced Raman Spectroscopy
SSC	Silver-Silver Chloride
SEV	Smart Electric Vehicle
SOFC	Solid Oxide Fuel Cell
SHE	Standard Hydrogen Electrode
SMES	Superconducting Magnetic Energy Storage
SEIRAS	Surface-Enhanced InfraRed Absorption Spectroscopy
SERS	Surface-Enhanced Raman Spectroscopy
SURMOF	SURface mounted Metal-Organic Framework
TW/GW/MW/kW	Terawatt/Gigawatt/Megawatt/Kilowatt
TES	Thermal Energy Storage
TCRE	Transient Climate Response to Cumulative CO_2 Emission
UPS	Uninterrupted Power Supply
VR	Vanadium Redox
V2G	Vehicle to Grid
VSFG	Vibrational Sum-Frequency Generation
WWS	Water, Wind, and Solar
WE	Working Electrode
XAS	X-ray Absorption Spectroscopy
XRS	X-Ray Scattering
ZnBr	Zinc Bromide

Nomenclature/Symbols

Symbol	Description	Unit
A	Area	m^2/cm^2
C	Capacitor/Capacitance	Farad (F/μF)
$C_{dl}/Z_{dl}/q_{dl}$	Capacitance of the double-layer	$\mu F\ s^{1-n}\ cm^{-2}$
Q	Charge density	$\mu C\ cm^{-2}/nC\ cm^{-2}$
C	Concentration	M/mM/μM
Z or Q	Constant Phase Element	$S\ s^n$
	Cost of Energy	Euro/kW
D	Diffusion coefficient	$cm^2\ s^{-1}$
E	Energy	J/mJ
E	Energy density	$MJ\ m^{-3}/Wh\ kg^{-1}$
F	Fluence	$mJ\ cm^{-2}$
f/ν	Frequency	s^{-1}/Hz/GHz
G	Gerischer element	$S\ s^{1/2}\ \&\ s^{-1}$
H/h	Height/Distance	m/km
H_{hyd}	Hydration energy	$kJ\ mol^{-1}$
L	Inductor/Inductance	Henry (H)/$kg\ m^2\ s^{-2}A^{-2}$
B/H	Magnetic field	T/mT/μT
ρ	Mass density	$g\ cm^{-3}/\mu g\ cm^{-2}$
P	Power	W/mW
R	Resistor/Resistance	Ohm
	Scan rate	$mV\ s^{-1}$
μ	Shear modulus	$g\ cm^{-1}\ s^{-2}$
	Tafel slope	$mV\ dec^{-1}$
T	Temperature	K/°C
t/T	Time	s/ms/minutes
V	Voltage/Potential	Volt (V)
V	Volume	m^3
V	Velocity/Speed	$m\ s^{-1}$
W	Warburg impedance	Ohm/Ohm cm^2
ϕ	Work function	eV

Name of Chemical	**Description**
ACN	Acetonitrile
CO	Carbon monoxide
CsOH	Cesium hydroxide
CD_3OD	Deuterated methanol
DMF	Dimethyl formamide
DMSO	Dimethyl sulfoxide
HCl	Hydrochloric acid
H_2O_2	Hydrogen peroxide
OH^-	Hydroxyl
LiOH	Lithium hydroxide
$LiClO_4$	Lithium perchlorate
CH_3OH	Methanol
CH_2Cl_2	Methylene bichloride
NiCd	Nickel Cadmium
NiMH	Nickel Metal Hydride
N_2O	Nitrogen oxide
$HClO_4$	Perchloric acid
KOH	Potassium hydroxide
K_2SO_4	Potassium sulfate
H^+	Proton
RbOH	Rubidium hydroxide
$NaCH_3COO$ (NaOAc)	Sodium acetate
NaCl	Sodium chloride
NaCl-KCl	Sodium chloride – Potassium chloride
NaOH	Sodium hydroxide
$NaNO_3$	Sodium nitrate
$NaClO_4$	Sodium perchlorate
Na_2SO_4	Sodium sulfate
NaS	Sodium sulfide
H_2SO_4	Sulfuric acid
O_2^-	Superoxide
H_2O	Water

Table of Contents

List of Publications - Manuscripts IV

Conference Contributions V

Abstract/Synopsis VI

Kurzfassung IX

Acknowledgments XII

Glossary - Acronyms/Abbreviations XIV

Nomenclature/Symbols XVIII

Table of Contents XX

1.0 Introduction and General Overview 1

- **1.1 The Current Global Energy-Related Challenges** 2
- **1.2 Reducing the Over-reliance on Fossil Fuels: Renewable Energy and Other Alternatives** 7
- **1.3 Energy Storage Systems** 9
- **1.4 The Hydrogen-Based Economy** 14
- **1.5 Methodological Perspectives** 19
- **1.6 Scope and Goals of the Dissertation** 21

2.0 Theoretical Underpinnings - Electrochemistry 23

- **2.1 Electrochemistry** 23
  - 2.1.1 Electrode 24
  - 2.1.2 Electrolyte 24
- **2.2 Electrocatalysis** 25
- **2.3 The Electrified Solid/Liquid Interface** 27
  - 2.3.1 The Electric Double Layer 27
- **2.4 Electrochemical Cell Potential and Overpotentials** 31
  - 2.4.1 Faraday’s Laws 33
- **2.5 Reaction Kinetics at the Electrode Surface** 34
- **2.6 The Principle of Mass Transport** 39
  - 2.6.1 Diffusion 39
  - 2.6.2 Convection 40
  - 2.6.3 Migration 41
- **2.7 Ohmic Drop (Uncompensated Resistance)** 42
- **2.8 Sabatier Principle, The Volcano Plot & Scaling Relations** 42
- **2.9 Active Sites** 46
- **2.10 Essential Electrocatalytic Reactions** 47
  - 2.10.1 Electrochemical Water Splitting 47
  - 2.10.2 Fuel Cells – Fundamental Concepts 54

3.0 Fundamentals of Interfacial Processes & Characterization 63

- **3.1 Water Layer Structure at the Interface** 63
- **3.2 Potential of Zero Charge and Potential of Maximum Entropy** 66

3.3 Techniques for Determining the PZC and PME ... 71
3.3.1 Electrocapillary Method ... 71
3.3.2 Capacitance Method ... 72
3.3.3 CO Charge Displacement Method ... 74
3.3.4 N_2O Reduction Method ... 76
3.3.5 Other Methodologies ... 78

3.4 Overview of the Laser-Induced Transient Techniques ... 79
3.4.1 Theoretical Considerations of the Laser-Induced Current Transient Technique ... 80
3.4.2 Origin of a System Response during a Laser-Induced Current Transient Experiment ... 83
3.4.3 Important Laser Parameters and Specifications for the LICT Measurements ... 86

3.5 The Impact of Electrolyte Components in Electrocatalysis ... 87
3.5.1 Solvent Effect ... 89
3.5.2 Cation Effect ... 89
3.5.3 Anion Effect ... 91
3.5.4 pH Effect ... 93

4.0 Other Experimental & Characterization Techniques ... 95

4.1 Electrochemical Techniques ... 95
4.1.1 Electrochemical Three Electrode Setup/Configuration ... 95
4.1.2 Voltammetric Techniques ... 97
4.1.3 Electrochemical Quartz Crystal Microbalance Electrode ... 100
4.1.4 Chronoamperometry ... 101
4.1.5 Electrochemical Impedance Spectroscopy ... 102

4.2 Electron Paramagnetic Resonance Spectroscopy ... 105

5.0 Experimental Methodological Aspects ... 108

5.1 Electrochemical Cell ... 108

5.2 Electrochemical Measurements ... 110
5.2.1 Preparation of Electrodes ... 111
5.2.2 Preparation of Electrolytes ... 115
5.2.3 Electrochemical Cleaning and CV Measurements ... 116

5.3 Laser-Induced Current Transient Technique Measurements ... 117
5.3.1 LICT Setup ... 117
5.3.2 LICT Measurements for the AT-cut Polycrystalline Au Quartz ... 118
5.3.3 LICT Measurements for SURMOFs ... 119
5.3.4 LICT Measurements for Pd MLs on Au EQCM ... 120
5.3.5 LICT Measurements for PBA Battery System Deposited on Au QCM ... 121

5.4 Electrochemical Impedance Spectroscopy ... 122

5.5 Electron Paramagnetic Resonance Spectroscopy ... 122
5.5.1 Sample Preparation for the *In-Situ* EC-EPR Measurement ... 122
5.5.2 Electrochemical Investigations - Cyclic Voltammetry ... 123
5.5.3 Specifications of the Electron Paramagnetic Resonance Spectroscopy Device & *In-situ* EC-EPR Measurement ... 123

5.6 Design and Construction of the *In-situ* EC-EPR Cell ... 124
5.6.1 Discussion on the Design Evolution ... 124

6.0 Results & Discussions ... 132

6.1 Interface Structure and pH Effect ... 133

6.2 pH Effect in the Presence of Alkali Metal Cations ... 136

6.3 Cation Effect on Surface-Mounted Metal-Organic Framework Derivatives ... 148

6.4 Anion Effect on Prussian Blue Analog Battery Electrodes ... 152

6.5 pH Effect on Pd Monolayers Deposited on Au QCM Electrodes ... 155

6.6 Cation Effect on Pd Monolayers Deposited on Au QCM Electrodes in Alkaline Media ... 160

6.7 Electron Paramagnetic Resonance Spectroscopy ... 162
6.7.1 Hydrogen Adsorption on Pt ... 162

7.0 Concluding Remarks and Perspectives ... 169

8.0 Appendix /Annex ... 173

8.1 List of Figures ... 175

8.2 List of Tables ... 184

8.3 Related Publications ... 185

9.0 Bibliography ... 209

1.0 Introduction and General Overview

The so-called hydrogen economy, which involves electrochemical-based technologies (*e.g.*, electrolyzers and fuel cells), is arguably the most promising driver of "green" energy. It is vital to ensure that global energy generation (stationary, portable, and mobile) is decoupled from the relatively high carbon emission cycle. The realization of the hydrogen-based economy would invariably result in a massive reduction of carbon emissions, especially in air pollution, which originates from the fossil fuels often used in generating electricity, other energy-related demands, and in the internal combustion engine of most vehicles, thereby essentially addressing the significant and urgent global environmental challenges of global warming and climate change. In this respect, this chapter explicitly reveals the emerging/eminent energy crises and makes a strong case for employing renewables, principally highlighting the significance of hydrogen as fuel. The discussion proceeds to tackle the essential fundamentals necessary to understand the principles behind the various technologies. More specifically, the paramount interest lies in comprehending the underlying principles of electrocatalysis at the electrified electrode/electrolyte interface, which will be discussed in detail in subsequent chapters.

1.1 The Current Global Energy-Related Challenges

Advances in innovations and technology, especially since the "Industrial Revolution," have triggered mammoth transformations and improvements, specifically in the health and industrial sectors. These vital milestones and developments have led to progress in the quality of human life. While the global birth rate has declined significantly, especially in the last 50 years, global maternal and infant mortality has fallen, and global health outcomes and life expectancy have improved. Therefore, it is no surprise that humankind's population continues to surge astronomically. Statistics show that in 1804, the world's population stood at 1 billion, and currently (October 2022), this figure has risen to *ca*. 7.98 billion, with an average growth rate of *ca*. 1% annually.[1] The United Nations predicts a population of *ca*. 10 billion by 2057, provided no significant alteration in the current trend occurs.[2] **Figure 1.1** provides supplementary information on the statistics.

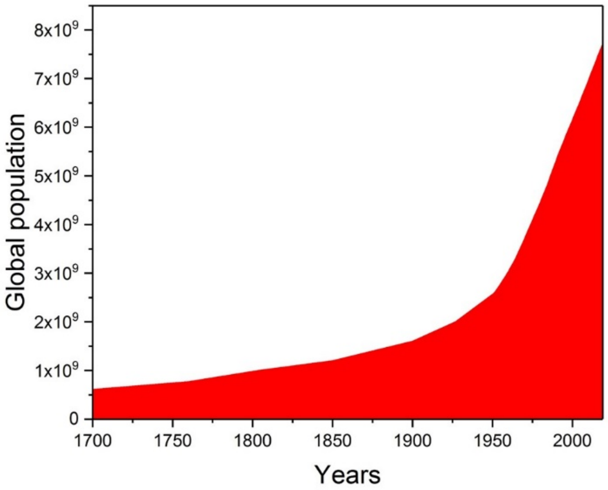

Figure 1.1. *A clear depiction of the accelerated growth in the global population from 1700 to the present time (2022). The statistical data for the plot was obtained from reference.*[1]

The dramatic and continuous population hikes come with accompanying challenges, namely, increasing energy and vital amenities demands, especially as developing countries have set ambitious electrification, industrialization, and modernization (urbanization) agendas. This intriguing but well-envisaged development is already underway, as evident in the following statistics: 17% of the global population, based mainly in Sub-Saharan Africa and developing Asia, representing 1.278 billion people lived without electricity in 2013, and this reduced marginally to *ca*. 14%, *i.e.*, 1.071 billion people in 2016.[3] Due to the recent global challenges, including but not limited to the COVID-19 pandemic, the deteriorating world economy, and energy price hikes, the progress made in increasing universal access to electricity plateaued from 2020 to 2021.[3] It declined for the first time in two decades in 2022 to 774 million people from 754 million people in 2021. Another remarkable development in global electricity production was the giant leap observed between 1973 and 2013. A little over 280% rise in universal electricity production was recorded for the already mentioned period, representing *ca*. 23,391 TWh from the initial 6,144 TWh.[4] In 2019, the figure rose to *ca*. 28,000 TWh, and this trend is projected to further increase by 80% to *ca*. 50,000 TWh in 2050.[5]

From a different perspective, the global average energy consumption rate in 2018 was pegged at *ca*. 18.6 TW and was *ca*. 13.5 TW in 2001.[6] The forecast indicates that by 2050, it will amount to *ca*. 30 TW. On the other hand, the universal total power generation capacity stood abysmally at *ca*. 7 TW in 2018 and was estimated to be *ca*. 7.9 TW in 2021.[6] Meanwhile, on the premise of the growing global energy demand, this trend will surge in the coming years, with a 37% increase forecast in the next decade, and a doubling is projected to be evident by 2050.[7] These looming statistics imply that sufficient (available, reliable, stable, and non-erratic) energy must be generated to meet the world's growing energy consumption rate, which is worryingly turning into a global energy crisis and has been termed the "terawatt challenge", or more generally, "generation *versus* consumption" challenge by Smalley.[8]

Current attempts to address this issue heavily rely on non-renewable primary energy sources, particularly fossil fuels, whose reserves are witnessing consistent and continuous depletion. It is well known that these hydrocarbon resources are rare and in limited supply across the globe. According to research, at the current consumption rate of these non-renewable primary energy sources, in addition to their scarcity in the world, most of them will be exhausted even before the next century (coal ~100 years, natural gas ~60 years, crude oil ~40 years) if this trend is not abated.[9,10] While fossil-based energy sources provide about 80% of the current energy mix,[9] it is paramount to have alternatives for the future, *e.g.*, renewable energy sources. Nevertheless, fossil fuels will likely continue to supply more than 60% of the world's energy demand by 2040.[11] That notwithstanding, the exclusive reliance on certain or few energy sources will render economies susceptible to innumerable problems, such as political instabilities, market fluctuations, and so on, besides the occurrence of natural disasters and resource depletion. Conversely, diversifying energy sources is mainly concomitant with improving the stability of energy provision, which tremendously affects economic and political stability. Thus, sustaining the diminishing rate of non-renewable primary energy sources such as fossil fuels is yet another vital reason for the terawatt challenge to tackle the predicted calamitous energy crisis.

There is apparent clarity that the massive and continuous global use of fossils will be inevitable, at least in the next two decades. As such, carbon dioxide (CO_2) molecules usually generated through the oxidation of carbon atoms in fossil fuels will continue contributing immensely to global warming.[12,13,14] This means that substantial adverse effects on the environment, atmosphere, and by extension, the weather patterns and climate of the planet Earth, which is a measure that impacts human life, are to be expected. This invariably initiates tremendous modifications in the hydrological cycle, cryosphere, atmospheric circulation patterns, and even with the oceans concerning rising sea levels, etc. Consequently, the magnitude and frequent occurrence of unprecedented natural disasters like hurricanes, tornados, floods, typhoons, droughts, and so on will be rife and on the ascendancy for every *ca*. one (1)°C change in atmospheric temperature.[15,16,17]

The adverse effects of such disasters are not far from now and can be vividly corroborated by recent occurrences. One such example would be the 2021 flash floods in Germany's Rheinland-Pflaz region. To address the issue, an estimated 40.5 billion Euros were spent on damages only.[18] In a similar incident recorded in 2018-2019, the heat and drought period across Germany resulted in damages to the tune of 40 billion Euros.[18] The dire consequences of climate change have already been witnessed all over the world. Besides the drastic economic impacts accompanying this crisis mentioned above, it also immensely impacts the global political, biological (health), and social ecosystems if the trend continues.[19] For instance, sea level rise affects the habitability of delta regions like Bangladesh, salinization of fresh water, species extinction, crop failure, etc. Therefore, innovative, solid decisions and bold measures must be adopted and implemented to curb the occurrence of such disasters. To achieve this ambitious but inevitable goal, it is imperative to consciously reduce the constant emissions of greenhouse gases (GHGs), especially CO_2.

In this light, to reverse and mitigate the impact of the ongoing climate change, 196 UN member states met in Paris in December 2015. They adopted a legally binding charter aimed at limiting global warming to a threshold of 2°C compared to pre-industrial levels by 2050.[17,20] Additionally, stringent measures are to be followed to limit the temperature upsurge to 1.5°C.[17] Prior to adopting and implementing the Paris Agreement, a similar commitment had earlier been made in the so-called Kyoto Protocol held in December 1997. Despite these strong desires to curb global warming, only CO_2 emissions from the energy sector (emanating from the impact of human activities and lifestyles) on the climate systems still account for *ca*. 60% of all global greenhouse gas emissions.[21] Specifically, the concentration of CO_2 emission in 2022 was reported to be 417 ppm (averaged marine surface annual mean value). Meanwhile, it was approximately 315 ppm in 1960, constituting an annual average growth of 2 ppm, particularly in the last decade.[22] This implies that the advanced and industrialized countries must lower nearly 80-95% of their GHG emissions by 2050 compared to 1990.[23] A deliberate decline in fossil fuel consumption is required. Therefore, larger-scale clean energy grids and substitutes for conventional internal combustion engines (ICEs) for vehicles are advocated and must be the way forward to improve the quality of life, mainly in urban areas. Incredibly, this objective has seen massive progress since the Paris Charter, as the intentional push to diminish the use of CO_2 emissions in highly developed countries has yielded substantial growth. Unfortunately, the reverse is the case in developing countries, which have recorded steady increases in CO_2 emission rates due to the drive to industrialize and modernize their societies. The next step to stem this trend is perhaps penalizing developing countries for flouting such enactment to emit more CO_2 in the name of industrialization. However, this will be unfair as the developed economies were engaged in the same act (situation) decades ago. In this regard, developed countries should have a moral imperative to assist developing economies by investing in green technologies to achieve their industrialization agenda without causing further harm to climate patterns. Studies portray that in 2017, the universal greenhouse gas emissions already accrued over 1°C temperature rise relative to the pre-industrial level[17] (*cf.* **Figure 1.2**[24]), a clear indication of non-compliance by some member states. A closer look at **Figure 1.2** reveals that provided there is no alteration in the current rate of global temperature rise (*ca.* +0.2°C per decade), the threshold global warming value of 1.5°C will be in sight between 2030 and 2052.[17,24] However, according to reliable projections, global warming can be kept well below the 1.5°C threshold provided 80% and 100% net zero emission energy is achieved in 2030 and between 2040 and 2055, respectively.[25]

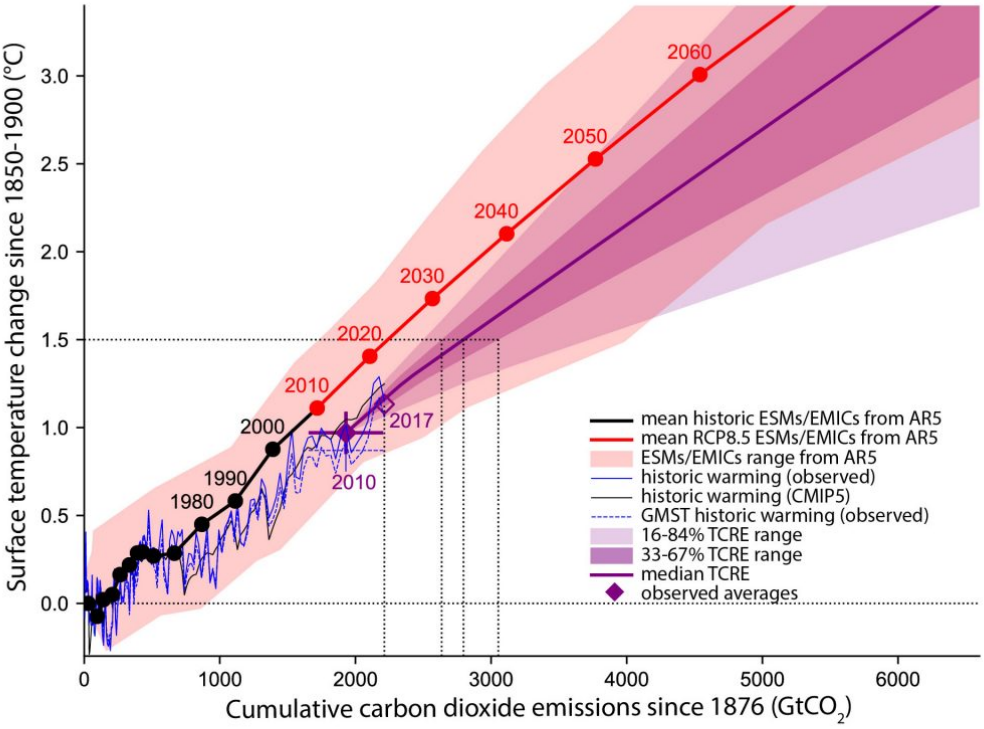

***Figure 1.2**. Graphical depiction of the eminent global warming. It is important to remark that most of the data relate to the fifth assessment report (AR5) released in 2013-2014. The AR5 data originated from 15 Earth system models (ESMs) and 5 Earth system models of Intermediate Complexity (EMICs). Displayed in black are the historical observations, the representative concentration pathway (RCP)8.5 scenario is in red, and the red-shaded plume portrays the range across the models. The solid line with dots depicts the globally averaged near-surface air temperature response to cumulative carbon dioxide (CO_2) emissions in addition to non-CO_2 forcers. The purple-shaded plume and the line signify the temperature response to cumulative CO_2 emissions and the non-CO_2 warming transient climate response to cumulative CO_2 emission (TCRE) distribution. The filled purple diamond represents the 2010 observation of surface temperature change (0.97°C based on the 2006-2015 mean compared to 1850-1900) and cumulative carbon dioxide emissions from 1876 to the end of 2010 of 1,930 $GtCO_2$. Shown as a hollow purple diamond is the value for 2017 based on the latest cumulative carbon emissions up to the end of 2017 of 2,220 $GtCO_2$ and a surface temperature anomaly of 1.1°C based on an assumed temperature increase of 0.2°C per decade. The thin blue line reveals the annual observations, with CO_2 emissions and estimated globally averaged near-surface temperature from scaling the incomplete coverage and blended HadCRUT4 dataset. The thin black line shows the coupled model intercomparison project (CMIP)5 multimodel mean estimate with CO_2 emissions. The thin black line portrays the global mean surface temperature (GMST) historical temperature trends, displaying lower temperature changes (0.87°C) up to 2006-2015, consequently leading to a larger balance in the carbon budget. The dotted black lines illustrate the remaining carbon budget estimates for 1.5°C. It is important to note that these remaining budgets exclude possible Earth system feedback that could reduce the budget, such as CO_2 and CH_4 release from permafrost thawing and tropical wetlands. Reproduced from reference.[24] Open access, permission of unrestricted use.*

As a holistic approach to resolving the problem of climate change, a rigorous search for alternative exoplanets by astrophysicists was activated, leading to the successful discovery of thousands of exoplanets.[26,27] That notwithstanding, only *ca.* ten (10) of these planets are hypothetically habitable per the Earth similarity index (ESI), a measure of similarity in planetary properties in comparison with the Earth's stellar flux and mass or radius (Earth = 1.0). Strictly speaking, a habitable zone is a range of distances or a region around a host star within which liquid water, a critical necessity for life, may exist on an orbiting planet's surface. On this basis, it might be possible to attempt to make at least one other planet besides Earth habitable in the future. However, the budget to execute this project might be exceptionally huge and non-existent, invariably leading to the current reality that the Earth is the only planet supporting life in our solar system.[28] As such, it is expedient to continue to preserve and keep the earth habitable through a conscious effort to regulate human activities that negatively impact the global climate of the planet Earth. This move is essential since the quality of life on a planet is significantly dictated by the nature of the atmosphere and, by extension, the climate.

In a nutshell, to resolve the urgent global warming issue on earth, a transition toward a clean, "green" (net zero)/low-carbon emission energy system is indispensable. Therefore, it is no secret that the world needs radical, innovative, and permanent (long-term) solutions to the current energy-related challenges. On this note, the next section will address the potential of renewable energy sources and how effectively they can help combat climate change.

1.2 Reducing the Over-reliance on Fossil Fuels: Renewable Energy and Other Alternatives

As earlier established, there is a pressing need to develop sustainable alternatives to fossil fuels further to meet the rapidly soaring energy demands, substantially assuage the impact of climate change, and hasten the transition to the envisioned low-carbon emission society.[29,30,31,32] As such, swift and effective actions were adopted since the Paris Agreement, leading to tremendous upgrades in almost all renewable energy sources, not limited to wind, wave, solar, tidal, geothermal, hydroelectric, and bio (biomethane, biofuels, biomass) energy, to meet the high commercialization and upscaling standards/demands.[33,34,35]

Remarkably, the BP Energy Outlook 2022 captures the gradual shift of the global dominance of hydrocarbon-based fuels to more clean, low-carbon emission, and sustainable options, including renewables and other non-fossil fuel sources.[36] This is mainly seen in the sharp decline in the overall contribution of fossil fuels toward the global primary energy supply. Simply put, non-fossil contribution to the universal primary energy demand is forecast to be between 60% and 20% in 2050, whereas fossils contributed *ca*. 80% in 2019.[36] **Figure 1.3** illustrates the emerging dominance of clean energy alternatives (renewables and others, including nuclear), further buttressed by the International Energy Agency (IEA) projection that renewable energy and other clean energy sources will contribute over 50% of the global energy capacity expansion by 2050. Leveraging the Paris Agreement, various world leaders' social and political snags towards the upscaling and full-scale implementation of cleaner energy technologies have witnessed dramatic reduction. Consequently, solar (photovoltaics) and onshore wind power are reported to account for a considerable chunk of the global renewable energy generation besides hydro energy.[37,38,39] Put differently, estimates indicate that several TWs of renewable energy sources, mainly water (hydro), wind, and solar (WWS), should be fully installed by 2050, with substantial additional energy capacity already expected to be installed by 2030, provided no unforeseen economic situation hampers the progress.[39,40]

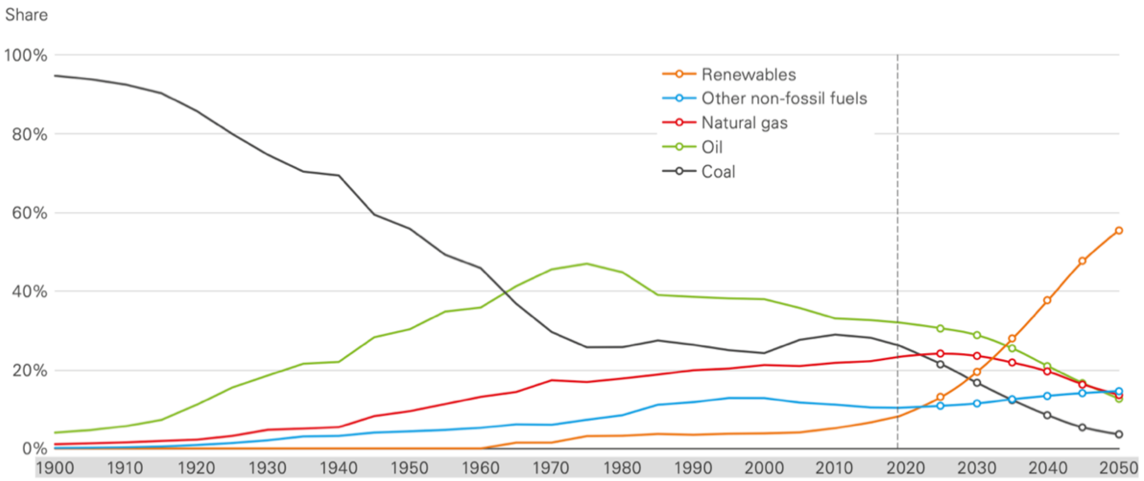

Excludes traditional biomass
Other non-fossil fuels includes hydro and nuclear

Figure 1.3. *The gradual global shift from the over-reliance on fossils to clean, green, low-carbon emission replacements. In 2020, oil contributed over 30%, coal ca. 30%, and natural gas over 20%, indicating ca. 80% of the global energy generation was based on high-carbon emission fossil fuel sources. The narrative in 2050 will be substantially the opposite as the reliance on fossils is predicted to dwindle while renewables, nuclear, and other sources will dominate. Adapted from reference.*[36] *Open access, permission of unrestricted use.*

One critical question worth answering is whether the WWS technologies and other renewables can adequately solve the terawatt challenge. The good news is that the combined theoretical potential of wind and solar energy sources surpasses the predicted future energy demands. Estimates indicate that solar energy can deliver up to 240-340 TW, and wind energy (*i.e.*, wind speeds over 7 m/s and over land or near the shore) can deliver approximately 72-170 TW.[41] The main impediments to the broad commercialization and use can trace their roots from the stochastic and erratic nature of the various renewable energy sources, as they rely heavily on climatic, environmental, and even atmospheric patterns.[42,43]

Another promising substitute to fossils is nuclear energy, thanks to its relatively low CO_2 emission, high volumetric and gravimetric energy densities, and providing a stable and controllable supply of power/energy at a suitable price. However, serious drawbacks exist that exacerbate its potential, which should be tackled head-on. These include the dependence on the limited stores of Uranium/Plutonium, the likelihood of incidents such as the ease of nuclear weapons proliferation, and the unresolved issues regarding nuclear/radioactive waste disposal.[41,44,45,46]

1.3 Energy Storage Systems

Owing to the energy fluctuation and intermittency drawbacks accompanying most renewable energy sources and the need to consume energy upon generation immediately, the so-called "generation *vs*. consumption" challenge occasioned by a discrepancy in energy demand and provision arises/ensues. To smoothly seal and close the erratic/stochastic gap (time and space), employing energy storage systems (ESSs) is prudent. Moreover, some of these energy sources are generated cheaply at locations without any urgent demand for power supply. Hence the need to have mechanisms to store such energies, upscale them to the TW level and transport them elsewhere or for future use. Energy storage involves converting electrical energy from a power network into a form of energy for storage and converted back to electrical energy when needed.[47] Energy storage systems consist of energy/power input (charging) and its corresponding output (discharging) scheme and two energy converters sandwiched between the storage device. Simply put, each energy storage facility is equipped with the following fundamental components: storage medium, power conversion system, and balance of plant.[48]

However, some basic requirements must be fulfilled to implement ESSs effectively. The prerequisites are not restricted to the following: high energy and power densities, high efficiency, reasonable costs for installation and maintenance, long lifetime, quick response rate, and little losses of stored energy due to self-discharge. Admittedly, diverse types of energy storage systems have been developed and are usually categorized by energy storage, *i.e.*, thermal, mechanical, electrical (electromagnetic), chemical, or electrochemical.[49,50,51] In general, with the implementation of an energy storage facility, electricity can be generated and delivered when there is either low demand, low generation cost, or when unreliable energy sources are deployed. These become necessary when there is a high demand for electricity, high generation cost, or other energy generation sources are unavailable.[47,52]

Thermal energy storage (TES) is applicable in special situations and at specific locations. They operate by storing energy in latent heat, sensible heat, or *via* thermochemical means (*i.e.*, adsorption and absorption) in a cold/heat storage medium.[53,54,55] Particularly, when mounting a solar thermal power plant, a typical desert with arid diurnal sunlight is a crucial prerequisite. Apart from storing energy, this technology (*i.e.*, solar chimney, concentrating solar thermal power technologies) can deliver energy (electricity and heat) on demand. Employing solar collectors as the energy source, one can effectively tap into the practicality of molten salt technology[56,57] by generating a by-product like fresh water (for cooking, drinking, etc.) through desalination.

Mechanical energy storage (MES) systems can be categorized into potential energy storage, comprising pumped hydroelectric storage (PHS) and compressed air energy storage (CAES), and kinetic energy storage, namely, flywheel energy storage (FES). The PHS technology is by far the most advanced in this category, boasting large volumes, a relatively low capital cost per unit of energy, and a long storage duration.[58] Therefore, several countries have already operationalized it. PHSs typically offer large capacities (*i.e.*, ranging from MW to several GWs), long life cycles, and high efficiency between 60 and 80%.[59] Regarding capacity, PHSs are well suited in mountainous regions as dams require such geographical locations to augment the width and height of the reserved/trapped water. The dam's operation produces hydroelectricity, which can be fed into the power utility grid. More so, the excess energy generated can be utilized in a different form of energy, where water is pumped from a lower to a higher basin/sink. The current global overall installed PHS generation capacity amount to over 100 GW (over 200 PHS systems), amounting to approximately 3.6% of the universal total energy consumption and 99% in terms of electricity storage capacity.[39,49,58,60,61] Despite these irresistible statistics, PHSs embody some primary drawbacks like geographical conditions (great differential elevation, sufficient rainfalls, large land areas), a very low energy density (for instance, 3 Wh m^{-3} for a 1 m height difference), demanding capital investments, and long construction duration. Additionally, lack of benign environmental conditions, including the removal of trees and vegetation from the vast area of land before the reservoir can be flooded, and the likelihood of flooding inhabited lands closer to the proposed dam site before, during, or even after its construction eventually leads to huge resettlement costs.[49,50,51,62]

As the name suggests, compressed air energy storage (CAES) systems store energy by way of compressed gasses, particularly air, and represent a different type of currently commercially available mechanical ESSs.[63] They are employed for grid operational support functions such as load shifting and regulation control.[63] Amazingly, only two plants of CAES are presently in operation globally, despite their applicability as long-duration and large-scale energy storage.[63] One exists in Huntorf, Germany, and the other in McIntosh, Alabama, USA. The good news is that some proposed projects, mainly in Europe and the USA, are underway, with others stalled.[63] CAESs provide a large capacity (hundreds of MW-level), small self-discharge losses, high efficiency (*ca.* 70-89%), low capital cost, fast ramp rates, and high-power capacity.[58,64] Nonetheless, CAESs are not appropriate for ESSs of renewable energies due to their topographical application limitations in addition to the consumption of fossil fuels occasioned by the system's dependency.[49,58] Discussions are currently underway to operationalize them as supplementary energy storage for remotely located (offshore) wind power plants. This has been mainly hampered by suitable geology that permits CAES in windy regions.[63]

Flywheel energy storages (FESs), on the other hand, exhibit some merits like high energy efficiency (over 85%), little maintenance cost, long life cycles (> 15 years), low environmental impacts, 1:1 charge-to-discharge ratio, and high power and energy densities compared to other mechanical ESSs.[65] They are mainly deployed as short-duration energy storage technology. Therefore, typical fields of their application are not limited to the following: local peak power supply, storage of recuperated energy in vehicles, uninterrupted power supply (UPS) systems in hospitals, etc., and storage buffers for fluctuating energy supply, especially in satellites.[66] Regardless of their many benefits, some impediments like short operation lifetime and high self-discharge losses (idling losses due to friction or magnetic forces) must be circumvented to enhance their operation.[67]

Electrical energy storage (EES) systems can be subdivided into electrostatic (capacitors, supercapacitors, etc.) and magnetic/current energy storage (superconducting magnetic energy storage-SMES) schemes. Capacitors operate by storing energy through the polarization of charge carriers at two electrodes. The commonly known capacitors, *i.e.*, conventional capacitors, appear in a configuration of two metal plates with (electrically) insulating media between them, exhibiting characteristics like high efficiency, swift response time, and several thousands of life cycles. However, because of their very low energy density, they are not deployed as ESSs. Through research, diverse types of capacitors, namely, pseudocapacitors, double-layer capacitors, and supercapacitors, exhibiting high energy densities, have been introduced. Despite this development, the so-called advanced capacitor types still possess short storage time caused by the high cost (1100-1500 Euro/kW), which is a significant disincentive in addition to the high self-discharge loss. Besides, supercapacitors[68] and superconducting magnetic energy storage[49,69] are mainly deployed to compensate/makeup for the short-term fluctuation in the power distribution as they tend to operate with high energy (20-70 MJ m^{-3}) and power densities, long life cycles (10^6 cycles), and optimum efficiencies (90-99%, mostly > 95%). As the intermittency duration increases, they prove ineffective because they suffer from low energy storage densities and are not applicable in such scenarios.[70,71]

Chemical energy storage (CES) usually functions and is classified by the kind of material that goes through reversible chemical reactions. They possess several admirable properties, including ease of storage and transport, high energy density, and can rely on existing infrastructure. Metal-air batteries, synthetic natural gas, biofuels, and hydrogen (fuel cells, molten-carbonate fuel cells - MCFCs) are perfect examples of this form of energy storage system.[53,55,72] Thermochemical energy storage (solar hydrogen, solar metal, solar ammonia dissociation-recombination, and solar methane dissociation-recombination) is another CES category. Hydrogen storage will be further elaborated in **section 1.4**.

Electrochemical energy storage systems (EESSs) form a group with an appealing response to the erratic nature of most renewable energy sources.[73,74] Their operations center on reversible chemical and electrical energy conversion in a substance. Conventional, advanced, and flow batteries are the standard, most popular, and commercially available types of EESSs. Batteries primarily dispense electricity *via* internal electrochemical reactions and are mainly classified by their rechargeability prowess: primary (non-rechargeable) and secondary (rechargeable) batteries. Rechargeable batteries, with their alluring properties such as high energy and power density, high round-trip efficiency, negligible self-discharge, relatively long cycle life, very low standby losses, and quick response time[58,75,76] have gained traction for deployment as energy storage systems for renewable energy sources. In that sense, a myriad of rechargeable batteries displaying matured technologies, namely, lead (Pb)-acid, Ni-Cd, NiMH, and NaS batteries, have been commercialized to serve the automotive subsector as well as for other industrial and individual purposes. The operations of the aforementioned rechargeable batteries can be likened to large conventional batteries because of their shared similarities.[48] They function by immersing two electrodes in an electrolyte, triggering a chemical reaction, and generating current when required. They all encounter significant limitations overshadowing their merits, hindering their global use as grid-scale ESSs for renewable energy sources. Popular among the drawbacks are low depth of discharge (DoD), short life cycle,[58] memory effect, relatively low efficiency, the apparent toxicity of cadmium (Cd),[48,49,77] high self-discharge, and high-pressure failure. Flow batteries initiate a chemical reaction by pumping two charged electrolytes to the cell stack, which creates current from the device whenever demanded.[48] Vanadium Redox (VR), Polysulfide-Bromide (PSB), and Zinc-Bromine (ZnBr) flow batteries are significant examples of flow batteries. VR and PSB flow batteries operate similarly with enhanced characteristics such as high efficiency (*ca.* 75-85%), charge/discharge ratio of 1:1, fast response time (*ca.* 1-20 ms), high overload capacity, and long-life cycle (2,000 to 10,000 cycles). The power and energy capacities are decoupled from each other for both VR and PSB flow batteries. The power capacity is usually in the kW range and is determined by the cell stack size. In contrast, the volume of the electrolyte (size of the tank) indicates the energy capacity (usually in the kWh regime). The power capacities of both VR and PSB flow batteries have the potential to be upscaled to the MW scale. VR flow batteries can primarily be deployed for UPS, load leveling, telecommunications, peak shaving, and electric utility purposes. Designed with a versatility function, VR flow batteries can help to integrate renewable energy resources into the grid.[48] However, VR flow batteries suffer many demerits, including having the lowest power density and requiring several cells to obtain the same power output as other flow batteries. ZnBr flow batteries, with their electrolytes separated by microporous membranes, operate slightly differently from VR and PSB flow batteries. Key characteristic merits of this kind of flow battery include the display of high efficiency (75-80%), suffering from no memory effect, having a high cycle life (2000 cycles), charge/discharge ratio of 1:1, and showing the highest energy density of 75 to 85 Wh kg^{-1}, and a cell voltage of 1.8 V. ZnBr flow batteries are readily deployed for load management, UPS, supporting transmission and distribution grids, substations, microturbines, and solar generators, with the main drawback being the inability to upscale to the MW regime because the modules can only be linked electrically and not both electrically and hydraulically.[48]

For advanced rechargeable batteries such as Li-ion batteries (LiBs), optimum characteristics such as high energy and power density, high efficiency (80-90%), and long lifetime best describe them.[78,79] Thanks to their incontrovertible exhibition of the highest gravimetric energy density and substantially improved technology, they are well suited for mobile applications such as laptops, tablets, phones, and in electric and the so-called hybrid vehicles.[80] Several drawbacks, including but not restricted to the low abundance, or scarcity and uneven distribution of Lithium (Li) and Cobalt (Co), which serve as electrode compounds, limit their broad use in both grid-scale ESSs and the electric vehicle (EV) market because of the skyrocketing prices emanating from the high market demand.[81,82,83] Other factors that pose significant impediments to the stationary grid-scale application of LiBs are installation cost and safety concerns.[84,85] Several safety hazard examples can be cited regarding facilities and devices that deployed LiBs. These include the universal explosion of a few Samsung Galaxy Note 7s in 2016,[86] the explosion of several Tesla cars recorded in 2013 and beyond,[87] as well as the eruption/fire ignition of *ca*. 27 ESS facilities in Korea.[88] As such, these concerns are held more prominent/supreme over their enhanced gravimetric energy densities. Delightfully, the safety issues appear to be resolved as no new cases have been reported, but then comes the question of the sustainability of the global lithium reserves for the grand transition into grid-scale ESSs and still support the EV and other portable device industries. An alternative in Sodium (Na) instead of Li appears to be a more prudent solution as adequate reserves of the former in various forms (compounds, etc.) can be found in the oceans and all over the earth. More so, Na-ion batteries with aqueous electrolytes have proven viable for grid-scale applications.[85,89,90,91,92]

1.4 The Hydrogen-Based Economy

From the discussions in the previous sections, it is clear that there are intense advocacies for a complete transition to cleaner, “green” energy sources to preserve the earth and its inhabitants from global warming and climate change. However, the bottleneck to circumvent is the stochastic and erratic nature of the alternatives, namely, renewables, as they render the energy utility grid unreliable. A successful approach (the way forward) to resolving/addressing the new challenge entails an enhanced mechanism of converting and storing energy for reuse, especially when power outages and fluctuations set in. From the many energy storage systems or schemes adequately elaborated in **section 1.3**, it was evident that each ESS has some limitations regarding the widespread scope of application, cost of installation, inability to support grid-scale operations, optimal integration of renewables to the grid, and so on. In other words, there is a lack of efficiency and sustainability in almost every ESS.

Hydrogen, one of Earth's simplest and most abundant elements, comprises a single proton and one electron. However, hydrogen is not often found as a stand-alone molecule or chemical compound but intertwined with, for instance, oxygen to form water or carbon in hydrocarbons. Additionally, it does not naturally exist in the form of fuel.[93] The deployment of hydrogen in transitioning to cleaner energy sources as an energy carrier comes with its production, storage, and use. Hydrogen is important in contemporary energy architecture as an energy carrier because of its remarkable characteristics, such as the convenience of storage and transport, high energy density, and theoretically high energy conversion efficiency.[94,95,96,97] In this regard, hydrogen easily flexibly permits renewable energy storage, balancing energy demand and supply.[98,99] Ultimately, renewables that cannot be deployed directly can be stored as hydrogen and its derivatives and later used to provide low-carbon emission electricity.

It is significant to remark that the transportation sector accounts for *ca*. 28% of the global CO_2 emissions (and cars and water navigation constitute *ca*. 75% of them in the European Union (EU), **Figure 1.4A**), and hence targeting that industry will substantially impact the global climate.[100] Since the Paris Agreement, several companies have begun to lead the charge toward the green energy transition by developing and applying hydrogen-based technologies.[101] Similarly, many countries, including Germany, are acting in line (complying) with the Paris Agreement with a long-term policy aimed at reducing carbon footprints, especially in the transportation sector.[102,103,104]

Until now, hydrogen is mainly produced from the orthodox high carbon emission approaches through the gasification of oil, coal, and petroleum coke, as well as *ca*. 71% from natural gas *via* steam reforming.[105,106,107] This implies, in real terms, a continuous increase in CO_2 emissions as the advocated "clean" hydrogen is primarily obtained *via* the deployment of fossil fuels.[108] To substantially make hydrogen production cleaner and greener (carbon emission-free), renewable and nuclear resources must replace fossil fuels (*cf*. **Figure 1.4B**).[109]

A)

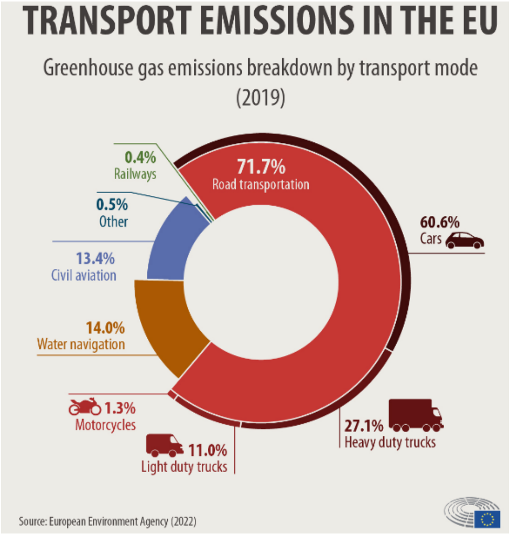

Source: European Environment Agency (2022)

B)

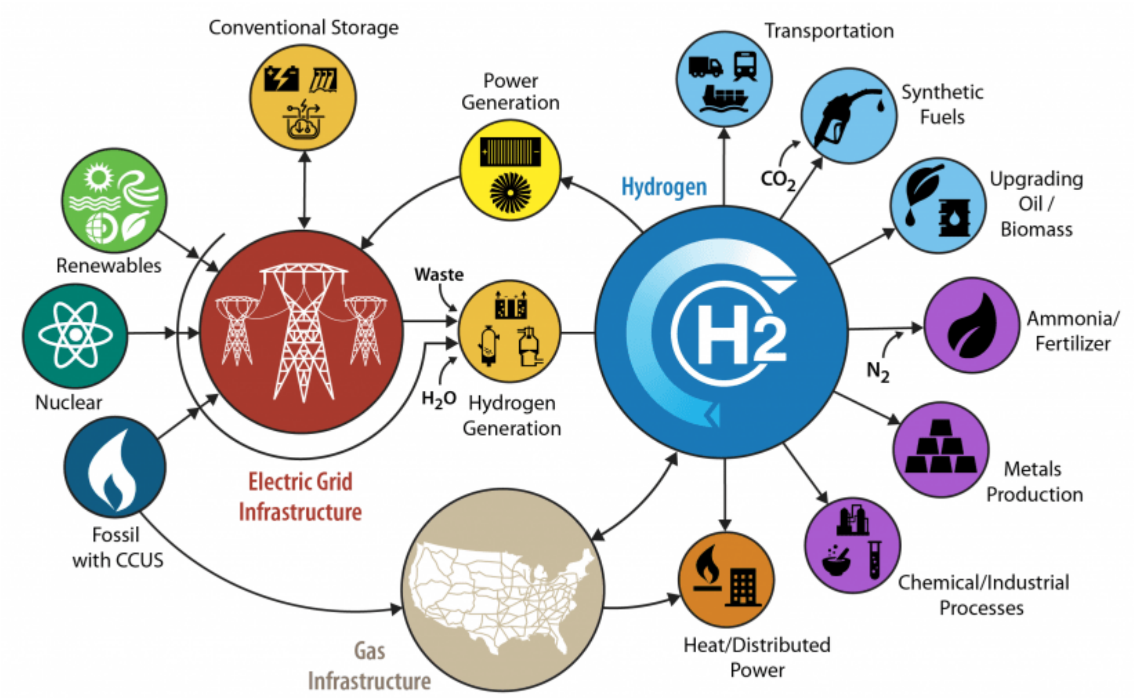

***Figure 1.4**. **A)** Transport emissions in the European Union (EU) in 2019. **B)** Schematic depiction of the enormous potential of electricity and a hydrogen-powered universe. Herein, the numerous ways hydrogen can be generated and its scope of use are highlighted. The goal is to produce hydrogen utilizing a "green" and clean methodology, i.e., via electrolysis from a renewable energy source. Hydrogen is mainly employed in the production of ammonia. It is believed that eventually, the application of hydrogen will be dominant in the chemical production, metal refining, and fuel cell industries as the oil refining and synthetic gas production industries take the backstage. Reproduced from reference.*[109] *Open access, permission of unrestricted use.*

Splitting water (into hydrogen and oxygen) by classical electrochemical means, also known as water electrolysis, presents a cost-effective avenue to producing "green" hydrogen. Nowadays, other approaches besides the primitive water splitting strategy, including photochemical water splitting, thermochemical water splitting, and biological pathways, are also deployed.[110] Presently, only 4% of hydrogen is produced by water electrolysis (using water and electricity from renewables), thereby offering the possibility for further exploitation.[111] It is significant to remark that water electrolysis reactions employ the so-called electrolyzer.[112] Following production, oxygen can be discharged into the atmosphere. In contrast, hydrogen (chemical energy) can be stored and transported in either a liquid or gaseous state (*e.g.*, high-pressure tanks) and eventually reconverted to electricity using the so-called fuel cells. The MYRTE platform is an example of a device that combines an electrolyzer transforming H_2O into H_2 and O_2 and completes the cycle by converting the generated electricity from solar panels into chemical energy and storing it in high-pressure tanks.[113] Subsequently, the eminent recombination of H_2 and O_2 in a fuel cell is a sure possibility of ensuring the "green" generation of heat and electricity.[114] In this regard, the hydrogen economy is achieved, for instance, when natural gas is changed to hydrogen for heating purposes. Electrolyzers and fuel cells encounter operation bottlenecks and hence suffer inefficiencies, stability, and selectivity issues.[115,116] For electrolyzers, the drawback primarily occurs at their anode, where the oxygen evolution reaction (OER) occurs. In contrast, fuel cells experience their setback at the cathode end housing the oxygen reduction reaction (ORR). Solutions through developing efficient and effective catalysts to cure the sluggishness at either end of the various reactions and optimize them are among the current hot research topics.

Nowadays, fuel cells and, by extension, hydrogen are mainly deployed in the transportation sector for submarine, airplane, ship, train, and vehicular applications.[117] Thus, in realizing the so-called hydrogen economy, H_2 as a low-carbon energy source is set to replace diesel or gasoline as a transport fuel. The so-called electric vehicles (EVs) lead the implementation charge, an intention/idea incubated/hatched several years ago. EVs needed more support to break through for mass production due to the popularity and efficiency of vehicles powered by conventional internal combustion engines employing fossil fuels. There is now an unsurprising resurgence of the EV industry occasioned partly by the overall public interest and environmental awareness and the automobile companies investing heavily in research. These happenings can be attributed to the damning reality of climate change and global warming and the acceptance and/or recognition that the way forward involves a shift to EVs. It is essential to clarify that EVs can be distinguished by the type of storage device that fuels the vehicle. In this respect, there are fuel cell electric vehicles (FCEVs), battery electric vehicles (BEVs), and hybrid electric vehicles (HEVs). Another way of classifying them is based on the means of recharging; hence, BEVs, Smart Electric Vehicles (SEVs), and Vehicle to Grid (V2G) exist.[48] BEVs function by plugging into the electric grid, behaving as an additional load. By contrast, SEVs reserve the prospect of communicating with the grid. In this regard, it automatically recharges the EV when the grid peaks. V2G electric vehicles operate similarly to SEVs, with the added feature of the capability to supply power back to the grid, increasing the flexibility levels within the system.

Leveraging the factors mentioned above, the much-enhanced technology, and the Paris Agreement, the advent of the Tesla Model S in 2012 received much attention in terms of purchases.[118] Consequently, many automotive industry players have either already started or still wield the desire/ambition to manufacture hydrogen-powered EVs as of 2019. Popular among them are Toyota,[119] Hyundai,[120] BMW,[121] Honda,[122] Daimler,[123] and Tesla.[124] Until recently, BEVs have always outperformed commercially available FCEVs. However, thanks to a conscious agenda to further optimize FCEVs, commercially available models such as the Toyota Mirai[119] and Hyundai Nexo[120] can now outperform state-of-the-art BEVs like the Tesla Model X[125] in terms of driving range (over 600 km) and refueling time. Moreover, a fast-refueling duration of between 3 to 5 minutes, comparable to the readily available diesel- and gasoline-powered cars, has been instituted into these hydrogen-powered EVs.[120] For long-distance journeys, there is certainly the need to refuel, and this reveals the significant limitation in owning EVs as a handful of H_2 gas stations exist. This is a major disincentive to the choosing power of consumers when purchasing EV cars compared to ICE cars.[126] Another bottleneck to circumvent to make EVs appealing is the influx of several car manufacturing companies producing varied models of EVs, as it is with the ICE cars to attract customers' attention, as several choices are made available. For the insufficient H_2 gas stations, existing gasoline, diesel, etc., infrastructure can be adapted and equipped with H_2 gas networks to cure the challenge. It is worth noting that EVs can feed directly from the power grid while stationary at individual homes or common recharging points, such as car parks or stations.[127] The cost of owning EV cars compared to conventional ICE cars is another major hindrance consumers consider. Perhaps some financial incentives should be considered to cushion consumers and make owning EV cars attractive. Hydrogen vehicles have a much larger driving range than electric vehicles, although hydrogen vehicles are much less efficient.[48] Therefore, technology preference is subject to the dominant factors among the different energy systems.

Besides deploying hydrogen primarily for petroleum refining, its use in the ammonia industry is quite substantial (*cf.* **Figure 1.4B**).[109,128] Additionally, hydrogen can produce several chemicals, particularly as a starting material in synthesizing methanol and the like, and plays a vital role in the metal refining industry.[129]

In a nutshell, hydrogen as an energy carrier holds enormous potential, especially as it helps to integrate renewables into the utility grid. Challenges concerning inefficiencies arise, hampering its widespread commercial availability. Therefore, current research works are primarily dedicated to addressing the issue to make it more viable for the future. In this regard, an upscale to the TW regime is a chief consideration.

1.5 Methodological Perspectives

In liquid electrochemistry, a big part of electrocatalysis research in recent years is keen on investigating the behavior of interfacial water dipoles on the electrified electrode/electrolyte interface. Other electrolyte components,[130,131,132,133] including cations, pH, and anions, as well as the electrode's structure and composition,[134,135,136,137] have all gained center stage in electrochemistry research. In this regard, little attention is devoted to the processes and mechanisms that occur in the electrolyte solution. Electron Paramagnetic Resonance (EPR) spectroscopy can determine intermediate paramagnetic species on the electrode surface or inside the active material as a non-destructive technique. The advocacy for applying this methodology makes perfect sense, as EPR spectroscopy helps to monitor and detect paramagnetic reaction intermediates in solution after desorption and identify species on the electrode surface.[138] Primarily, EPR was used in conjunction with electrocatalysis in what is known as *in-situ* electrochemical EPR (EC-EPR) or *in-situ* EPR-spectroelectrochemistry for the detection and identification of paramagnetic radical species generated or consumed during electrochemical reactions.[139,140] This crucial investigation provides valuable information on selectivity (*i.e.*, the reaction pathway/mechanism) and clarifies the kinetic parameters involved. More so, elusive interactions between, for instance, the radical and its environment can be elucidated.[141]

It is significant to acknowledge that a larger percentage of EC-EPR studies in the late 2000s still involve organic materials at the forefront regarding the nature of the reactions investigated, with the X-band microwave frequency regime being the most popularly used EPR range. Usually, the solvents used are organic in nature, ranging from methanol (CH_3OH),[142,143] acetonitrile (ACN), [142, 144, 145, 146, 147, 148] dimethylformamide (DMF),[142,146, 149] dimethyl sulfoxide (DMSO),[143] deuterated methanol (CD_3OD)[143] to methylene bichloride (CH_2Cl_2).[150] It is intriguing to note that the most prominent electrode employed for the EC-EPR investigations remains Pt as both working and counter electrodes with Ag wire or Ag/AgCl as the reference electrode.

Interestingly, water,[147,151] with a high dielectric constant, has also been used as a solvent in EC-EPR measurements. Nonetheless, the nature of the reactions investigated was organic. Aqueous electrolytes generally lead to several complications, including dampening electromagnetic radiation and deterioration of the cavity's sensitivity, among other pertinent factors.[147] To address this, special cell types, resonators, etc., must be designed to overcome the challenges encountered in electrochemistry and EPR measurements. Another aspect worth tackling in developing a functional *in-situ* EC-EPR cell is the dimensions of the wires (electrodes) to be employed. Essentially, utilizing microelectrode dimensions, the electrochemical performance in terms of ohmic drop, cell time constants, and mass transport can all be significantly enhanced.[152] Nonetheless, some drawbacks still exist in applying microelectrode dimensions for EC-EPR applications. This mainly stems from the tiny currents that accompany their use, resulting in the generation of insufficient radical concentrations. In this regard, studying the short-lived intermediates or radicals may prove futile using the EPR methodology. The good news is that using microcylindrical geometry can generate a significant current to detect adequate quantities of radicals *via* the EC-EPR technique.[153]

Therefore, the aim is to design, construct, and test a working *in-situ* EC-EPR cell to investigate the hydrogen underpotential deposition (H_{upd}) using Pt as both the working and counter electrodes and adapting it to several reference electrodes. 0.1 M $HClO_4$ is employed as the electrolyte, even though its use is hardly seen in the EPR community's literature. The choice of this electrolyte and the acidic pH were due to the relative simplicity in realizing and verifying the hydrogen adsorption pathway. Besides, $HClO_4$ does not specifically adsorb compared to other readily available commercial electrolytes like H_2SO_4. Thus, it is arguably the most used electrolyte in electrocatalysis.

In-situ laser-induced current transient (LICT) technique has already been well-developed and established by my predecessors in our chair.[131, 154, 155, 156, 157, 158, 159, 160, 161] Leveraging the knowledge of the methodology, several experimental data are recorded. Particularly, the potential of maximum entropy (PME) is recorded for each set of experiments. By so doing, the stability, activity, and selectivity of electrochemical processes or reactions can be correlated to the PME and other solvation effect parameters. Specifically, solvent, anion, cation, and concentration of H^+ and OH^- ions (denoted as pH) effects of electrolyte components or compositions are highlighted under various LICT experiments.

Electrochemical Impedance Spectroscopy (EIS), another robust and well-developed methodology, is also deployed to measure the minimum of the double layer (C_{DL}) capacitance, augmenting the data and results of the LICT measurements.

1.6 Scope and Goals of the Dissertation

This dissertation, therefore, sets out to utilize several electrochemical techniques, such as laser-induced current transient methodology, impedance spectroscopy, and *in-situ* electrochemical electron paramagnetic resonance spectroscopy, to address various electrochemical challenges. In doing that, the findings would bring incredible insights and new ideas regarding the challenge.

The objectives of the dissertation are the following:

- To contribute to designing, constructing, and testing an *in-situ* electrochemical electron paramagnetic resonance spectroscopic cell to investigate and confirm or otherwise the reaction pathway of various electrochemical reactions. The H_{upd} is targeted for the hydrogen adsorption pathway and studied on the Platinum (Pt) polycrystalline electrode in this work.

- The LICT methodology is deployed to reveal the PME of gold (Au) quartz crystal microbalance (QCM) electrode in the presence of argon (Ar) saturated cation mixture of 0.5 M K_2SO_4 and 0.5 M Na_2SO_4 at pH = 8. The cation mixtures were studied at five (5) varying ratios, namely, 0.5 M K_2SO_4:0.5 M Na_2SO_4 = 0:100; 25:75; 50:50; 75:25; 100:0. Prior to this, several measurements were performed at several pHs (0, 2, 4, 6, 8, and 10) of 0.5 M K_2SO_4 and 0.5 M Na_2SO_4 electrolytes in both Ar and oxygen (O_2) atmosphere. Correlation to the hydrogen evolution reaction (HER) and oxygen reduction reaction (ORR) activities were the main objectives.

- Utilizing the Palladium (Pd) monolayers (MLs) deposited strategically *via* atomic layer deposition (ALD) on an original Au electrochemical quartz crystal microbalance (EQCM) electrode, the LICT methodology was employed to identify the PME in the presence of varying concentrations (pH) of Ar-saturated $HClO_4$. Herein, the various concentrations were 0.01 M, 0.1 M, and 1 M $HClO_4$, corresponding to pH of 2, 1, and 0, respectively. Electrochemical impedance spectroscopic data were also recorded to obtain the capacitance of the double layer, which is somewhat within the vicinity of the PME, to supplement the PME findings. The reaction under consideration was the activity of the hydrogen evolution reaction.

- Furthermore, the Pd monolayers were electrochemically deposited on the Au QCM electrode, and the LICT methodology was used to determine the PME with various Ar-saturated 0.1 M alkali metal (*AM*) hydroxide solutions as the electrolyte. More specifically, LiOH, NaOH, KOH, and CsOH electrolytes, all with a pH of approximately 13, were utilized. Herein, the PME was correlated with the hydration energy and other parameters like hydrogen evolution reaction activity.

- Using surface-mounted metal-organic framework (SURMOF) derivatives as the electrode material, the cation effect on the oxygen evolution reaction (OER) activity *via* the PME determination was investigated using different Ar-saturated 0.1 M *AM*OH (pH = 13) as electrolytes. *In-situ* Raman Spectroscopic measurement and results coupled with density functional theory (DFT) calculations, verifying the catalytic activity trend in the presence of different alkali metal cations complemented this.

- The Prussian Blue Analog (PBA) electrode, i.e., NiHCF was also experimented with to reveal the anion effect on the PME. Ar-saturated 0.25 M $NaClO_4$, $NaNO_3$, NaCl, NaOAc, and Na_2SO_4 were employed as electrolytes. The intercalation and deintercalation mechanisms were also studied.

2.0 Theoretical Underpinnings - Electrochemistry

To fully grasp the working principle of all the methodologies employed in this work and to relate with the discussions expounded, it is paramount first to understand the basics of electrochemistry. Therefore, the following discussion will be centered on the phenomena in the electrified solid/liquid interface, principles in thermodynamics, kinetics, mass transport, and electrochemical techniques since they form the fundamentals for fully comprehending this dissertation. This then serves as a platform to commence the discussion on electrocatalysis. A massive chunk of this chapter is published in:

- Sarpey, T. K., Keleş, E., Gubanova, E. L., & Bandarenka, A. S., Probing the electrified solid-liquid interfaces with laser-induced transient techniques. In: Wandelt, K., and Bussetti, G., (Eds.), ***Encyclopedia of Solid-Liquid Interfaces***, Elsevier: Amsterdam, First Edition (Volume 1), 2024, 43-58.[162]
- Ding, X.,‡ Sarpey, T. K.,‡ Hou, S., Garlyyev, B., Li, W., Fischer, R. A., & Bandarenka, A. S., Prospects of Using the Laser-Induced Temperature Jump Techniques for Characterisation of Electrochemical Systems., ***ChemElectroChem***, 2022, *9*(4), e202101175.[163]
- Haid, R. W.,‡ Ding, X.,‡ Sarpey, T. K., Bandarenka, A. S., & Garlyyev, B., Exploration of the electrical double-layer structure: Influence of electrolyte components on the double-layer capacitance and potential of maximum entropy., ***Current Opinion in Electrochemistry***, 2021, 100882.[164]

2.1 Electrochemistry

Electrochemistry is sub-zoomed under physical chemistry and/or chemical physics and focuses on the relation between electrical and chemical effects of reactions. This field mainly handles the study of chemical changes occasioned by the passage of an electric current and the generation of electrical energy *via* chemical reactions. As a result, electrochemistry covers many kinds of phenomena, such as electrophoresis or electroplating (corrosion), which forms part of the focus of this study. In chemical phenomena, charge separation typically leads to charge transfer that occurs either homogeneously in solution or heterogeneously on a solid/liquid (an electrode/electrolyte) interface. In real systems, the electroneutrality is preserved by at least two charge transfer half-reactions occurring in opposite directions. Apart from homogeneous redox reactions, other reactions are separated in space and mainly occur at the solid/liquid interfaces of different electrodes in a cell. An electronic/electrical connection through the electrolyte (ionic conductor) and employing external wires (electronic/electrical conductor) permits charge transport between the electrodes.[165]

2.1.1 Electrode

An electrode is a term for an electronic/electrical conductor (not necessarily metallic) that is usually in contact with a nonmetallic part of an electric circuit (usually and herein referred to as an electrolyte).

2.1.2 Electrolyte

The term electrolyte principally describes a conducting medium in which the current flow is transported by the movement of charged matter known as ions. In essence, while an electrolyte triggers ion transport, it is immune to electron transport, *i.e.*, it acts as an insulator to electrons. Hence, any substance that produces an electrically conducting solution when dissolved in a polar solvent is termed an electrolyte. A perfect example occurs when a chemical salt like bulk sodium chloride (NaCl) is immersed in water. The NaCl will dissolve in the water and eventually metamorphose into Na- and Cl-ions. Subsequently, the ions leave the solid lattice into the liquid, thus creating a salt solution of NaCl. During the ensuing dissolution process, the positive Na-ion (or cation) will be surrounded by a water molecule in such an arrangement that the negatively charged part of the molecule will orient itself towards the cations. Likewise, the Cl-ion (or anion) will be surrounded by the water molecules with an inverse orientation of the water molecules. A solvated ion or, more generally, the solvated shell can be defined as a structure in which water molecules (or other molecules from solution) surround an ion to screen/shield the charge from the ions.

Invariably, the size of the solvation shell depends on the ion. In that light, comparing the size of the solvation shells for Cl^- and Na^+, the former exhibits larger size even though both possess a charge of 1 (or more precisely, a charge of -1 and +1, for Cl- and Na-ions, respectively). This difference can be ascribed to the differences in the radii of both ions, resulting in different electric field strengths. This implies that the solvation shell of elements in the same period on the periodic table increases with increasing atomic/ionic radii. Hence, the ion of elements in the same group in the periodic table, for example, Na-ion and K-ion, will also portray different sizes of their solvation shells. With these vital terms defined, it is significant to clarify the relations between the parameters now.

The conductivity κ of an electrolyte with concentration c relies on the nature of ions. It can be calculated using the relation:

$$\kappa = c\Lambda_m \tag{2.1}$$

Where Λ_m denotes the molar conductivity. Strong electrolytes are known to dissociate completely at low concentrations and, as such, follow Kohlrausch's law:

$$\Lambda_m = \Lambda_m^o - K\sqrt{c} \tag{2.2}$$

K represents an empirical constant, and Λ_m^o is the limiting molar conductivity, which is a sum of the cation and anion conductivity. The latter can accordingly be expanded and is given by:

$$\Lambda_m^o = \upsilon_+\lambda_+^o + \nu_-\lambda_-^o \tag{2.3}$$

Here, $\upsilon_\pm$ is the number of moles of cations and anions, respectively, created from the dissociation of one (1) mole electrolyte. $\lambda_\pm^o$ denotes the limiting molar conductivities of the individual ions.

2.2 Electrocatalysis

A catalyst is a substance that enhances the reaction kinetics without participating in the overall chemical reaction. Therefore, it can be reused in subsequent reactions as it is not consumed in the process (not a by or side product). By convention, a catalyst can be subdivided into three groups: homogenous, heterogeneous, and enzyme (bio) catalysts.[166,167]

In the scenario of a *homogenous catalyst*, the reactants and catalyst are in the same aggregate physical phase. For instance, if both reactants and catalyst are in the liquid or gaseous (fluid) phase. However, if the reactants and catalyst exist in different physical phases, the catalyst is called a heterogeneous catalyst. An *enzyme/biocatalyst,* on the other hand, depicts a special kind of protein that increases/accelerates the rate of a chemical reaction.

As this dissertation focuses on heterogeneous catalysis, it is essential to zoom further into its other categories. In this respect, one can classify a *heterogeneous catalyst* into two main subdivisions:

- *Photocatalyst*, which best describes a substance that facilitates a reaction when illuminated by a light source.
- *Electrocatalyst*, representing a substance that acts as a catalyst (*i.e.*, fast tracks the reaction kinetics) in an electrochemical process or reaction. It is worth remarking that, in most cases, a specific electric potential is introduced into the substance. However, the potential application is not required or optional in exceptional cases like Pt catalyzing the H_2O_2 decomposition into hydrogen and water.

Heterogeneous catalysts, particularly electrocatalysts, are an important class of functional energy materials. Primarily, heterogeneous catalysis involves five essential reaction steps: diffusion of reactant molecules to the catalyst surface, adsorption on the active surface, reaction on the surface, desorption of product molecules, and outward diffusion. Electrocatalysis comprises multiple elementary reaction steps. The intermediate species' adsorption and desorption equilibrium at the active sites in each elementary step (grade) determines the reaction process. Rational design and implementation of new generational efficient catalytic materials will largely determine the future of sustainable energy conversion and provision. The development of electrocatalysts considers that three key factors, namely, activity, selectivity, and stability, determining their performance are optimized. The activity depicts the number of catalytic cycles per time per active site, characterizing the turnover frequency. The selectivity of a catalyst primarily ensures the formation of desirable product(s) at the end of a chemical reaction. This property essentially limits the formation of large amounts of unsought side products. Its stability is vital for a catalyst to function efficiently and effectively, as constant degradation will render it unreliable. While methodologies to rationally design more active catalysts are available, addressing stability and especially selectivity remains, in most cases, challenging. Developing and optimizing efficient electrocatalysts is perhaps a more difficult task than material development in "classical" heterogeneous catalysis. The LICT methodology examines activity enhancement through the potential of maximum entropy determination relative to several parameters, like the hydration energy.

Applying the LICT technique in electrocatalysis can help to get valuable information regarding the properties of the electric double layer (EDL), which forms between the electrode and electrolyte. For instance, knowing the effect of the electrode structure and electrode/electrolyte composition on the PME/potential of zero charge (PZC) can significantly improve the development of an effective catalytic system for a defined catalytic reaction. To be more precise, *the closer the PME value is to the thermodynamic equilibrium potential of a particular electrocatalytic reaction, the faster the kinetics of this reaction should be*. Specific examples of LICT application in electrocatalysis will be discussed in the following. The selectivity is also exploited using the *in-situ* EC-EPR and the LICT methodologies. More details will be discussed in **sections 3.4** and **4.2**.

2.3 The Electrified Solid/Liquid Interface

This section deals with the effects, not excluding electrochemical reactions at the electrode/electrolyte interface. The formation of the double-layer capacitance at the interface is explained. A brief discussion of electrochemical (electrode) reactions and their kinetics follows. The Nernst and the Faradaic equations are expounded, and subsequently, the Butler-Volmer equation and its related consequences are tersely shown. The theory and principle of mass transport, which occurs in the electrode and serves as a limiting factor for the reactions at the interface, is further highlighted.

2.3.1 The Electric Double Layer

The fundamental requirement in fruitfully designing efficient electrochemical systems dwells mainly on comprehending and appreciating the electric double-layer properties as their essential role in batteries, fuel cells, supercapacitors, electrolyzers, and several others cannot be overlooked. The EDL gives information regarding the relationship between the solid (electrode surface) and the liquid (electrolyte) at the interface. Hence, to enhance several electrocatalytic reactions, optimizing the interfacial processes is crucial; therefore, adequate knowledge of the EDL structure is required. The EDL structure mainly comprises an array of charges and corresponding potential at the solid/liquid interface. This classification was first heralded in

1853 by Hermann L. F. von Helmholtz[168] when he suggested a simplified EDL structure, thereby earning the name Helmholtz model. In this model, the charged/electrified electrode (electron(ic) conductor) surface (*i.e.*, when submerged in an electrolyte) repels similarly charged ions and attracts counter-ions in the electrolyte (ion(ic) conductor) to its surface. Practically speaking, suppose a metal serving as the electrode is immersed into an electrolyte (for instance, aqueous NaCl solution). For a positively charged metal electrode, a few negatively charged solvated ions and some water molecules will experience a Coulomb force. Subsequently, a double layer of ions is formed on the electrode surface. The resulting charge layers act like a standard capacitor with two planar parallel electrodes disconnected by a dielectric material upon applying a potential. It is essential to add that a distance, say H, separates the two formed charge layers in the Helmholtz model.

Since the influence of the thermal motion of ions in the double layer (*e.g.*, ion-ion interaction) is not negligible, Louis Georges Gouy[169] and David Leonard Chapman[170] accounted for that through the extension of the Helmholtz model by proposing a diffuse layer at the interface. The diffuse layer principally extends beyond the distance H and incorporates a distribution of ions of opposite polarity to the electrode surface. In the diffuse layer, the charge distribution of the ions can be explained/determined by the distance from the electrode surface. In turn, the region under consideration follows the Maxwell-Boltzmann statistics and displays an exponential decrease in the electric potential from the electrode surface.[171] Based on the failure of the Gouy-Chapman model to recognize the Helmholtz layer, defined by H from the Helmholtz model, it faced some setbacks.

In that light, the two models, namely, Helmholtz and Gouy-Chapman models, were subsequently merged by Otto Stern[172] to describe the size and ion distribution in the Helmholtz and diffuse layers. The Stern model, therefore, comprises two separate charged regions, the Helmholtz layer (otherwise termed the Stern layer) and the diffuse layer. However, this reformation still needed to be improved in adequately describing the molecular dynamics at the interface. On that score, David Caldwell Grahame[173] modified the Gouy-Chapman-Stern model, inferring that the Helmholtz layer can be further divided into two planes, the inner and the outer Helmholtz planes. In brief detail (*cf.* **Figure 2.1**), specifically adsorbed species lose aspects of their solvation shell and, therefore, mainly attach to the electrode surface, together with the water molecules, and from their center to the electrode surface is termed the inner Helmholtz plane (IHP). From a less complicated standpoint, the Helmholtz layer refers to the entire region between the electrode surface and the IHP.

In turn, the outer Helmholtz plane (OHP) comprises the non-specifically adsorbed species known to retain their full solvation shells and hence cannot approach closer to the electrode surface. Therefore, they are distant and eventually form another layer called the outer Helmholtz plane. As mentioned, due to thermal agitation, another layer comprising the bulk electrolyte and some fully solvated/hydrated species forms outside the outer Helmholtz plane. This region is known as the diffuse layer. It is paramount to remark that regardless of the electrode surface polarity, anions can be specifically adsorbed at the interface because of their intrinsic interaction with the electrode surface. Besides, every species, from ions to solvent molecules, can be adsorbed at the electrode surface from interactions, such as chemical reactions between surface and adsorbates (chemisorption), van-der-Waals (physisorption), or even Coulombic forces.

Although the models have been polished unendingly, they remain the basis of today's research concerning the double-layer structure at the solid/liquid interface. It is, therefore, not surprising that besides the electrode structure and composition,[174,175,176,177,178,179,180,181,182] the electrolyte components play a crucial role regarding the electrocatalytic performance (most especially activity and selectivity) of the electrode[183,184,185,186,187,188] upon exploring the concepts of the EDL.

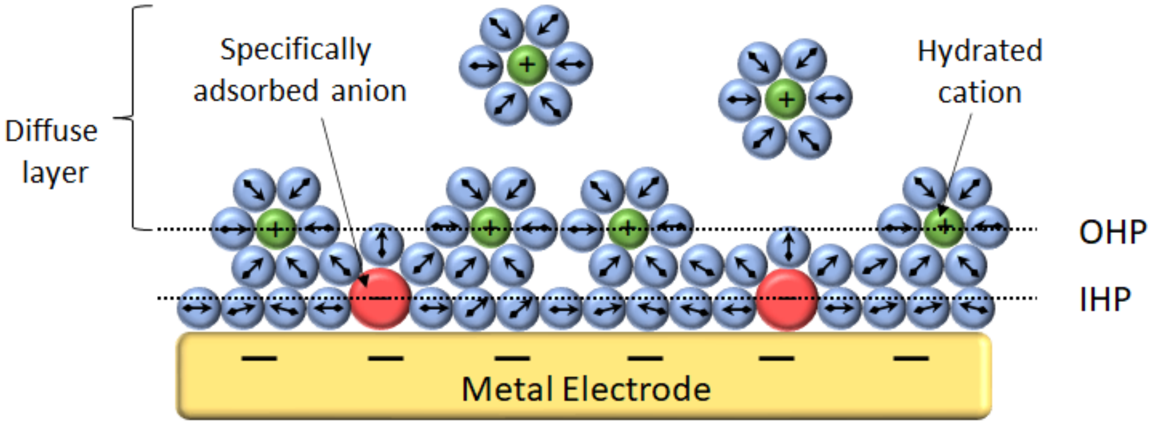

***Figure 2.1**. Modified schematic demonstration of the electric double-layer model on a negatively charged metal electrode. The inner and outer Helmholtz planes, as well as the diffuse layer, are exhibited. Water molecules are shown as blue spheres with arrows, whereas the hydrated cations are depicted in green, with the specifically adsorbed anion species in red. Figure adapted from reference.*[189]

The effect of the space-charge region, *i.e.*, an electrically neutral region, due to the balancing of the net charge (depletion layer) in a hitherto conductive area can be neglected when metallic electrodes are employed, as is the case in this dissertation. From a different perspective, to assume electroneutrality, one can consider the ions as point charges attracted by the electrode, constituting a total charge of the diffuse layer that coincides with the electrode surface charge.

In a macroscopic view of the potential profile of the electrode/electrolyte solution interface, an analogy to an electric circuit can be made to simplify system analysis. In that sense, the Helmholtz and diffuse layers can be modeled as two capacitors in series. More precisely, both IHP and OHP can each be modeled as capacitors. This is because the behavior of any solid/liquid interface is like that of a capacitor, where opposite charges attract each other in different media.[190] The Helmholtz capacitance, which is defined by the capacitance of the IHP (C_{IHP}) and the OHP (C_{OHP}), viewed as two capacitors in series, is represented by the equation:

$$C_H = \left(\frac{1}{C_{OHP}} + \frac{1}{C_{IHP}}\right)^{-1} \tag{2.4}$$

Furthermore, the electrolyte can be represented by a resistive element connected in series with the capacitors since the electrolyte possesses a resistance towards the conducting ions. In **Figure 2.2**, the equivalent electric circuit of this electrode/electrolyte interface is illustrated. It is important to stress that the equivalent electric circuit should be modified for a more complex electrochemical process.

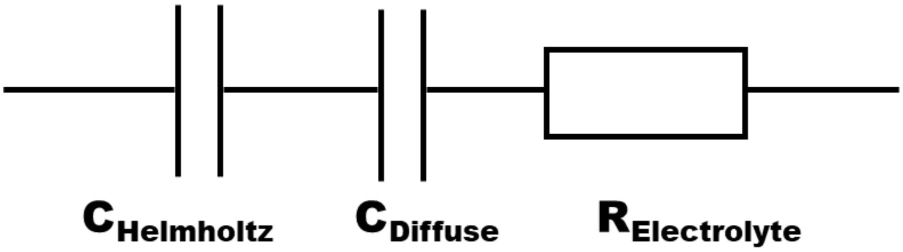

Figure 2.2. *Equivalent electric circuit model of the electrode/electrolyte interface.*

2.4 Electrochemical Cell Potential and Overpotentials

The behavior of ions and molecules in solution when exposed to an electrode (usually charged) has been explained in **section 2.3.1**. Some molecules and ions primarily adsorb on the electrode's surface or undergo a long-range interaction with the electrode. A much more positively (or negatively) charged electrode results upon applying a higher potential to the electrode. Consequently, an electron from the electrode will gain enough energy, leading to an electron transfer between the electrode and electrolyte. Simply put, a chemical reaction is triggered at a certain potential at the electrode surface. In the following, the equilibrium potential for a redox reaction (a reaction in which reduction and oxidation occur concurrently and proceed with either the gain or loss of electrons/charged species) will be determined, which is usually the potential sufficient to initiate the charge transfer reaction.

To begin with, the energy of each phase of the electric double layer, *i.e.*, the power/energy of each electrode and electrolyte separately, will be critically examined. Two interactions contribute to the total energy of each phase. The first is the interaction between the species and the chemical environment, which gives rise to the *chemical potential* μ. The chemical potential also represents the energy released to the environment (or acquired from the environment) during a chemical reaction. The chemical potential is related to the species' *activity* a and the temperature T in Kelvin by:

$$\mu = \mu_o + RTln(a) \tag{2.5}$$

Here μ_o corresponds to the chemical potential, which is the chemical potential at standard conditions, *i.e.*, at room temperature and a pressure of 1 bar. Activity a is the entropic driving force of the reaction.

The second interaction is the electrical interaction originating from the electric field of the charged species. To sum it up, the total energy for species-i can be written as:

$$\overline{\mu}_i = \mu_i + z_i F\phi \tag{2.6}$$

Here, the first term relates to the chemical potential in the system, and the second term corresponds to the electrostatic energy of the system in which z is the number of transferred electrons, F is the Faraday constant, and ϕ is the inner potential of the species (also called Galvani potential). The total energy depicted in **Equation (2.6)** is called the *electrochemical potential* $\overline{\mu}_i$. Physically, the electrochemical potential can be seen as the Fermi level of the system. Put differently, the electrochemical potential of the system represents the average energy of an available electron in any given phase.

Based on the definition and description of the electrochemical potential for each phase, the electrode/electrolyte interface can now be explored or considered in detail. The solid (electrode) and liquid (electrolyte) have their respective inner and electrochemical potentials. It is common knowledge in the Physics of Fermi level that when two substances come into contact, their Fermi levels (or electrochemical potentials in this case) must be equal to reach equilibrium. Hence, the condition at equilibrium is: $\bar{\mu}_{interface}^{Solid} = \bar{\mu}_{interface}^{Liquid}$. By combining this condition with **Equations (2.5)** & **(2.6)**, the potential difference between the electrode/electrolyte interface can then be determined:

$$\phi^S - \phi^L = \frac{\mu_o^L - \mu_o^S}{zF} + \frac{RT}{zF} ln\left(\frac{a^L}{a^S}\right) = \phi_o^S - \phi_o^L + \frac{RT}{zF} ln\left(\frac{a^L}{a^S}\right) \tag{2.7}$$

From **Equation (2.7)**, ϕ_o^S, ϕ_o^L are defined as the standard potential of the solid and liquid phases, respectively. According to **Equation (2.6)**, there exists a theoretical possibility to calculate the potential difference between the solid (electrode) and the liquid (electrolyte). As the use of concentration is more convenient or preferred in experiments than the activity, the two parameters are linked *via* the relation:

$$a_i = \gamma_i \frac{C_i}{C_o} \tag{2.8}$$

Here, C_i is the concentration of species-i in the solution (C_o corresponds to the standard concentration of species, which is 1 mol/l (1 M) for all solids), and γ_i is the activity coefficient of the species (for low concentrated/dilute solutions, it is assumed that: $\gamma_i \simeq 1$).

For water electrolysis, it is expedient to use a pH-independent reference, which is the so-called reversible hydrogen electrode (RHE) with the potential:

$$E_{RHE} = E_{SHE} + 0.0591 * pH \tag{2.9}$$

Here, E_{SHE} is the potential for the standard hydrogen electrode (SHE).

Since **Equation (2.9)**, *i.e.*, the RHE is often used as the benchmark reference electrode, almost all potentials are converted to the RHE scale in this dissertation's experimental and results section to ease the comparison and fully fathom the measured activities. Merging **Equations**

(2.7) & **(2.8)** and taking activity of 1 for solid species, as well as assuming that $\gamma_i \simeq 1$, the potential difference between the solid and liquid can be rewritten as:

$$\Delta\phi = \phi_o^S - \phi_o^L + \frac{RT}{zF} ln\left(\frac{a^L}{a^S}\right) = \Delta\phi_o + \frac{RT}{zF} ln(C^L) \tag{2.10}$$

If there are more than one species in the electrolyte, a more general form of **Equation (2.10)** must be used:

$$E_{eq} = \Delta\phi = E^o + \frac{RT}{zF} ln\left(\prod_i C^{v_i}\right) = \Delta\phi_o + \frac{RT}{zF} ln\left(\prod_i C^{v_i}\right) \tag{2.11}$$

Where v_i is the stoichiometric coefficient of species-i, with E_{eq}, E^o representing the equilibrium potential and the standard equilibrium potential, respectively, being the potential differences between the solid (electrode) and the liquid (electrolyte)**. Equation (2.11)** is popularly called the *Nernst equation.* The equilibrium potential given in the Equation (E_{eq}) corresponds to the potential required for an electron transfer across the electrode/electrolyte interface.

2.4.1 Faraday’s Laws

Faraday established the fundamental laws governing electrochemistry. These so-called Faraday’s laws fundamentally correlate the amount of substance liberated in an electrochemical reaction to the electric charge, for instance, in electrolysis.

The first law states that the amount of substance n precipitated at an electrode is directly proportional to the Faradaic electrical charge $Q^{Farad} = \int_0^t I^{Farad}(t)dt$ passing the electrolyte over time t.

The second law links the mass m of this substance to the molar mass M and the stoichiometric number of electrons z. In short, Faraday’s laws can be summarized as follows:

$$n = \left(\frac{Q^{Farad}}{F}\right)\left(\frac{1}{z}\right) \tag{2.12a}$$

$$m = \left(\frac{Q^{Farad}}{F}\right)\left(\frac{M}{z}\right) \tag{2.12b}$$

2.5 Reaction Kinetics at the Electrode Surface

Section 2.4 highlighted that the Nernst equation gives vital information regarding the electron transfer across the electrode/electrolyte interface. It fundamentally indicates the potential needed to drive a chemical reaction, which subsequently triggers the electron transfer across the electrode/electrolyte interface. Besides the equilibrium potential, other aspects of the reaction must be considered. Significant among them is the reaction rate because it corresponds to the speed at which the electron transfer occurs across the electrode/electrolyte interface. In that respect, there is the need to formulate another mathematical expression in addition to the Nernst equation to determine the electron transfer rate at the electrode/electrolyte interface. In general, the electron transfer at the interface can be represented by the chemical equation:

$$O + ze^- \underset{k_b}{\overset{k_f}{\Leftrightarrow}} R \tag{2.13}$$

For which *O* and *R* denote the oxidized and reduced species, respectively, while e^- stands for the transferred electron, and *z* represents the number of transferred electrons (sometimes written as *n* in other kinds of literature). k_f and k_b represent the reaction rate constants for the forward and backward reactions, respectively, with dimensions of s^{-1}. The equation (*cf.* **Equation 2.13**) shows that the reaction can occur in both directions, implying that both the electron transfer from the electrode to the electrolyte and the transfer from the electrolyte to the electrode happen at the interface. The rate of reaction might, however, be different for each direction.

As was explained earlier in **section 2.4**, a certain amount of energy must be provided to initiate the electron transfer and, eventually, the chemical reaction. The required amount of energy is called *activation energy,* E_A. The activation energy is related to the rate constant by the Arrhenius equation:

$$k = Ae^{\frac{-E_A}{k_B T}} \tag{2.14}$$

In which k represents the rate constant, A is a prefactor, which is constant for each chemical reaction, E_A denotes the activation energy or more accurately, the Gibbs free energy of activation, k_B stands for the Boltzmann constant, and T is the temperature in Kelvin. From **Equation (2.14)**, one can infer that to increase the rate constant and thereby hasten the electron transfer and the reaction, either the temperature must be increased, or the Gibbs activation energy must be decreased/lowered. Increasing the temperature ensures the system has higher thermal energy, leading to a faster reaction. This leads to one undeniable reason for the need to operate some fuel cells at high temperatures. These include the solid oxide fuel cells (SOFCs) operated around 800°C-1000°C and the molten carbonate fuel cells (MCFCs) operated at approximately 600°C. However, running secondary batteries or fuel cells at high temperatures is not practicable for some systems like portable and household applications. Instead, increasing the reaction rate by lowering the Gibbs free energy of activation is a more feasible option for these kinds of applications. In order to comprehend how to reduce the Gibbs free energy of activation, the physical origin of the activation energy will be explored to understand better how the electron transfer takes place at the electrode/electrolyte interface.

As in the earlier discussions, an electrode immersed in an electrolyte is considered. No chemical reaction exists at the electrode surface before applying the Nernst potential to the electrode. Put differently, before supplying sufficient energy to the chemical species at the electrode surface, the species are in a stable state or at the minimum of the potential energy profile. This stable state before the reaction is represented on the left side of **Equation (2.13)** and is known as *reactant(s)*. After the application of the Nernst potential, however, enough energy is transferred to the species. It drives a chemical reaction in which the chemical species (reactants) evolve into another chemical species. These are called the *product(s)* and are represented on the right side of the chemical equation in **Equation (2.13)**. It is valid to assume that as the product species are also stable, they must lie in a potential energy minimum. Then, by comparing the potential energy of the reactants and products from the least energy principle, it can be quantitatively said that the product(s) have a lower minimum energy for a spontaneous reaction. Taking all of this into consideration, a qualitative plot of the potential energy of the reaction can be made, as illustrated in **Figure 2.3**.

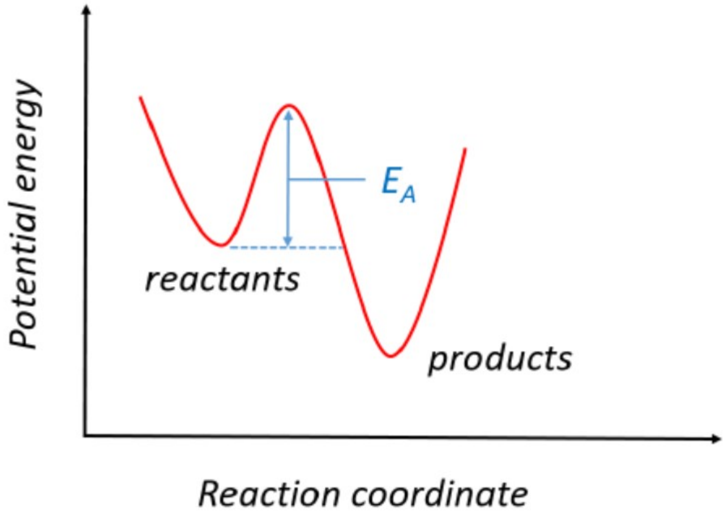

Figure 2.3. *Typical schematic representation of the potential energy profile of a chemical reaction.*

From **Figure 2.3**, the system's potential energy as the electron transfer reaction progresses can be observed. Here, the reaction coordinate indicates the progress of the reaction, so as the reaction advances, reactants are transformed into products. This implies that electron transfer is induced after the Nernst potential is applied and a current is produced. This current causes the system to move from the equilibrium condition and shifts the potential from the Nernst equilibrium potential. Now the focus will be to explain and understand how this phenomenon affects the potential energy diagram.

Suppose the reduced and oxidized species in **Equation (2.13)** have a parabolic free energy profile along the reaction coordinate. As described above, the Nernst potential $E°$ applied to the electrode drives an electron transfer. However, current is produced following this, causing the electrode potential to shift from the Nernst equilibrium potential to another potential E. This change in potential shifts the potential energy parabola of the species by $zF(E - E^o)$, in which z is the number of transferred electrons and F is the Faradaic constant.

The current is measured instead because measuring the reaction rate experimentally is challenging. Therefore, establishing a relation between the two parameters (reaction rate and current) is necessary. The number of moles is related to the species' concentration C and the volume V, *via* $C = \frac{n}{V}$.

Also, the electric current is defined as the rate of charge moving on any given surface:

$$i = \frac{dQ}{dt} \tag{2.15}$$

Where i is current, and t is time. The rate of reaction represents the concentration of species consumed as the reaction progresses; in other words, the number of moles of species consumed per unit of time. By expressing this and substituting **Equations (2.12)** and **(2.15)**, the equation can be reformulated as:

$$\frac{dn}{dt} = \frac{d}{dt}\left(\frac{Q}{zF}\right) = \frac{1}{zF}\frac{dQ}{dt} = \frac{i}{zF} \tag{2.16}$$

Equation (2.16) explicitly indicates the relation between the rates and the current. This, therefore, provides a leeway/platform to evaluate rates from the measured current in an experiment. Even so, to precisely determine the rates, one correction must be added in **Equation (2.16)**. In a heterogeneous system like an electrode/electrolyte interface, rates are mostly determined by incorporating the surface area of the electrode in contact with the electrolyte. Therefore, in an electrode/electrolyte system, **Equation (2.16)** is generally normalized to the surface area of the electrode in contact with the electrolyte:

$$v = \frac{\left(\frac{dn}{dt}\right)}{A} = \frac{1}{zF}\frac{i}{A} = \frac{j}{zF} \tag{2.17}$$

In which v is the reaction rate, j is the current density, and A is the surface area of the electrode.

Solving **Equation (2.17)** for the current density and substituting the reaction rate with the net reaction rates at one electrode, the Equation can be written as:

$$j_{net} = zFv_{net} = zFk^{\circ}\left(C_{Ox}e^{\frac{(1-\alpha)zF(E-E^{o})}{k_BT}} - C_{R}e^{\frac{-\alpha zF(E-E^{o})}{k_BT}}\right) = \tag{2.18}$$

$$zFk^{\circ}\left(C_{Ox}e^{\frac{(1-\alpha)zF\eta}{k_BT}} - C_{R}e^{\frac{-\alpha zF\eta}{k_BT}}\right)$$

This Equation is called the *Butler-Volmer equation,* with α as a symmetric constant ranging between zero and unity. The Butler-Volmer equation represents, in physical terms, the net current density across *one electrode* for a given electric potential. As seen from **Equation (2.18)**, the first term in the bracket represents the current generated from the oxidized species, also called the *anodic current*. At the same time, the last term in the bracket stands for the current generated from the reduced species, also called the *cathodic current*. A new relation/term has been introduced in **Equation (2.18)**: $\eta = E - E°$. This term denotes the so-called *overpotential*, the difference between the equilibrium potential and potential observed during an experiment. In other words, the overpotential can be defined as the potential difference between a thermodynamically determined potential for the redox event and the potential at which this event is experimentally observed. It is interesting to observe how the current density changes as a function of the potential according to **Equation (2.18)**. The current-overpotential dependency is illustrated in **Figure 2.4**.

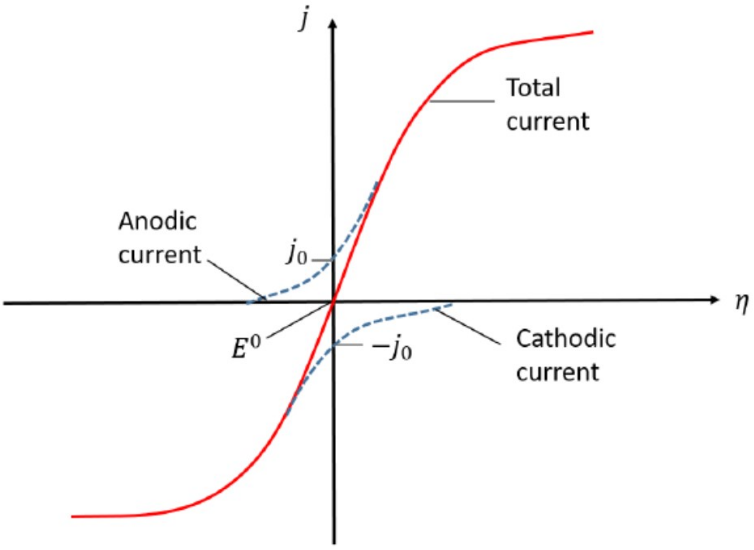

Figure 2.4. *A plot of current density as a function of the calculated overpotential from the Butler-Volmer equation. As calculated via the Nernst equation, the equilibrium potential herein is termed the Zero overpotential. The red curve indicates the total current density calculated using the Butler-Volmer equation. The blue curves depict the anodic and cathodic current densities corresponding to one electrode's oxidation and reduction currents.*

The intersection between the anodic and the cathodic current part of the Butler-Volmer equation and the current density are marked as j_o and $-j_o$, respectively (*cf.* **Figure 2.4**). The j_o is called the exchange *current density* and is usually written in a more compact form in the Butler-Volmer equation as follows:

$$j = j_o\left(e^{\frac{(1-\alpha)zF\eta}{k_BT}} - e^{\frac{-\alpha zF\eta}{k_BT}}\right) \tag{2.19}$$

This exchange current density is a material property. The exchange current density plays a significant role in electrochemical energy storage devices, and by extension, in catalysis. Although an exponential dependence of the applied overpotential on the current is implied by **Equation (2.19)**, this is only true for sufficiently small currents when mass-transport effects (as discussed in the next section) can be neglected.

For larger values of η, an exponential term in **Equation (2.19)** becomes negligible, resulting in the so-called *Tafel equation*:

$$\eta = \frac{RT}{\alpha F} \ln\left(\frac{j}{j_o}\right) \tag{2.20}$$

2.6 The Principle of Mass Transport

The limitations that emanate from the kinetics aspects have been pointed out in **section 2.5**. At higher overpotentials, the current/current density does not follow the exponentially growing curve as witnessed in **Equation (2.19)** and **Figure 2.4**. This occurs due to the limitation of mass transport. The solvated ions (reactant species) present in the electrolyte move at different velocities. The charge and size of the solvation shell determine the rates (velocities). Generally, the transport of the ions can occur through diffusion, convection, or migration.[191]

2.6.1 Diffusion

Without applying any potential (*i.e.*, electric effects), the spontaneous movement of species in solution through establishing a concentration gradient is termed *diffusion*. This is governed by the so-called Fick's first law given by the relation:

$$J_{ij} = -D\, \partial c_i / \partial x_j \tag{2.21}$$

J_{ij} represents the diffusion flux of species-i in the direction x_j , c_i is the concentration gradient, and D (with typical values of 10^{-5} to 10^{-6} cm^2 s^{-1}) is the diffusion coefficient for ions in an aqueous solution. Its value can be calculated using the Stokes-Einstein equation:

$$D = \frac{k_B T}{6\pi\eta r} \tag{2.22}$$

Herein, T is the temperature in Kelvin, r is the radius of the species with a solvation shell, k_B is the Boltzmann constant, and η is the viscosity of the solution.

Fick's second law governs the variation of the concentration with time:

$$\frac{\partial c_i}{\partial t} = D_i \Delta c_i = D_i \nabla^2 c_i \tag{2.23}$$

A reaction in which reactants are consumed at an electrode surface leads to a difference in concentration compared to the bulk electrolyte. This eventually gives rise to a gradient shifted towards the electrode.

The *diffusion layer* is the region where the concentration is significantly lower than in the bulk. Apparently, the thickness of the diffusion layer grows with time *t* when the concentration of the reactants at the electrode becomes zero ($c_o = 0$) and is defined as:

$$\delta = (\pi D t)^{1/2} \tag{2.24}$$

To compare it with the reaction kinetics, it is prudent to introduce a mass transfer coefficient k_d which is related to the diffusion layer thickness. Neglecting convection at this point, a microscopic planar electrode that possesses the exact dimensions of a heterogeneous rate constant can be derived as:

$$k_d = D/\delta = (D/\pi t)^{1/2} \tag{2.25}$$

2.6.2 Convection

Applying some force (flow, rotation, or even gravity) on the electrolyte yields what is termed *convection*. There exist two types of convection; natural and forced convection. Natural convection is caused by small thermal or density fluctuations (differences) by mixing the solution randomly/haphazardly. This can happen in any solution.

Intentionally introducing convection to a system *via* stirring or rotating the disk electrode leads to *forced convection*. Forced convection is several orders of magnitude higher than natural convection. This effectively removes the random aspect from the experimental measurement. The convection flux is given by:

$$J_{ij} = c_i v_j \tag{2.26}$$

Here, v_j is the linear velocity in the direction x_j

2.6.3 Migration

Herein, a gradient in the electrical potential triggers the movement of ions, termed *migration*. The migration relation is described by the Nernst-Planck equation and is given as follows:

$$J_{ij} = -D_i \left\{ z_i c_i \frac{F}{RT} E_j \right\} \tag{2.27}$$

With the applied electric field, $E_j = \frac{\partial \phi}{\partial x_j}$.

Finally, all the factors contributing to mass transport can be summed up to obtain the total flux J_{ij} of species-i in the direction x_j as:

$$J_{ij} = -D_i \left\{ \frac{\partial c_i}{\partial x_j} + z_i c_i \frac{F}{RT} E_j \right\} + c_i v_j \tag{2.28}$$

In hydrodynamic systems, forced convection increases the flux of species to even reach a point corresponding to the thickness of the diffusion layer from the electrode. Mass transfer rates are more prominent than just by diffusion alone (*cf.* **Equation (2.28)**). Therefore, the relative contribution of mass transfer to electron transfer kinetics is minimal. Instead, since quick steady-state can be reached, the double-layer charging can be excluded at steady-state.

2.7 Ohmic Drop (Uncompensated Resistance)

The potential drop ΔE_U due to the so-called *uncompensated resistance* R_u at a current I follows Ohm's law:

$$\Delta E_U = R_u I \tag{2.29}$$

In a nutshell, Ohmic resistance can be divided into three categories:[192] resistance due to ion migration within the electrolyte, electron transport within the components of the circuit, and contacts between the two.[193] Under experimental conditions, the latter two can often be significantly reduced, whereas the resistance of the electrolyte dominates. The resistance of the electrolyte solution between the tip of the Luggin capillary and the working electrode (WE) is a function of several parameters like temperature, cell and electrode geometry, current density, and hydration state of the ions and ion concentration.[192,194,195] The resistance can be determined by employing electrochemical impedance spectroscopy.[196] The uncompensated resistance is measured at a constant potential with EIS or specific steps, whereas in cyclic voltammetric (CV) measurements, the voltage is not constant but varies over time. As such, the correction of CVs is only partially physically accurate.

2.8 Sabatier Principle, The Volcano Plot & Scaling Relations

Having discussed the various interaction between the catalyst surface and reactants (reaction intermediates/adsorbates) in **sections 2.4** and **2.5**, it is now ripe to focus on boosting the features of the catalyst. Paul Sabatier proposed in the early 1900s that the characteristics of a suitable catalyst lie in the interaction between its surface and the reaction intermediates[1] (reactants), as that is pivotal in catalyzing the reaction.[197,198,199] Based on that, he theorized that the binding energy between the catalyst (catalyst surface) and the reactant (reaction intermediates) should

---

[1] A chemical generated in one reaction step but used up in the following step is called a *reaction intermediate*.

be neither too strong nor too weak. The Sabatier principle can be further elaborated in the following.

The catalyst (catalyst surface) will fail to activate the reactants (reaction intermediates) in case there is too weak interaction. On the other hand, a too strong interaction (adsorption) between the catalyst surface and the reactants leads to the blocking of the catalyst surface by the intermediates or products. The binding energy/strength between the catalyst surface sites and the reaction intermediates should be "just right" to guarantee efficient catalysis.[200,201] Although very useful, this fundamental concept in chemical heterogeneous catalysis provides only qualitative information.

According to the Sabatier principle, the activity of different catalyst materials can be plotted as a function of the binding energy (or Gibbs energy of activation) for any given chemical reaction. Activity can be best described as the parameter that shows the increase in the chemical reaction rate. The rate increases linearly as the activity. For an optimum catalyst, having the right binding strength yields the highest activity, often represented in a plot with a triangular or volcano-like shape. As a result, the graph is popularly referred to as a *volcano plot* and was first announced by A. A. Balandin.[202] It remains a well-established practice in heterogeneous catalysis since the work by S. Trasatti to visualize and quantify activity trends through this so-called volcano plot, giving physical meaning to the Sabatier principle.[203] Through the volcano plot, a variable connected to the catalytic reaction activity, like the current density, overpotential, half-wave potential, etc., is plotted against an appropriate "descriptor" having a direct correlation to the stability of the reaction intermediates. In principle, any selected descriptor must correlate to the rate law. Therefore, the descriptor is usually the calculated surface binding energy for a single intermediate or a variable logically linked to it (*e.g.*, the heat of formation of a bulk compound or adsorption energy of reaction intermediates/reactants).[204,205,206]

Figure 2.5 shows the volcano plot pattern for the oxygen reduction reaction on several metal electrode surfaces.[207] The activity is plotted *versus* the binding energy (descriptor) of one of the reaction intermediates (specifically, adsorbed oxygen species). The thermodynamically modeled catalyst, in this case, is Pt since it is the closest to the pinnacle of the volcano plot, representing the highest activity at which the binding energy of the catalyst surface and the adsorbed oxygen species is neither too weak nor too strong. On the contrary, catalysts to the left and right sides of Pt indicate strong (too strong) and weak (too weak) binding, respectively, of their individual catalyst surface sites to the reaction intermediate (adsorbed oxygen).

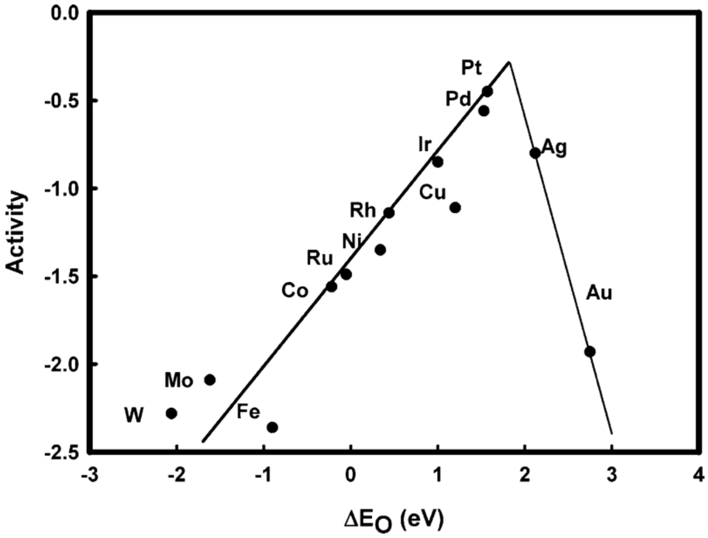

***Figure 2.5**. Volcano plot for the oxygen reduction reaction. Herein, the activity is plotted as a function of the binding energy of adsorbed oxygen for different metal electrode surfaces. Pt exhibits close to optimum binding energy as well as activity. Reprinted with permission from reference.*[207] *Copyright © (2018), Royal Society of Chemistry.*

Scaling relations. Until now, the volcano plot (*cf.* **Figure 2.5**) portrayed considers one of the many reaction intermediates for the graph. However, other volcano plots exist that rightly combine the Sabatier principle with the so-called linear scaling relations (*cf.* **Figure 2.6**).[208] Using several elementary electrochemical reactions,[208] the mechanism of the complex ORR can be well understood.

$$O_2 + H^+ + e^- \rightarrow OOH_{(ads)} \qquad (2.30a)$$

$$OOH_{(ads)} + H^+ + e^- \rightarrow O_{(ads)} + H_2O \qquad (2.30b)$$

$$O_{(ads)} + H^+ + e^- \rightarrow OH_{(ads)} \qquad (2.30c)$$

$$OH_{(ads)} + H^+ + e^- \rightarrow H_2O \qquad (2.30d)$$

It has been proven through studies by several researchers that there exists a correlation between the free energies of adsorption ΔG (binding energies) of the intermediate species ($i.e.,$ $O_{(ads)}, OH_{(ads)}, and\ OOH_{(ads)}$).[208,209,210] In this regard, deploying the features of a single reaction intermediate as the descriptor to represent the others is meaningful. Hence, examples of **Figure 2.5** continue predominantly in the literature. **Figure 2.6** indicates that the optimization of an electrocatalyst for **Equation (2.30a)**, which requires a strong binding of the $OOH_{(ads)}$ species, is detrimental to **Equation (2.30d)**, which needs a weak binding of the $OH_{(ads)}$ species. The difference of the energy of adsorption ΔG between the $OH_{(ads)}$ and $OOH_{(ads)}$ species is a constant and is given by $\Delta G_{OOH_{(ads)}} - \Delta G_{OH_{(ads)}} \cong 3.2$ eV.[208] Put differently, each reaction step requires optimization of the binding energy, but the challenge is that independent adjustments are not straightforward due to the scaling relations. Hence, the optimum implies a compromise. In that regard, an ideal catalyst for the ORR should follow the Sabatier principle and, by extension, the volcano plot. The scaling relations are an inevitable embodiment of the Sabatier principle and volcano plot as they function together to tailor/dictate catalyst design and material selection.

There are occasions when the scaling relations are not strictly followed. These occur when the linear scaling of a few typical reactions requires strong binding whiles others need weak binding. Therefore, the scaling relations are inapplicable in such circumstances. Several measures have been successfully adapted to circumvent the scaling relations.[211,212,213,214] Nowadays, the strength of computational calculations or models with roots from the density functional theory (DFT) eases the derivation of binding energies for catalysts and surface sites.[215,216,217,218]

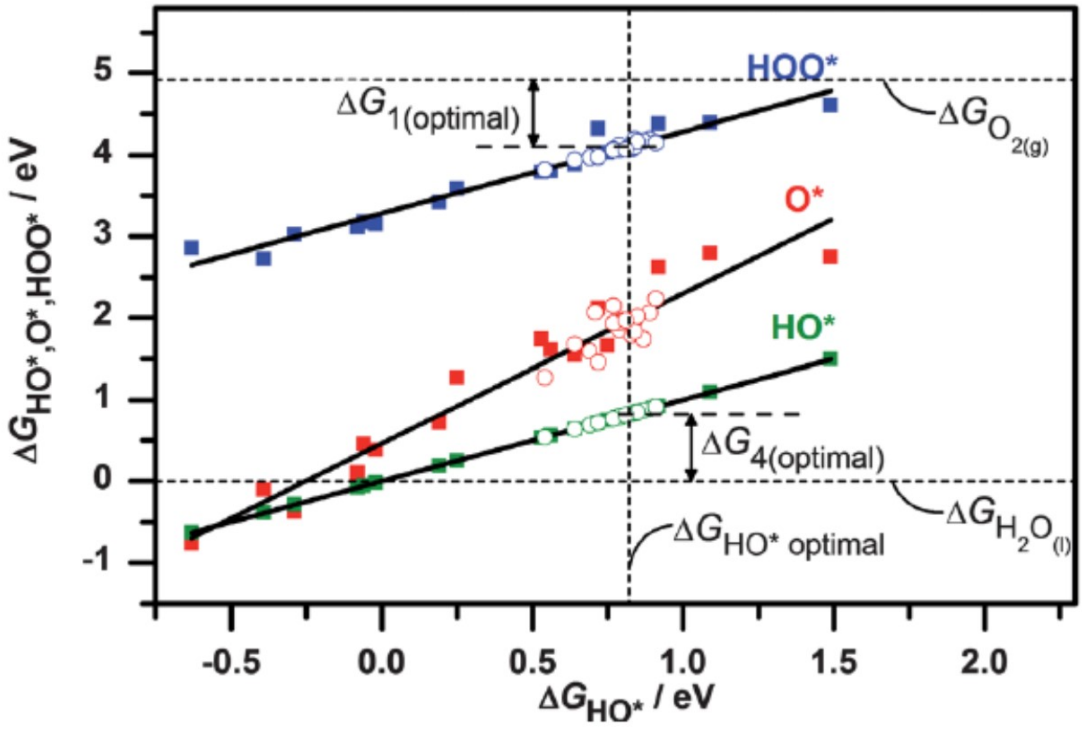

***Figure 2.6**. Theoretical predictions of the free energies of adsorption of $HOO_{(ads)}$ (HOO^*), $HO_{(ads)}$ (HO^*) and $O_{(ads)}$ (O^*). A plot of ΔG_{HOO^*}, ΔG_{HO^*}, and ΔG_{O^*}, respectively against ΔG_{HO^*} for (111), (100), and (211) for pure metal surfaces (filled squares) and Pt overlayers on Pt-alloy surfaces (open circles). Reprinted with permission from reference.[208] Copyright © (2005), Elsevier B. V.*

2.9 Active Sites

Having obtained the necessary tools and mechanisms to identify and design optimum performing catalytic materials (*cf.* **section 2.8**), it is incumbent to further zoom into the exact location where the reactions occur on the catalyst surface. In addressing the issue, I. Langmuir, in 1922, was the first to opine that the catalyst surface does not consist of identical sites and, therefore, is not homogeneously distributed at the atomic level.[219] In this respect, the corresponding adsorption energies toward intermediates can vary for specific catalyst surface sites due to dissimilar localized electronic and/or geometric structures. Put differently, only specific "active sites" on the catalyst surface and not the entire surface contribute to its overall activity. Tersely, Langmuir posited that the catalyst surface could be regarded as an area consisting of a definite number of elementary sites that determine the overall activity.

Three years on, the work by Hugh Stott Taylor further enriched the understanding of the concept of active sites, stating the existence of different active sites for specific reactions.[220] This can be interpreted as the adsorption activation of specific atomic sites on the catalyst surface for particular reactions. Active sites are dependent on the chemical reaction and can be classified as a single atom, an arrangement of atoms, or structural motifs. Generally, two categories of reactions, namely, structure-sensitive and structure-insensitive, can be identified. The structure-sensitive ones require the reaction to occur at specific sites, suggesting a relatively strong interaction between the reaction intermediates (reactants) and the catalyst surface. The structure-insensitive ones are characterized by weak interactions of reaction intermediates (reactants) with the catalyst surface and are not dependent on such structural motifs.[221]

Accurately identifying the active sites at the solid/liquid interfaces, either theoretically or experimentally, is a prerequisite to better understanding the mechanisms involved, leading to the enhancement of catalyst design.[222,223,224] An effective experimental tool to achieve this goal dwells on analyzing the noise level of the electrochemical scanning tunneling microscopy (n-EC-STM) signal.[225,226,227] In effect, the nature of the most active sites of a catalyst for particular reactions can be obtained, thus enhancing the predictive power of surfaces.

2.10 Essential Electrocatalytic Reactions

It has been revealed in the previous sections that specific electrocatalytic processes, *i.e.*, electrochemical water splitting and fuel cell technology, are pivotal to the realization of the energy conversion and storage of the much-anticipated "green" hydrogen economy. It has been established that the potential required to trigger and drive an electron transfer, a critical phenomenon, can be harnessed for the production and storage of energy. As has been elaborated earlier (see **Chapter 1**), water splitting *via* electrochemistry is vital to producing "green" hydrogen, which will serve as the source fuel in the other device, namely, fuel cells. Fuel cells require an oxidant to operate, which is also produced *via* water electrolysis, albeit the atmosphere (*i.e.*, air) has an abundance of it. As this dissertation centers on the aforementioned electrocatalytic processes, it is necessary to discuss the main reactions that constitute the core underpinning it.

2.10.1 Electrochemical Water Splitting

There are notions that the maiden practice of electrochemistry can be traced back to the third century BC and could have included water electrolysis. It is also debated that several scientists, including van Troostwijk, Deinman, and Alessandro Volta, might have already experimented with and observed the water electrolysis phenomenon by 1789.[228] However, according to the accessible scientifically documented evidence, electrolysis of water was first discovered in 1800 by William Nicholson and Anthony Carlisle, both of English descent.[229] Driven by the voltaic pile developed by Alessandro Volta, German scientist Johann Wilhelm Ritter constructed the first reported electrochemical cell (water electrolyzer) equipped with the capability of evaluating the to-be-produced hydrogen and oxygen gases in the same year.[230] Water-splitting technology reached a stage where its practical realization was possible owing to the development of novelties such as the realization of the direct current electrical generator in 1860.[231] It is significant to remark that the technology underwent further development, and by 1939, the construction of the first large-scale water electrolyzer was completed. Its capacity was announced to be in the region of 10,000 m^3 (H_2)/hr.[232] In brief, a water electrolyzer (*cf.* **Figure 2.7**)[233] splits and/or decomposes H_2O into its constituent gases (*i.e.*, O_2 and H_2). In effect, the generated H_2 is useful as the source fuel in fuel cells. The electrolyzer requires the application of an external potential to trigger the water-splitting reactions, namely, the HER, on the cathode and the OER, on the anode. The accompanying equations for the two half-cell reactions in acidic media and the resulting overall reactions are as follows:[189]

Cathode (HER): $$4H^+(aq) + 4e^- \rightarrow 2H_2(g) \tag{2.31a}$$

Anode (OER): $$2H_2O(l) \rightarrow O_2(g) + 4H^+(aq) + 4e^- \tag{2.31b}$$

Overall reaction: $$2H_2O(l) \rightarrow 2H_2(g) + O_2(g) \tag{2.31c}$$

A)

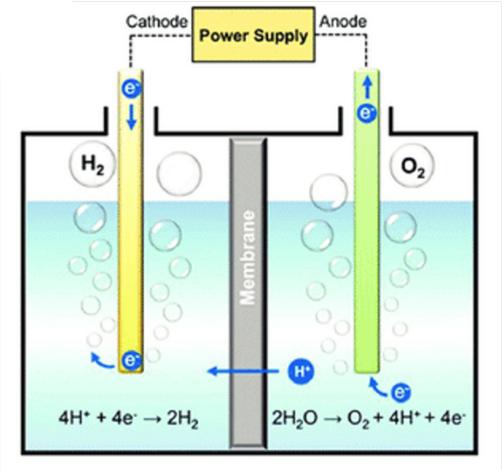

B)

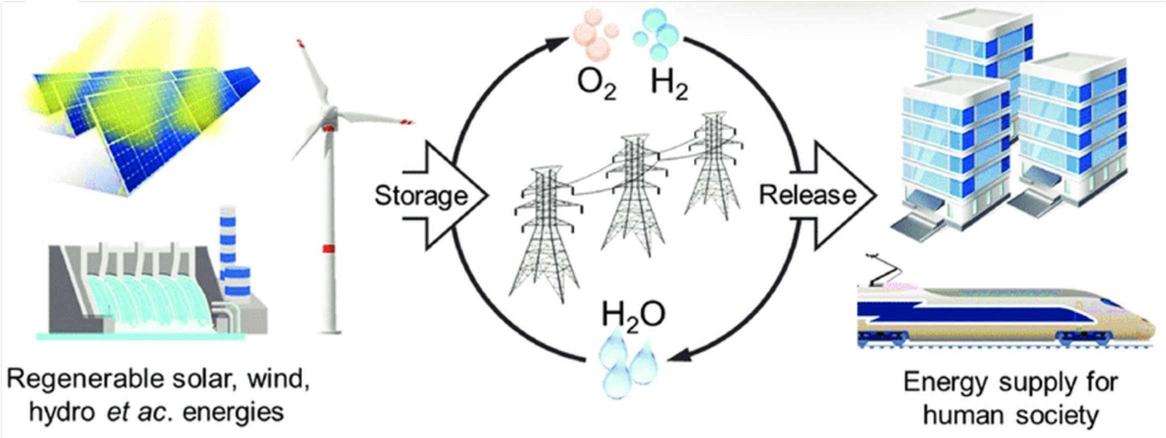

***Figure 2.7**. **A)** Schematic depiction of a typical water electrolyzer, with the HER taking place at the cathode and the OER occurring at the anode. **B)** Schematic representation of the water splitting process, which has its source of electricity to decompose water into its gas components from renewables. Reproduced from reference[233] with permission from the Royal Society of Chemistry. Open access, published under a CC-BY license.*

To facilitate the discussions, the next section focuses on the reaction pathways in various electrolyte solutions (either alkaline and/or acidic) for each reaction (HER, OER) deployed in this dissertation.

2.10.1.1 Hydrogen Evolution Reaction

The electrolyte pH is a specific parameter for the HER mechanism under consideration. The overall reaction of the HER in acidic media progresses as given in **Equation (2.31a)**. Typically, HER charts a 2-electron transfer reaction, encompassing one (1) catalytic intermediate, H*. The general consensus regarding the HER is that it follows two separate mechanisms (i.e., Volmer-Heyrovsky or Volmer-Tafel mechanism) for both alkaline and acidic electrolytes.[234] In each pathway, the first step, i.e., the Volmer step, involves the adsorption of a hydrogen atom (combining a proton from the electrolyte and an electron from the electrode) to the catalyst surface.

Volmer step: $H^+ + e^- + * \rightarrow *H$ (2.32a)

Heyrovsky step: $H^+ + e^- + *H \rightarrow H_2 + *$ (2.32b)

Tafel step: $*H + *H \rightarrow H_2 + 2*$ (2.32c)

Herein, * represents an adsorption site on the catalyst surface.

Subsequently, the adsorbed hydrogen atom (Volmer step) proceeds to the second step *via* two distinguishable pathways, namely, the Heyrovsky step or Tafel step. The former (*cf.* **Equation (2.32b)**) occurs when the adsorbed hydrogen atom from the Volmer step merges with a proton and an electron, yielding a hydrogen molecule. The latter (*cf.* **Equation (2.32c)**) happens if the adsorbed hydrogen atom (Volmer step) combines with a nearby adsorbed hydrogen atom to produce a hydrogen molecule. The last step, which is either the Heyrovsky or Tafel step, characterizes the desorption of the produced molecular hydrogen (H_2) from the catalyst surface.

The overall HER in alkaline media proceeds as follows:

$$2H_2O(l) + 2e^- \rightarrow H_2(g) + 2OH^-(aq) \tag{2.33}$$

In principle, the high electrolyte pH of alkaline electrolytes makes the HER undergo different Volmer, Tafel, and Heyrovsky pathways/steps. The form of the various reaction steps is presented below:

Volmer step: $H_2O + e^- + * \rightarrow *H + OH^-$ (2.34a)

Heyrovsky step: $H_2O + e^- + {}^*H \rightarrow H_2 + OH^- + {}^*$ (2.34b)

Tafel step: ${}^*H + {}^*H \rightarrow H_2 + 2{}^*$ (2.34c)

For high electrolyte pH, the Volmer step proceeds with the merging of an electron from the electrode with an H_2O molecule on the catalyst surface. Following the Volmer step, the HER advances in two distinct phases. While the Tafel step in alkaline electrolytes follows the same process as in acidic electrolytes, the Heyrovsky step in higher pH solutions combines an adsorbing hydrogen atom with another water molecule and an electron to yield a hydrogen molecule. Of course, the desorption of the produced hydrogen molecule *via* either the Heyrovsky or Tafel step epitomizes the end of the entire process.

In a nutshell, the HER mechanism follows either Volmer-Heyrovsky or Volmer-Tafel reaction pathway. A single-bound intermediate, *i.e.*, *H, is a critical criterion for assessing catalytic performance in each pathway.[235] It is essential to state that the features of the electrified solid/liquid interface, the nature of the catalyst, and the overpotential immensely influence the kind of HER pathway that will be followed. In certain instances, both types of electron transfer can concurrently exist.[236,237,238] The HER mechanism can be inferred from the Tafel plot, a direct product of the polarization curve. The Tafel slope reveals the deep-rooted nature of the catalyst, such as the rate-determining step, and hence, its deployment to justify the HER mechanisms.[239,240] In case the rate-limiting step of the HER corresponds to the Volmer step, the Tafel slope will be around 120 mV dec^{-1}. Contrarywise, smaller Tafel slopes of 40 and 30 mV dec^{-1} are obtained for the HER rate determined by either the Heyrovsky step or the Tafel step, respectively.[241] Nevertheless, it should be revealed that several factors not limited to mass transfer, adsorption processes, and electrode potential inhibit the Tafel slope.[242] Accordingly, the rate-determining step of the HER could be altered by those factors.

The open question worth answering is, which materials are outstanding candidates to enhance the HER activity? In this respect, platinum and platinum group metals (PGMs) are deemed the ideal pure metal catalysts that exhibit optimum activities towards the HER. For instance, Pt shows an almost thermo-neutral free energy binding towards the adsorbed hydrogen species. Based on the Sabatier principle, it has its roots in the hydrogen binding energy on the platinum surface close to the summit of the volcano plot.[242] As cost-effective and high-efficient materials are being contemplated as substitutes to remedy the dwindling PGMs reserves, especially in alkaline electrolytes, non-noble metal-based materials such as nickel and nickel-based alloy have been found to have high activity and long-term stability.[135] Additionally, carbon-based catalyst materials are emerging as alternatives.[235]

2.10.1.2 Oxygen Evolution Reaction

Ideally, the thermodynamic equilibrium potential of the OER on the anode of the water-splitting process is 1.23 V *vs.* RHE. High overpotentials usually accompany real-world water-splitting devices, even when using standard catalysts like metal-oxides and perovskite structures. This arises from the involvement of the OER in a four-proton-electron transfer, comprising several reaction intermediates (*OOH, *OH, and *O), thereby making the mechanism of the OER much more multifaceted than the HER.[242] It is significant to add that because the binding energies of the multiple reaction intermediates are strongly correlated, decoupling them is almost impossible due to the scaling relations. In this sense, the OER is reckoned as the bottleneck of the overall water-splitting process owing to its sluggish kinetics.

Unsurprisingly, the OER mechanism relies on the pH of the electrolyte, as in the HER scenario. **Equation (2.31b)** provides the overall reaction of the OER in acidic media. In this regard, some plausible reaction pathways of the OER in acidic media can be represented as follows:

$$H_2O + * \rightarrow *OH + H^+ + e^- \quad (2.35a)$$

$$*OH \rightarrow *O + H^+ + e^- \quad (2.35b)$$

$$*O + H_2O \rightarrow *OOH + H^+ + e^- \quad (2.35c)$$

$$*OOH \rightarrow O_2 + H^+ + e^- + * \quad (2.35d)$$

By contrast, upon introducing high pH (alkaline) electrolytes, the OER is depicted differently:

$$4OH^-(aq) \rightarrow O_2(g) + 4e^- + 2H_2O(l) \quad (2.36)$$

It is worth remarking that the reaction pathways in alkaline electrolytes are comparable to the case in acidic media:

$$OH^- + * \rightarrow *OH + e^- \quad (2.37a)$$

$$^*OH + OH^- \rightarrow {}^*O + H_2O + e^- \tag{2.37b}$$

$$^*O + H_2O + OH^- \rightarrow {}^*OOH + H_2O + e^- \tag{2.37c}$$

$$^*OOH + OH^- \rightarrow O_2 + H_2O + e^- + {}^* \tag{2.37d}$$

For both low and high electrolyte pHs, oxygen gas or molecule (O_2) could be directly generated by combining two *O intermediates following the second reaction pathway of the OER as indicated below:

$$^*O + {}^*O \rightarrow O_2 \tag{2.38}$$

It is paramount to remember that the thermodynamic barrier of this reaction pathway is always higher than the reaction(s) forming *OOH intermediate.[243]

As already alluded to, the complex mechanism of the OER instigates sluggish kinetics and low energy efficiency for the overall water electrolysis. Several attempts have been devoted to enhancing the OER activity to remedy the sluggishness. One well-accepted approach is increasing the number of active sites on the electrocatalyst surfaces.[244,245] Consequently, the binding energies of the reaction intermediates (*i.e.*, *OOH, *OH, *O), according to the Sabatier principle, are well balanced.[246,247] A new suggested equally-refreshing approach involving the promotion of mass transfer was recently opined by Liang *et al.*[248] Moreover, the electrolyte composition also considerably influences the OER activity. As a poignant example, Michael *et al.* systematically investigated the effect of alkali metal cations on the OER activity for nickel oxyhydroxide catalysts in the presence of varying alkaline electrolytes.[249] It was established that the performance of the OER improves in the presence of Cs^+, whereas Li^+ lowers the OER activity. An analogous trend of the alkali metal cation effect on the OER activity was reported by Garcia *et al.* for a nickel oxyhydroxide catalyst.[250] Until now, most of the appealing catalyst materials deployed are relatively abundant. However, the quest to gradually eliminate rare and valuable metals as catalyst materials must be seriously considered. More research is required to fully fathom the internal OER mechanism and eventually resolve the sluggish kinetics and poor energy efficiency, despite the progress in deploying various methods to enhance the OER performance. In this respect, this dissertation aims to contribute a piece to help address the bottleneck.

2.10.2 Fuel Cells – Fundamental Concepts

It has been established (see **section 1.4**) that one of the appealing technologies behind the electric vehicle concept, providing solutions in the automobile industry with devices such as airplanes, submarines, trains, heavy-duty trucks, buses, and cars, thrives on fuel cells. The already elaborated electron transfer phenomenon is leveraged to generate electrical power, with the significant merit being the production of water as the only "waste". Therefore, in this section, a brief history of fuel cells will be given, anchored on the underlying concept of the technology. Most significantly, the reactions critical to the subsequent discussions in this dissertation will be elucidated.

Historic archives confirm that the *galvanic cell* was the first device that employed principles of electrochemistry. The galvanic cell basically comprises two sets of half-cells placed in a bath containing two electrodes immersed in their respective electrolytes. These half-cells are then connected to form a single configuration. More specifically, the electrodes are connected by electrically/electronically conducting materials (*e.g.*, wires), and both electrolytes are connected *via* a salt bridge. A chemical reaction occurs in each half-cell, and electrons are transferred from the electrode to the electrolyte or vice versa.

The underlying idea of the cell is to harvest this electron transfer by forcing electrons through an outer electronic conductor. Of course, this can eventually be used to power an electric/electronic device. Meanwhile, ions move freely through the electrolyte. One of the reactions is called the *oxidation* reaction because the species' oxidation number increases as electrons are transferred to the electrode. The electrode for this reaction is called the *anode*. The other reaction is called the *reduction* reaction because the oxidation number of the species gets reduced when the species receive one or more electron(s) from the electrode. Herein, the electrode is called the *cathode*. State-of-the-art technologies like fuel cells and battery systems were developed from the basic principles of the galvanic cell. The key distinguishing feature between galvanic cells and fuel cells emanates from the immersion of both electrodes in the same electrolyte for the latter. In contrast, for the former, both electrodes are inserted into two separate electrolytes and linked through a salt bridge.

From the anecdote/short narrative, an energy conversion device that supplies electricity using a spontaneous spatially separated redox reaction between a source fuel (*e.g.*, hydrogen) and an oxidant is called a *fuel cell* (see **Figure 2.8**).[251] The source fuel could be almost anything that can be oxidized, including hydrogen, methane, methanol, diesel fuel, and so on. The oxidant can be, *e.g.*, atmospheric oxygen (from air). The implementation of fuel cells is usually only possible with ionic conductors. It is worth noting that electrolytes are not necessarily liquid. Hence, any substance that can conduct ions, as a poignant example, solid electrolytes like stabilized zirconia and stabilized bismuth oxides, are another type of electrolyte. In that regard, an electrolyte can be either conventional, *i.e.*, in the liquid state (an acidic or alkaline electrolyte solution), or less traditional, *i.e.*, fused salts (*e.g.*, molten NaCl-KCl eutectic). Ionically conductive polymer (*e.g.*, Nafion®, polyethylene oxide-$LiClO_4$) is yet another possibility. Fuel cells are mainly characterized by their electrolytes because the electrolyte dictates key operating parameters/factors, including the operating temperature. Therefore, there exist solid oxide fuel cells (SOFCs), alkaline fuel cells (AFCs), molten carbonate fuel cells (MCFCs), direct hydrocarbon fuel cells (DHFCs), phosphoric acid fuel cells (PAFCs), polymer electrolyte or proton exchange membrane fuel cells (PEMFCs), and a host of others.[252]

The concept of fuel cells was first discovered and experimentally demonstrated between 1837-1842 by Christian Friedrich Schönbein, who described the so-called fuel cell effect (the hydrogen/oxygen chain between two Pt foils connected by acidified water and fed with H_2 and O_2), inverse electrolysis.[253,254] Around the same period, precisely in 1839, Sir William Robert Grove was the first to design a complete fuel cell system.[255,256] Later, Francis Thomas Bacon in 1932 showcased the first practical hydrogen-oxygen fuel cell at King's College, London, and Trinity College, Cambridge. He proposed using fuel cells (specifically, AFC) in submarines and eventually demonstrated a successful six-kilowatt forty-cell battery in 1959.[257, 258] Within a similar timeline, further technology development was ongoing, and from that, NASA's space program emerged with the first practical device.[259,260] Fuel cells have since evolved to cover a wide range of applications and systems, including transportation, versatile stationary power generation, and portable energy devices.

There is much interest in developing fuel cells for commercial applications. This interest is driven by fuel cells' technical and environmental advantages, including high-performance characteristics, reliability, durability, and "clean" power. It uses an electrochemical process to convert chemical energy into electricity directly. Unlike batteries, fuel cells can continuously produce electricity provided the source fuel and oxidant are supplied. In reference to this, several fuel-cell electric vehicles are currently in operation (see **section 1.4**).

The most outstanding candidate out of the variety of fuel cells available is the *PEMFC*. PEMFCs are captivating energy conversion devices. For instance, PEMFCs operate at relatively low operating temperatures, *ca*. 60-80°C. Hence, they are attractive for applications in the automotive industry.[252,260] PEMFCs also portray high power density, can vary output quickly, release zero toxic emissions, and exhibit relatively good performance compared to other fuel cells. Additionally, they are well-suited to power applications (e.g., automotive industry) where quick or short startup time is required.[261] More so, PEMFCs have operational advantages, including using a solid polymer electrolyte that reduces corrosion and doubles as an effective means of minimizing fuel crossover. PEMFCs are anticipated to be durable but are exposed to various contaminants, either present in air and hydrogen (source fuel) or released by fuel-cell system materials, leading to potential deleterious performances.[262,263] Hence, improvements (catalytic activity, selectivity, and stability) are still required to meet the strict demands of the automotive and other markets, which is one of this work's primary goals.

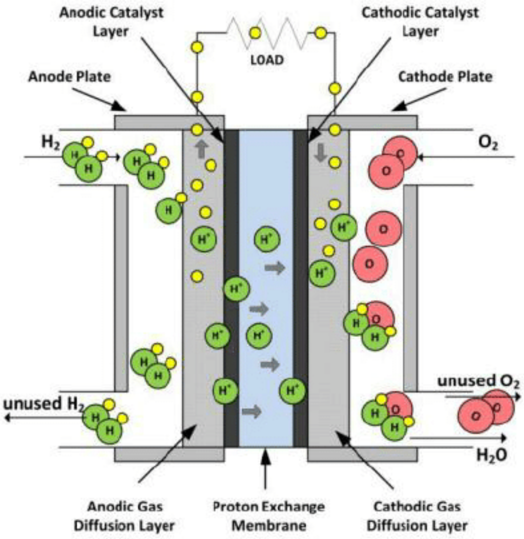

Figure 2.8*. Schematic representation of a typical PEMFC. The anode has the source fuel* H_2 *where the HOR occurs, whereas the cathode with the oxidant (atmospheric oxygen) exhibits the ORR. Reproduced with permission from reference.[251] Copyright © (2000), WILEY-VCH Verlag GmbH, Weinheim, Fed. Rep. of Germany.*

According to **Figure 2.8**, the PEMFC comprises two catalytic layers (CLs), an electronic separator, and flow-field plates (gas diffusion layers - GDLs). The two *catalytic layers* showcase the catalytic layer for the cathode and the anode, where the ORR and fuel oxidation (H_2 in this case) occur, respectively. Each catalytic layer is in contact with a *gas diffusion layer*. The *separator* acts as an ionic conductor between the two catalytic layers, which is polymer-based (in PEMFC). The *flow-field plates* (illustrated in **Figure 2.8** as *anode* and *cathode plates*) serve as the electronic conductor for the electrons produced/consumed by the electrochemical reactions. Additionally, they allow the distribution of gases, first to the GDLs (the macroporous - microporous carbon layer), which supplies a homogeneous flux of gases and removes the water produced by the electrochemical reactions (see **Equations (2.33 a-c)**) and then ultimately to the catalytic layers. The membrane, the CLs, and GDLs make up what is called the *membrane electrode assembly* (MEA).

Hydrogen and oxygen are fed through flow channels and diffuse through the GDLs to the catalyst on their respective sides of the MEA. Hydrogen is oxidized to form protons and electrons activated by the anode's catalyst. The protons move through the PEM, and the electrons travel from the anode through an external circuit to the cathode. At the cathode catalyst, oxygen reacts with the protons that move through the membrane, and the electrons travel through the circuit to form water and heat. Indeed, fuel cells are not limited by the Carnot efficiency since hydrogen and oxygen react to produce electricity directly rather than indirectly, as in a combustion engine. Although more efficient than combustion engines, the fuel cell does produce some waste heat. Hence, the typical efficiency for hydrogen fuel cells that also employ Nafion® as the membrane ranges from *ca.* 50 to 83%.[264]

At 25°C (298 K), the standard hydrogen electrode measurements for the PEMFC are as follows:

Anode (HOR): $$2H_2(g) \rightarrow 4H^+(aq) + 4e^- \tag{2.39a}$$

Cathode (ORR): $$O_2(g) + 4H^+(aq) + 4e^- \rightarrow 2H_2O(l) \tag{2.39b}$$

Overall reaction: $$2H_2(g) + O_2(g) \rightarrow 2H_2O(l) \tag{2.39c}$$

Overpotentials occur on both fuel cell electrodes, particularly the cathode. This manifests because the voltage produced from fuel cells is lower than the ideal voltage, which is the thermodynamic equilibrium potential difference for both electrodes. In a PEMFC, as illustrated in **Figure 2.8**, the hydrogen is oxidized at the anode at a thermodynamic equilibrium potential of 0 V *vs*. SHE (see **Equation (2.39a)**). Meanwhile, the oxygen is reduced at the cathode at a thermodynamic equilibrium potential of +1.23 V *vs*. SHE (see **Equation (2.39b)**).

The PEMFC should generate an ideal voltage of 1.23 V (the difference of equilibrium potential of cathode and anode). Nonetheless, less than 1.23 V is generated in reality because of the so-called overpotential. This implies that it is prudent and desirable to produce just as little overpotential as possible to produce a higher voltage when the fuel cell draws current. Then arises the inevitable and obvious question: how can the overpotential be lowered?

As discussed in **section 2.5**, the exchange current density is a property of the material. The higher the exchange current density, the closer the potential is towards the thermodynamic equilibrium potential as far as iR mass transfer is kept negligible. Put differently, using a material with a higher exchange current density or putting more catalysts will lower the system's overpotential at the same current density. That is the fundamental idea behind using a specific material to reduce the overpotential. The material that lowers the overpotential is called *an electrocatalyst*, as discussed in **section 2.2**. It was established in **section 2.5** that the overpotential is generated because activation energy is needed for the electron transfer across the electrode/electrolyte interface, leading to the electrochemical reaction conversion of chemical energy into electrical energy. The *activation overpotential* or *loss* stems from the sluggish reaction kinetics occurring at either both electrodes or just one electrode. Several other parameters contribute to the overpotential besides the activation overpotential in real systems.[207] Some of these are:

- *Ohmic overpotential/Ohmic drop*: According to Ohm, every substance has a certain amount of electrical resistance. The electrolyte and the electrode are indifferent since they are prerequisites to guarantee the successful transportation of ions through external circuits, *i.e.*, wires. Losses from electronic transport are deemed negligible, whereas ion conduction, emanating principally from the less efficient hopping mechanism, is saddled with high losses. These losses can be compensated or largely managed using electrolytes with high ionic conductivities or reducing the membrane thickness of devices like fuel cells and electrolyzers.
- *Mass transport/transfer overpotential*: A few ions are required at the electrode surface for initiating chemical reactions. For instance, two or four electrons/protons are needed for the ORR's occurrence. It takes some time, however, for the ion to move from the anode to the cathode. Hence, a loss is encountered if the electron transfer occurs faster than the ion transfer from one electrode to the other. Thus, diffusion and migration of ions affect the overpotential. Diffusion of oxygen, which forms just 21% instead of 100%, inadvertently leads to additional Nernst shift. In summary, the continuous supply of reactants to the electrode surface and the timely removal of products from the electrode surface are significant for the reactions' effectiveness and efficient progress.

- *Chemical side reactions*: As already mentioned, an electron transfer reaction occurs at two electrodes for a fuel cell to generate electricity - the oxidation reaction at the anode and the reduction reaction at the cathode. However, sometimes a reduction reaction occurs at the anode, while an oxidation reaction occurs at the cathode. Involuntarily, this process generates losses and, therefore, decreases the efficiency of the fuel cell. This process is termed a *parasitic reaction*, with H_2 crossover as an example. Apart from parasitic reactions, a reaction of different pathways can sometimes occur at an electrode. For instance, peroxide formation influences stability, especially when carbon (usually the support) corrodes. Reactions of specific pathways run slower (some pathways are energetically unfavorable; hence, their reaction rates run significantly slower) than other pathways. Therefore, a reaction in other pathways is unfavorable to the system, decreasing its efficiency.

As mentioned earlier, all the parameters contribute to the overpotential and increase the overpotential of the fuel cell.

2.10.2.1 Hydrogen Oxidation Reaction

Once again, the pH of the deployed electrolyte is crucial as it serves as a platform to distinguish between the HOR mechanism being considered. Under this aspect, different HOR pathways exist for acidic- and alkaline-based electrolytes. **Equation (2.39a)** illustrates the HOR in acidic media. However, for high pH (alkaline media), it is represented as follows:

$$2H_2(g) + 4OH^-(aq) \rightarrow 4H_2O(l) + 4e^- \qquad (2.40)$$

The pivotal role that the HOR, generally recognized as the reverse of the HER, plays in the lead-up to developing hydrogen-based energy sources cannot be downplayed. Both HER and HOR involve only one intermediate, adsorbed hydrogen, during the reaction. Moreover, the HOR follows either the Volmer-Heyrovsky or Volmer-Tafel mechanism as well. In most cases, the performance of these two reactions should be comparable.

The rate of the HOR in alkaline electrolytes, like its reverse counterpart, the HER, is slower than in acidic solutions. Again, platinum, platinum alloys, and platinum group metals are regarded as the state-of-the-art pure metal catalysts for the HOR, despite various efforts towards developing abundant, less noble metal, bimetallic/alloy, and metal-free catalysts.[265, 266, 267, 268, 269] Recently, Jin *et al.* explored the performance of Ni-based electrocatalysts, which have been touted as promising alternatives to PGMs. The study revealed that several effective strategies could help optimize the interaction with intermediates and eventually promote the HOR kinetics in alkaline solutions.[270]

2.10.2.2 Oxygen Reduction Reaction

Knowledge from the Sabatier principle has established that the interactions between the reactants and the catalyst determine the performance of a catalyst. Additionally, it has been adequately clarified that the catalytic performance of a material will essentially be different for different reactions. Therefore, in this section, the ORR mechanism and how the reaction is catalyzed will be discussed in detail. Later, this section will identify and highlight the optimum catalyst for the ORR. Premised on this, the four-proton-electron pathway in an acidic medium will be discussed in detail. This is vital since it is preferable for several applications (*e.g.*, fuel cells), and as an acidic medium was primarily employed in this dissertation.

As one of the reactions in electrochemical energy conversion technologies, the ORR remains significant for delivering a global green future. It encompasses similar reaction intermediates (*OOH, *OH, *O) as its reverse counterpart, the OER, but considerably differs in terms of their reaction mechanisms. Broadly speaking, O_2 electroreduction can occur through two different pathways for any electrolyte pH (*i.e.*, either acidic or alkaline media) and proceeds *via* a multi-proton-electron transfer process. The first possibility is a four-proton-electron pathway in which oxygen is directly reduced to water. The second likelihood consists of a two-proton-electron pathway in which oxygen receives two electrons, forming a reaction intermediate. Afterward, the intermediate receives two electrons, completing the reduction reaction process.

In summary, the ORR encompasses sluggish/slow kinetics, translating to losses in the operating voltage. This is mainly/partly due to the complex reduction mechanism. To circumvent this, huge overpotentials are usually used in PEMFC devices.

Details of the various steps and pathways for varying electrolyte pH of the ORR are presented as follows:

i. In acidic media, the ORR can occur *via* two pathways: the reduction of O_2 to H_2O *via* a four-proton-electron process or the reduction of O_2 to H_2O_2 and subsequently to H_2O through a series of two-proton-electron steps.

Four-proton-electron: $O_2(g) + 4H^+(aq) + 4e^- \rightarrow 2H_2O(l)$ (2.39b)

First two-proton-electron: $O_2(g) + 2H^+(aq) + 2e^- \rightarrow H_2O_2(l)$ (2.41a)

Second two-proton-electron: $H_2O_2(l) + 2H^+(aq) + 2e^- \rightarrow 2H_2O(l)$ (2.41b)

ii. In alkaline media, however, O_2 can be reduced to OH^- and HO_2^- *via* either a four-proton-electron or a two-proton-electron pathway.

Four-proton-electron: $O_2(g) + 2H_2O(l) + 4e^- \rightarrow 4OH^-(aq)$ (2.42a)

First two-proton-electron: $O_2(g) + H_2O(l) + 2e^- \rightarrow OH^-(aq) + HO_2^-$ (2.42b)

Second two-proton-electron: $HO_2^- + H_2O(l) + 2e^- \rightarrow 3OH^-(aq)$ (2.42c)

It is worth stating that O_2 can also be reduced to superoxide (O_2^-) in non-aqueous aprotic electrolytes, which involves the transfer of one electron.[271]

Several researchers concur that the ORR on Pt electrodes typically follows the four-proton-electron transfer process in both acidic and alkaline aqueous electrolytes.[272] The reaction mechanism proceeds *via* either the associative or dissociative pathway.[207] Considering Pt in acidic media for illustration purposes, these two mechanisms can be summarized as follows:

i. Dissociative mechanism:

$$O_2 + 2^* \rightarrow 2^*O \quad (2.43a)$$

$$2^*O + 2H^+ + 2e^- \rightarrow 2^*OH \quad (2.43b)$$

$$2^*OH + 2H^+ + 2e^- \rightarrow 2H_2O + 2^* \quad (2.43c)$$

ii. Associative mechanism:

$$O_2 + * \rightarrow *O_2 \tag{2.44a}$$

$$*O_2 + H^+ + e^- \rightarrow *OOH \tag{2.44b}$$

$$*OOH + H^+ + e^- \rightarrow *O + H_2O \tag{2.44c}$$

$$*O + H^+ + e^- \rightarrow *OH \tag{2.44d}$$

$$*OH + H^+ + e^- \rightarrow H_2O + * \tag{2.44e}$$

Studies have revealed that due to the ORR's sluggish kinetics, even benchmark Pt-based catalysts require much higher Pt mass loading to yield an adequately good activity.[271] Additionally, the relatively poor long-term stability of ORR electrocatalysts is also a significant hurdle. As a practical precept, reports indicate that ORR activity significantly decreased after long-cycling times for commercial Pt/C (Pt on carbon support).[273,274] To this end, developing cost-effective, excellent-performing, and long-term durable electrocatalysts is imperative.

Furthermore, studies indicate that the electrolyte components impact the catalyst's ORR performance. Mainly, the ORR activity varies contingent on the different cations present in the solution. Anion adsorption must also be considered, as it can affect the ORR processes.[275,276] For instance, the strongly adsorbed anion in the electrolyte can substantially decrease the ORR activity. Remarking that the pH effect does not match in acidic and alkaline media is worth it.[277,278]

3.0 Fundamentals of Interfacial Processes & Characterization

Herein, theoretical considerations of the various methodological approaches possible to be deployed in characterizing interfacial processes are elaborated. Most especially, several methods for measuring and evaluating the potentials of zero charge and maximum entropy are highlighted. It is then narrowed down to the main methodology deployed for characterizing and determining the interfacial parameters, which is at the forefront of this dissertation. Most of this chapter is published in references.[162,163,164]

3.1 Water Layer Structure at the Interface

The net orientation of solvent molecules, *i.e.*, the water layer structure (as the often-applied solvent in most electrolytes is water) at the electrified electrochemical interface, one of the indispensable interfacial properties, can immensely impact the electrochemical processes such as the electrode activity and the charge and mass transfer at the interface.[279,280,281] Electrochemical energy conversion and storage and corrosion systems can eventually benefit from the obtained data.[282,283] Refreshingly, relying on robust methodologies like the laser-induced transient techniques, vital parameters (potentials of maximum entropy and zero charge) can be determined near the electrified electrode/electrolyte interface. Their knowledge supplies the pertinent facts necessary to better grasp the electrode/electrolyte interface structure. By extension, the electrochemical processes taking place in a structure (*i.e.*, adsorption of charged and uncharged species at the surface) and their kinetics can also be well understood.[279,280]

The interfacial water layer structure is primarily influenced by the electrode potential, electrolyte composition/components, and electrolyte pH.[130,131,284,285] In short, sufficient data on the electrode's surface charge is crucial to ascertain the net orientation of the interfacial water layer structure. In this vein, one can predict that when the surface charge on the electrode is negative, as exhibited in **Figure 3.1A**, the hydrogen end of the water molecules will tend to orient more towards the electrode surface. The reverse can be expected for a positively charged electrode surface, in which the oxygen end of the water molecule drifts toward the electrode surface, as portrayed in **Figure 3.1B**.

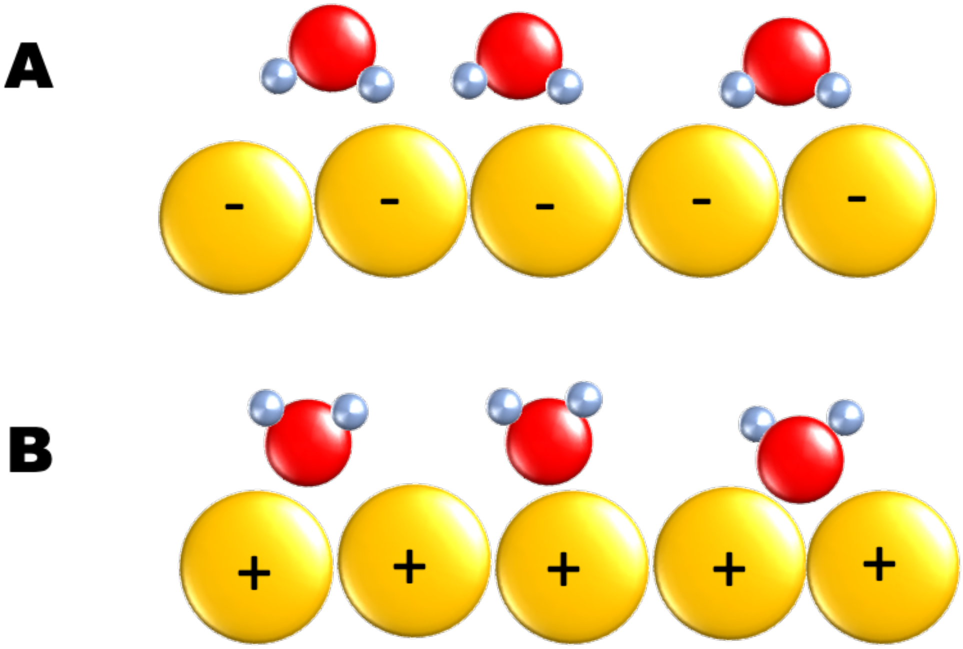

Figure 3.1. *Schematic depiction of the orientation of water molecules at the electrode surface for **A**) a negatively charged and **B**) a positively charged electrode surface, respectively. For the water layer structure, oxygen is shown in red, whereas hydrogen is represented in silver/grey.*

It is significant to point out that the simple instance illustrated in **Figure 3.1** is only sometimes the case. Most techniques available for such evaluations do so at potentials near the potential of zero charge (PZC). This is rooted in the type of electrode materials employed, as some electrodes undergo a complex interaction with the interfacial water molecules at specific biased potentials. In some recent publications by Wang *et al.*, the enterprising behavioral pattern of the water layer structure at the Pd electrode/electrolyte interface when subjected to bias potentials was studied using *in-situ* shell-isolated nanoparticle-enhanced Raman spectroscopy (SHINERS) and *ab initio* molecular dynamics (AIMD) simulations.[286,287] They elucidated that as the potential becomes more negative, the interfacial water layer structure transforms from a random distribution to a more ordered distribution. The ordered distribution composition was in the sequence of "one-H-down" followed by a "two-H-down" type interfacial water. It is worth adding that the H atoms of ordered water would be close to the Pd surface thanks to the ever-changing water structure (*cf.* **Figure 3.2**). In short, a framework for obtaining optimum outcomes at such interfaces was proposed. This analogy is peculiar, particularly for a negatively charged atomically flat Pd single-crystal electrode (Pd(*hkl*)). Analogous explanations can be proffered for the other single-crystal electrodes (Au, Ag, Cu) investigated by the same authors.

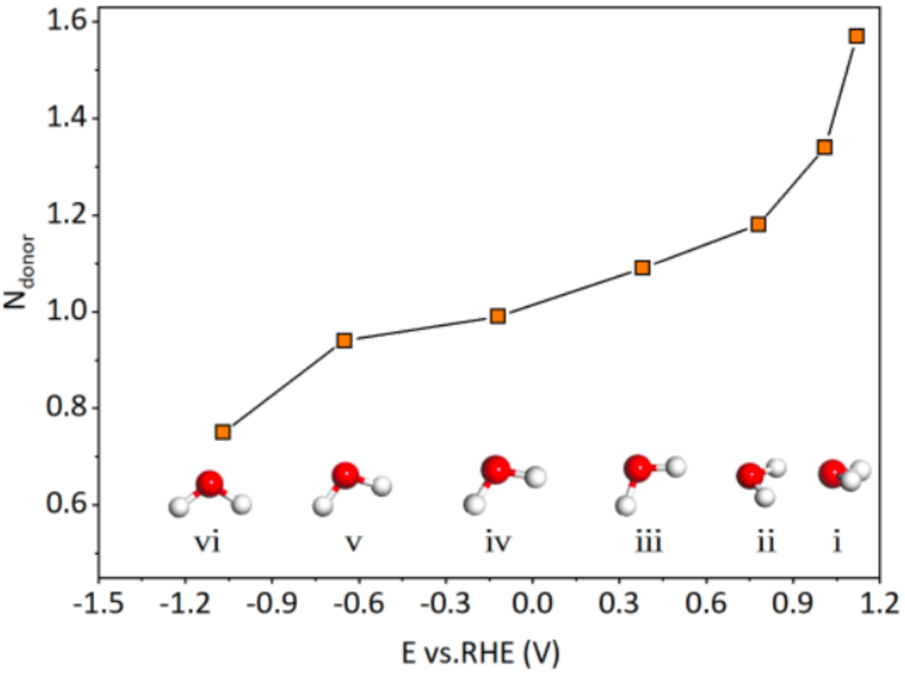

***Figure 3.2**. AIMD simulation results showing the calculated N_{donor} of interfacial water molecules as a function of the potential. Potential-dependent structures of the interfacial water layer are shown in the inset, labeled i to vi. The dynamics of interfacial water layer structure reveal constantly evolving patterns of the hydrogen molecules, from (i) two-H-sideways, (ii) to (v) one-H-down, and (vi) two-H-down. Reproduced with permission from reference.*[287] *Copyright © (2021), The Author(s), under exclusive license to Springer Nature Limited.*

Another typical example of this scenario was reported by Tong *et al.*, where the interfacial water molecules did not orient themselves with either their oxygen or hydrogen toward the Au electrode but instead deployed dangling O-H bonds to embark on such interactions.[288] This occurs because of the interaction between the permanent water dipole and the surface field. Moreover, the electrode surface charge morphs from negative to positive upon an increase in the density of the interfacial water molecules. More so, according to the studies by Li *et al.*, the interfacial interaction between a negatively charged Au electrode surface and the water layer structure considerably alter at particular points.[289] They further explained that the distribution and alignment of the interfacial water molecules could differ for negatively charged electrode surfaces due to the potential difference between the applied potential and the PZC. Moreover, the interfacial water keeps the “one-H-down” pattern at specific potential differences but transforms to the “two-H-down” orientation when the applied potential approaches extreme negative values.

According to the publications available, an upward trajectory of *in-situ* characterization techniques is being used to probe interfacial water molecules’ role in aqueous electrochemical processes. These include surface-enhanced infrared absorption spectroscopy (SEIRAS),[290,291] vibrational sum-frequency generation (VSFG) spectroscopy,[288,292] x-ray scattering (XRS) spectroscopy,[290] surface-enhanced Raman spectroscopy (SERS),[293,294] shell-isolated nanoparticle-enhanced Raman spectroscopy,[286,287] and x-ray absorption spectroscopy (XAS).[290,295,296] Despite the availability of numerous techniques,[297] most of them only give information about interfacial water close to the PZC. Since many electrocatalysis processes tend to occur at vicinities remote from the PZC, other approaches like *ab initio* molecular dynamics simulations have been successfully deployed to investigate the interfacial water layer structure.[286,287,298] Usually, by merging two of the techniques mentioned above, the structure and composition of the interfacial water layer at extreme electrocatalytic potentials can be obtained. Besides, recently the water layer structure at the interface of both monocrystalline and polycrystalline electrodes are accessible.

However, a complete understanding of the interfacial water layer structure’s role in aqueous electrochemical processes remains elusive. This dissertation seeks to contribute a piece to comprehend such dynamics and, by extension, better elucidate electrocatalysis. To this end, essential parameters, namely, the PZC and potential of maximum entropy (PME), will be significant.

3.2 Potential of Zero Charge and Potential of Maximum Entropy

The first announced concept of the potential of zero charge was devised in 1928 by A. Frumkin.[299] The PZC corresponds to the potential where there is ostensibly no net accumulation of excess charge on the electrode surface. In other words, it signifies the potential where the excess charge on the electrode surface vanishes as the applied potential varies. On this note, the PZC can be regarded as a function of the electrode material and the electrolyte chemistry.

Primarily, the electrode surface charge depends on the applied potential. Taking the surface of a metal electrode as an example, the charge per unit area is given by:

$$q^m = -F\sum_i \Gamma_i z_i \tag{3.1}$$

Here, q^m denotes the charge of the metal, which is equal but opposite in sign to the charge of the solution in the EDL, *i.e.*, ($q^m = -q^s$), Γ_i stands for the excess surface charge (in moles per unit area) of the ionic species, i in this case, in the interface, z_i represents the charge with the sign of the component, i.

At invariable temperature and pressure, the following equation can result:

$$d\sigma = -q^m dE + \sum_i \Gamma_i d\mu_i \tag{3.2}$$

with σ as the interfacial tension. It is worth noting that the interfacial tension can be determined as a function of the electrode potential. Accordingly, the excess charge density on the metal can be expressed by:

$$q^m = -\left(\frac{\partial\sigma}{\partial E}\right)_{T,P,\mu_i} \tag{3.3}$$

In this light, it can be anticipated that the potential where the derivative $(\partial\sigma/\partial E)_{T,P,\mu_i}$ amounts to zero corresponds to the state where no excess charge appears on the metal electrode surface, which is the location of the PZC.

As a first approximation, the PZC is associated with the work function for transition metals and can be expressed by the following equation:

$$E_{PZC} = {}^{\Phi}/_{e_0} + K_s \tag{3.4}$$

where, Φ denotes the metal's work function of the electrode material for thick electrodes. However, for thin electrodes, it relates to both the electrode and the EDL resistance to the electron transfer, e_0 signifies the electron charge, and K_s is an interfacial constant depicting the influence of the solvent on E_{PZC} of the electrode.

Essentially, two types of PZCs exist contingent on the nature of the electrode material, as the PZC is not an inimitable property of the metal but substantially depends on the detailed composition of the whole system. Stemming from that, one can isolate the condition that considers adsorption processes at the electrified electrode/electrolyte interface and hence depends on the electrolyte pH from the other, which is independent of adsorption processes. The latter is usually referred to as the potential of zero free charge (PZFC) and is defined as a type of PZC that occurs when the free, electronic net charge of the electrode surface is zero in any given applied potential.[163,300,301] By contrast, the former is called the potential of zero total charge (PZTC) and happens as a consequence of the sum of the free, electronic net charge density and the charge density transferred throughout reversible adsorption (Faradaic) processes are zero in any applied potential.[162,163] The only outlier is that ideally polarizable electrode materials do not exhibit specific adsorption (hydrogen, hydroxyl - OH^-, and anions) processes induced by charge transfer. Therefore, in this situation, the PZFC and PZTC overlap.[302] When this is the case, the value of the PZFC can be obtained from the PZTC measurement as it is the only experimentally accessible parameter.[176,177] The scenario is different, particularly for platinum group metals (Pd, Pt, Ir, Rh) which involve adsorption processes, triggering the PZTC and PZFC not to coincide.[303,304,305]

The PZTC can be experimentally determined, for instance, from voltammetry.[176,177] Deploying the same conventional methodologies, namely, voltammetric and potentiostatic techniques to measure the PZFC proves futile, as these techniques cannot the decouple double-layer charging current density from the total current density.[306] Moreover, additional measurements and critical thermodynamic assumptions are required to evaluate the PZFC from the electrochemical measurements.[307] Specifics concerning the various methods for determining the PZC are further elaborated in **section 3.3**.

Meanwhile, the potential of maximum entropy indicates the potential where the disorder of the water molecules close to the electrode surface reaches its zenith.[308] Simply put, the entropy of the double-layer formation peaks at the PME. Consequently, the PME is significant in assessing the rigidity or looseness of the interfacial water layer structure and is closely related to the PZC, particularly the PZFC, in most cases. This close association originates from the water dipoles' electrostatic interactions with the interface's electric field. To be more accurate, the PME is located at a slightly negative potential relative to the PZC due to the strong directional bond existing between the oxygen of the water molecule and the (unoccupied) d-orbitals of the (uncharged) transition metal electrode surface.[309] Admittedly, relatively high energy is required to break the bond from the PZC to the PME. Therefore, the latter tends to occur at a more negative (lower) potential than the former. **Figures 3.3A** and **B** elucidate the positioning of some vital parameters significant in describing the properties of the electrified electrode/electrolyte interface.

Remarkably, striking nomenclatures, including the potential of turnover of the water molecules, the potential of water reorientation, and the potential of zero transient (PZT), have all been validly used to represent the PME. The deployment of such terms can be justified from the witness of the flipping (upwards or downwards) of the hydrogen and oxygen in the water molecules at the PME. It is, therefore, unsurprising to observe faster reaction kinetics for electrochemical reactions in the vicinity of the PME. This observation can be explained by lowering the energy barrier triggered by the loose water layer structure, permitting the easy movement of species (charges, mass, etc.) through the EDL.[310] By contrast, at potentials far off from the PME, the solvent (mostly water) layer structure becomes stiff, elevating the energy barrier, which decelerates the reaction kinetics. In this regard, mass and charge transfer through the EDL progresses slowly. **Figure 3.3C** further elaborates on the concept and significance of the PME.

A)

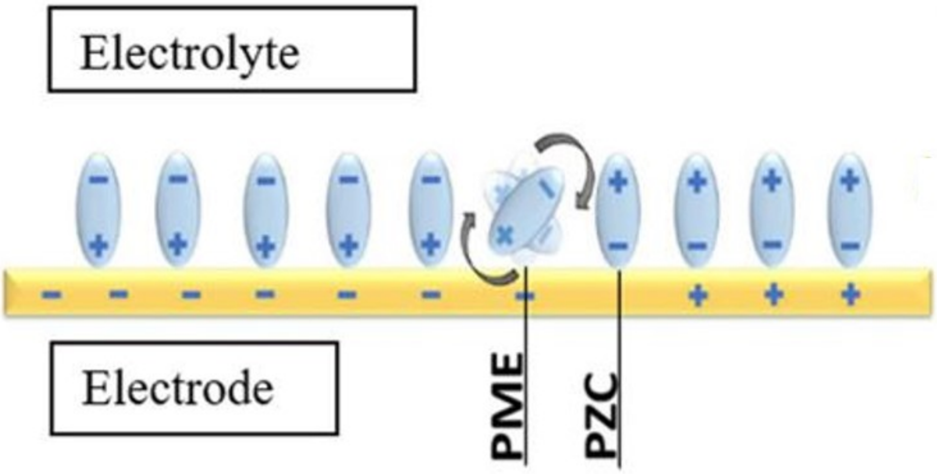

B)

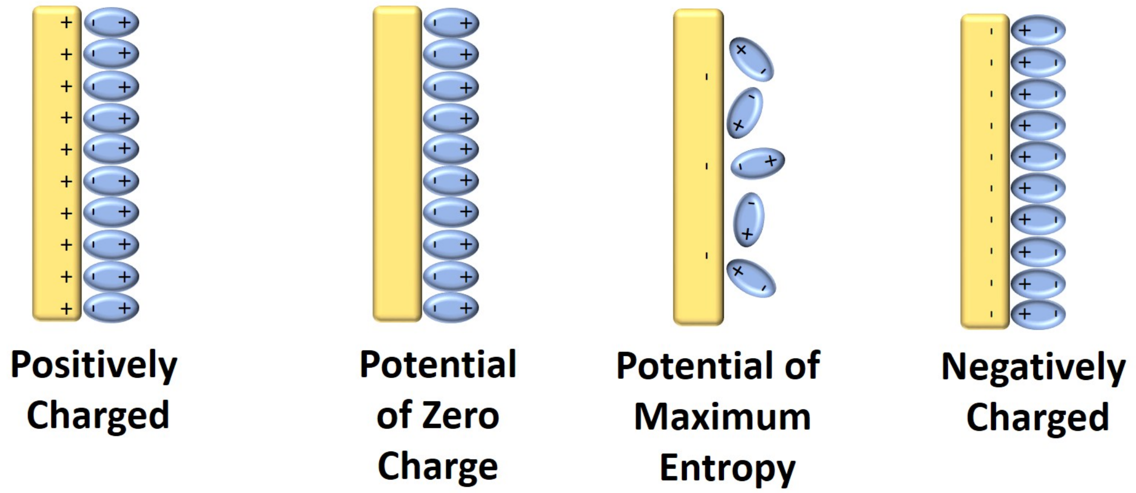

C)

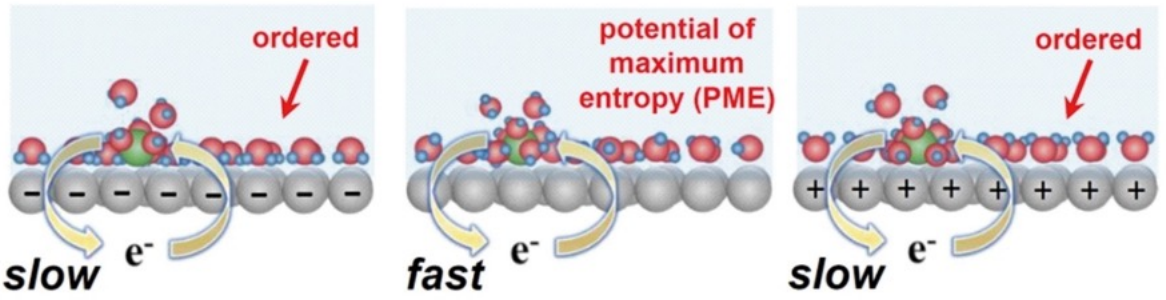

***Figure 3.3**. **A**) The double layer structure of a negatively charged electrode surface and the arrangement of the water layer structure around it. The PME is depicted as the potential with the most chaos and where the flipping of the signs of the water dipole occurs, whereas at the PZC, no net charge exists on the electrode surface. Figure reprinted from reference.[157] **B**) A schematic explanation of the arrangement of interfacial water dipoles and net electrode surface charges for key interfacial parameters like the potentials of zero charge and maximum entropy. Figure modified from reference.[161] **C**) Schematic depiction of a possible expectation at the potential of maximum entropy. Thanks to the enormous degree of chaos at the PME, species can be exchanged rapidly, which leads to faster kinetics and enhanced performance. Meanwhile, for the other instances showing either positive or negative electrode surface charge, the water layer structure is well ordered; hence the exchange of species proceeds rather slowly. Figure reproduced with permission from reference.[160] Copyright © (2021), The Authors. ChemElectroChem published by Wiley-VCH GmbH. Open access, published under a CC-BY license.*

3.3 Techniques for Determining the PZC and PME

Following the unambiguous descriptions of the PZC and PME, it now paves the way to critically examine some of the available methodologies deployed to determine these parameters. It is essential to acknowledge that determining the PZC and PME, particularly for solid electrodes, has always been challenging despite their grave importance. A myriad of methodologies, however, exist, enabling the determination of the PZC, primarily the PZTC, since the PZFC is currently not experimentally accessible. The electrode type mainly determines the desired methodology since the various methods are tailored toward specific purposes. The procedures comprise the electrocapillary, capacitance, CO charge displacement, N_2O reduction, scrapping, laser ablation voltammetry, and many other methods. As the role of interfacial water molecules is crucial in attaining significant improvements in the design and enhancement of electrocatalytic systems, dissociating the potential interference of its response from the water in the bulk of the solution is pivotal in the established techniques.

3.3.1 Electrocapillary Method

Electrocapillary describes the relationship between the interfacial tension or stress and the electrode/electrolyte potential. To this end, this method employs the electrocapillary equation,[311,312] which also incorporates the so-called Lippmann equation.[313] In this method, the PZC is recognized as the potential where the electrocapillary curve reaches its peak (*cf.* **Figure 3.4**). Several authors have reported accurate measurements of the interfacial tensions for liquid/liquid interfaces.[314,315,316] The electrocapillary method has also been successfully applied to determine the PZC of some unique materials, including liquid metals (mercury, gallium, and its alloys).[317] Recently, this method has been applied to determine the PZC of certain metal-free electrodes like carbon aerogel.[318]

According to Lippmann's proposition, the electrocapillary curves of liquid metals can be measured with a device called a capillary electrometer.[313] This device can chronicle the pressure required to force the electrode material (mostly liquid metal) down to a pivotal point of a conical capillary, which is wetted by the electrolyte solution. In operating the device, one must essentially ensure that the entire capillary walls are thoroughly soaked in the electrolyte solution. The basic equation governing this methodology considers the surface tension of the electrode material γ as a function of the EDL capacitance per unit area C and is given by:

$$\gamma = \gamma_O - \frac{1}{2}CV_{EDL}^2 \tag{3.5}$$

Where γ_O denotes the surface tension that exists between the electrolyte and the conductor even at the minimum electric field of zero, and V_{EDL} represents the applied potential across the EDL.

Primarily, the scope of use of the electrocapillary method is limited, as the dependency of surface tension on the electrode potential is explored in this method. Simply put, it is experimentally impossible to access the absolute interfacial tension at the solid/liquid interface due to several complexities in estimating the interfacial stress of solid electrodes. Moreover, solids generally do not exhibit surfaces that are in equilibrium, which is a prerequisite for employing this method.

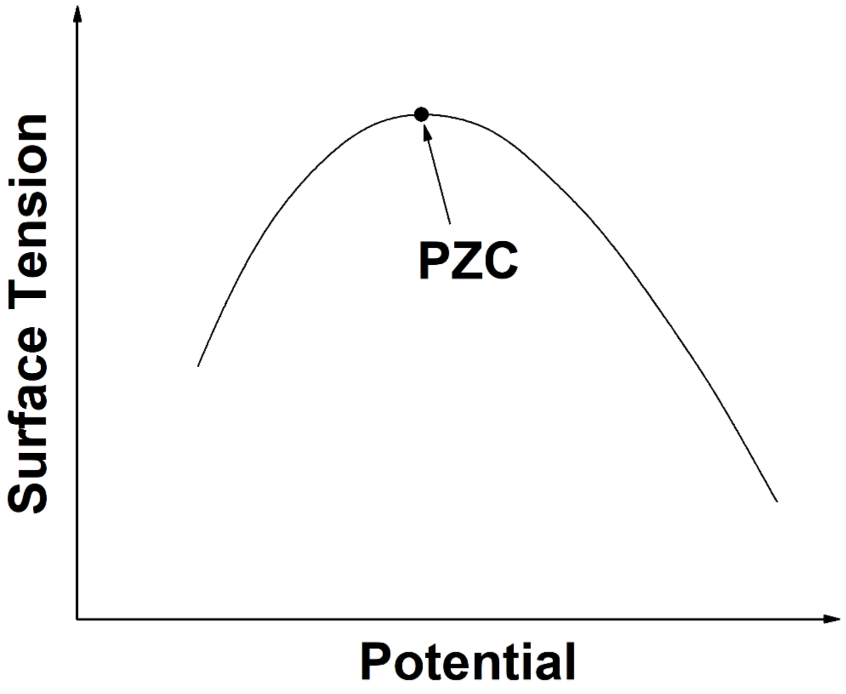

Figure 3.4. *Schematic depiction of a typical electrocapillary curve. In other words, the surface tension of an electrode is plotted as a function of the applied potential. The PZC is indicated with a dot and arrow, corresponding to the apex of the surface tension.*

3.3.2 Capacitance Method

Section 3.2 extensively revealed that the PZC is one of the significant parameters at the electrified electrode/electrolyte interface. It is also not in doubt that the double-layer capacitance (C_{dl}) is an essential electrode/electrolyte interface descriptor. Therefore, it is pragmatic to correlate the PZC to the C_{dl}. The PZC is the potential where the C_{dl} is at minimum (*cf.* **Figure 3.5**). Theoretically, the PZC should be located at the minimum of the differential capacitance, C_d. This method of PZC determination first originated from Vorsina and Frumkin.[319] Although the capacitance method is very useful, it comes with its limitations and hence can only be deployed for dilute solutions and without specific adsorption. This emanates from the inner Helmholtz double layer C_i typically dominating the C_{dl} at high electrolyte concentrations, as shown in **Equation (3.6)**, obtained from the Gouy-Chapman-Stern model of the EDL.

$$\frac{1}{C_{dl}} = \frac{1}{C_i} + \frac{1}{C_d} \tag{3.6}$$

Here, C_i and C_d represent the capacitance of the inner Helmholtz double layer and the differential capacitance of the diffuse layer, respectively.

Consider an example to serve as a model in which the dilute electrolyte solution has a very low concentration of $ca.$ 10^{-3} M. In this light, C_i will be invariable, and C_d will be the only parameter dependent on the applied potential and is represented as follows:[320]

$$C_d = (\partial q^m / \partial E)_{T,P,\mu_i} \tag{3.7}$$

With q being the free charge density on the surface of the electrode material, mostly solid metal, and E the potential of the electrode. Of course, **Equation (3.7)** originally corresponds to the C_{dl}.

Therefore, the capacitance method can scarcely be employed for the PZC determination in the case of high electrolyte concentrations,[321] electrodes such as PGMs, and electrolytes that specifically adsorb like sulfates.

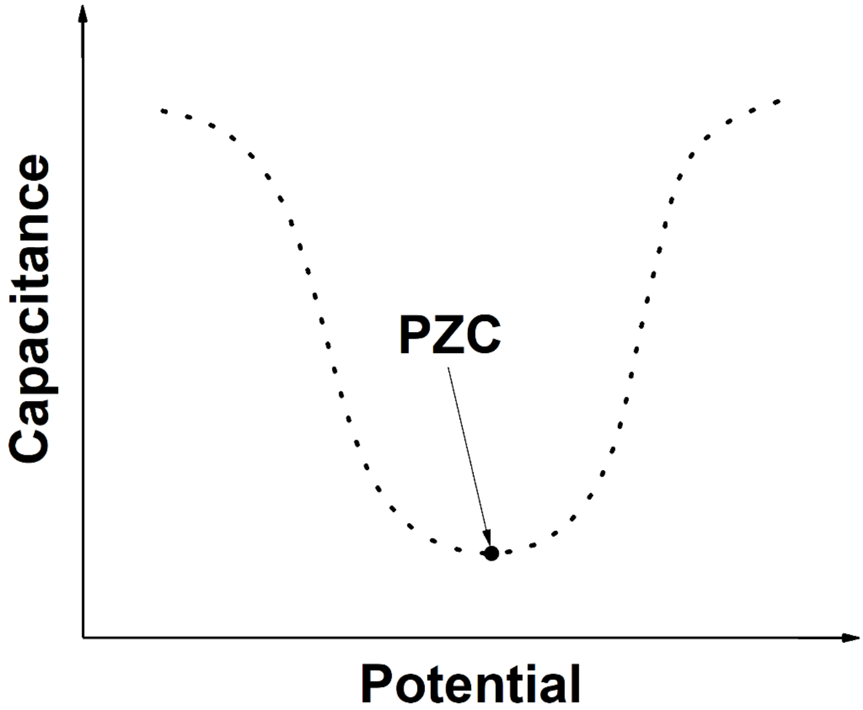

***Figure 3.5**. Typical graphical representation of the double layer capacitance (C_{dl}), which depicts the capacitance plotted as a function of the potential. The minimum of the capacitance-potential curve is known to be the minimum of the differential double-layer capacitance and corresponds to the PZC.*

3.3.3 CO Charge Displacement Method

The CO charge displacement method is particularly suitable for determining the PZC of some prominent noble metal electrodes.[322,323] This method operates through the complete exposure of noble metal surfaces, especially Pt group metals (Pt, Pd, Ir, Rh), to CO adsorption till saturation is reached. **Equation 3.8** underpins the operations of the methodology.

$$q_{dis} = q_f - q_i \tag{3.8}$$

Where q_{dis} is the charge measured during the CO adsorption process, q_i represents the total electrode charge before the CO adsorption (initial total electrode charge), and q_f denotes the total electrode charge after the CO adsorption (final total electrode charge).

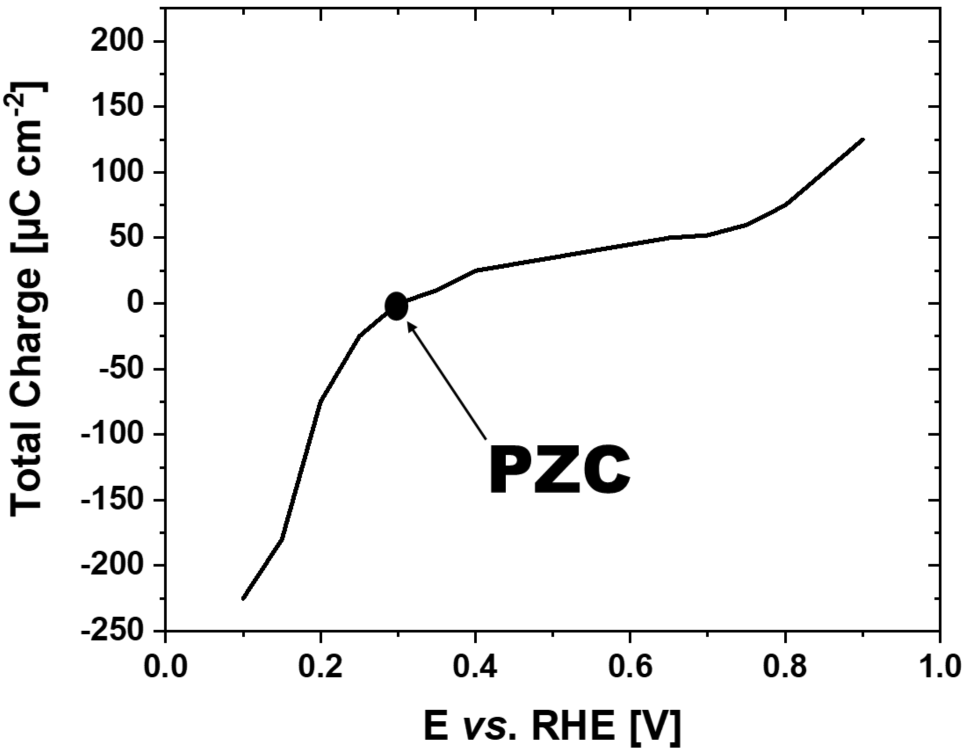

Figure 3.6. *Graphical representation of the total charge plotted as a function of the electrode potential. The PZC is captured as the potential corresponding to a total electrode charge (charge density) of zero.*

During the CO adsorption process, the oxidation states of the noble metal are expected to be invariable. Consequently, the charge measured during the CO adsorption process, $\boldsymbol{q_{dis}}$, should be equivalent to the difference between the total electrode charge before ($\boldsymbol{q_i}$) and after ($\boldsymbol{q_f}$) CO adsorption. However, as $\boldsymbol{q_f}$ cannot be directly determined but is assumed to be negligible when compared to $\boldsymbol{q_i}$, and therefore, **Equation (3.8)** further approximates to:

$$q_{dis} \approx -q_i \tag{3.9}$$

Following several measurements at varying potentials for a particular electrode, the PZC can be evaluated as the potential where $\boldsymbol{q_i}$ is zero (*cf.* **Figure 3.6**).[324,325] Although the CO displacement method can also be used to evaluate the dependence of the PZC on stepped single crystal surface[324] and electrolyte pH,[323] its benefits mainly lie in noble metal electrodes.

Furthermore, this method becomes redundant at high anodic potentials, as CO oxidation must be prevented.

3.3.4 N_2O Reduction Method

Premised on the findings from initial research conducted by Ebert *et al.*,[326] Attard *et al.*[327] claimed that the N_2O reduction method could be considered a surface probe to determine the PZC based on N_2O's sensitivity to the total local charge. A perfect example is deploying the N_2O reduction method to uniquely characterize the difference between local PZTCs in a specific study sample.[326]

Noteworthy, Ebert *et al.* are acknowledged to have premiered the PZC investigation on single crystal Pt surfaces using the N_2O reduction method. So far, this method has been applied to only noble metals such as Ir, Rh, Pd, and Pt electrodes,[326,327] which limits its broad applicability. **Figure 3.7** highlights an instance involving a Pt(111) electrode in 0.1 M $HClO_4$. Accordingly, the maximum current peak of N_2O reduction is located at 0.34 V. Another limitation has its roots in the structure type; this method is applicable. To illustrate this, Climent *et al.* deployed the N_2O reduction method to confirm that this methodology is fundamentally limited to interfacial structures sensitive to N_2O reduction reactions.[325]

One distinguishing inference from the studies by Ebert *et al.* and Attard *et al.* dwelt on the N_2O reduction mechanism, particularly on Pt electrodes. The former opined that the reaction was structure sensitive, and by extension, adsorbed hydrogen must be regarded as an integral catalytic intermediate, and is given by:

$$N_2O_{(ads)} + H_{(ads)} \rightarrow N_{2(g)} + OH_{(ads)} \tag{3.10}$$

Contrarywise, the latter believed that the N_2O reduction mechanism should be a characteristic feature of the pre-equilibrium step:[328]

$$Pt + N_2O_{(g)} \rightleftharpoons Pt - N_2O_{(ads)} \tag{3.11}$$

And this will be followed by:

$$Pt - N_2O_{(ads)} \overset{k_1}{\rightarrow} Pt - O + N_{2_{(g)}} \qquad \text{(slow)} \tag{3.12}$$

$$Pt - O + 2H^{+} + 2e^{-} \overset{k_2}{\rightarrow} Pt + H_2O \qquad \text{(fast)} \qquad (3.13)$$

In this respect, one can anticipate and/or expect that with a copious amount of adsorbed N_2O, the rate of N_2O reduction would be high. This analogy makes perfect sense, especially in situations that induce competitive adsorption between N_2O and other adsorbed species like anions, hydrogen, and water on the electrode surface. The consequence is observing the highest N_2O reduction rate where the maximum number of available free sites for N_2O adsorption exists.

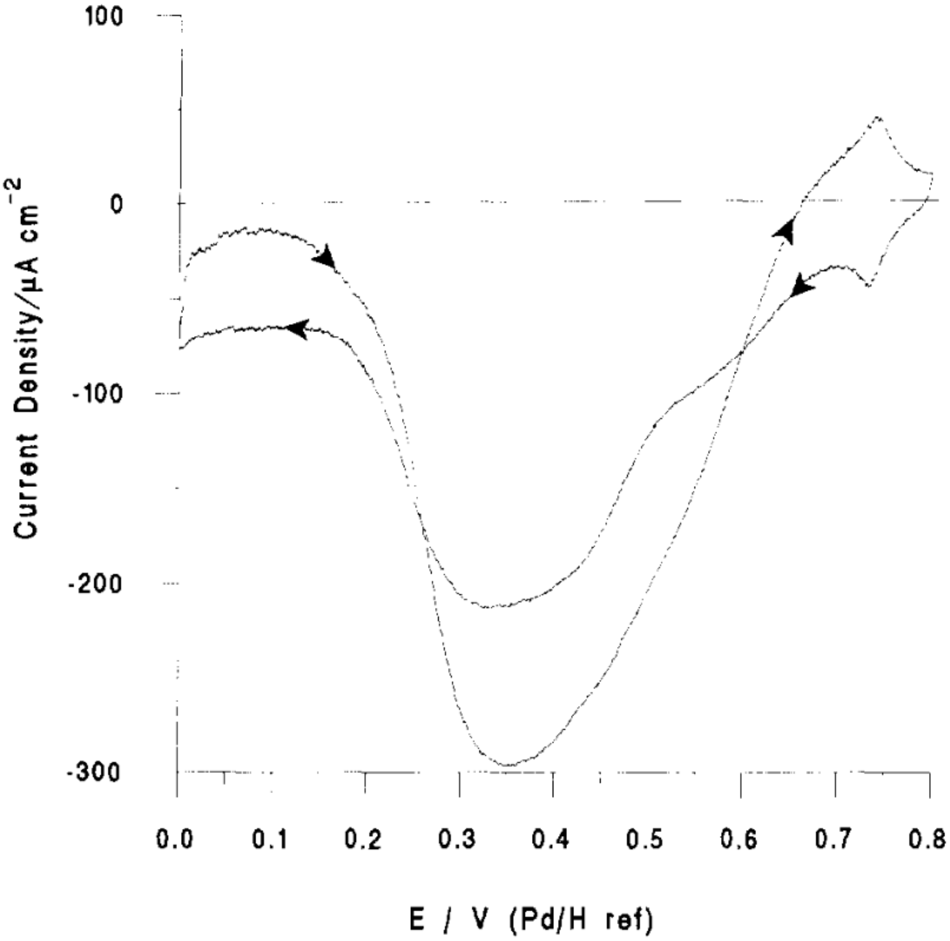

***Figure 3.7**. Graphical representation of an N_2O reduction plot conducted on Pt(111) in 0.1 M $HClO_4$. The maximum current peak of N_2O reduction, which is also the PZC, was found to be 0.34 V. Scan rate: 50 mV s^{-1}. Reprinted with permission from reference.[327] Copyright © (1995), Published by Elsevier B. V.*

3.3.5 Other Methodologies

Other captivating approaches, such as the vibrational properties of water molecules in the interface,[291,329] the scrapping method,[330] and even the laser ablation voltammetry method,[331] have all been equally used to determine the surface charge of electrode materials. However, all these methods have some limitations, like the ones mentioned earlier. Due to the ostensibly destructive nature of the latter two approaches, they cannot be applied to single crystals. For instance, in the scrapping method,[330] the electrode charge is extracted through the regeneration of the metallic surface. Meanwhile, for the laser ablation voltammetry method,[331] the surface of electrode materials can be destroyed entirely, and this approach was first employed on a molybdenum electrode.

Besides these promising methodologies, even more enterprising and improved computational (theoretical) and experimental techniques are springing up. An example of the latter is the recent phase-sensitive second harmonic generation optical methodology studies by Xu *et al.* aimed at determining the potential of zero charge of Pt electrodes.[332] Usually using the so-called jellium-Poisson-Boltzmann model, a host of simulations, such as density functional theory molecular dynamics (DFTMD), DFT calculations, AIMD, and so on, have been deployed to determine the PME and PZC, fundamental concepts in interfacial electrochemistry.[333,334,335,336,337] The electrodes investigated included Ag(100), Ag(111), Au(111), Pt(111), and Pd(111). In some of the studies, the PZC was referred to as the charge of maximum capacitance (CMC), whereas the PME was called the charge of maximum entropy (CME).

In brief, all the various methods so far enumerated here have numerous limitations in their broad applicability to several material types. Therefore, it is imperative to find alternative techniques that are robust, versatile, and can be employed for many different materials without/with little restrictions. In that regard, the laser-induced transient methods can help realize and overcome most of the limitations the already discussed methods pose.

3.4 Overview of the Laser-Induced Transient Techniques

Previous sections (**sections 2.3**, **3.1**, **3.2**, **3.3**) have shown that in any attempt at optimizing electrode processes or electrocatalytic reactions, the electrified electrode/electrolyte interface must be considered, as it plays a crucial role in the overall rational design process. Stemming from this, it is paramount to determine parameters like the PZC and PME at the vanguard of the electrified solid/liquid interface. Yet, one critical question worth answering is, how can these parameters be measured effectively and help close the gap between simplified theoretical models and dynamic actual electrocatalytic systems? More so, resolving and clarifying the role interfacial solvent (mostly water) plays in these reactions and electrochemical systems must feature prominently.

By deploying the laser-induced transient techniques, which involve directly measuring the electrode surface charge or sign, most, if not all, of the answers to the unsettled questions can be obtained. The earliest acknowledged use of this methodology was reported by Benderskii and co-workers[338] in 1978 when short, powerful laser pulses were employed to investigate the mercury electrode/electrolyte interface. In a short while, Benderskii's group and others deployed an analogous technique to reveal information on the kinetics of electrochemical processes occurring on platinum electrodes.[339,340,341,342] The method has further been explored to probe the electrified interface of several electrochemical reactions and systems predicated on these feats. Prevalent among the wide-scope application of the methodology in recent years include investigating the surface charge of gold,[130,343,344] platinum,[160,345,346,347] and iridium[308] electrodes. As a means to further extend the frontiers and scope of application of this technique, our group has experimented on materials such as aqueous metal-ion batteries,[154,155] manganese oxide,[156] copper,[158] and surface-mounted metal-organic framework[131] electrodes, with the prospects of examining other electrodes apparent.

The laser-induced transient techniques use the so-called temperature jump effect. In that regard, when the surface of a non-transparent electrode is irradiated with a robust and ultrafast (submicrosecond - ns, fs, etc.) laser source, a rapid surge (*ca.* 20-40 K) in the temperature of the interfacial region is activated. Undeniably, the working electrode and the electrolyte (the majority being water) build a double layer when a constant potential is supplied to the system. This system initially reaches an equilibrium state. Once the laser pulses are launched to target the interfacial region, *i.e.*, the double layer, the equilibrium is briefly destabilized. Fascinatingly, the system's response is displayed as current or potential transients corresponding to the electrode surface charge. More precisely, the system's reaction mainly highlights the influence of the quick temperature upsurge on the structure of the inner Helmholtz plane.

The technique is applicable in assessing parameters like the PZC, closely associated with the PME, where water molecules reorient more easily. Thus, independent and valuable information on the interfacial properties and structure can be retrieved. Therefore, a typical example of the direct application of the technique is the determination of the kinetics and mechanism of various electrode processes. It can be true, provided that the only influence of the laser illumination is heating the electrode surface. In this respect, fast processes occurring at the electrode/electrolyte interface can be investigated. Depending on the significant difference between the rate of the temperature change and the relaxation time, thermodynamic and kinetic data can be decoupled, thereby permitting the seamless retrieval of the information of interest.[130] Thermodynamic information is obtained when the temperature change rate is slower than the relaxation time, while the opposite is true for the latter, kinetic. Ultimately, combining results from the laser technique with data obtained from methods like electrochemical impedance spectroscopy and electrochemical quartz crystal microbalance yields in-depth characterization, validity, and a better understanding of solvation effects in electrochemical systems. Accordingly, the behavior of interfacial water molecules on several electrodes, particularly on the surfaces of metal and metal oxides, under *in-situ* conditions can be determined with high selectivity.

3.4.1 Theoretical Considerations of the Laser-Induced Current Transient Technique

Following briefly introducing the technique and its range of applications, discussing the fundamentals fortifying it is paramount. **Section 3.4** highlighted two main methods founded on almost the same principles. However, this dissertation focuses on one of them: the laser-induced current transient (LICT) methodology. On that note, subsequent discussions will most often center on this particular methodology.

The temperature change after a laser pulse can be conveniently defined by **Equation (3.14a)** on the assumption that the penetration depth of the applied light (laser, in this case) is negligible.

$$\Delta T(t) = \frac{1}{\sqrt{\pi \kappa c d} + \sqrt{\pi \kappa_s c_s d_s}} \int_0^t q(t - t') \frac{1}{\sqrt{t'}} dt' \tag{3.14a}$$

Here, κ, c, and d and $\kappa_s, c_s,$ and d_s represent the thermal conductivity, thermal capacity, and density of the metal and the aqueous electrolyte (solution).

As an alternative, the temperature change on the electrode surface occasioned by the absorption of the laser right after the end of the short laser pulse can be estimated as follows:

$$\Delta T(t) = \frac{I(1-R)}{\sqrt{\pi \kappa c d}} \left(1 + \sqrt{\frac{\kappa_s c_s d_s}{\kappa c d}}\right)^{-1} \sqrt{t_0} \tag{3.14b}$$

Where *I* stands for the intensity of the laser light, *R* defines the reflectivity of the surface, and t_0 is the duration of the laser pulse.

The function q describes the power density adsorbed at the metal surface and relies on the temporal shape of the laser pulse *via* the following equation:

$$q(t) = (1 - R)I(t) \tag{3.15}$$

Where $I(t)$ describes the intensity or the time-dependent energy flux per unit area.

It is vital to add that for any uniform laser pulse, integrating **Equation (3.14a)** yields the following key formulas:

$$\Delta T(t) = \frac{2(1-R)I}{\sqrt{\pi \kappa c d} + \sqrt{\pi \kappa_s c_s d_s}} \sqrt{t} \quad (t \le t_0) \quad Heating \tag{3.16}$$

$$\Delta T(t) = \frac{2(1-R)I}{\sqrt{\pi \kappa c d} + \sqrt{\pi \kappa_s c_s d_s}} \left[\sqrt{t} - \sqrt{t - t_0}\right] \quad (t > t_0) \quad Cooling \tag{3.17}$$

When the laser pulse irradiates the electrode surface for a long duration, it essentially leads to an expansion of the term $\sqrt{t - t_0}$. Correspondingly, the higher terms in the series become redundant, resulting in a decrease in the temperature change with time as follows:

$$\Delta T(t) = \frac{1}{2}\Delta T_m \sqrt{\frac{t_0}{t}} \tag{3.18}$$

Where $\Delta T(t)$ describes the rate of decay of the current after the laser pulse or the temperature of the metallic surface fall. ΔT_m defines the maximum temperature change achieved at the end of the pulse.

A linear relationship between the temperature and the potential change can be obtained in situations where the temperature change is small enough, as depicted below:

$$\Delta E = \left(\frac{\partial E}{\partial T}\right)\Delta T = \left(\frac{\partial E}{\partial T}\right)_q \frac{1}{2}\Delta T_m \sqrt{\frac{t_0}{t}} \tag{3.19}$$

In essence, the temperature coefficient of the open circuit potential can be calculated from the gradient after plotting ΔE *vs.* $1/\sqrt{t}$. Notably, from the electrocapillary equation, the following invariable equation ensues:[348]

$$\left(\frac{\partial E}{\partial T}\right)_q = -\left(\frac{\partial \Delta S}{\partial q}\right)_T \tag{3.20}$$

With ΔS denoting the interfacial entropy of formation. By integrating the slopes obtained from plotting $\Delta E\ vs.\ 1/\sqrt{t}$ as a function of the double layer charge, a graphical representation of ΔS can be fabricated. As a consequence, one can safely predict that $\left(\frac{\partial \Delta S}{\partial q}\right)_T$ will be zero when the curve ΔS *vs.* q reaches its peak. Concurrently, deducing from **Equation (3.20)**, it is not out of place to infer that the change of the electrochemical potential elicited by the abrupt but brief temperature rise *via* laser illumination will correspondingly be zero. It is impressively evident that this technique sanctions the identification of the PME of double-layer formation.

The caveat worth highlighting is that the equations derived so far did not consider all the possible contributions accompanying the irradiation of an electrode surface with laser pulses. In principle, the response of the potential to the sudden increase of the temperature due to the laser illumination can be segregated into three categories, namely, the temperature coefficient of the potential drop through the electric double layer $\left(\frac{\partial E}{\partial T}\right)_q$, which is the main contributor to the thermodiffusion potential arising from the difference in the temperature between the solution in contact with the working and reference electrodes and the temperature gradient in the metal electrode. Generally, the temperature coefficient of the metal/solution potential (E^{M-S}) drop through the EDL can be further fragmented into three contributions and is given as follows:

$$\left(\frac{\partial E^{M-S}}{\partial T}\right)_{q,M} = \frac{1}{e}\left(\frac{\partial \Phi}{\partial T}\right)_{q} + \left(\frac{\partial E^{2}}{\partial T}\right)_{q} + \left(\frac{\partial E^{W}}{\partial T}\right)_{q} \tag{3.21}$$

Where Φ is the work function at the given charge q, E^{W} is the potential drop emanating from solvent (re)structuring, and E^{2} depicts the potential drop at the diffuse layer.

Incredibly, the discussion above does not account for the influence of thermodiffusion potential on the open circuit potential after laser illumination heating. This gap can be filled by estimating the so-called Eastman entropy of transfer from the ions involved. This is given as:

$$\frac{\Delta E_{Thermodiffusion}}{\Delta T} = -\frac{1}{F}\sum \frac{t_i}{z_i}\hat{S}_i \tag{3.22}$$

With t_i, z_i, and $\hat{S}_i$ being the transport number, the charge, and the Eastman entropy of the ion i, respectively. It is explicitly implied following a glance at **Equation (3.22)** that the thermodiffusion potential substantially relies on the nature of the electrolyte. It is equally important to point out that the applied electrode potential does not influence this potential contribution. In that accord, in accounting for the highly significant responses from the EDL, the thermodiffusion effect is often neglected.[346,349] A similar reasoning can be followed for metal electrodes to evaluate the temperature gradient. This leaves the undeniable notion that the temperature coefficient of the potential drop through the electric double layer is at the forefront of this technique.

3.4.2 Origin of a System Response during a Laser-Induced Current Transient Experiment

Section 3.4.1 elaborated on the theoretical principles underpinning the laser-induced transient techniques, particularly the LICT technique. Before proceeding further, some vital aspects of the discussions thus far are worth reiterating. It has been established that upon irradiating the surface of a non-transparent electrode with a laser source, a sudden hike in the temperature (*ca.* 20-40 K) of the interfacial region arises. The temperature variation prompts the manifestation of a series of transients. With this change in place, it is possible to extract valuable information regarding the interface by monitoring the current or potential transients, which hitherto is not available in *in-situ* techniques. One outstanding feature of the method is that the high-power laser illumination yields a sudden temperature change, which is very fast, and isolating the double layer response from the charge transfer processes is possible.

According to the universally recognized model, in the absence of specifically adsorbed ions, the innermost plane of the solid/liquid interface, termed the inner Helmholtz plane, is composed of a solvent monolayer.[189**Error! Bookmark not defined.**] Imperatively, the actual system response to the short laser irradiation unveils the influence of the electrode temperature on the structure of the inner Helmholtz plane of the electric double layer. In aqueous electrolyte systems, one can envisage that the polarized water molecules will adjust their average orientation according to the sign of the excess surface charge resulting from the applied potential.[349,350] The positioning of solvent molecules is a function of the interactions between their dipole moment and the electric field produced by the electrode surface charge (E_{Charge}). As a result of the relatively large dipole moment of the electrode surface charge, the potential drop of the electrode originates to a large degree from the water molecules E_{dipole}.[349] Consequently, the potential generated between the electrode surface and the electrolyte solution E_{M-S} can be described by:

$$E_{M-S} = E_{Charge} + E_{dipole} \tag{3.23}$$

A swift temperature jump emanating from the laser illumination randomizes the solvent adlayer for a brief period, altering E_{dipole} and, eventually, E_{M-S} (**Equation (3.23)**). Crucially, the exposure of the excess charge accumulated at the electrode surface emerges, producing potential drops. The current or potential transients can be detected once the double-layer interface relaxes.

The potential jumps are portrayed as current or potential transients, with their sign coinciding with the sign of the electrode surface charge. With this phenomenon at center stage, the so-called laser-induced current transient and laser-induced potential transient (LIPT) methods, or more generally, the laser-induced transient techniques (LITT), or laser-induced temperature jump (LITJ) techniques, can be applied to check the electrode surface charge. For the LIPT technique, which is realized coulostatically, a change is induced at the open circuit potential, signifying the orientation of the water dipoles depending on their sign. Contrarywise, the LICT technique is performed potentiostatically. At this juncture, it is useful to mention that the laser-induced transient methods can be mainly categorized into two, namely, LICT and LIPT techniques. The former is implemented under coulostatic conditions to monitor the change of the open-circuit potential, *i.e.*, potential transients. By contrast, the LICT technique is executed under potentiostatic conditions (keeping the electrode potential constant) to record the current transients flowing through the external circuit after the laser pulse.

During the measurement, the reorganization of the EDL initiated by the laser illumination can be documented as the current transient. A positively charged electrode is projected to show positive current transients, whereas an identified negatively charged electrode will produce negative current transients from the laser pulse results. The PME is ascribed to the potential where the sign of the current transient flips, as shown in **Figures 3.8A** and **B**. The 3D graphical representation (*cf.* **Figure 3.8A**) of the current spikes reveals increasing magnitudes of the current transients in both negative and positive directions and an almost zero point, the PME. As designated in **Figure 3.8A**, the orientation of water dipoles is depicted as oxygen (red color) down when the electrode excess surface charge is positive (positive current transient) and hydrogen (grey/silver color) down for negatively charged electrodes (negative current transient). It is essential to comment that **Figure 3.8B** was fashioned from **Figure 3.8A**. Accordingly, the peak (extreme/maximal) current transient values were isolated and plotted as a function of the applied potential to streamline and distinctly illustrate the location of the PME in the 2D plot. The zero-crossing point symbolizes the PME, as is manifest in **Figure 3.8B**.

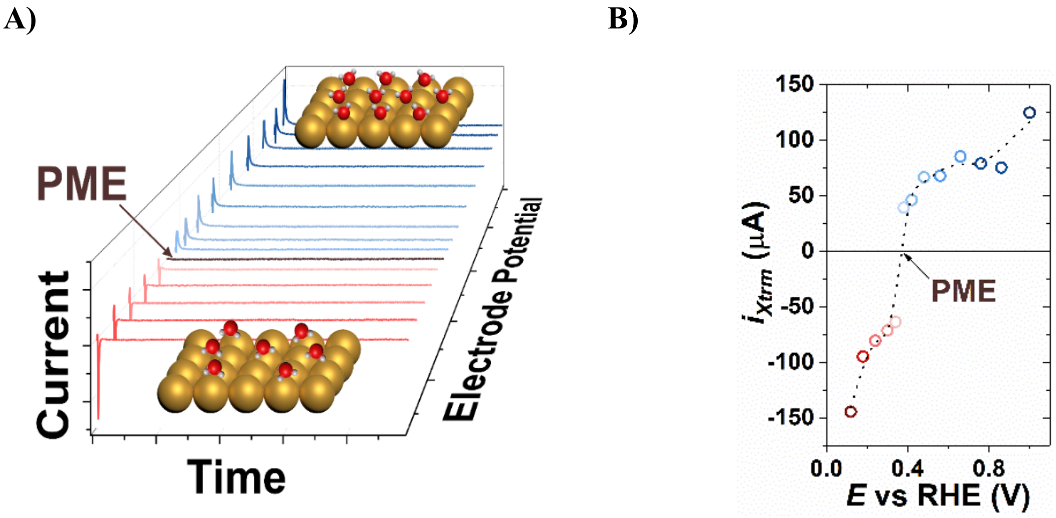

***Figure 3.8**. **A)** An example of a 3D plotted current transients recorded during the laser measurement at various electrochemical potentials. The potential at which the current transients flip its sign corresponds to the PME, and the sign of the current transients coincides with the sign of the electrode surface charge. The figure was obtained from measurements conducted on polycrystalline gold in 0.5 M O_2-saturated Na_2SO_4 solution (pH 2) and was reprinted with permission from references.*[161,130] *Copyright © (2021), The Authors. Published by Wiley-VCH GmbH. Open access, published under a CC-BY license. **B)** An instance of a 2D*

current transient diagram with the extreme current transients plotted as a function of the applied potential on the reversible hydrogen electrode (RHE) scale. The data for plotting B was obtained from ***A****). It is necessary to note that only some of the current transients are presented in this illustration. Reproduced from reference.*[161]

3.4.3 Important Laser Parameters and Specifications for the LICT Measurements

The LICT experiments in our laboratory are performed *via* deploying a Quanta-Ray INDI pulsed Nd:YAG laser (Spectra-Physics Lasers, USA) with a repetition rate of 10 Hz and 5-8 ns pulse duration. Essentially, an apt selection of the laser illumination wavelength is strategic in evading side effects, such as the photoemission of electrons. It is worth stating that the photoemission threshold for typical metal electrodes is approximately 200-300 nm (*i.e.*, representing a work function of *ca*. 4-5 eV).[344] Beyond that, other critical laser parameters, such as energy, power, or intensity, must be chosen carefully. Fundamentally, the intensity of the laser beam is contingent on the nature of the electrode and electrolyte under investigation. On that note, an appropriate laser beam intensity should permit a rapid increase in temperature without causing any destruction to the metallic electrode surface.

The wavelength of the laser device applied in all our LICT measurements is 532 nm (*i.e.*, the second harmonic generation of the fundamental frequency of this laser), which is discernibly above the photoemission of electrons and, therefore, prevents the stated side effect. Another parameter that can be tailored or fixed is the diameter of the laser beam. In our case, it is kept at 9 mm for every LICT measurement. Crucially, since the energy originating directly from the laser beam can reach 200 mJ, constituting a fluence of *ca*. 314 mJ cm^{-2}, which is excessively high and can destroy the working electrode, a motorized beam splitter (VA-CB-532-CONEX, Newport Corp.) operates as an attenuator (*cf.* **Figure 3.9**). By so doing, proper energy control of the laser pulses that will ultimately reach the working electrode is achieved. A tabletop controller or a GCR control software (Spectra Physics Lasers, USA) can be employed to operate the laser. The attenuator is manipulated by a Variable Attenuator software (model: CCVA-PR-CD, Spectra-Physics Lasers, USA) to regulate the laser beam energy.

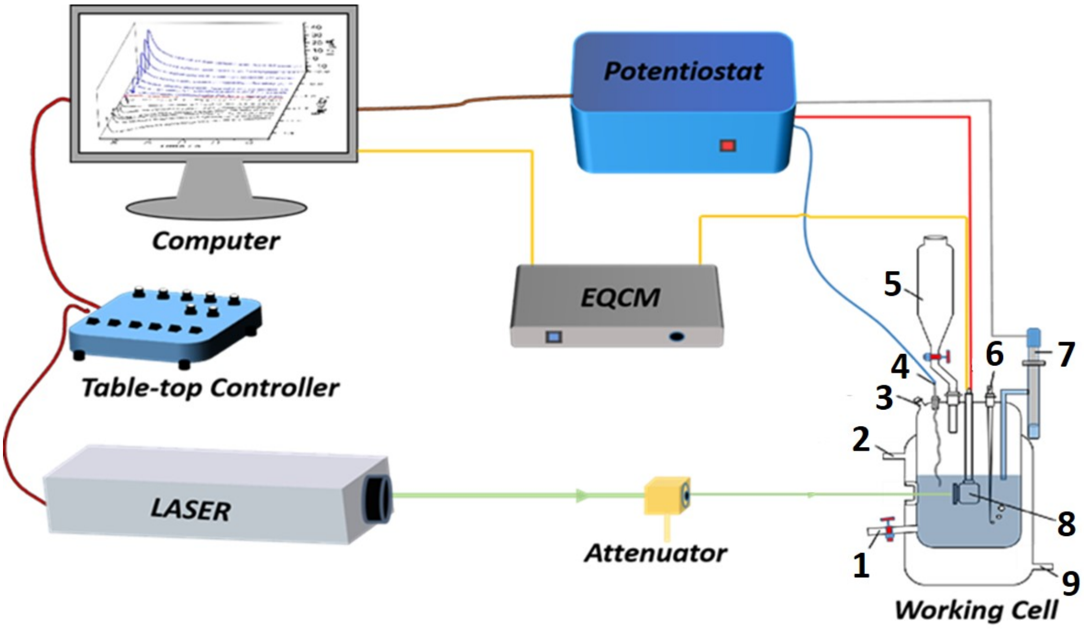

Figure 3.9. *Representative scheme of the laser-induced current transient (LICT) technique setup. The laser head is shown on the left, with the three-electrode configuration electrochemical working cell on the right. The various numerically labeled parts are described as follows: 1 - electrolyte inlet, 2 - hot-water outlet, 3 - gas outlet, 4 - counter electrode (CE), 5 - electrolyte inlet/preconditioning chamber, 6 - gas inlet, 7 - reference electrode (RE), 8 - working electrode (WE), and 9 - hot-water inlet. Essentially, the relative positions of the electrodes, as portrayed in* ***Figure 3.9****, do not precisely correspond to the real measurement configuration, where the RE is located in between the WE and CE instead. Figure modified with permission from references.*[161,162] *Copyright © (2023), Elsevier Inc. All rights reserved.*

3.5 The Impact of Electrolyte Components in Electrocatalysis

One of the research challenges in electrocatalysis is understanding how the catalyst surface's physical or chemical state affects intermediate species' adsorption and desorption equilibrium at each step and, ultimately, its impact on the ensuing catalytic performance. Generally, considerable literature exists on the effect and modulation of catalysts' extrinsic physical properties or core electronic structure on the kinetics of catalytic reactions. These control the crystal plane, defect engineering, strains, particle size, and surface adjustment.[351,352,353] In perspective, electrocatalysis research primarily focuses on improving the catalytic activity to enhance the electrode structure and composition.[354,355] The role of the electrode structure in electrocatalysis is most pervasive in structure-sensitive reactions. For instance, the oxygen reduction reaction can be promoted on the Pt electrocatalyst by introducing surface defects such as steps and concavities.[354,355] Understanding the electrode structure/activity and the electrode composition/activity relations can assist the rational usage of active materials by developing effective catalyst design.

Nowadays, there is a gradual rise of studies focusing on understanding the crucial role electrolyte components, the so-called "spectator species", play in optimizing the performance of electrocatalytic systems. Remarkably, it reveals that the catalytic system's activity is closely related to the electrolyte composition and the corresponding local disparate chemical environment.[356] Surprisingly, in certain instances, the electrolyte components' effect outperformed the activity of the same electrolytes for different electrode structures and electrode compositions (*cf.* **Figure 3.10**).[357,358]

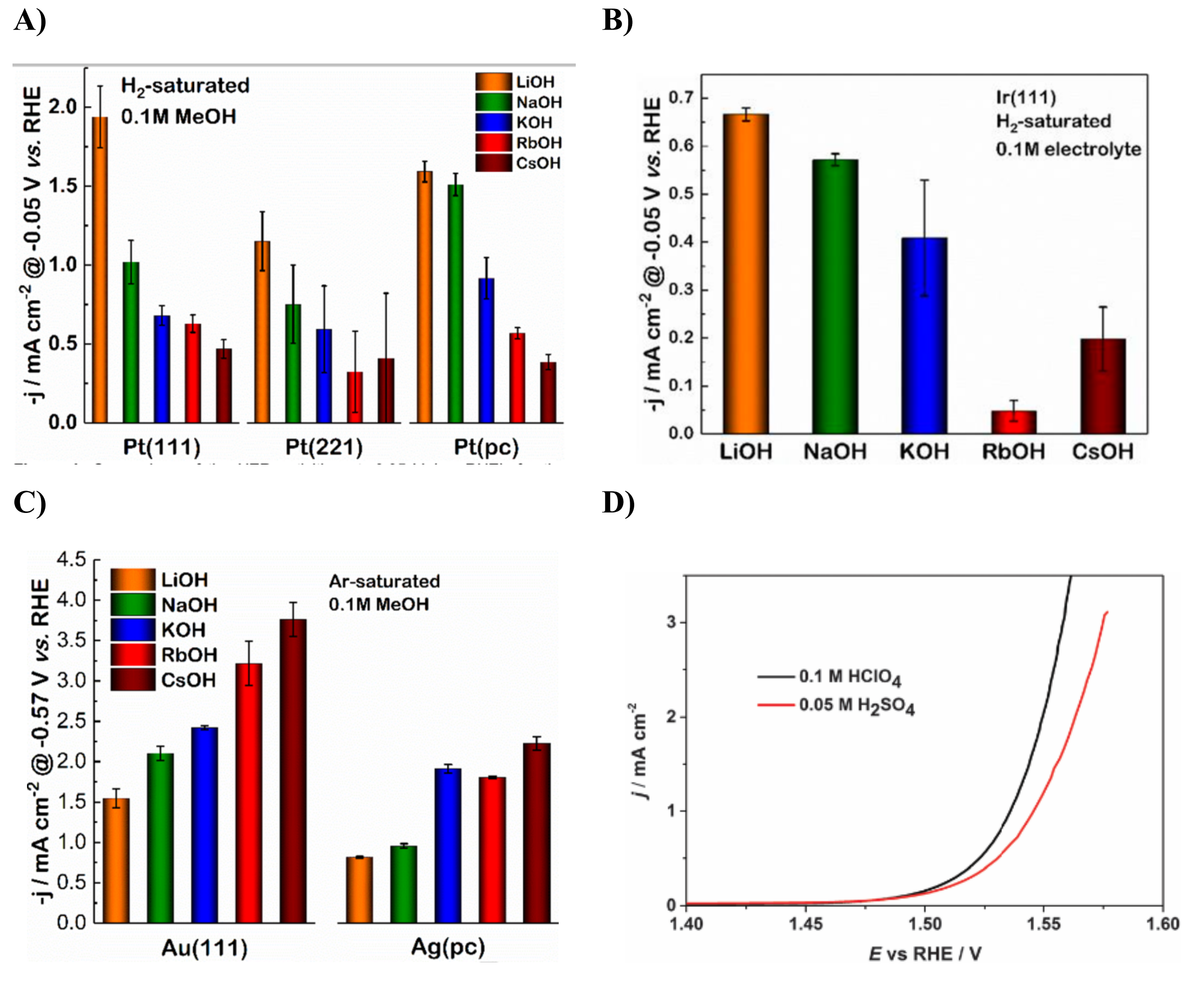

***Figure 3.10**. A bar chart plot depicting a comparison of the hydrogen evolution reaction activities of **A)** Pt(111), Pt(221), and Pt_{pc} electrodes in H_2-saturated 0.1 M MeOH electrolytes ($Me^+ = Li^+$, Na^+, K^+, Rb^+, Cs^+), **B)** Ir(111), **C)** Au(111) and Ag_{pc} electrodes.[357] **D)** OER activities of Ir-oxide thin films in $HClO_4$ and H_2SO_4 at pH = 1 (the curves have been iR-corrected).[358] The conditions and electrolyte components for each measurement are provided in the respective Figures. The so-called spectator species significantly impacts the hydrogen and oxygen evolution reactions, i.e., water electrolysis. Reproduced with permission*

from references.[357,358] Copyright © (2018), Wiley-VCH Verlag GmbH & Co. KGaA, Weinheim; Copyright © (2015), Royal Society of Chemistry.

3.5.1 Solvent Effect

As established in **section 3.5**, besides the electrode structure and composition, the role of electrolytes in electrocatalytic systems should not be underestimated. As such, in recent years, ballooning attention has been dedicated to investigating the effects of electrolyte pH and alkali metal cations, anions, and even the impact that certain ionic liquids have on the activity of the catalytic system.[356,359,360]

In principle, anions or cations in the electrolyte are surrounded by solvent molecules referred to as "solvated ions", serving as the charge carriers (see **section 2.3.1**). In this light, the solvent type and properties are essential for catalytic reactions. Water exhibits several merits, such as abundance, availability, cost-effectiveness, and high sustainability, leading to widespread usage and reliance.[361] As such, aqueous solvents and solutions are used in many electrocatalytic systems. Intriguingly, aqueous solutions are one of the most critical factors regulating catalytic performance for reactions involving proton-coupled electron transfer or using H_2O as a reactant. Nonaqueous solvents are also used in many catalytic systems. Interestingly, protons' absence can constrain proton depletion reactions, and aprotic solvents usually offer a higher potential window than water.[362,363,364]

3.5.2 Cation Effect

Studies have revealed that cations residing in the electrolyte and, by extension, the EDL, especially in neutral or alkaline solutions, can considerably influence the reaction rate.[310,365,366,367] Due to their vast laboratory and industrial applications, alkali metal cation-containing electrolytes remain the most relevant example investigated.[368,369] A typical example is the exploitation of impedance spectroscopic studies on Pt microelectrodes in alkaline media by Taji *et al.*, revealing a change in the HER reaction pathway in the presence of alkali metal cations.[370] The activity follows the trend: $Li^+ \geq Na^+ > K^+ > Cs^+$, with the highest activity occurring in 0.1 M LiOH electrolytes at low overpotentials (*cf.* **Figure 3.11A**). Additionally, it was demonstrated that the nature of the alkali metal cations modifies the relative contribution of the Volmer-Heyrovsky and Volmer-Tafel mechanisms to the overall reaction, with the former being more significant for LiOH electrolytes (*cf*. **Figure 3.11B**).

A)

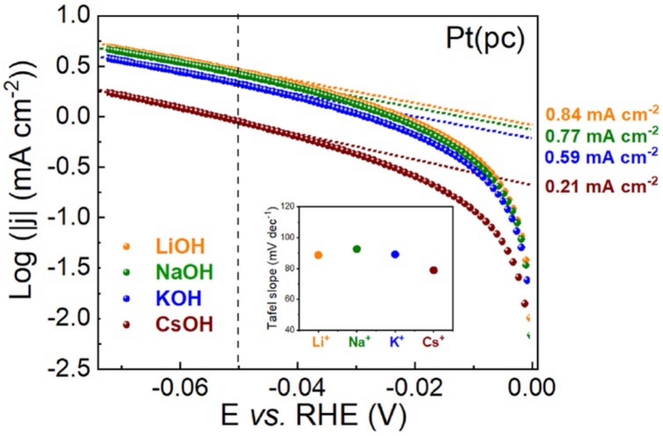

B)

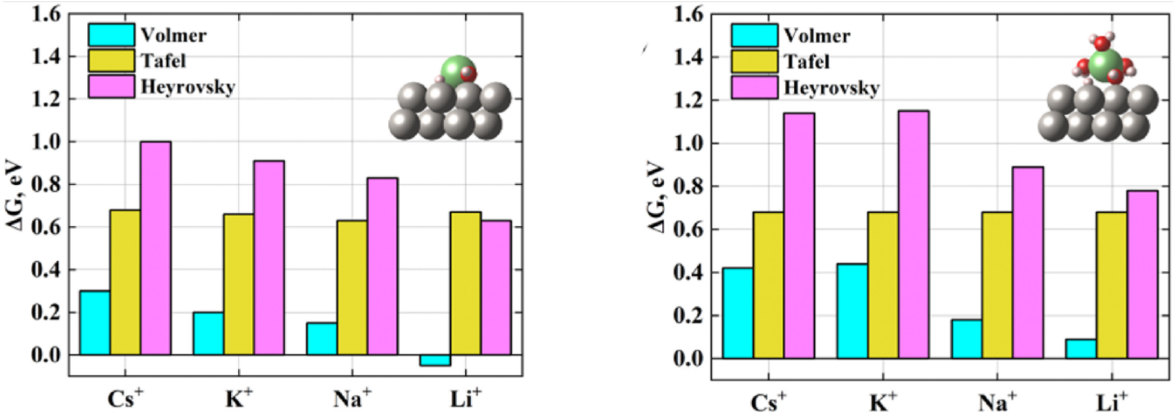

***Figure 3.11**. **A)** A plot of the activity trend of the HER for Pt(pc) electrodes in 0.1 M AMOH electrolytes (AM = Li^{+}, Na^{+}, K^{+}, Cs^{+}). Insert: Information on the Tafel slopes for the different electrolytes. **B)** Bar chart depicting the reaction-free energies computed for the Volmer, Tafel, and Heyrovsky steps of the HER on the pristine Pt(111) surface and in the presence of alkali metal cations. The results for bare and solvated cations are presented on the left and right sides, respectively, with the exemplary atomic-structure snapshots for the Li^{+} case. Only the most energetically favorable reaction pathways obtained for each step are displayed for clarity. Reproduced from reference.[370] Copyright © (2022), Chongqing University. Production and hosting by Elsevier B.V. on behalf of KeAi. Open access, CC-BY-NC-ND 4.0.*

Earlier, Xue *et al*. discovered that for electrodes like Pt(111), Pt(221), and polycrystalline Pt (Pt($_{pc}$)), the electrochemical HER activity measured in alkaline electrolytes followed a strict trend $Li^+ > Na^+ > K^+ > Rb^+ > Cs^+$.[357] Notably, the HER current densities of all Pt electrodes in LiOH were four-fold better than those measured in the CsOH electrolyte, regardless of the electrode surface structure (*cf.* **Figure 3.10A**), suggesting that alkali metal cations strongly impact the HER activity of different Pt electrodes.

Besides the impact of alkali metal cations on the HER, its effect has also been established on other reactions, like the ORR, OER, and HOR.[371,372,373] For instance, Strmcnik *et al.* demonstrated that the non-covalent interactions between hydrated alkali metal cations and adsorbed OH species correlate to Pt(111)'s oxygen reduction reaction activities.[373] In detail, the ORR activity on Pt(111) follows the trend of $Cs^+ > K^+ > Na^+ > Li^+$, which is inversely proportional to the hydration energies of the corresponding cations.

3.5.3 Anion Effect

The discussion thus far has established the critical role of cations in the electrocatalytic performance of reactions. Similarly, the role of anionic components of electrolytes must be elucidated. Anions specifically adsorb onto the electrode surface, poisoning the local catalytic centers at the electrified electrode/electrolyte interface through chemical interactions with other electrolyte species.[374,375] For instance, Santos *et al.* investigated the modifications witnessed on Pt surfaces in perchloric, sulfuric, phosphoric, and hydrochloric acid solutions in the potential range of 0.05 V to 0.8 V *versus* hydrogen electrode in the same solution (HESS) using CV and EQCM methods.[376] They observed mass incorporation of *ca.* 39 ng cm^{-2}, corresponding to a complete monolayer of adsorbed water, due to the adsorption of water molecules replacing the UPD H atoms in every case. The potential range associated with water adsorption varied from 0.05 V to a final value (*cf.* **Figure 3.12A**) depending on the anion adsorption's strength on Pt (0.4 V for ClO_4^- and 0.3 V for Cl^-). Moreover, they asserted that the mass incorporations in the potential region between 0.4 V and 0.8 V were associated with the adsorption of the corresponding hydrated anions, *i.e.*, $ClO_4^-\cdot 2H_2O$, $HSO_4^-\cdot 2H_2O$, HPO_4^{2-} and $Cl^-\cdot 6H_2O$ (*cf.* **Figure 3.12B**).

Lamy-Pitara *et al.* investigated the electrocatalytic hydrogen oxidation and evolution reactions on a rotating disk platinum electrode. They reported that the strongly adsorbed anions (SO_4^{2-}, Cl^-) could cause a decrease in the electrocatalytic oxidation of hydrogen of Pt.[377] Meanwhile, the hydrogen evolution reaction probed in the underpotential and low overpotential regions is independent of the nature of the supporting electrolyte (*i.e.*, $HClO_4$, H_2SO_4, HCl). Hunter *et al.*

observed that the electrocatalytic water oxidation activity is a function of anion basicity. Put differently, the Brewster or Lewis basicity of the anion plays a role in the mechanism of water oxidation.[378]

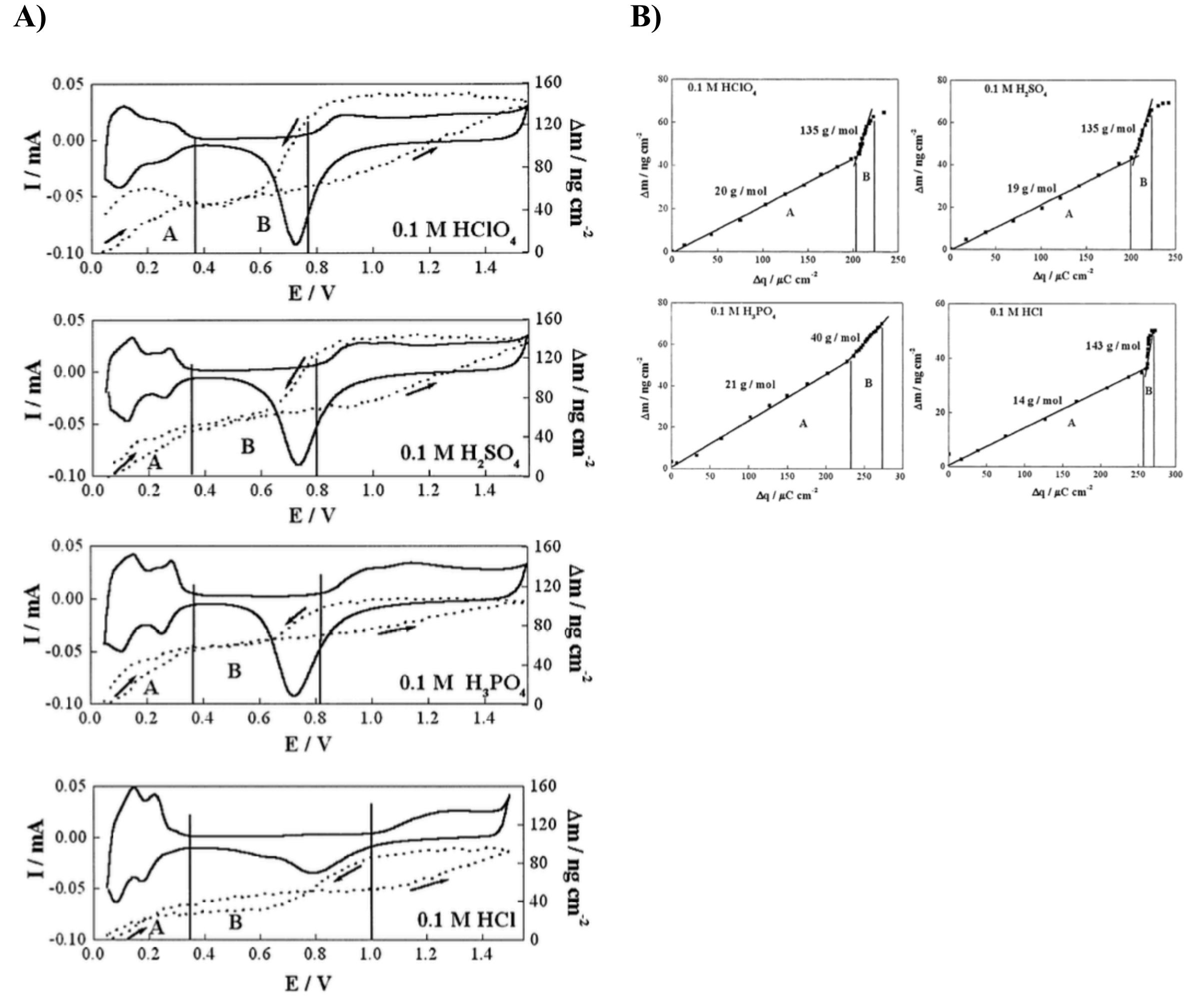

Figure 3.12. ***A)*** *Graphical representation of cyclic voltammograms (—) and concurrently recorded mass change (...) of a quartz-supported Pt electrode in the various electrolytes indicated in the figures. Scan rate: 100 mV* s^{-1}. ***B)*** *Absolute values of* Δ*m versus* Δ*q obtained from **Figure 3.12A**. The mass variations and charge densities correspond to the electrochemical area of the Pt electrode. Reproduced with permission from reference.*[376] *Copyright © (2000), Elsevier Science S. A. All rights reserved.*

Shin *et al.* probed the impact of anions (Cl^-, Br^-, I^-, ClO_4^-, BF_4^-, PF_6^-) on the ORR activity of palladium nanoparticles in acidic media. They affirmed that the influence of anions emanated from the interactions between the anions and the electrolytes affecting the local proton concentration around the catalyst surfaces, *i.e.*, the local pH.[379]

3.5.4 pH Effect

pH dependence plays a pivotal role in determining the mechanism and kinetics of many electrode processes and electrochemical reactions, especially those involving the consumption/production of H^+/OH^-. Systematic investigation of the pH effect over a wide pH range can provide beneficial information about the reaction mechanism(s) and help to establish the optimum reaction conditions.[380] The reaction activity and product selectivity can be efficiently tuned, provided the electrolyte pH is appropriately regulated.

Due to the vast activity difference for various electrodes in alkaline and acidic media, the electrolyte pH's role is crucial for electrocatalytic reactions, such as the HER and ORR.[381,382,383] For fast electrode reactions in solutions of medium pH and low buffer capacity, correcting the effects induced by the shift of local pH near the electrode/electrolyte interface (pHs) is a prerequisite for untangling the intrinsic kinetics and its pH dependence. Despite these facts, a comprehensive appreciation and interpretation of the pH effect on a specific reaction remain challenging.[384] For example, many researchers deem the metal-H_{ad} bond energy the sole descriptor for the HER mechanism.[203] However, adequate information is required to sufficiently explain the lower HER activity in alkaline solutions. The nature of the proton source and the presence of surface adsorption must be considered.[385]

Zheng *et al.* employed four carbon-supported platinum-group metal (PGM) nanocatalysts to study the effect of pH (broad pH ranging from 0 to 13) on the activity of the HOR and HER.[386] They reported that the HOR/HER activities on Pt/C, Ir/C, Pd/C, and Rh/C decreased monotonically with rising pH (*cf.* **Figure 3.13A**), consistent with the theory that higher hydrogen binding energy (HBE) quells catalytic performance. Moreover, a linear correlation was observed between hydrogen binding energy and pH for all four catalysts, implying that the pH dependence of HBE is metal-independent. The desorption peaks for H_{upd} on Pd/C nanoparticles shift to more positive potentials as the electrolyte pH increases, indicating an increase of HBE with pH (*cf.* **Figure 3.13B**). Principally, as the trend on all investigated metals was coherent (exchange current density and HBE), it suffices to infer that the same elementary steps and rate-determining steps can be assigned to all of them and that the HBE is the dominant descriptor for the HOR/HER activities.

Strmcnik *et al.* investigated the pH effect on the HER activity of Au(111) and other electrodes in various pHs of 0.1 M $NaClO_4$ solutions.[385] For Au(111), increasing the electrolyte pH from

1 to 4 changes the typical HER polarization profile, indicating that the HER is controlled by the mass transport of reactive hydronium species in this case.

The cation and anion effect must be considered when investigating the pH effect, especially when involving specifically adsorbed anions.[387,388] This makes it significantly challenging to decouple the pH effects and contributions from cations and anions. Disentangling the intrinsic pH effects in electrocatalysis is of great importance for a deep understanding of the reaction mechanism(s) and kinetics and for improving the operating conditions of electrochemical energy conversion and storage devices.

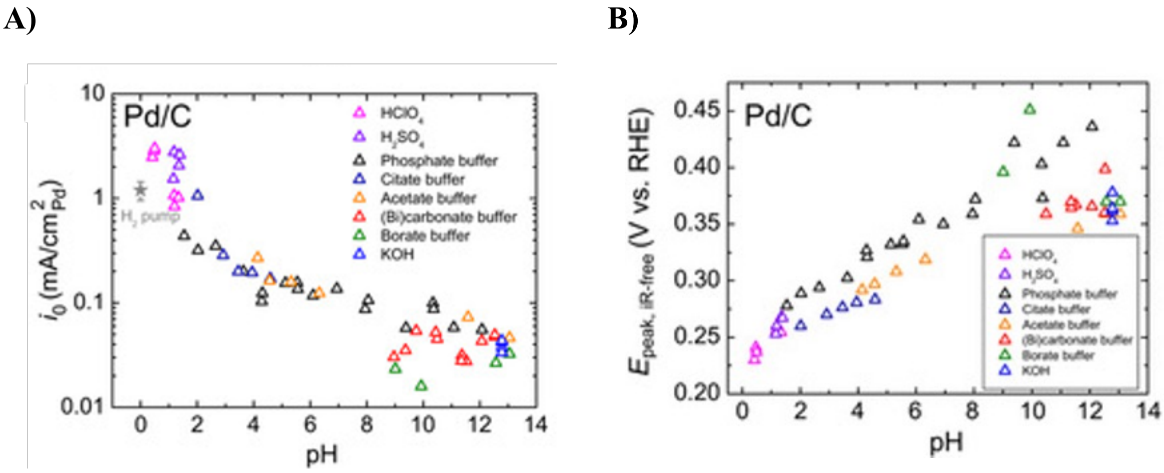

Figure 3.13. ***A)*** *A graphical representation of the exchange current density of HOR/HER plotted as a function of electrolyte pH on Pd/C nanocatalyst. The HOR/HER polarization curves were recorded via the rotating disk electrode (RDE) method in* H_2*-saturated electrolytes at 293 K. Scan rate: 1 mV* s^{-1}*, rotation speed: 1600 rpm.* ***B)*** H_{upd} *desorption peak potentials obtained from cyclic voltammograms of Pd/C plotted against electrolyte pH. From reference.*[386] *Reprinted with permission from AAAS. Copyright © (2016), The Authors. Open access, Creative Commons Attribution-NonCommercial license.*

4.0 Other Experimental & Characterization Techniques

This section presents an overview of the fundamentals governing the other interfacial science experimental and characterization techniques deployed in this dissertation besides the LICT methodology. These additional techniques are highly significant to complement, authenticate, and help disclose detailed data regarding the interfacial processes under study. Electrochemical methods such as cyclic voltammetry (CV), chronoamperometry (CA), and electrochemical impedance spectroscopy, all deploying the three-electrode configuration, were utilized to reveal the ongoing electrode processes fully. *In-situ* interfacial spectroscopic tool for characterizing the electrified electrode/electrolyte interface is also highlighted here. A succinct theoretical background and its related working principles are elucidated.

4.1 Electrochemical Techniques

After outlining the primary concepts underpinning certain electrochemical aspects, discussing the various electrochemical techniques useful to comprehend surface and interfacial electrochemistry better is imperative. Characterizing electrode materials in segments not limited to activity, selectivity, and stability is paramount to aid further insights into such materials.

4.1.1 Electrochemical Three Electrode Setup/Configuration

It is essential to profile the theoretical aspects governing using the three-electrode configuration. This sub-section directs its focus toward the electrochemical three-electrode setup.

The electric potential difference for many materials is easily obtained through a voltmeter. Employing this same principle to measure the electric potential of an electrode/electrolyte system, however, always proves abortive. Given the described limitation emanating from using a voltmeter in both systems, a modification is warranted to measure an electrode's electric potential. By nomenclature, the potential of the electrode under study, the so-called working electrode (WE), can be evaluated from the potential difference or electromotive force (emf) provided the electric potential of the benchmark electrode, often termed the reference electrode (RE), is known. Suppose a chemical reaction (*e.g.*, electron transfer from an electrode to an electrolyte) occurs at one electrode. In that case, it triggers a counter-reaction at the corresponding electrode, called auxiliary or counter electrode (CE), to ensure charge balancing. More precisely, using three electrodes to conduct practical and effective electrochemical measurements is advocated in the electrochemistry community. Conventionally, a potential is applied between the RE and WE such that the current flowing between the CE and WE can be measured. It is essential to add that the RE always possesses a very high impedance compared to the CE or the WE. Because of this, almost no current flows through the RE, making its potential invariable under certain standard conditions. **Figure 4.1** highlights the three electrodes (WE, CE, and RE) required to implement an electrochemical three-electrode configuration.

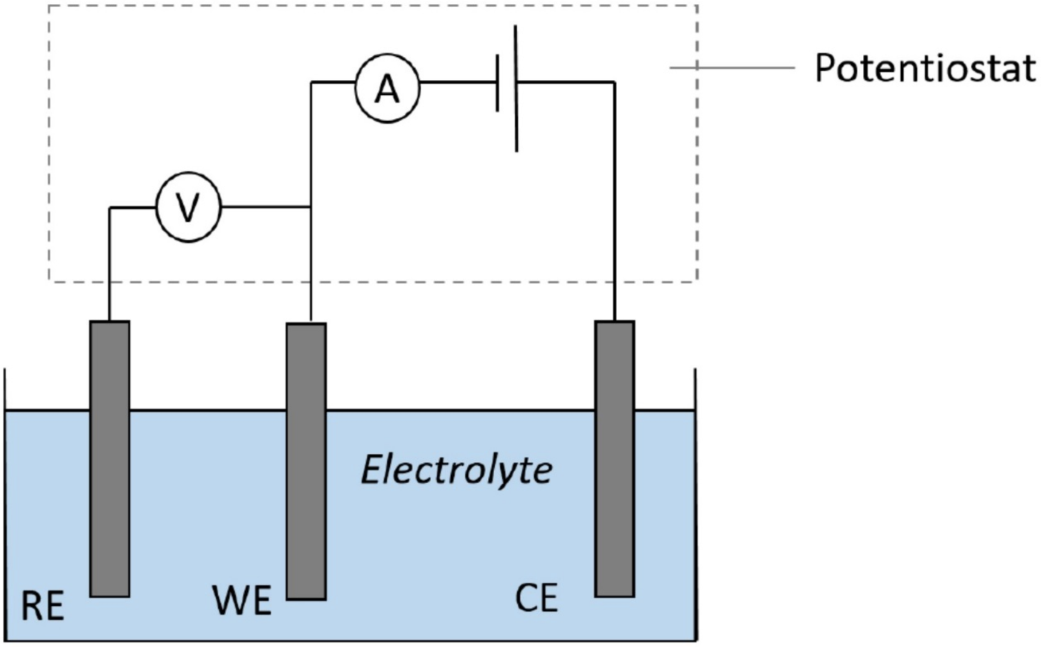

Figure 4.1. *Simplified scheme of a typical three-electrode setup. The reference, working, and counter electrodes are denoted by RE, WE, and CE, respectively. The electrolyte is depicted as blue color, whereas the voltmeter and ammeter are represented by V and A, respectively.*

The voltmeter measures the potential difference between the WE and RE. Correspondingly, the working electrode potential can be determined thanks to the already-known reference electrode potential. As shown in **Figure 4.1,** a potentiostat serves as an ammeter, a power source, etc., and is placed between the WE and CE. As current is drawn from the CE, the ammeter and the power source control the current in the system. On that note, the CE is chosen as a typical inert material (*e.g.*, Pt) that does not readily corrode or produce any foreign substance from electrolysis. This is relevant to primarily safeguard the CE from altering the system's behavior.[389]

At this juncture, it is paramount to enquire into how the potential of the RE can be determined. By convention, certain reactions' standard potential under specific conditions is often set to fixed values. Consequently, the potentials of other electrochemical reactions are pitched relative to this particular reference reaction. The frequently used RE, the so-called standard hydrogen electrode (SHE), follows the HER (*cf.* **Equations (2.31)** and (**4.1)**) with Pt serving as the electrode material at standard conditions (*i.e.*, the pressure of 1 bar).

$$2H^{+}(aq) + 2e^{-} \rightarrow H_2(g) \qquad 4.1$$

Following the application of the Nernst equation (*cf.* **Equation (2.11)**) to the HER (*cf.* **Equation (4.1)**), the standard potential of the HER is set to zero (*i.e.*, $E^0 = 0\,V$). From a broader perspective, there exist several REs to deal with the impracticalities of always using the SHE as the RE in experiments.

Unless otherwise stated, the three-electrode configuration was used for all the performed experiments in this dissertation. Often the reference electrode of choice for experimental purposes is the mercury-mercurous sulfate (MMS) RE. However, in the analyzed data or presentation of results, the reversible hydrogen electrode RE is preferred as that is the standard for reporting most electrocatalysis findings in the literature.

4.1.2 Voltammetric Techniques

Numerous voltammetric techniques have been developed for quantitative electrochemical analysis to aid in measuring and regulating the current as a function of the electrode potential (*i.e.*, electrochemical processes).[390,391] Four primary voltammetric modes exist, such as potentiostatic, galvanostatic, potentiodynamic, and galvanodynamic. The electrode potential remains invariable and varies over time for the potentiostatic and potentiodynamic voltammetric modes. The latter involves a relatively fast and robust approach, which can be deployed for investigating non-stationary electrocatalytic systems. The drawbacks include the inability to isolate Faradaic processes from double-layer currents distinctively. Regarding the galvanostatic mode, the potential is varied by the potentiostat such that the current remains fixed while the current is varied over time in the galvanodynamic mode.

Following its advent, cyclic voltammetry (a well-known voltammetric technique) has evolved into one of the most popular and arguably the most frequently used electrochemical methods to investigate electron transfer-initiated processes.[392,393,394] This way, valuable information concerning the understudy electrochemical system is discovered. Of course, characterizing the electrified electrode/electrolyte interface's behavior falls within the technique's ambit. The voltammetric approach is also associated with the examination of capacities and the performance of electrochemical depositions.

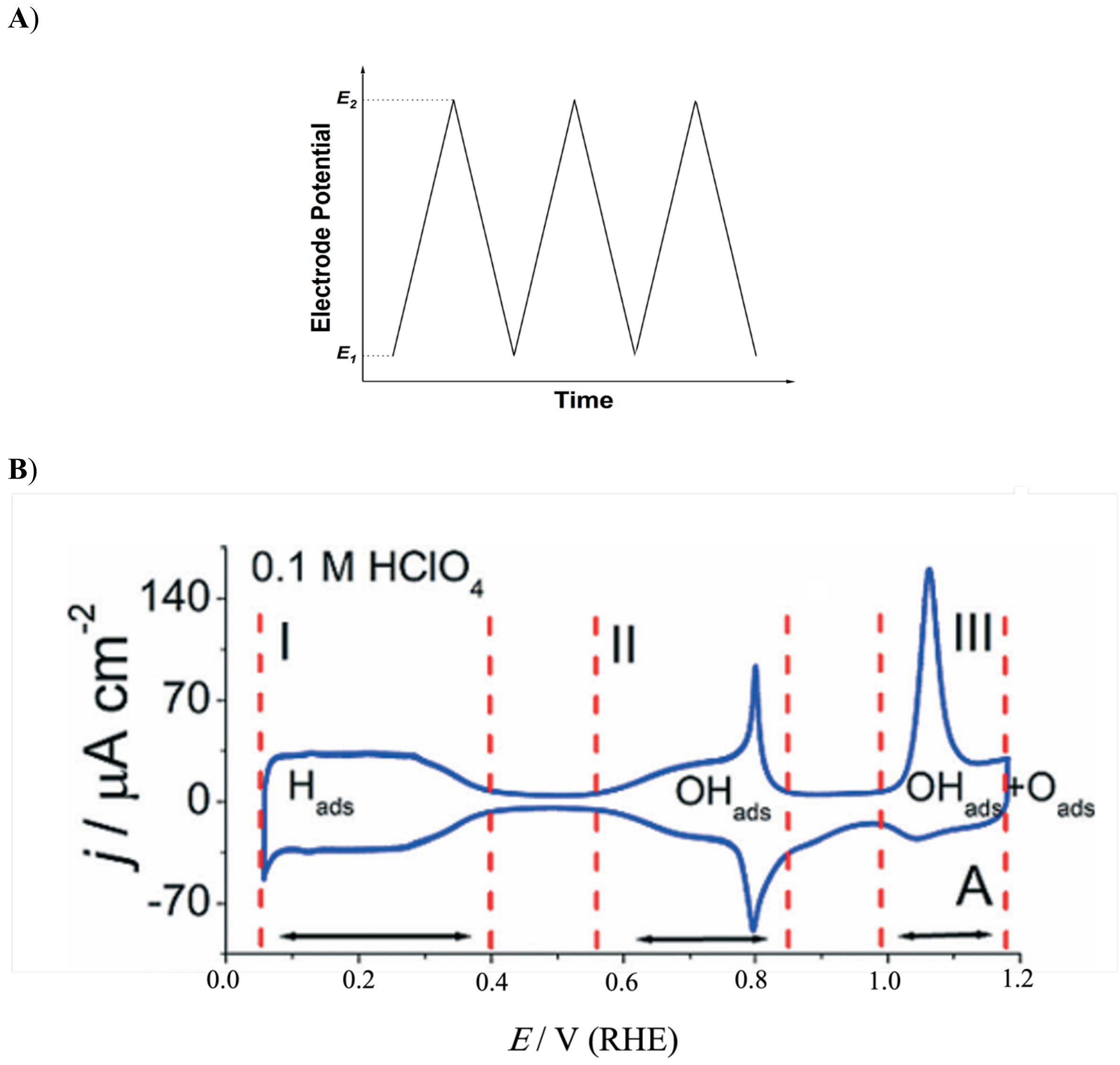

__Figure 4.2__. __A)__ A model cyclic voltammetric plot indicating the time dependence relative to the applied electrode potential. E_1 and E_2 represent the minimum initial and maximum final electrode potentials. Essentially, parameters like the potential range and scan rate immensely influence the shape of the CV. ***B)***

A recorded typical stable cyclic voltammetric profile of a well-ordered Pt(111) electrode in 0.1 M $HClO_4$ electrolyte at a scan rate of 50 mV s^{-1}. Three distinguished regions can be observed: the hydrogen regime, the double-layer region, and the oxygen region. These separate regions are labeled I, II, and III, respectively. Figure reproduced with permission from reference.[395] *Copyright © (2014), Royal Society of Chemistry.*

Cyclic voltammetry is an easily applicable technique belonging to the potentiodynamic voltammetric class. In its operations, it commences from an initial minimum potential E_1, and the electrode potential is linearly ramped over time upwards (anodic scan) or downwards (cathodic scan) until a final maximum potential E_2 is reached. Afterward, the scan direction is reversed until the potential corresponds to the starting potential E_1. This is characteristically repeated several times while the current is recorded, as shown in **Figure 4.2A**. For clarity, the cyclic and periodic potential is introduced to the working electrode. The potential limits (E_1 and E_2), number of scans, and the slope dE/dt of the potential variation over time termed the scan rate with units [mV s^{-1}] are vital parameters that require further consideration.[189,396]

For a classical cyclic voltammogram, the current is plotted as a function of the applied potential. A typical instance presented in the reproduced **Figure 4.2B**, from the literature, features a stable cyclic voltammogram recorded for the model Pt(111) electrode in Ar-saturated 0.1 M $HClO_4$ electrolyte. Three separate regions can be identified corresponding to the processes occurring at the electrocatalyst surface. The demarcation labeled I, closer to the cathodic limit, represents the hydrogen adsorption/desorption region. Adsorption of protons on the Pt(111) surface results when cathodic potentials ranging from 0.3 V *vs*. RHE are applied.

Notably, the proton transfer automatically initiates the transfer of electrons. A reverse reaction, oxidation of protons, occurs when the applied potentials are probed anodically. At these potentials, popularly termed underpotential deposition (UPD), adsorbates are energetically propitious to produce a single monolayer. Primarily, the UPD allows the estimation of the so-called electrochemical active surface area (ECSA) of Pt electrodes by integrating the charge of the resulting peak. Region II, which encompasses the non-occurrence of redox reactions or processes, takes effect at slightly more anodic potentials. An almost zero current (electric double-layer capacitance) emanating from the capacitive behavior of the electrode is witnessed in this region, hence earning the name double-layer regime. The third region, labeled III, is called the oxygen region and is characterized by higher potentials. In this light, the platinum surface begins to oxidize, forming an oxide layer at higher anodic potentials. The oxide layer is subsequently reduced at the cathodic scan. As compared to the adsorption of protons, the oxidation/reduction of the platinum surface is less reversible, implying that the peaks are energetically shifted away from each other.

Fundamentally, CVs provide insights and valuable information, such as reactant, intermediate, and product stability of electrode processes and reactions and quantifying electron transfer kinetics. In this sense, CVs often serve as the first characterization tool deployed for analyzing every system, including new ones. To investigate any specific reaction, limiting the CV to the corresponding potential window for that reaction is necessary. The shape of a cyclic voltammogram, a function of the electrode type and electrolytes used, can be very characteristic of certain electrocatalyst surfaces. For instance, a Pt(111) surface can be easily distinguished from polycrystalline or stepped platinum surfaces by CV. Additionally, CVs of materials under certain conditions are used as fingerprint representations to ascertain the cleanliness and wholesomeness of the surface under study.

In this dissertation, CVs are deployed for many different purposes. For instance, CVs were deployed to ensure the surface cleanliness of electrodes. More precisely, the electrodes are cleaned from contaminations or residual catalyst films by cycling the electrodes in a relatively large potential window in acidic electrolytes. Furthermore, CVs were used to condition working electrodes as reference electrodes. Short potential range CV measurements were performed before the laser ignition, mainly within the double-layer region. CVs were also employed for the electrochemical deposition of the Pd MLs on the Au electrodes. Finally, cyclic voltammetry was utilized to investigate the electrocatalytic activities of the different electrodes.

4.1.3 Electrochemical Quartz Crystal Microbalance Electrode

The electrochemical quartz crystal microbalance is an uncomplicated, cost-effective, and non-destructive technique used to monitor deviations in the electrode mass on the ng to µg scale. The QCM is a vital tool in electrochemical research for measuring the modifications in mass loading on the electrode during the electrochemical investigation. The device comprises a thin piezoelectric quartz crystal sandwiched between two metal electrodes. It operates by creating an alternating electric field across the crystal, constituting the vibrational motion of the crystal at its resonance frequency. Notably, the resonance frequency is sensitive to the mass of the crystal.[397] Therefore, the electrode mass loading can be accessed *via* a QCM electrode, a precise and sensitive technique to monitor small mass changes by measuring the frequency change of a quartz crystal resonator.[398]

The observed variations are usually instigated by material deposition at the electrode or its removal from the surface. It finds application in many electroanalytical studies, such as underpotential deposition of metals, intercalation/deintercalation of ions, or adsorption/desorption of species.[399]

According to Sauerbrey's equation, the shift of the quartz resonance frequency (Δf) is a function of the mass change (Δm) on the quartz crystal and the electrodes:[397]

$$\Delta m = -\left(\frac{A\sqrt{\mu\rho}}{2{f_0}^2}\right)\Delta f = -C_f\Delta f \tag{4.2}$$

where f_0 represents the fundamental resonance frequency of the quartz crystal (Hz), A depicts the piezoelectrically active crystal area (cm^2), μ is the shear modulus of quartz for AT-cut crystal (2.947 $\times 10^{11}$ g cm^{-1} s^{-2}), ρ stands for the density of quartz (2.648 g cm^{-3}), and C_f is the calibration constant or sensitivity factor.

4.1.4 Chronoamperometry

Chronoamperometry or transient amperometry is a technique that involves the application of a constant potential to a particular system (*e.g.*, electrode/electrolyte interface) and eventually measuring its response in the form of current. The chronoamperometric response can be used to obtain valuable information, including the diffusion coefficient of electroactive species.[400,401,402] Another application is the investigation of the reaction mechanisms occurring at the electrode/electrolyte interface through deploying several potential step chronoamperometry.[403,404]

In this dissertation, the CA technique was utilized during the laser measurements to record the emanating system's response, *i.e.*, current transients, at specific potentials. Several potentials are measured at fixed potential steps or intervals to get a complete experimental insight.

4.1.5 Electrochemical Impedance Spectroscopy

Electrochemical Impedance Spectroscopy, another tried and tested tool, is an indispensable and non-destructive electroanalytical technique deployed in this dissertation. In the modern era, one can attribute an enormous chunk of the enhancement of EIS to the research conducted by E. Warburg. In this study, EIS was applied to investigate the analysis of redox reactions.[405] The EIS field was further strengthened following the research works of J. E. B. Randles,[406] H. Gerischer,[407,408,409,410] and D. C. Grahame.[411] EIS primarily provides information about electrode reaction kinetics and physicochemical properties (*i.e.*, electrode capacitance and electrolyte and contact resistances). Even from a cursory look, one can project that the probing of porous electrode properties, determination of the dielectric and transport characteristics of materials, and examining the properties of passive surfaces can all find applications with EIS. Additionally, mechanisms of electrochemical processes such as adsorption/desorption, intercalation/deintercalation, catalytic reactions, and even corrosion fall within the remit of EIS, owing to its capacity to distinguish several constituent components, the invention of potentiostats, and the development of frequency response analyzing tools.[412,413,414,415]

However, the interpretation of the obtained EIS data sometimes leads to complexities. Resolving or circumventing it necessitates the deployment of certain initial assumptions. In certain instances, the analyzed data can result in ambiguous interpretations of the electrochemical processes. In this situation, using other complementary techniques are essential to stem misapprehension.

EIS is a frequency domain measurement that involves the application of a sinusoidal electrochemically perturbed signal (potential or current) to a system. To explore the frequency-dependent complex resistance, *i.e.*, the so-called impedance Z, EIS is usually executed under quasi-stationary conditions at a fixed potential, although nonstationary EIS applications exist. Practically speaking, a fixed potential $E(w, t)$ is applied and modulated with a small sinusoidal signal E_0 or small amplitude, and angular frequency w, while the current $i(w, t)$ is measured for potentiostatic EIS. The measurement is typically repeated for a broad range of frequencies.

Mathematically, the sinusoidal input signal can be expressed as:

$$E(w,t) = E_0 \sin(wt) \qquad 4.3$$

Here, E_0 is the amplitude, $w = 2\pi f$ stands for the angular frequency, and t is the time.

Correspondingly, the system's output produces a current, which is phase-shifted and with a different amplitude:

$$i(w,t) = i_0 \sin(wt + \phi) \qquad 4.4$$

Where i_0 is the amplitude of the current response and ϕ corresponds to the phase shift.

Therefore, the system's impedance, $Z(w,t)$, can be formulated as:

$$Z(w,t) = \frac{E(w,t)}{i(w,t)} = \frac{E_0}{i_0} e^{j\phi} = |Z(w)| e^{j\phi} \qquad 4.5$$

With $|Z(w)|$ being the absolute value of the impedance.

Galvanostatic EIS usually finds industrial-based applications in devices like fuel cells and electrolyzers. In this approach, the current is regulated in such a manner enabling the potential to be recorded.

Generally, the response of an electrochemical system toward a perturbation is non-linear. That notwithstanding, a quasi-linear response results from sufficiently small sine-shaped perturbation, implying that it also follows a sine-shape with the same frequency but is phase shifted by ϕ (see **Equation 4.4**). Remarkably, for EIS data to meet the validity standard, four criteria, namely, linearity, causality, stability, and finiteness, must be fulfilled.[416] Regardless of the mode, either potentiostatic or galvanostatic, EIS is performed in, the amplitude of the applied potential/current must be sufficiently small (which depends on the degree of local linearity of the electrochemical system at the chosen potential/current) but also large enough not to interfere with the background noise. From common practice, amplitudes ranging from *ca*. 2 mV to 30 mV are usually preferred in the potentiostatic mode.

The quality and validity of the recorded EIS data can be scrutinized using the Kramers-Kronig (KK) transform test, correlating the frequency-dependent real part *ReZ(w)* or *Z'* to the imaginary part *ImZ(w)* or *Z"* of the impedance. It's worth clarifying that realizing the demands of the KK relations is no substitute for poorly collected impedance data. Put differently, obtaining good impedance data must be the starting point before proceeding to reliably fulfill the requirements of the KK relations, which is also paramount. The universal nomenclature of representing impedance data is by relating *-ImZ vs. ReZ (-Z" vs. Z')* in the so-called Nyquist plot (*cf.* **Figure 4.3A**). Although the Nyquist plot is the most standard and relatively comprehensive way of presenting impedance data, the frequency information is always latent.

In addressing the challenge, the Bode plot representation, which reveals the modulus $|Z(w)|$ and ϕ *vs*. the angular frequency w (*cf.* **Figure 4.3B**), is used as the alternative.[189,417] The Bode plot is significant when inductive and capacitive effects are the main focus during EIS investigations.

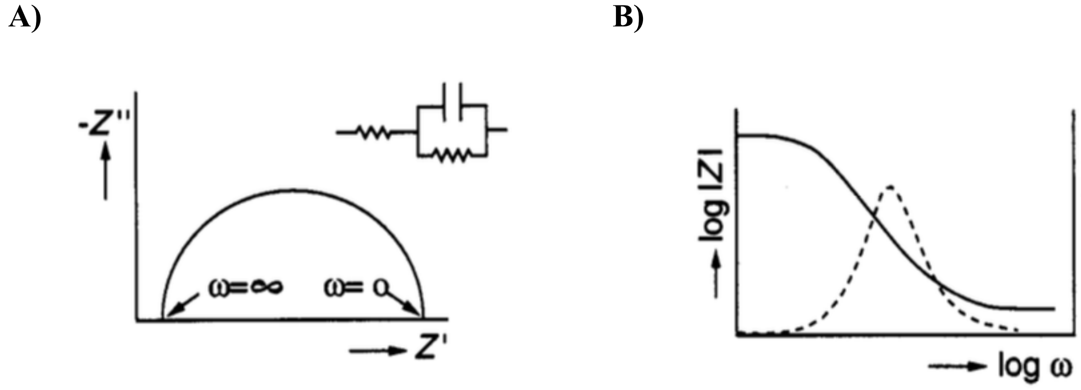

***Figure 4.3**. **A)** Prototypical Nyquist plot representation of EIS data and the insert is the electrochemical equivalent circuit depicting the type of reaction ongoing. **B)** Standard Bode plot representation for the EIS data corresponding to the Nyquist plot. Figures reproduced with permission from reference.[418] Copyright © 1994 IUPAC.*

As earlier stated, the analysis of EIS data sometimes comes with complexities. Therefore, prior familiarity with the electrochemical system will guide in predicting the feasible reactions and their mechanism(s) likely to occur at the electrode (or system) under investigation. Correspondingly, the assumptions can be used to formulate equations to describe the Faradaic and non-Faradaic currents resulting from small perturbations. In turn, this can be used to derive an equation for the total impedance of the system. Often, this equation is (if possible) represented in the form of an equivalent electric circuit (EEC), which facilitates understanding. However, it must be emphasized that the EECs in this dissertation are not arbitrary but based on electrochemical phenomena and their influence on impedance. EECs typically comprise three ideal and real electric circuits or components: resistors, *R*; *capacitors*, *C*; and inductors, *L*. Other non-existing circuits, like constant phase element (CPE) symbolized by *Z* or *Q*, describe the capacitances exhibited by porous systems. The Warburg impedance element, denoted by *W*, best depicts the diffusion occurring in the system. The Gerischer impedance element, often represented by *G*, merges Faradaic and non-Faradaic reactions, thereby significantly influencing the diffusion process. Accordingly, the model can be applied to fit the recorded impedance data. In cases where the model cannot fit the impedance data sufficiently or some parameters are not well defined (*e.g.*, if a side reaction was accounted for but did not contribute), the model needs to be readjusted. Once a good fitting is attained, the model should be further validated and checked for plausibility. For instance, experimental conditions are varied, and the influence on the fitting parameters must be carefully evaluated and compared with theoretical predictions.[189,417]

4.2 Electron Paramagnetic Resonance Spectroscopy

Nowadays, the application of Electron Paramagnetic Resonance spectroscopy does not feature conspicuously in electrocatalytic research compared to other techniques like CV and EIS. Hence, an introduction and a brief overview of the basic concepts governing the electron paramagnetic resonance spectroscopy method are outlined herein.

Electron Paramagnetic Resonance spectroscopy has been a familiar technique since the 1950s in both the biological and chemical sciences to detect and identify free radicals (chemically stable or transient) and irradiation-induced effects.[419,420,421,422,423] The fundamental principle underpinning EPR spectroscopy is hinged on one significant condition, requiring the inclusion of enough species with unpaired electrons in one of the atomic orbitals of the material under investigation. This is a prerequisite to reveal the magnetic dipole moment and, by extension, the paramagnetism of the material under study. It suffices to state that EPR spectroscopy deals with the interaction of electromagnetic radiation with magnetic dipole moments originating from unpaired electrons. Interestingly, certain oxidation states of transition metals belong to the group of paramagnetic materials. Ultimately, the scope of materials besides the aforelisted readily available to probing by EPR spectroscopy is substantially limited as just a handful of materials are inherently paramagnetic.

EPR spectroscopy is akin to nuclear magnetic resonance (NMR) spectroscopy, with the difference being that the magnetic dipole moments arise from the nuclei for the latter, premised on the earlier statements. Consequently, resonance frequencies lie within the microwave range (in this dissertation, X-band: ~ 9 GHz). From a broader perspective, EPR spectroscopy can be regarded as part of the giant umbrella of molecular absorption spectroscopy. As such, insightful information on the molecular structure of materials can be obtained. In realizing these spectrum types, the absorption of the sample under investigation is plotted as a function of the applied magnetic field strength. Correspondingly, the electron's spin can now orient either parallel or anti-parallel toward the magnetic field direction in an external magnetic field. In this way, the energy difference ΔE_S between both spin states (Zeeman splitting) can be estimated using the expression:

$$\Delta E_S = g\mu_B B \qquad 4.6$$

Here, g is the so-called g value or factor, which inherently depends on the material type (for instance, for free electrons, $g = 2.0023$), μ_B denotes the Bohr magneton, and B is the magnetic field.

Invariably, $\Delta E_S = h\nu$ with h being the Plank's constant and ν being the microwave frequency. In this sense, it suffices to claim that in triggering an electron transition with μ_B as its intrinsic magnet moment, the energy difference, ΔE_S , must precisely correspond to the supplied microwave energy, $h\nu$. Until recently, the B-field was the parameter that was always varied, while the microwave frequency remained invariable and has become the convention, particularly in the continuous wave mode. In consequence, spin $S = \frac{1}{2}$ species, and its corresponding g value can be identified according to the position of the observed absorption peak. Besides the Zeeman effect, hyperfine interaction can play a role, provided the magnetic moment of nuclei interacts with the electron's magnetic moment. This takes precedence when the nuclear spin I and the number of affected nuclei n lead to the further splitting of possible spin states of the local magnetic field of a nucleus. In effect, a total of $(2nI + 1)$ hyperfine lines can usually be spotted. To illustrate this scenario, following the coupling of an unpaired electron to one nucleus with $I = 3/2$, one can anticipate that four hyperfine lines will be observed. The resulting hyperfine lines are arranged symmetrically around the resonance B-field without hyperfine interaction B_0 and are separated according to the relation:

$$\Delta B_I = \frac{A}{g\mu_B} \qquad 4.7$$

Here, A denotes the hyperfine constant (*cf.* **Figure 4.4**). More detailed information featuring the anisotropies of both hyperfine constant and g factors is extensively discussed elsewhere.[424]

The narrative so far has solely focused on single electrons. Remarkably, one can adjust the already discussed principle to the surroundings of a single spin. The coupling to this so-called lattice is crucial to aid in fully comprehending why many samples do not show the expected EPR signal. In this case, a characteristic spin-relaxation time T_1 measures how efficiently the lattice couples to a particular spin, such that as T_1 gets smaller, the better the coupling becomes. This especially becomes problematic for transitional elements, as their spins usually exhibit fast relaxation, leading to a broadening of the signal to the extent that renders them undetectable. Therefore, cooling to cryogenic temperatures is often deployed to decrease the spin-relaxation time.[424,425]

Paramagnetic radicals, often transient species like OH^-, can, for instance, be formed in aqueous electrolytes. Their reactivity leads chemically to short lifetimes resulting in an extremely low steady-state radical concentration, typically below the EPR detection limit. Special spin traps are deployed to fixate the spins such that an EPR spectrum can be recorded to salvage that.[426]

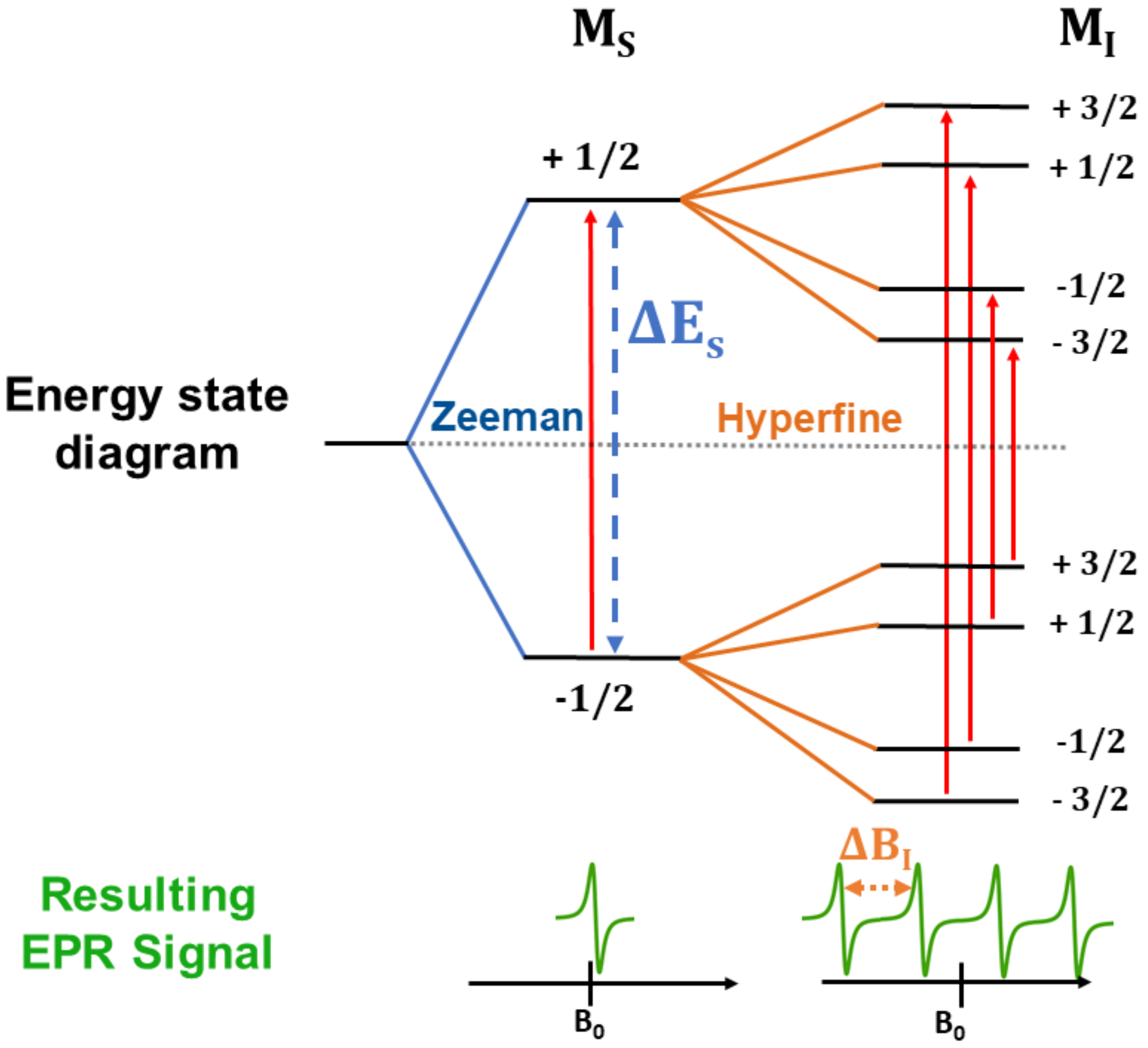

Figure 4.4. *Energy state diagram of an element with spin* $S = ½$ *interacting with a nuclear spin of* $I = 3/2$

5.0 Experimental Methodological Aspects

The fundamental principle underlying the experimental measurements, and the characterization techniques, have been discussed in **chapters 3** and **4**. This chapter outlines the detailed experimental procedure for the cyclic voltammetric, laser, EIS, and EPR measurements. Additionally, various experimental setups for the electrochemical characterization are provided. Precisely, to carry out the electrochemical measurements, the appropriate setups employed will be illustrated.

5.1 Electrochemical Cell

Two different electrochemical cells were used in this dissertation. One of the electrochemical cells was purposely deployed for the voltammetry, EIS, and laser measurements, and the other electrochemical cell was designed specifically for the *in-situ* EC-EPR spectroscopy experiments (see **section 6.7**). The three-electrode configuration was the setup employed in both electrochemical cells. All glassware was cleaned with a piranha solution comprising a 3:1 mixture of H_2SO_4 (96% Suprapur™, Merck, Germany) and H_2O_2 (30% Suprapur™, Merck, Germany) to get rid of trace amounts of organic residues, etc. before the measurements. Subsequently, every compartment of the respective electrochemical cells was rinsed several times with cold and near-boiling ultrapure water (MilliQ water system - Merck Millipore & Evoqua, Germany).

To specify, the electrochemical cell for the cyclic voltammetric, EIS, and laser-induced current transient measurements was made up of two parts, namely, the preconditioning compartment (1) and the main compartment (2) (*cf.* **Figure 5.1)**. The electrolyte solutions were preconditioned by purging gases (Ar 5.0 and O_2 4.7, Air Liquid, were used in this dissertation) in the compartment labeled (1) before being introduced to the second compartment, named (2). It is significant to highlight a flat, light (laser, in this case) transmittable glass window, specially designed on the main compartment, named (2), which essentially permits the laser beam to directly irradiate the working electrode surface. Refreshingly, the inner atmospheric conditions of the electrochemical cell can be regulated *via* a gas inlet and outlet on the main compartment (2) during the experiments. Of course, the temperature of the deployed electrolytes can be controlled *via* a water thermostat available for this electrochemical cell. However, the electrolyte temperature adjustment was not a vital requirement in this dissertation.

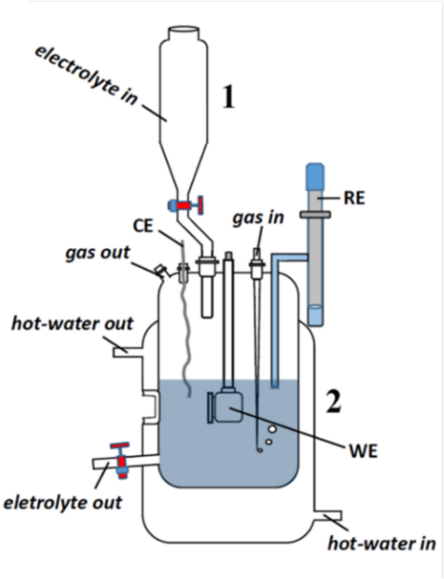

Figure 5.1. *Schematic depiction of the specially designed electrochemical cell for realizing several measurements, including CV, EIS, and LICT. Two compartments, namely, the preconditioning chamber, labeled (1), and the main compartment, named (2), make up the electrochemical cell. For completion, it is essential to mention that the three electrodes, the working electrode (WE), the counter electrode (CE), and the reference electrode (RE), are all placed in the main compartment. A distinct feature worth mentioning is the flat, light (laser, in this case) transmittable glass window, specially designed on the main compartment, named (2), permitting the laser beam to directly irradiate the working electrode surface. As represented in this figure, the relative positions of the various electrodes in the setup do not precisely correspond to their appearance in actual experimental measurements. Figure reprinted with permission from reference.*[130,161] *Copyright © (2021), The Authors. Published by Wiley-VCH GmbH. Open access, published under a CC-BY license.*

In some experiments, AT-cut quartz crystal wafer electrochemical quartz crystal microbalance (EQCM) electrodes (polycrystalline Au with a surface area of 1.37 cm^2, Stanford Research Systems, USA) were used as working electrodes for the CV and LICT measurements. To ensure the stability and electrical conduction of the AT-cut quartz-crystal wafer EQCM electrodes while measuring, a crystal holder (Stanford Research Systems, USA) was employed. In another experiment, 5 MHz QCM gold substrates (10 mm diameter) procured from Biolin Scientific, Inc., served as WE for the surface-mounted metal-organic frameworks synthesis, CV, and eventually the LICT measurements. For these purposes, a mercury-mercurous sulfate (MMS - $Hg/HgSO_4$) electrode (SI Analytics, Germany) and a mercury-mercurous oxide (MMO - Hg/HgO) electrode (1 M NaOH, Bio-Logic, France) served as the reference electrodes for the experiments of AT-cut wafer EQCM Au electrode and SURMOFs, respectively.

In other experiments, atomic layer deposition methodology was employed to deposit palladium monolayers on AT-cut EQCM wafer electrodes (polycrystalline Au with a surface area of 1.37 cm^2, Stanford Research Systems, USA). In a separate investigation, the Pd monolayers were electrochemically deposited on the AT-cut quartz-crystal wafer electrodes (polycrystalline Au with a surface area of 1.37 cm^2, Stanford Research Systems, USA). These modified Pd MLs on Au EQCM served as working electrodes for the CV, EIS, and LICT measurements. Battery electrodes, precisely, Prussian Blue Analog (specifically $Na_2Ni\square Fe(CN)_6\square$- NiHCF) electrode, also deposited on original AT-cut wafer EQCM electrodes (polycrystalline Au with a surface area of 1.37 cm^2, Stanford Research Systems, USA), were experimented on as the WE. Here, a silver-silver chloride (SSC - Ag/AgCl) electrode was employed as the RE.

Crucially, the deployed reference electrodes were connected to the electrolyte through a Luggin capillary. A Pt wire served as the counter electrode for all the experiments. All measurements were performed using a VSP-300 potentiostat (Bio-Logic, France), operated with the software *EC-Lab V11.43*.

5.2 Electrochemical Measurements

Herein, the effects of voltammetric measurements on various electrodes are conducted. As described in **section 4.1.2**, the CV reveals the characteristic fingerprint of the electrode type under investigation. The so-called electrochemical cleaning always preceded the performance of a proper CV (either narrow, broad, or both range(s)). The preparation before the electrochemical measurements is laid out in addition to how the measurements were performed.

5.2.1 Preparation of Electrodes

Before commencing the main experiments, the AT-cut polycrystalline Au EQCM wafer electrodes (10 mm diameter, see **Figure 5.2A**) were electrochemically cleaned. More precisely, the Au electrode was electrochemically cleaned in an Ar-saturated 0.1 M H_2SO_4 electrolyte in the potential range of 0.40-2.10 V *vs*. RHE and was repeated for several cycles till a stable voltammogram was obtained. In realizing the corresponding CV, the potential window was narrowed to 0.50-1.70 V *vs*. RHE. The scan rate used for this measurement was 50 mV s^{-1}. This step was necessary to validate the quality of the working electrode surface. The ensuing CV results were compared with the existing reports in the literature to confirm the fingerprint characteristics of the electrode under investigation. This procedure was repeated for every freshly introduced electrode, including Au, SURMOFs, etc.

In the case of the Ni|Fe-[TA]-SURMOF-derived electrodes, a layer-by-layer (LBL) deposition method was deployed to accomplish that. The LBL deposition aimed at growing MOF thin films (SURMOFs) was performed in a homemade pump system and was controlled by a LabVIEW program. Before the deposition, the QCM Au substrates (Biolin Scientific, Inc.) were functionalized for 12 hours in a mixed ethanol solution incorporating 20 μM 16-mercapto hexadecanoic acid (MHDA, 90%, Sigma Aldrich) and acetic acid (5 vol.%). Subsequently, the electrodes were rinsed severally with absolute ethanol to remove any soluble organic molecules. A 0.2 mM deprotonated organic linker solution was prepared *via* stirring a solution mixture composed of 0.185 mmol terephthalic acid (TA, Sigma Aldrich), 1.02 L ethanol (99.9%, Th. Geyer GmbH & Co. KG, Germany), 60 mL distilled water, and 0.8 mL trimethylamine (Et_3N, Acros) for 24 hours. To begin the Ni|Fe-[TA]-SURMOF deposition procedure, the Au substrates were immersed into the 0.25 mM $NiCl_2 \cdot 6H_2O$ (99.3%, Alfa Aesar) solution for *ca*. 10 minutes. This was followed by washing the electrodes with ethanol for *ca*. 2 minutes, principally aimed at removing the unadsorbed species. Eventually, the electrode was submerged into the already-prepared 0.2 mM deprotonated organic linker solution for *ca*. 10 minutes to generate the metal-organic bonds. Subsequently, the system was cleaned for *ca*. 2 minutes with ethanol. The realization of the Ni-[TA] then proceeded following 45 deposition cycles constituted *via* four immersion processes corresponding to one LBL deposition cycle. In incorporating the top layer, *i.e.*, Fe-[TA], 15 additional cycles in 0.25 mM $FeCl_3$ (98%, abcr GmbH & Co. KG, Germany) solution were performed. The as-prepared heterostructured Ni|Fe-[TA]-SURMOF electrode was carefully rinsed with absolute ethanol severally and dried at room temperature to end the synthesis procedure.

The electrochemical activation and activity measurement of the Ni|Fe-[TA]-SURMOF electrode was performed using a conventional three-electrode configuration. However, the laser measurement was conducted in the three-electrode setup depicted in **Figure 5.1**. The electrochemical derivation and activation always preceded the laser measurements.

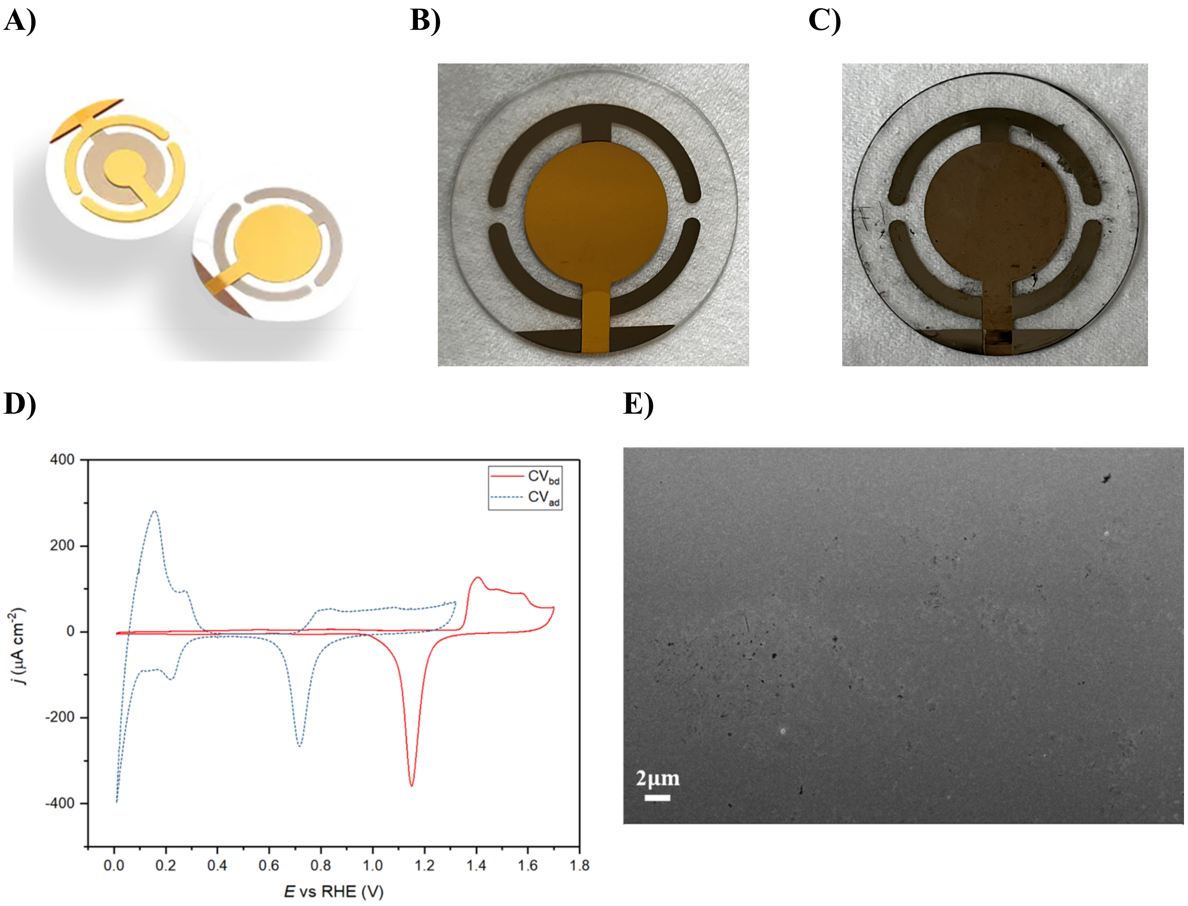

***Figure 5.2**. AT-cut EQCM electrode **A)** Au **B)** Electrochemically deposited Pd MLs on the Au electrode **C)** Atomic layer deposition deposited Pd MLs on the Au electrode **D)** Graphical illustration of the CVs of the Au QCM electrode before (red-labeled CV$_{bd}$) and after (blue-labeled CV$_{ad}$) the electrochemical deposition in 0.1 M H_2SO_4 and 0.1 mM H_2PdCl_4. The CVs were conducted in an Ar-saturated 0.1 M H_2SO_4 at a scan rate of 50 mV s^{-1}. **E)** Scanning electron microscope image showing the topology of the freshly electrochemically deposited Pd MLs on the Au electrode. Almost the entire surface is homogeneously covered with Pd MLs. The few dark spots represent the Au electrodes that were not adequately covered due to mechanical failure and other defects.*

For the Pd MLs deposited on the AT-cut quartz crystal wafer electrodes (polycrystalline Au with a diameter of 10 mm and a surface area of 1.37 cm^2, Stanford Research Systems, USA) by ALD methodology (*cf.* **Figure 5.2C**) or electrochemical means (*cf.* **Figure 5.2B**), electrochemical cleaning and CVs were performed in a broad potential window on both electrodes. For the latter, the electrochemical deposition was conducted in an electrolyte mixture of 0.1 M H_2SO_4 and 0.1 mM H_2PdCl_4 at a scan rate of 1 mV s^{-1} and within the potential range of 0.96 V to 0.25 V *vs*. RHE.[427,428,429,430,431] The CVs (*cf.* **Figure 5.2D**) of the Au QCM before and after the deposition prompt/indicate the success of the process. The CVs were performed in an Ar-saturated 0.1 M H_2SO_4 at a scan rate of 50 mV s^{-1}.[428,429,430,432] **Figure 5.2E** reaffirms that the CVs obtained from the as-received electrode and the electrochemical deposition were the Au and Pd MLs on the Au electrode, respectively. The morphology from the scanning electron microscope (SEM) micrograph (*cf.* **Figure 5.2E**) indicates that the Pd MLs are homogeneously distributed all over the surface of the Au electrode, with just a few dark spots occasioned by some defects or mechanical errors from the initial Au electrode.

Figure 5.3A portrays an example of the broad and narrow range CVs performed on the ALD-deposited Pd MLs on an Au QCM electrode in an Ar-saturated 0.1 M $HClO_4$ electrolyte. In this illustrated instance, a scan rate of 50 mV s^{-1} was used for both the narrow and broad potential windows. A maximum of 3 CV cycles were performed in the wide potential window, and *ca*. ten (10) CV cycles were conducted within the double layer range. Interestingly, the obtained results (*cf.* **Figure 5.3A**) concurred with the results from the literature.

One instance of the broad and narrow range CVs performed on the electrochemically deposited Pd MLs on an Au QCM electrode in an Ar-saturated 0.1 M KOH electrolyte is shown in **Figure 5.3B**. A lower scan rate of 10 mV s^{-1} was used for the narrow potential window, whereas a scan rate of 50 mV s^{-1} was used for the broad potential range. A maximum of 3 CV cycles were performed in the wide potential window, and *ca*. ten (10) CV cycles were conducted within the double layer range. The obtained results (*cf.* **Figure 5.3B**) matched the expectations from the literature.

The CVs following the attainment of a stable cycle during the electrochemical cleaning were performed in different electrolytes, namely, 0.01 M $HClO_4$, 0.1 M $HClO_4$, and 1 M $HClO_4$. These correspond to pHs of 2, 1, and 0, respectively. The broad-range CV was performed within the potential window of 0.06 V and 1.20 V *vs*. RHE, and only three cycles were done. Afterward, 10 CVs were performed in a narrow potential window (*i.e.*, the double-layer), from *ca*. 0.52 V to 0.72 V *vs*. RHE.

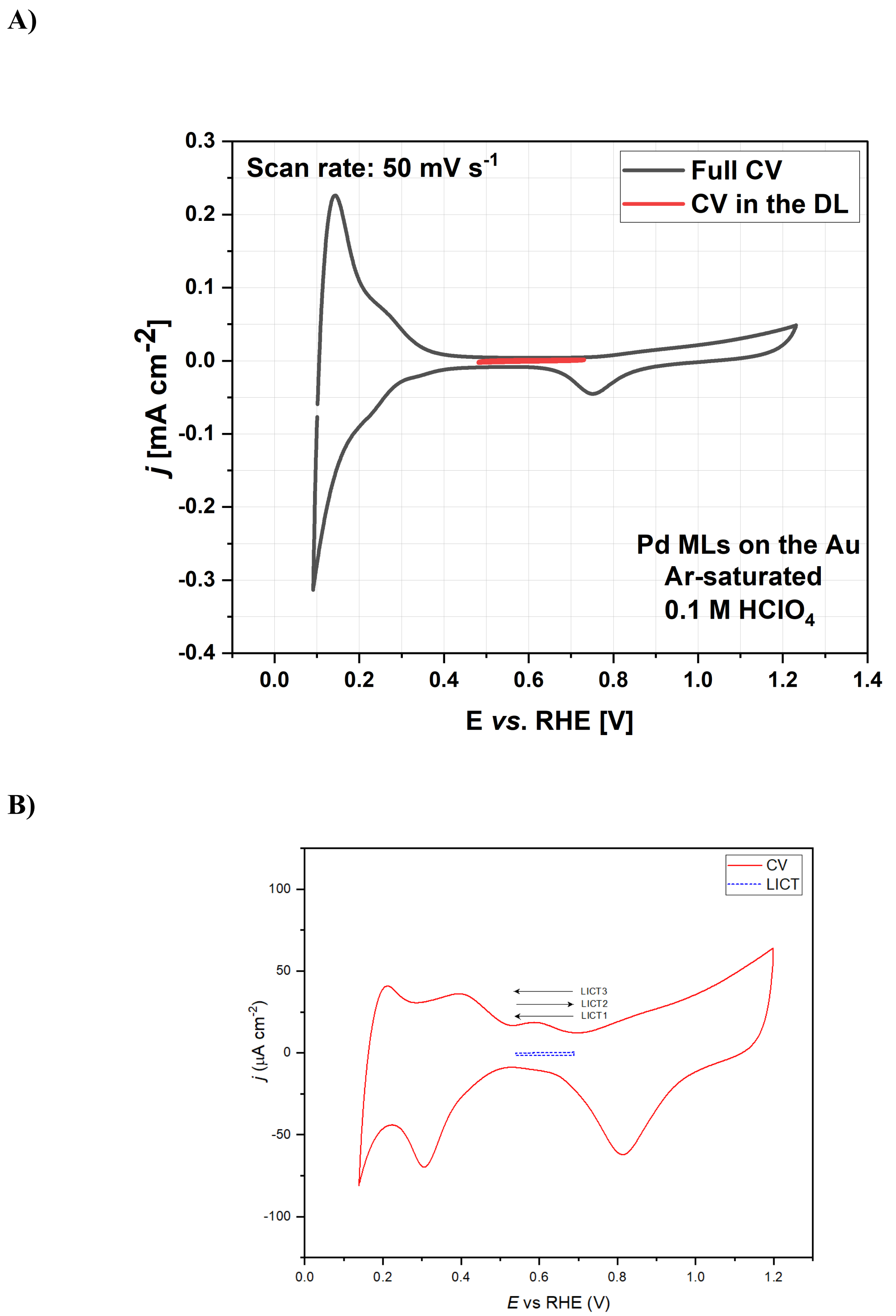

***Figure 5.3**. CV (cleaning and surface probing) obtained on the **A)** ALD Pd ML on the Au QCM electrode using Ar-saturated 0.1 M $HClO_4$ **B)** electrochemically deposited Pd ML on the Au QCM electrode using an Ar-saturated 0.1 M KOH. Only 3 CV cycles were performed at a scan rate of 50 mV s^{-1} for **A)** and **B)**. However, before the LICT, 10 CV cycles were done at a scan rate of **A)** 50 mV s^{-1} and **B)** 10 mV s^{-1}. The arrows indicate the direction of potential application for the laser measurements.*

The NiHCF thin films were synthesized *via* co-precipitating and applying an electrical contact using a slurry, comprising a mixture of the active and a conductive material, a polymeric binder, all as powders, and a volatile solvent, as a binder or adhesive. Before the LICT experiments, a cyclic voltammogram of *ca*. two (2) cycles in a broad potential window (-1 V to 0.8 V *vs*. SSC) was performed on the PBA (NiHCF thin film) electrode deposited on an original AT-cut quartz crystal wafer EQCM electrode (polycrystalline Ti-Au with a diameter of 10 mm and a surface area of 1.37 cm^2, Stanford Research Systems, USA). The few cycles warranted that the deposition would not degrade speedily. For each electrolyte, the same procedure was repeated. The electrolytes used in this case were $NaClO_4$, $NaNO_3$, NaCl, $NaCH_3COO$ (NaOAc), and Na_2SO_4.

5.2.2 Preparation of Electrolytes

In cleaning and subsequently performing the electrochemical measurements of the various working electrodes, different $HClO_4$ and H_2SO_4 electrolyte concentrations were prepared by diluting concentrated acid solutions with ultrapure water. In preparing the 0.5 M $(AM)_2SO_4$ (AM = Li^+, Na^+, K^+, Rb^+, and Cs^+) electrolyte solutions, corresponding salt powders (all 99.0%, Alfa Aesar) were dissolved with ultrapure water. To get the appropriate concentrations of the various 0.5 M $(AM)_2SO_4$ electrolytes, either H_2SO_4 or *AM*OH solutions (LiOH 99.995%, Alfa Aesar, NaOH 99.996%, Alfa Aesar, KOH 99.98%, Alfa Aesar, RbOH 99.995%, Alfa Aesar, CsOH 99.9%, Sigma Aldrich) was used to adjust the pH and monitored through a PHH222 portable pH meter (Omega) and later, Mettler Toledo FiveEasy pH meter F20.

In a separate experiment, *i.e.*, the SURMOF electrodes, 0.1 M *AM*OH (LiOH 99.995%, Alfar Aesar, NaOH 99.99%, Alfar Aesar, KOH 99.98%, Alfar Aesar, RbOH 99.995%, Alfa Aesar, and CsOH, 50 wt.% in H_2O, 99.9% trace, Sigma Aldrich) solutions were prepared by either dissolving the corresponding salt powders or diluting the solution.

To prepare the various concentrations (0.01 M, 0.1 M, and 1 M) or pHs (2, 1, and 0) of the perchloric acid (96% Suprapur™, or Extrapur™, Merck, Germany) used for the ALD deposited Pd MLs on the Au QCM electrode, the verified amounts of the stock concentrated acid solution were mixed with the corresponding amount of ultrapure water.

Finally, in preparing the 0.25 M $NaClO_4$, $NaNO_3$, NaCl, $NaCH_3COO$ (NaOAc), and Na_2SO_4 electrolyte solutions, the corresponding salt powders (all 99.0%, Alfa Aesar) were dissolved with the right volume of the ultrapure water.

Before the electrochemical measurements, the electrolytes were well-saturated with the suitable gas for at least 15 minutes. While performing the measurements, the chosen electrolyte was slowly purged with the appropriately selected gas.

5.2.3 Electrochemical Cleaning and CV Measurements

The polycrystalline Au QCM electrode (10 mm diameter and surface area: 1.37 cm^2) was electrochemically cleaned by submersing them into the 0.1 M H_2SO_4 electrolyte and cycling between 0.35 V-2.10 V *vs*. RHE at a scan rate of 50 mV s^{-1}. After getting stable CVs (see **Figure 5.4**), they were compared with the voltammograms accessible in the literature.

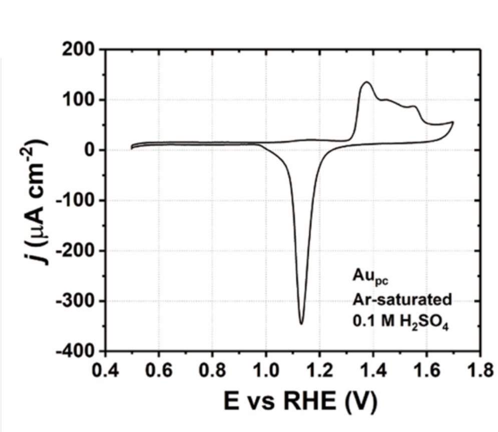

Figure 5 4. *Graphical representation of the stable cyclic voltammogram recorded using Au_{pc} QCM electrode and 0.1 M H_2SO_4 electrolyte following electrochemical cleaning of several cycles. Scan rate: 50 mV s^{-1}.*

The CVs obtained from the electrochemically deposited Pd MLs on the Au QCM electrode are shown in **Figure 5.5**. Relatively stable and consistent CVs before and after the LICT measurements are evident in all the used electrolytes.

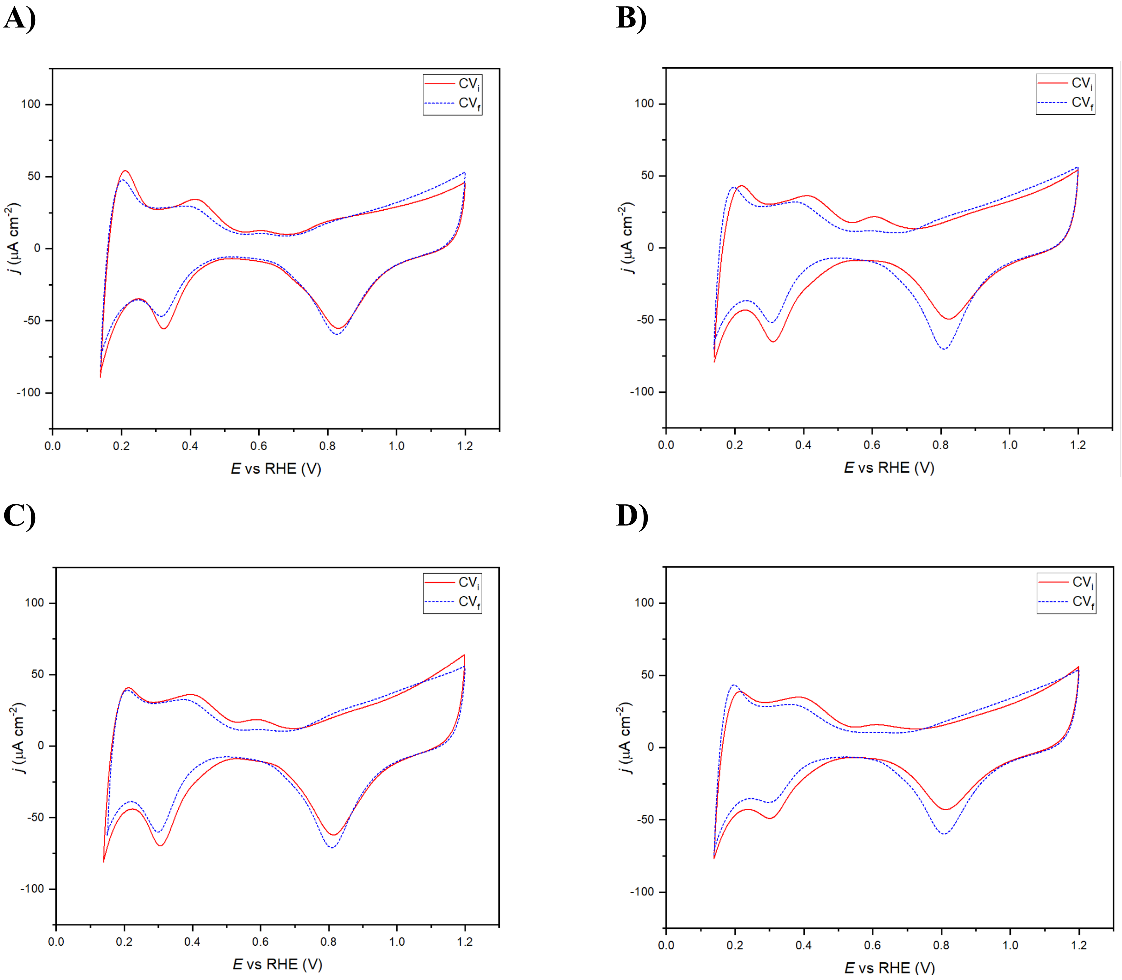

***Figure 5.5**. Various CVs performed on the electrochemically deposited Pd MLs on the Au EQCM electrode in Ar-saturated **A)** 0.1 M LiOH, **B)** 0.1 M NaOH, **C)** 0.1 M KOH, and **D)** 0.1 M CsOH. A scan rate of 50 mV s^{-1} was used for all the measurements. The red curve represents the starting or initial CV (CV$_i$) before the laser measurements, while the blue curve indicates the final CV (CV$_f$) or CV after the laser measurements.*

5.3 Laser-Induced Current Transient Technique Measurements

5.3.1 LICT Setup

Figure 5.6 depicts the setup deployed for the LICT investigations. Before the actual laser irradiation of the working electrode, the laser is warmed up for *ca*. 20 minutes, followed by testing the positioning of the working electrode using very low laser intensity and the controlled laser pulsing mode.

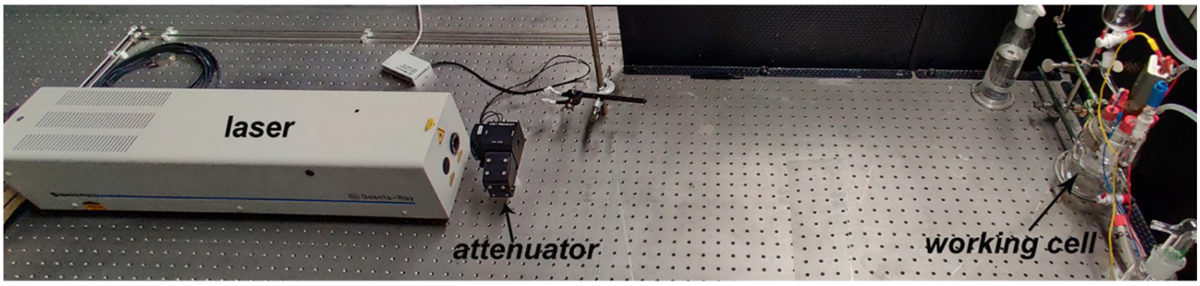

Figure 5.6. *Pictorial representation of the laser-induced current transient setup. The laser is depicted on the rear or furthest left part, with the attenuator placed a few centimeters away. The front or far right part is the position of the electrochemical cell, incorporating the three-electrode configuration. The working, counter, and reference electrodes are inserted at designated positions and connected to the potentiostat via clamps and wires. In detail, the WE is placed in the EQCM holder, and a clamp is inserted into the holder's head. The reference electrode is connected to the main cell, and by extension, the electrolyte via a Luggin capillary.*

5.3.2 LICT Measurements for the AT-cut Polycrystalline Au Quartz

Following the electrochemical cleaning, the polycrystalline Au electrodes were characterized at different pHs (2, 4, 6, 8, and 10) in Ar-saturated and O_2-saturated 0.5 M Na_2SO_4 and K_2SO_4 solutions with the LICT method. However, the laser beam energy was kept at *ca*. 20 mJ (32 mJ cm^{-2}) in this case. The potential ranges within which the LICT experiments were carried out slightly differ depending on the system under study. All the potential ranges during the LICT measurements for the Au_{pc} electrode system, the applied potential steps, and the electrolytes are listed in **Table 5.1**.

***Table 5.1**. Potential ranges and potential steps applied during the LICT measurements for the polycrystalline Au electrode.*

pH	Electrolyte	Potential range (V_{RHE})	Potential step (mV)
2	0.5 M Na_2SO_4, Ar-sat.	0.10 – 1.00	20
2	0.5 M Na_2SO_4, O_2-sat.	0.12 – 1.00	20
4	0.5 M Na_2SO_4, Ar-sat.	0.10 – 1.02	20
4	0.5 M Na_2SO_4, O_2-sat.	0.10 – 1.02	20
6	0.5 M Na_2SO_4, Ar-sat.	0.11 – 1.01	20
6	0.5 M Na_2SO_4, O_2-sat.	0.11 – 1.01	20
8	0.5 M Na_2SO_4, Ar-sat.	0.23 – 1.03	20
8	0.5 M Na_2SO_4, O_2-sat.	0.23 – 1.03	20
10	0.5 M Na_2SO_4, Ar-sat.	0.25 – 1.11	20
10	0.5 M Na_2SO_4, O_2-sat.	0.29 – 1.11	20
2	0.5 M K_2SO_4, Ar-sat.	0.08 – 1.12	20
2	0.5 M K_2SO_4, O_2-sat.	0.10 – 1.00	20
4	0.5 M K_2SO_4, Ar-sat.	0.10 – 1.10	20
4	0.5 M K_2SO_4, O_2-sat.	0.10 – 1.10	20
6	0.5 M K_2SO_4, Ar-sat.	0.61 – 1.37	20
6	0.5 M K_2SO_4, O_2-sat.	0.61 – 1.51	20
8	0.5 M K_2SO_4, Ar-sat.	0.39 – 1.45	20
8	0.5 M K_2SO_4, O_2-sat.	0.43 – 1.45	20
10	0.5 M K_2SO_4, Ar-sat.	0.40 – 1.50	20
10	0.5 M K_2SO_4, O_2-sat.	0.42 – 1.54	20
8	0.5 M Na_2SO_4+K_2SO_4, Ar-sat.	0.39 – 1.45	20
8	0.5 M Na_2SO_4+K_2SO_4, O_2-sat.	0.43 – 1.45	20

5.3.3 LICT Measurements for SURMOFs

A laser irradiation energy density of *ca*. 12.5 mJ cm^{-2} was applied to prevent electrode damage for all the investigated SURMOF systems. In this regard, the potential range was set between 0.81 V and 1.21 V *vs*. RHE. The LICT experiments were conducted potentiostatically with a potential step of 20 mV.

5.3.4 LICT Measurements for Pd MLs on Au EQCM

Under this section, two types of electrodes were utilized, all containing the deposition of Pd MLs on the AT-cut polycrystalline QCM Au electrodes. One of the depositions was performed using ALD, and the other was done electrochemically.

5.3.4.1 LICT Measurements for ALD deposited Pd MLs on Au QCM

The LICT measurements were performed at least three times within a similar vicinity (*i.e.*, double-layer region) as the narrow CV. Specifically, the first laser measurement was conducted from high to low applied potentials in the double-layer region. The potential step utilized for the laser measurements was 2 mV. This was followed by the performance of broad and narrow potential range CVs and the EIS measurements. Subsequently, further wide and narrow potential range CVs were conducted, and the second laser measurements followed suit. It must be mentioned that the second LICT measurements were performed in a reverse direction (from low to high double layer potentials) as compared to the first LICT measurements. The same procedure was followed, and the third laser measurements were eventually done. The third laser measurement followed the same direction as the first to ease comparison and predict reproducibility. In these scenarios, the laser power and beam energy were kept at *ca*. 140 mW and 14 mJ (corresponding to a fluence of 22 mJ cm^{-2}).

5.3.4.2 LICT Measurements for Electrochemically Deposited Pd MLs on Au QCM

An analogous measurement scheme was employed in this case, as presented in **section 5.3.4.1**. In detail, at least three laser measurements were conducted within the double-layer region at a potential step of 2 mV. Here, no EIS measurements were done, and hence, the first laser measurements were carried out after the 10-cycle CVs within the double-layer region. At the end of the laser measurements, the broad and narrow range CVs were reproduced to confirm or otherwise if the characteristic feature of the electrode was still intact. On this occasion, the laser power and beam energy were kept at *ca*. 140 mW and 14 mJ, respectively, corresponding to a fluence of 22 mJ cm^{-2}. An example of the LICT measurements obtained from this electrode using an Ar-saturated 0.1 M KOH is shown in **Figure 5.7**. In this instance, the PME was found to be *ca*. 0.65 V *vs*. RHE.

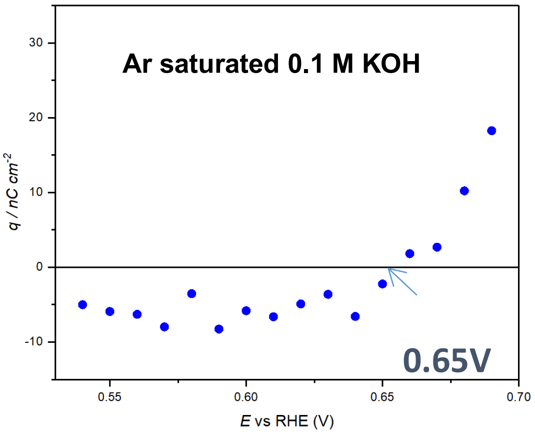

Figure 5.7*. An example of the LICT measurements performed on the electrochemically deposited Pd MLs on the Au QCM electrode in an Ar-saturated 0.1 M KOH electrolyte. The potential range used lies within the double-layer region, and the PME (signaled by the zero-charge crossing) was found to be 0.65 V vs. RHE, as depicted with the arrow.*

5.3.5 LICT Measurements for PBA Battery System Deposited on Au QCM

The LICT measurements using the battery Prussian Blue Analog electrodes deployed different anions and were investigated based on the degradation performance (from best to worst), as revealed in an earlier study. In this light, the order of the LICT experiments was 0.25 M $NaClO_4$, 0.25 M $NaNO_3$, 0.25 M NaCl, 0.25 M NaOAc, and 0.25 M Na_2SO_4. Before and after each set of LICT measurements, two (2) CV cycles were carried out. The CV measurements were conducted in the potential window 0.1 V-0.8 V *vs*. SSC at a scan rate of 50 mV s^{-1}. The potential range of -1.0 V to 0.8 V *vs*. SSC at 50 mV potential steps was used for the LICT measurements. The laser power and beam energy were kept at *ca*. 140 mW and 14 mJ, respectively, corresponding to a fluence of 22 mJ cm^{-2}.

5.4 Electrochemical Impedance Spectroscopy

Following the LICT measurements, a broad potential range CV was run on the system, and electrochemical impedance spectroscopy was performed. A capacitor was connected between the counter and reference electrodes to realize the EIS. The potential range deployed for the measurement was from 0.00 V to -0.30 V *vs*. MMS (double-layer region) in 10 mV potential steps.

5.5 Electron Paramagnetic Resonance Spectroscopy

5.5.1 Sample Preparation for the *In-Situ* EC-EPR Measurement

For the first cell design attempt, the cell components were assembled before performing the electrochemistry, *i.e.*, cyclic voltammetry. This was accomplished by properly inserting the quartz EPR tube into the Teflon main cell, followed by the various working and counter electrodes. Shortly thereafter, the reference compartment was assembled and connected to the main compartment through a capillary. The gas inlet and outlet parts were also connected using capillaries to complete the setup. The electrolyte was now introduced into the reference compartment under some pressure *via* a syringe such that the entire volume of the quartz EPR tube was filled with some remnant or additional electrolyte entering the Teflon main cell housing, mainly the counter electrode and the quartz EPR tube containing the electrolyte and working electrode. The commercially available mercury-mercurous sulfate reference electrode was then carefully introduced into the reference compartment, ensuring that the electrolyte remained in both compartments (main and reference). Gas (Argon - Ar) purging was initiated for *ca*. 15 minutes, ensuring saturation.

For the second cell (courtesy LIVEV ADANI, Belarus) attempt, the as-received electrode, namely, the working electrode (Pt), was placed in the quartz EPR capillary tube of outer diameter *ca*. 2 mm and inner diameter *ca*. 0.8 mm. Before introducing the counter and reference electrodes into the quartz EPR capillary tube, the tail end of the Ag wire (*ca*. 5-10 mm) was dipped for 30 seconds in a prepared mixture of $FeCl_3$ and H_2SO_4 solutions such that Ag/AgCl RE was produced. The remaining uncoated Ag parts served as the counter electrode, while the coated part was used as the reference electrode in the pseudo three (3) electrode system. The quartz EPR tube was now placed in its holder/protector, which also contained the connectors for the electrodes.

In the third cell design and construction attempt, a proper 3-electrode setup was built based on the setup employed in the second attempt. In the first trial, Pt wire was used as the working, counter, and reference electrodes. Following that, a Pd wire replaced Pt as the reference electrode in the second trial. In the final trial, Pd wire was initially used as the working electrode, with Pt serving as both reference and counter electrodes. With this configuration, Pd was charged by applying a potential in the hydrogen evolution reaction region to produce hydrogen in the bulk of Pd *via* absorption, thereby forming a PdH reference electrode. The PdH now served as the reference electrode, whereas Pt was utilized as both working and counter electrodes to implement the 3-electrode system in the EC-EPR measurements. It is essential to state that for the second and final trial, Pt wire was utilized as both the working and counter electrodes.

5.5.2 Electrochemical Investigations - Cyclic Voltammetry

All measurements are performed at room temperature. To realize the electrochemistry, cyclic voltammetry was performed in a wide potential range using VSP300 potentiostat (Biologic, France) first to ensure and ascertain the surface quality of the working electrode. Once this was achieved, the applied potentials were restricted to just the hydrogen underpotential deposition (H_{upd}) region (adsorption and desorption). Two different potentials were held for several minutes while simultaneously measuring the EPR response. The specifications used for the CV measurements were as follows: scan rate of 50 mV s^{-1} and later 200 mV s^{-1}.

5.5.3 Specifications of the Electron Paramagnetic Resonance Spectroscopy Device & *In-situ* EC-EPR Measurement

The used CW-EPR spectrometer is the SpinscanX from LINEV ADANI (Belarus). A modulation frequency of 100 kHz was kept for all described experiments. Other parameters are given specifically for each measurement. All measurements are performed at room temperature.

EPR spectra were recorded while holding both potentials (0.25 V and 0.30 V *vs*. PdH) in the H_{upd} region. Before this, the EPR spectrometer was tuned and retuned in case any sample modification was introduced in the cavity.

5.6 Design and Construction of the *In-situ* EC-EPR Cell

This section discusses the evolution of the experimental setup for the *in-situ* electrochemical EPR characterization of adsorbed hydrogen.

5.6.1 Discussion on the Design Evolution

Several approaches ranging from using flat cells to incorporating loop-gap resonators (LGRs) in the cavity in designing *in-situ* EC-EPR cells[433,434,435,436,437,438,439,440,441,442,443] are discussed in detail in this subsection. It has already been established that solvents of high relative permittivity (dielectric constant) non-resonantly absorb microwave radiations and eventually dampen the obtained signal. As a consequence of the significant dielectric losses at microwave frequencies, aqueous *in-situ* EC-EPR naturally demands the use of so-called flat cells or miniature sizes of quartz EPR tubes alongside specially designed cavity resonators capable of constraining the sample to a feasible extent away from the electric fields in the resonator.[444,445,446,447]

In this vein, Fielding, Dryfe, and coworkers[448] earlier developed and designed a functional EC-EPR cell for *in-situ* investigations of electrochemical systems (*cf.* **Figure 5.8A**). Subsequently, Wang *et al.*,[439,440,449] utilized the same EC-EPR cell design to *in-situ* study a variety of several materials, namely, activated carbon and graphene oxide. One outstanding feature in the investigations was the continuous use of aqueous electrolytes despite using different electrode types. For instance, using EPR spectroscopy, the electrochemical capacitance of activated carbon in aqueous electrolytes was *in-situ* monitored.[448] **Figure 5.8B** clearly depicts a schematic representation of the *in-situ* EPR cell design with activated carbon as the working electrode and Pt as the counter electrode, whereas silver-silver chloride (SSC - Ag|AgCl) was employed as the reference electrode. Of particular importance are the dimensions employed in the whole cell construction. These dimensions ((a) (supporting Pt wire (diameter

0.5 mm), WE; (b) GO membrane coated onto Pt wire, with a length of ~2 cm; (c) intertwined Pt wire (diameter 0.05 mm); (d) sealant epoxy, prevents the short circuit, not in the EPR detecting area; (e) RE, insulated Ag wire (diameter 0.2 mm, coated with PTFE) with one end oxidized; (f) insulated Ag wire (diameter 0.2 mm, coated with PTFE) to connect the WE and the potentiostat; (g) CE, Pt mesh; (h) quartz capillary (diameter 1 mm)) are similar to **Figure 5.8C**. It is evident that the reference electrode employed here was just a wire and not any recognized standard reference electrodes. Therefore, better control of the potential, in our opinion, is problematic.

In that respect, we envisage that there may be other problems associated with the cell design that must also be surmounted to achieve optimal electrochemical results. Some of these include significant Ohmic drops occasioned *via* the electrodes, specifically the working and reference electrodes, and even large capacitive currents, which limit the cell time constant.[441,442] These invariably lead to other challenges in EPR performance. For instance, deterioration of the resonator's quality factor (Q-value) can be triggered. Others include deterioration of the EPR sensitivity due to the interaction of the microwave electric field with the metal electrodes and the aqueous sample inside the resonator,[444] deterioration of the reproducible alignment of the electrochemical cell inside the resonator between experimental runs, and the inhomogeneity of the microwave magnetic field B_1 inside a cavity resonator.[443] Additionally, when flat cells (*cf.* **Figure 5.8E**) are utilized, they may be prone to convection during protracted electrolysis times,[450] resulting in distortion of both the electrochemical and EPR performance.

Based on the aforementioned cell designs and their predicted bottlenecks, a clear path to designing an ideal *in-situ* EC-EPR (*cf.* **Figure 5.8D**) was adopted following a rigorous search through various available research articles. The first implemented setup (*cf.* **Figure A1.1**) was only valuable for electrochemistry, but the EPR tuning and, by extension, the measurement proved futile. Following the apparent drawbacks of the initial setup, a different approach was adopted to address the challenge. Tamski *et al.*[435] revealed in their studies that accurate potential electrochemistry control can be achieved using micro-wires as working electrodes, especially for EPR investigations involving the electrochemical generation or consumption of radical species in aqueous samples.[451] The authors also opined that developing a loop-gap resonator (LGR) in conjunction with micro-wires could be a worthy substitute for the usual resonant cavities for energy dissipative samples. LGR basically confines the electric fields in gaps such that the understudy species will cover most areas of the EPR cavity to absorb the microwave with the magnetic fields resonantly.

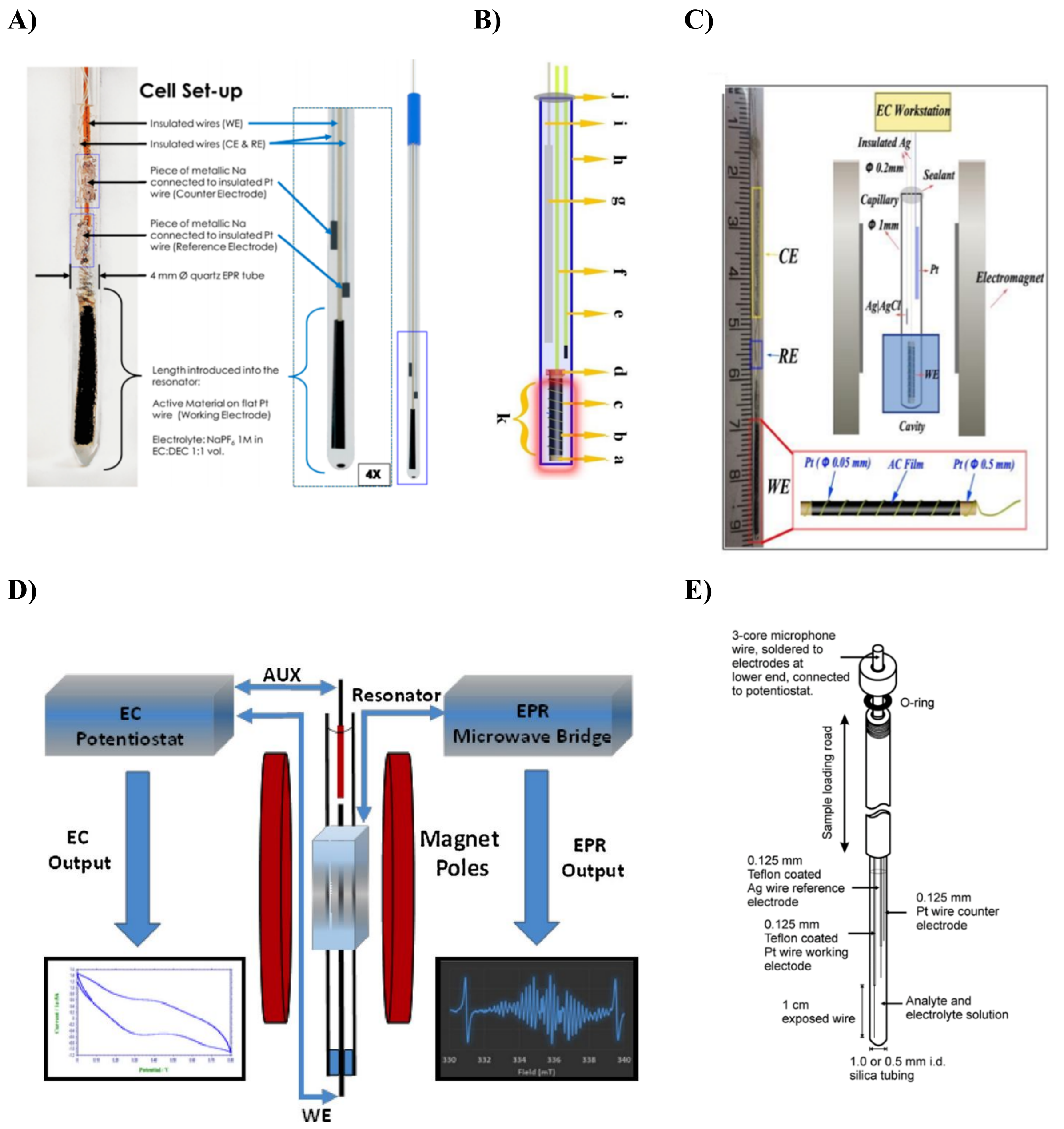

***Figure 5.8**. **A)** A pictorial (left) and schematic (right) representation of the in-situ electrochemical cell employed by reference in their investigation. Adapted from reference.[448] Copyright © (2022), American Chemical Society. **B)** Schematic representation of the in-situ EPR cell comprising a three-electrode configuration in the EPR capillary. Labeled a to k are: (a) Supporting Pt wire (diameter 0.5 mm); (b) WE, GO membrane coated onto Pt wire, with a length of ~2 cm; (c) intertwined Pt wire (diameter 0.05 mm); (d) sealant epoxy, prevents the short circuit, not in the EPR detecting area; (e) RE, insulated Ag wire (diameter 0.2 mm, coated with PTFE) with one end oxidized; (f) insulated Ag wire (diameter 0.2 mm, coated with PTFE) to connect the WE and the potentiostat; (g) CE, Pt mesh; (h) quartz capillary (diameter 1 mm); (i) aqueous electrolytes, e.g., Na_2SO_4/KOH; (j) sealant epoxy; (k) in-situ cell introduced into the EPR cavity. Adapted from reference.[449] Copyright © (2018), Royal Society of Chemistry. **C)** Schematic depiction of the in-situ EPR cell design used by reference[439] with a three-electrode configuration. Activated Carbon, Pt, and Ag|AgCl were the working, counter, and reference electrodes. Reprinted from reference.[439] Copyright © (2022), American Chemical Society. **D)** Schematic illustration of the entire EC-EPR cell design and*

construction as implemented by reference.[437] Reproduced with permission from reference.[437] Copyright © (2015), Elsevier. All rights reserved. ***E)*** *A schematic example of typical EC-EPR cell designs implemented for use in Q- and W-band EPR range as reported by reference.[451] Adapted from reference.[451] Copyright © (2011), Elsevier. All rights reserved.*

The advent of the LGR occurred in 1982 when W. Froncisz and J. S. Hyde published such a development in their paper.[452] For a while, LGR applied mainly for EPR purposes was employed for EC-EPR by Allendoerfer *et al.*,[453] allowing aqueous samples to be investigated with 50 to 100 times larger absolute sensitivities compared to other resonator-EC-EPR cell (*e.g.*, TE_{011}) combinations at the time (*cf.* **Figure 5.9C**). The constructed LGR (*cf.* **Figure 5.9A**) improves the research work of Allendoerfer *et al.*[453] The *in-situ* EC-EPR cell designed to fit in an LGR is portrayed in **Figure 5.9B**. The intriguing breakthrough worth highlighting is the extremely small dimensions used to implement the cell successfully.

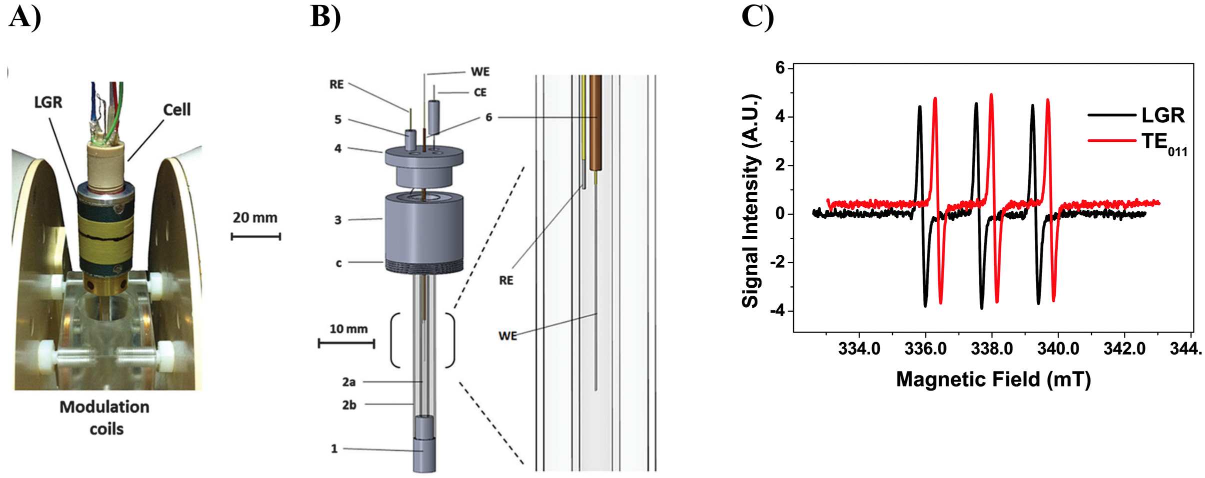

Figure 5.9*. **A)** Pictorial representation of the interior of the EPR device, particularly highlighting the LGR attached to the constructed EC-EPR cell. **B)** The EC-EPR cell specifically developed to fit into the LGR. Labeled 1 to 6 are: 1, 3 - capillary supports, 2a - EPR sample tube specifically for use in the Q-band regime, 2b - X-band EPR tube for structural support, 4 - an adaptor for electrodes and sample flow, 5 - pegs for electrode attachment, 6 - capillary aiding the insertion of the working electrode to the resonator's sensitive part. WE, CE, and RE stand for working, counter, and reference electrodes, respectively. **C)** The output signal intensity plotted as a function of the magnetic field. Enhanced EPR signal sensitivity is realized using the LGR relative to the typical* TE_{011} *resonator used in most resonator cavities. Reproduced from reference[435] with permission from the Royal Society of Chemistry. Copyright © (2015), Royal Society of Chemistry.*

The main challenge the use of an LGR addresses lies in the ideal confinement of the microwave electric field in the gaps of the resonator, thereby allowing the aqueous or other dielectrically lossy samples to occupy a larger volume relative to the resonator's size. Thus, the role of the LGR is to concentrate the B_1 field in the sample and make the signal produced by the change in magnetic susceptibility at resonance as large as possible. In effect, the use of LGR is particularly applicable to samples of limited volume, such as the concentration of short-lived radical species in the diffusion field during an electrochemical experiment. Therefore, a satisfactory EPR performance is achieved in aqueous media, especially when the sample volume is of the order of microliters.[454] Moreover, owing to the tiny size of the resonator, a large filling factor in the LGR is guaranteed. Therefore, the optimization of the electrochemistry is realized in miniaturized dimensions. On the contrary, the larger the inner diameter of the sample tube is, the closer the sample is to the fringing electric fields in the gaps of the LGR, leading to an increasing dielectric microwave loss.

Since our EPR device had electromagnets enclosed within a compact surrounding, implementing the LGR was impossible, leading to a boycott of the idea. The next solution dwelled on an industrial-related approach from the manufacturer of our EPR device (LINEV ADANI, Belarus). The main identified issue to correct was to employ a smaller diameter of the EPR tube, *ca*. 2 mm outer diameter or even less with an inner diameter of about 0.8 to 0.9 mm (see **Figure 5.10A**). This measure means the water/electrolyte volume in the EPR tube will be in the microliter range. It thus prevents, to a greater extent, the dampening of the EPR signal because of the high dielectric constant of the electrolyte (mainly water).

The next one involves using smaller diameters of electrode materials, etc., to avoid large Ohmic drops, and so on. The LINEV ADANI *in-situ* EC-EPR cell setup, which was implemented, encompassed solutions to almost all the identified drawbacks. A pictorial representation of the already inserted electrodes (WE, CE, and RE) can be seen in **Figure 5.10B**. Approximately 2-10 mm distance between the two electrodes (WE and RE) is essential to ensure that only the working electrode is within the resonator area of the EPR spectrometer. This minimum separation also minimizes the high ohmic drop between the reference and working electrodes. A Teflon tube holder is introduced to guarantee that a length of 95 mm is established between the upper part of the Teflon tube holder and the sample center within the quartz EPR tube. This further ensures that at least 10 mm of the working electrode's length lies inside the resonator area (*cf.* **Figure 5.10B**).

The assembled cell in **Figure 5.10B** is placed in the EPR spectrometer (**Figure 5.10C**), tightened, and connected initially with the connecting pins (*cf.* **Figure 5.10D**). Eventually, it is connected to the potentiostat (**Figure 5.10E**). It is essential to note that a 2-electrode or a pseudo-3-electrode system is employed by the LINEV ADANI setup, even though there is a clear intention to implement a 3-electrode cell configuration. This system is seen in the dipping of the tail end of the Ag wire into the prepared mixture of $FeCl_3$ solution and H_2SO_4 solution for close to 30 seconds, generating Ag/AgCl reference electrode. The CV obtained with the configuration described in **Figure 5.10** was not ideal. However, the EPR spectrometer was tunable. Due to specific defects, the EPR signals showed no significant differences or changes when the potentials were held at several spots in the H_{upd} for adsorption and desorption charges.

The major drawback of the above configuration was that a 2-electrode setup (or a pseudo-3-electrode configuration) was used, making it non-ideal for measurements, especially controlling the potential. Essentially, the counter and reference electrodes were implemented on the same electrode material, which could be better. The Ag, the counter electrode, was oxidized (always deposited on the working electrode), forming dark spots at the edge of the WE and the RE/CE. In other words, the CE was oxidized during the electrochemistry. This devastatingly affected the EPR measurements and may be an additional basis for the observed non-distinguishable EPR signals.

To solve this shortcoming, a proper 3-electrode setup was implemented in the *ca*. 2 mm outer diameter EPR tube. This was realized by insulating almost the entire length, leaving just 5 mm of the RE bare with an insulating spray, Plastic 70 (Kontakt Chemie), and later 3M Scotch® 1601. This was necessary to prevent possible short-circuiting within the quartz EPR tube or the resonator cavity. Initially, Pt was used as the working, counter, and reference electrodes (**Figure 5.11A**). The CV features did not reveal much activity in the hydrogen underpotential deposition region, and the currents produced were extremely negligible, partly due to the low scan rate of 50 mV s^{-1} that was used. Therefore, further improvement was necessary. Hence, in subsequent experiments, Pd instead served as RE, with Pt acting as both the counter and the working electrodes (**Figure 5.11B**). The CV was now relatively stable and exhibited tremendous enhancement in the H_{upd} region and the current values. However, the challenge was the robustness, capacity, and duration of the insulated spray's degradation (wearing off /detachment) on the RE. Based on the possible detachment of the insulation spray and other factors, the EPR signals were again indistinguishable. In effect, it was not easy to clearly establish the generation of radicals.

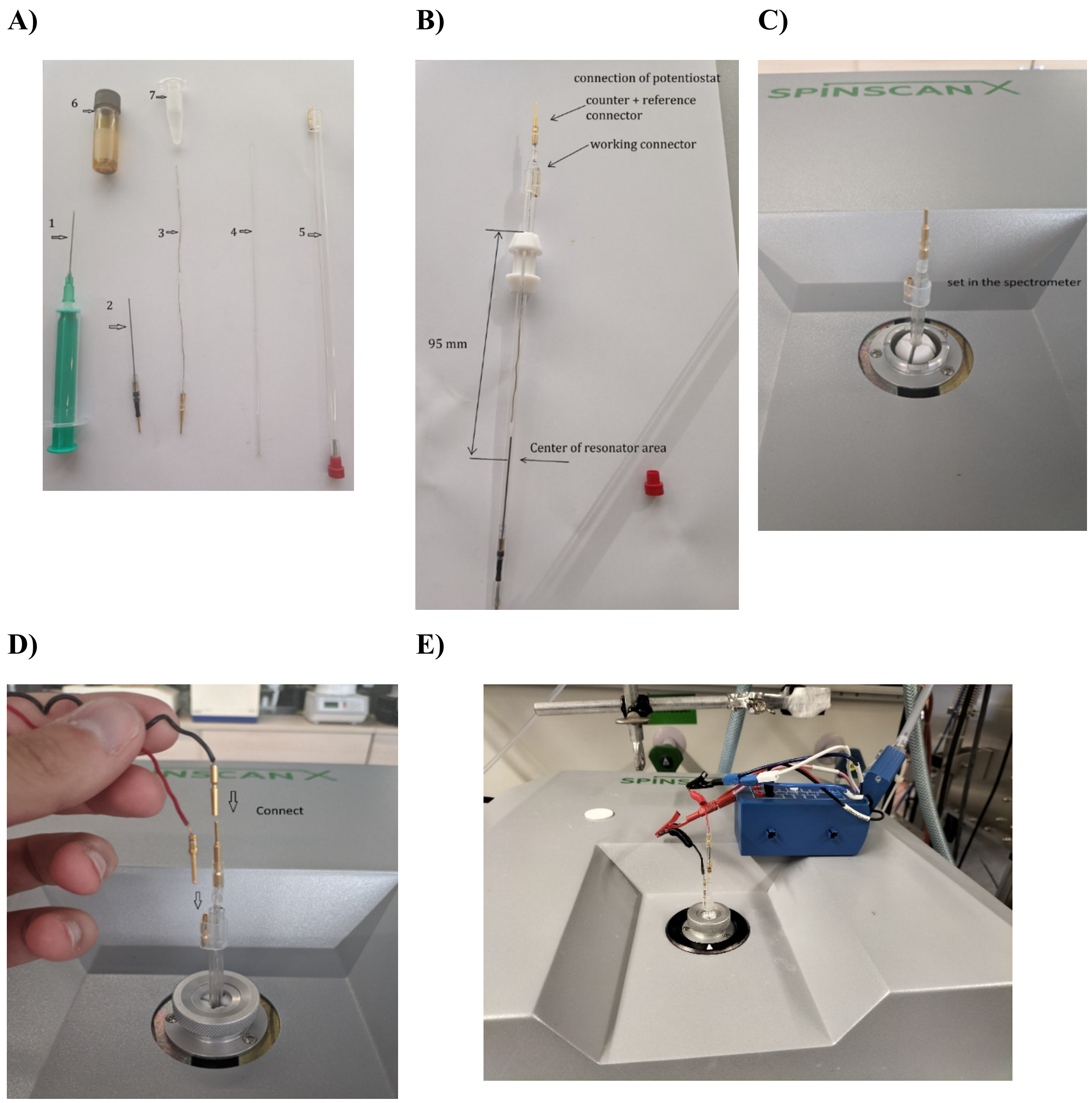

***Figure 5.10**. **A)** The in-situ EC-EPR cell components as-received from LINEV ADANI. Labeled 1 is the syringe, 2 - represents the working electrode, graphite in this case, 3 - is the counter/reference electrode; the tail end of the Ag wire has been coated with a mixture of $FeCl_3$ and H_2SO_4 to produce Ag/AgCl as the reference electrode, and the uncoated Ag parts represent the counter electrode, 4 - quartz EPR capillary tube of outer diameter 2 mm, inner diameter ca. 0.8-0.9 mm, 5 - tube holder/protector for the quartz EPR capillary tube, 6 - $FeCl_3$ solution, and 7 - ketoconazole solution in H_2SO_4. **B)** Pictorial depiction of the electrodes placed in the quartz EPR capillary tube. Particularly interesting is the display of the region where the center of the resonator is marked. **C)** Fully assembled EC-EPR cell **D)** The fully assembled EC-EPR cell in contact with their respective connecting pins. **E)** The connecting pins linked to the potentiostat.*

Before properly starting the *in-situ* EC-EPR measurements, a CV was performed in the hydrogen evolution reaction region in a 0.1 M $HClO_4$ open-air atmosphere to ensure enough hydrogen was produced using Pd as the WE. This was checked and realized whenever the current produced was *ca*. -1.0 mA and beyond, with bubbles observed on the WE (**Figure 5.11C**). During this process, Pt acts as both CE and RE. As a further check, the current is held at -1.0 mA for 5 minutes (*cf.* **Figure 5.11D**) to ensure that the Pd is charged/loaded with sufficient H to form PdH, which now serves as the RE. This newly produced RE is close to the RHE (*ca*. 50-150 mV deviation) scale and is also stable for prolonged measurement duration.

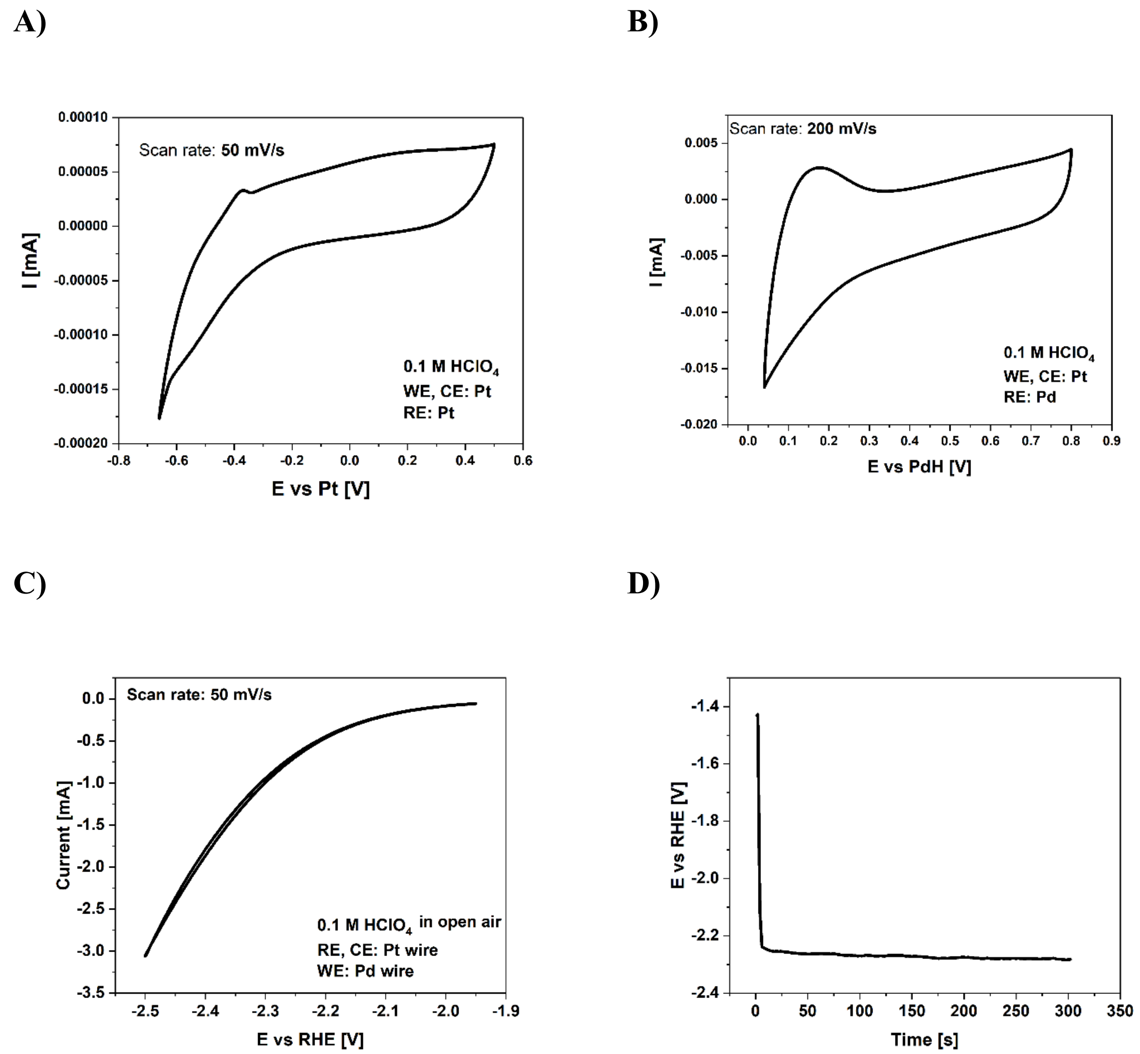

***Figure 5.11**. **A)** Cyclic voltammogram of Pt working electrode with Pt as CE and RE in an argon-saturated 0.1 M $HClO_4$ at a scan rate of 50 mV s^{-1}. **B)** CV implemented on Pt WE and CE with Pd as the RE in an argon-saturated 0.1 M $HClO_4$ at a scan rate of 200 mV s^{-1}. **C)** Graphical illustration of the hydrogen evolution reaction region performed using Pd as the working electrode and Pt as both counter and reference electrodes in 0.1 M $HClO_4$ in an open-air environment. **D)** Current held at -1 mA in the HER region for 300 seconds to further cause hydrogen adsorption in the bulk of Pd to produce a PdH reference electrode.*

6.0 Results & Discussions

It has been revealed from the previous chapters that a basic appreciation of the processes transpiring at the electrode/electrolyte interface is a prerequisite to developing highly efficient electrocatalytic performance successfully. The performance of a specific electrocatalytic reaction is primarily deemed to rely starkly on the composition and structure of the electrode surface.[455,456] However, the electrolyte composition tremendously influences electrocatalytic processes when considering aqueous electrolytes.[457,458] In this aspect, the degree of order of the electric double layer is regarded as a critical consideration underpinning the control of the interface structure and activity and, by extension, the electrocatalytic processes.[310] As the interfacial water layer structure becomes more ordered, extra energy is required to rearrange the water dipoles at the interface after the electron transfer. The process should be effortlessly executed at the potential of maximum entropy, at which the interfacial water molecules have the maximal disorder and hence relatively eases the movement of reactant species. Consequently, it is expected that the closer the PME is to the thermodynamic equilibrium potential of a specific reaction, the faster that reaction should be.

This chapter is subdivided into several sections, dealing extensively with interface structure, electrode activity, and cation and pH effects on the Au, SURMOFs, and Pd PMLs on the Au QCM electrodes. As such, the experimental results using polycrystalline Au electrodes in various electrolytes are discussed in the following. Specifically, the effect of the pH value in an acidic solution was analyzed, which led to examining the influence of alkali metal cations in the electrolyte. The well-known hydrogen evolution and oxygen reduction reactions, selected as model reactions, were investigated. The obtained results of the laser-induced current transient measurements were associated with the HER and ORR activity data measured in the corresponding systems. The results suggest that determining the PME with the LICT method can be a valuable way to evaluate and investigate the influence of the electrolyte composition on the electrocatalytic processes at the electrode/electrolyte interface. More so, electrochemical impedance spectroscopy was conducted to reveal the minimum double-layer capacitance on the Pd ML on the Au QCM electrode. The impact of anions using the Prussian Blue Analog battery systems is highlighted in another section. The final section centers on revealing the pathway of the electrochemical reaction under investigation by employing combined EPR and electrochemical techniques. Parts of the results section were performed alongside a few colleagues (Dr. Xing Ding, Dr. Shujin Hou, and Emre Keles) and are, therefore, duly acknowledged.

6.1 Interface Structure and pH Effect

In detail, this set of experiments was conducted on the Au_{pc} electrodes to explore the pH effect on the EDL properties at the electrode/electrolyte interface. The corresponding CV measurements are displayed in **Figure 6.1**. The typical anodic peaks between approximately 1.3-1.6 V_{RHE} and a sharp reduction peak at *ca*. 1.1 V_{RHE} are all noticeable. The surveyed CV features are consistent with those published in the literature.[459] When comparing the peak areas of the oxidation and reduction processes on the Au_{pc}, they are promoted in the electrolyte containing a higher concentration of H^+ ions. Notably, the shape and, most importantly, the features of the CV remained invariable even after the laser measurements.

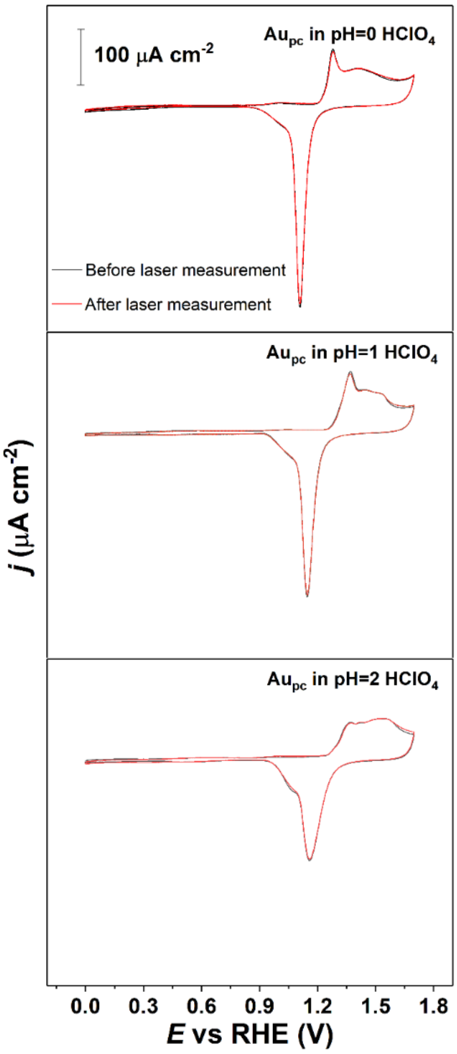

Figure 6.1. *Typical cyclic voltammograms of Au_{pc} measured at different pH values (0, 1, and 2) of the $HClO_4$ electrolytes. Scan rate: 50 mV s^{-1}. It is important to note that the CVs before and after the LICT measurements are almost indistinguishable. Reproduced from reference.*[161]

Mockup current transients acquired for the Au$_{pc}$ electrode are shown in **Figure 6.2**. The positive and negative current transients for the Au$_{pc}$ electrode are evident.

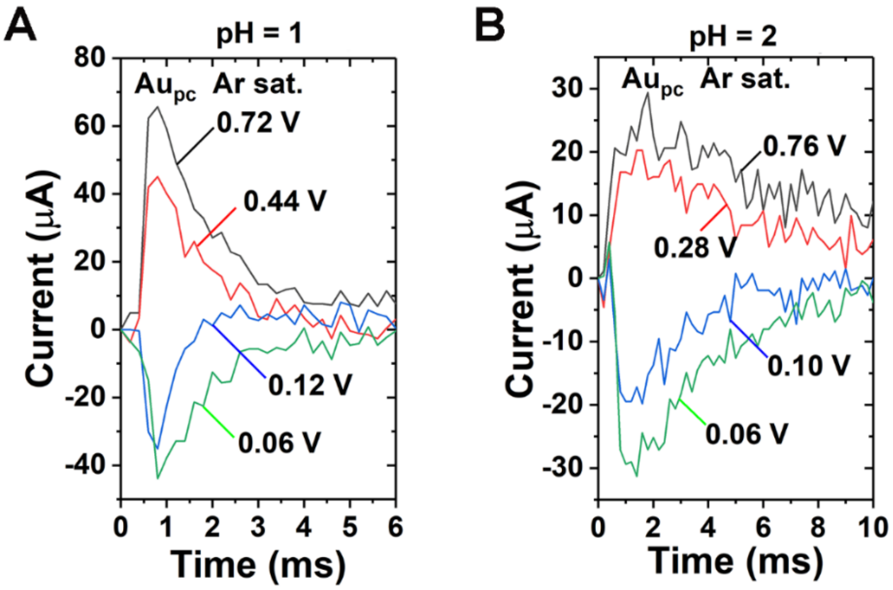

***Figure 6.2**. Model LICTs measured for Au$_{pc}$ in an Ar-saturated $HClO_4$ at **A)** pH 1 and **B)** pH 2. It should be noted that all initial current values of the obtained transient peaks have been normalized to zero to ease comparison. The PME is located between the two potentials where the sign of the current transient varies. Reproduced from reference.*[161]

The PME values of the Au$_{pc}$ electrode are ~0.07 V, ~0.13 V, ~0.20 V, ~0.27 V, and ~0.32 V *vs*. RHE at pHs of 0, 0.5, 1.0, 1.5, and 2.0, respectively, for $HClO_4$ electrolytes as shown in **Figures 6.3A** to **E**. Interestingly, the PME of the Au$_{pc}$ electrode displays a linear dependence on the pH value of the electrolyte (*cf*. **Figure 6.3F**). The assembled results are equivalent to previous literature data.[459,460] It is worth mentioning that the PME does not shift by *ca*. 59 mV per pH unit on the RHE scale when the PME lies within the double-layer potential region. That could be attributed to the reconstruction of the gold surface, which influences the location of the PME.[343]

Specifically, the PME of the Au$_{pc}$ drifts away from the onset potential of the HER towards the potential where the ORR takes place. An increase in pH makes the surface water layer at potentials close to the onset of the HER stiffer. Conversely, the order of the EDL decreases at potentials close to the ORR onset. Accordingly, it can be deduced that as the pH value rises, the activity of the Au$_{pc}$ electrode decreases towards the HER and increases towards the ORR.

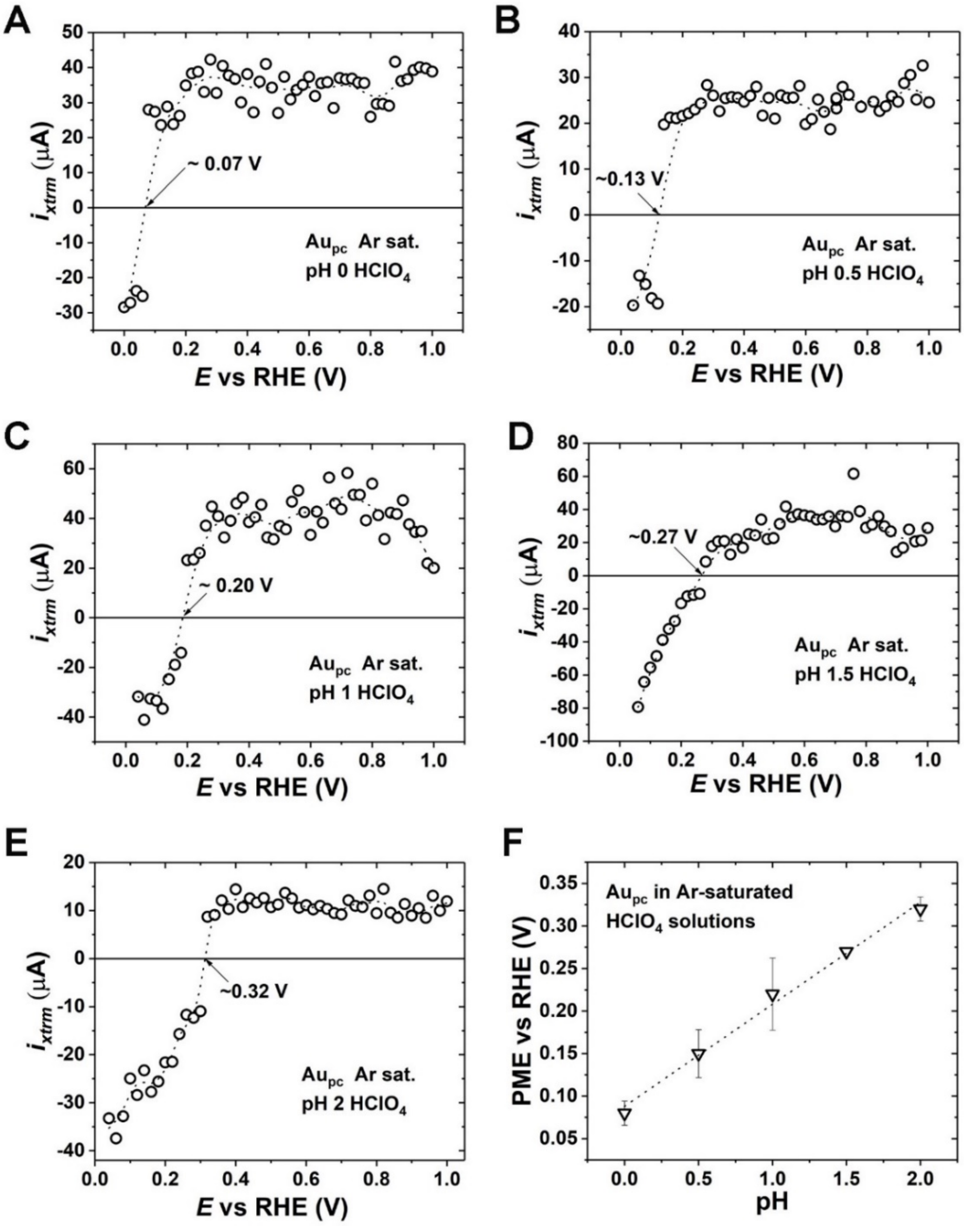

***Figure 6.3**. (**A** to **E**) Current extrema of the LICT results attained for the Au$_{pc}$ electrode at different pH values (0, 0.5, 1.0, 1.5, and 2.0) of Ar-saturated HClO$_4$ electrolytes. **F)** The PME of Au$_{pc}$ plotted as a function of the electrolyte pH. The PME of Au$_{pc}$ shifts towards more positive values because of the pH rise. Reproduced from reference. [161]*

To buttress these projections, measurements of the Au$_{pc}$ activity towards the HER and ORR were performed at several pH values (0, 1.0, and 2.0) of H$_2$-saturated (HER) or O$_2$-saturated (ORR) HClO$_4$ electrolytes (*cf.* **Figures 6.4A** and **B)**. Remarkably, the activity towards the HER increases at high H$^+$ electrolyte concentrations. By contrast, lower H$^+$ electrolyte concentrations enhance the activity towards the ORR. The HER activities (expressed as the exchange current density) of the Au_{pc} electrode portray a linear relationship with the PME values (*cf.* **Figure 6.4C**).

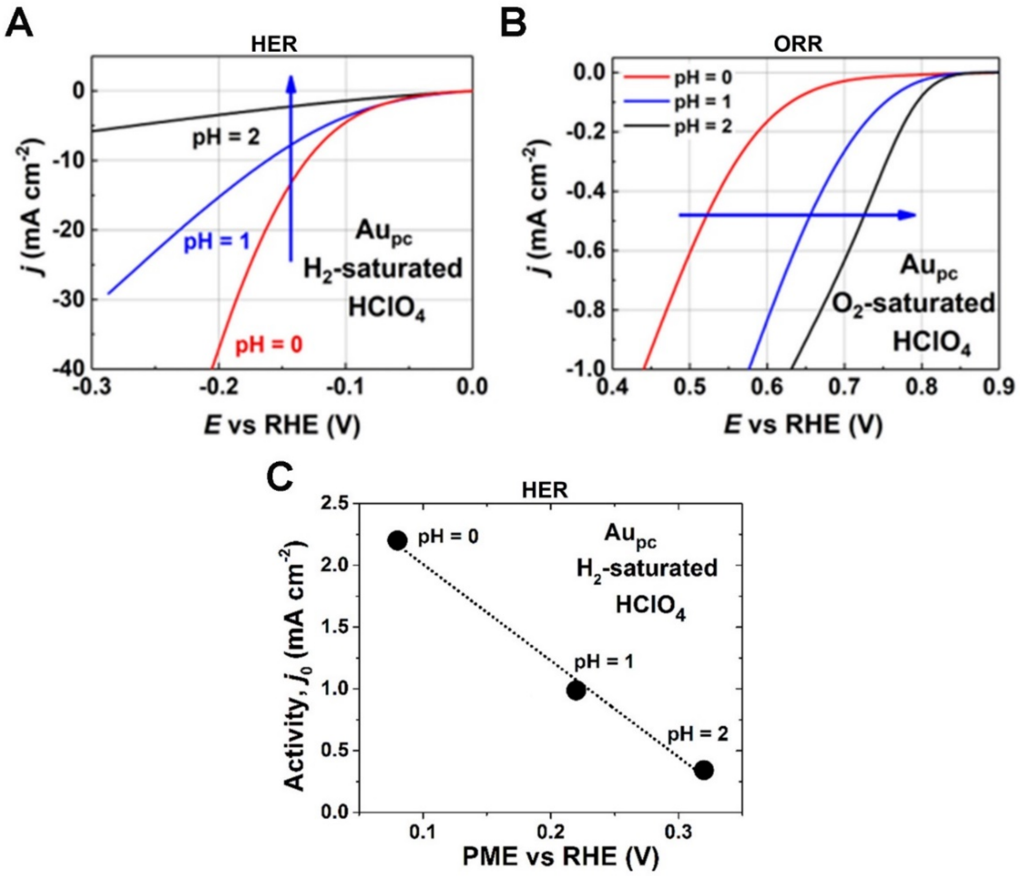

***Figure 6.4**. Characteristic **A)** HER and **B)** ORR polarization curves for Au_{pc} electrodes recorded at several pH values (0, 1.0, and 2.0) of H_2-saturated or O_2-saturated $HClO_4$ electrolytes. To augment the visibility, only the region dominated by the four-electron ORR kinetics is shown in **B)**. **C)** The HER activities of Au_{pc}, expressed as the exchange current density j_0, plotted as a function of the PME. A linear trend is observed between the PME and activity. Reproduced from reference.*[161]

6.2 pH Effect in the Presence of Alkali Metal Cations

The previous section significantly revealed that the pH effect of the PME on the electrocatalytic activity is substantial. Outstandingly, the impact of pH can be entirely different for assorted electrolyte compositions.[461,462] Several studies have established that electrocatalytic properties can be influenced by both H^+ and other ions in the electrolyte.[463,464,465] Recently, there has been an influx of research centered on the effect of alkali metal cations.[462,464] In a recent account, our group established the influence of the alkali metal cations on the EDL capacitance of several single-crystal electrodes.[466,467] Despite all these exciting developments, there is a need for a complete understanding of the alkali metal cations' effect on electrocatalytic processes. In this vein, a series of LICT measurements for the Au_{pc} electrode was performed to investigate further the effect of pH and electrolyte ions on the interfacial processes. These were conducted at various pHs (2, 4, 6, 8, and 10) in Ar-saturated and O_2-saturated 0.5 M Na_2SO_4 and K_2SO_4 electrolytes. It is significant to mention that since the hydration energies of the Na^+ (406 kJ mol^{-1}) and K^+ (322 kJ mol^{-1}) cations are much closer to that of the ClO_4^- (229 kJ mol^{-1}) anions, the SO_4^{2-} anions with higher hydration energy (1059 kJ mol^{-1}) were preferred since it helped to circumvent competition for the influence of other species in the electrolyte. In this regard, any variation in the interfacial properties would only correlate to the modifications in the H^+ concentration and the nature of the alkali metal cations in the investigated systems.

In executing the experiments, CVs of the Au_{pc} electrode were recorded in Ar-saturated 0.5 M Na_2SO_4 and K_2SO_4 electrolytes at different pHs to validate the surface quality of the electrode, as shown in **Figure 6.5**. Intriguingly*,* CVs of the Au_{pc} electrode in Na^+- and K^+-containing electrolytes at pH 2 are comparable with the results measured in 0.1 M H_2SO_4 solution (*cf.* **Figure 5.4**). The usual three distinctive anodic peaks between *ca.* 1.3 V-1.6 V_{RHE} and a sharp reduction peak at *ca.* 1.1 V_{RHE} are evident. Upon increasing the electrolytes' pH, both the oxidation and reduction processes on the Au_{pc} surface were influenced by both Na_2SO_4 and K_2SO_4 electrolytes. This influence was exceptionally noticed when the electrolyte pH reached 6. Two broad reduction peaks are observed for Na^+-containing electrolytes, and three reduction peaks in the presence of K^+ are visible within the investigated potential range. This could be attributed to the local protons at the interface having a low concentration in a nearly neutral pH electrolyte. Consequently, the generated and consumed protons during the oxidation and reduction processes on the Au_{pc} surface can easily alter the local pH. A typical example occurs during the O_2 electroreduction process, where the protons at the interface can be instantaneously consumed in a nearly neutral pH electrolyte, resulting in a lower reduction potential of Au oxide.[468,469,470]

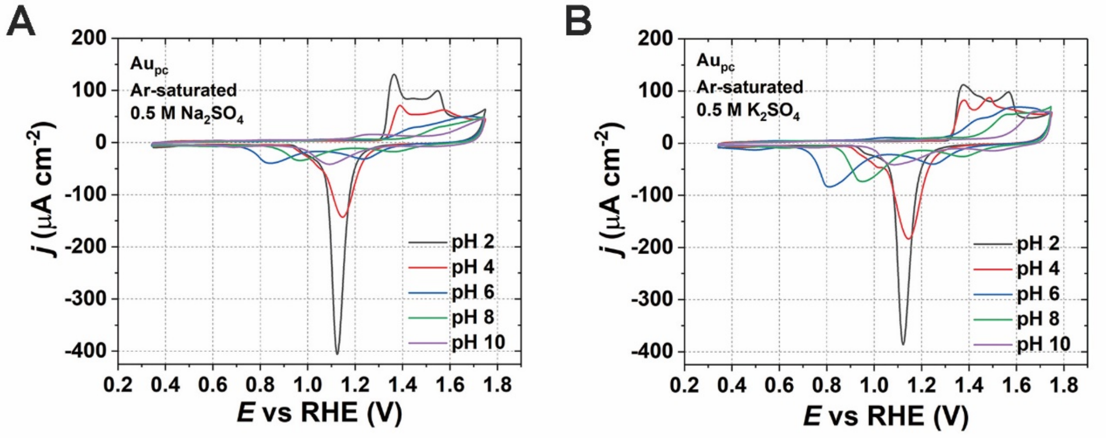

Figure 6.5. *Representative cyclic voltammograms of Au$_{pc}$ at various pHs (2, 4, 6, 8, and 10) in 0.5 M Ar-saturated **A)** Na$_2$SO$_4$ and **B)** K$_2$SO$_4$ electrolytes. The scan rate used was 50 mV s^{-1}. Reproduced with permission from reference.* [130,161] *Copyright © (2021), The Authors. Published by Wiley-VCH GmbH. Open access, published under a CC-BY license.*

When considering the same pH as a reference point, the influence of alkali metal cations on the Au$_{pc}$ electrode processes can be further observed. One typical example witnessed at pH = 6 is shown in **Figure 6.6**. K$^+$ cations promote the oxidation of Au, which is evident from the increased peak areas when compared to Na$^+$.

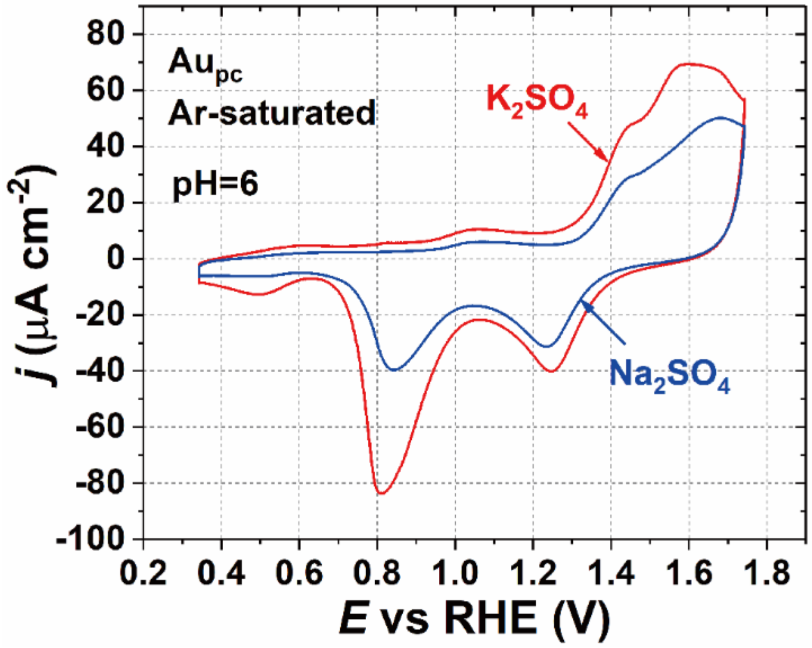

Figure 6.6. *Examples of cyclic voltammograms of the Au$_{pc}$ electrode in 0.5 M Ar-saturated Na$_2$SO$_4$ (blue) and K$_2$SO$_4$ (red) electrolytes at pH 6. Scan rate: 50 mV s^{-1}. Reproduced with permission from*

reference.[130,161] *Copyright © (2021), The Authors. Published by Wiley-VCH GmbH. Open access, published under a CC-BY license.*

CV measurements at different scan rates were conducted in 0.5 M K_2SO_4 solution as a supplement. **Figure 6.7** demonstrates that all the oxidation and reduction peaks increase with an increase in the scan rate quasi-linearly. Accordingly, the adsorbed species at the electrode surface likely dominate the observed oxidation and reduction processes.

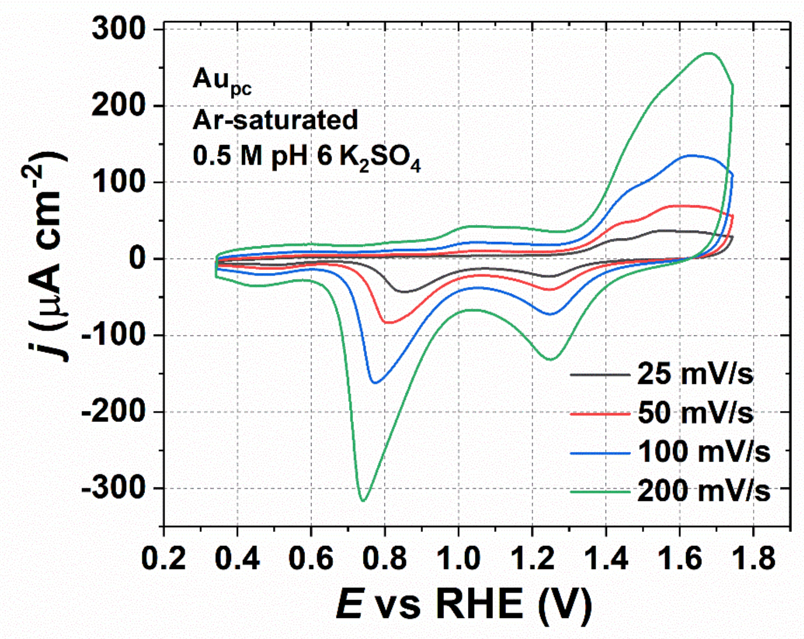

Figure 6.7*. Typical cyclic voltammograms of* the *Au$_{pc}$* electrode *in 0.5 M Ar-saturated K_2SO_4 electrolytes at different scan rates. Reproduced from reference.*[161]

To further explore the impact of pH and cations, LICT measurements were conducted to detect the PME. The LICT experiments were performed in Ar-saturated and O_2-saturated solutions (*cf.* **Figures 6.8A** and **B**). The relaxation peaks were spotted in Ar-saturated and O_2-saturated 0.5 M Na_2SO_4 solutions. The current transients' extreme values were plotted as a function of the working electrode potential (*cf.* **Figures 6.8C** and **D**) to locate the PME. The PME values for the Au$_{pc}$ electrode were evaluated to be ~0.19 V and ~0.35 V *vs*. RHE in the Ar-saturated and O_2-saturated 0.5 M Na_2SO_4 electrolytes (pH 2), respectively.

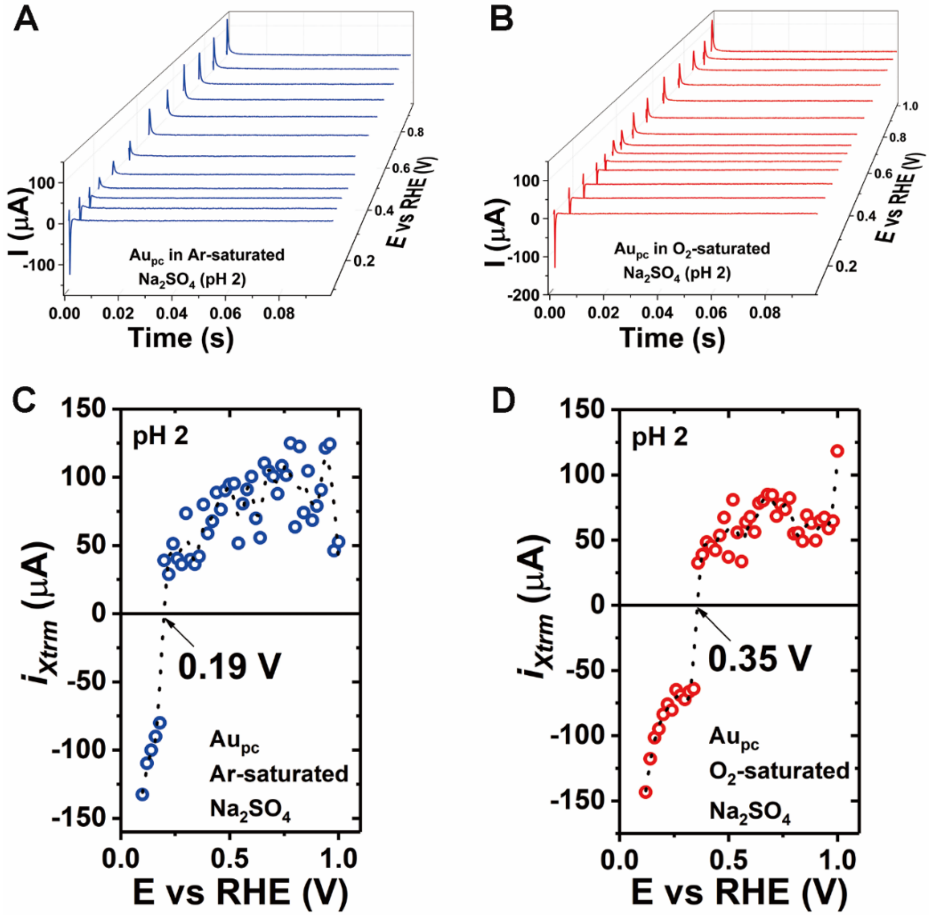

***Figure 6.8**. 3D schemes of the LICT results acquired for Au$_{pc}$ at pH 2 in **A)** an Ar-saturated and **B)** an O$_2$-saturated 0.5 M Na$_2$SO$_4$ electrolytes, respectively. (**C** and **D**) The corresponding 2D LICT graphs of the collected current extrema plotted as a function of the working electrode potential. Reproduced with permission from reference.*[130,161] *Copyright © (2021), The Authors. Published by Wiley-VCH GmbH. Open access, published under a CC-BY license.*

Amazingly, the PMEs become more positive as the pH increases in both Ar-saturated and O$_2$-saturated 0.5 M Na$_2$SO$_4$ solutions. The evaluated PME values for the Au$_{pc}$ electrode in the Ar-saturated 0.5 M Na$_2$SO$_4$ solutions; ~0.25 V, ~0.34 V, ~0.58 V, and ~0.88 V *vs*. RHE for pHs 4, 6, 8, and 10, respectively are displayed in **Figures 6.9A** to **D**. In the case of O$_2$-saturated 0.5 M Na$_2$SO$_4$ electrolytes (*cf*. **Figures 6.9E** to **H**), the PME values for the Au$_{pc}$ electrode move towards ~0.39 V, ~0.46 V, ~0.66 V, and ~0.98 V *vs*. RHE for pHs 4, 6, 8, and 10, respectively.

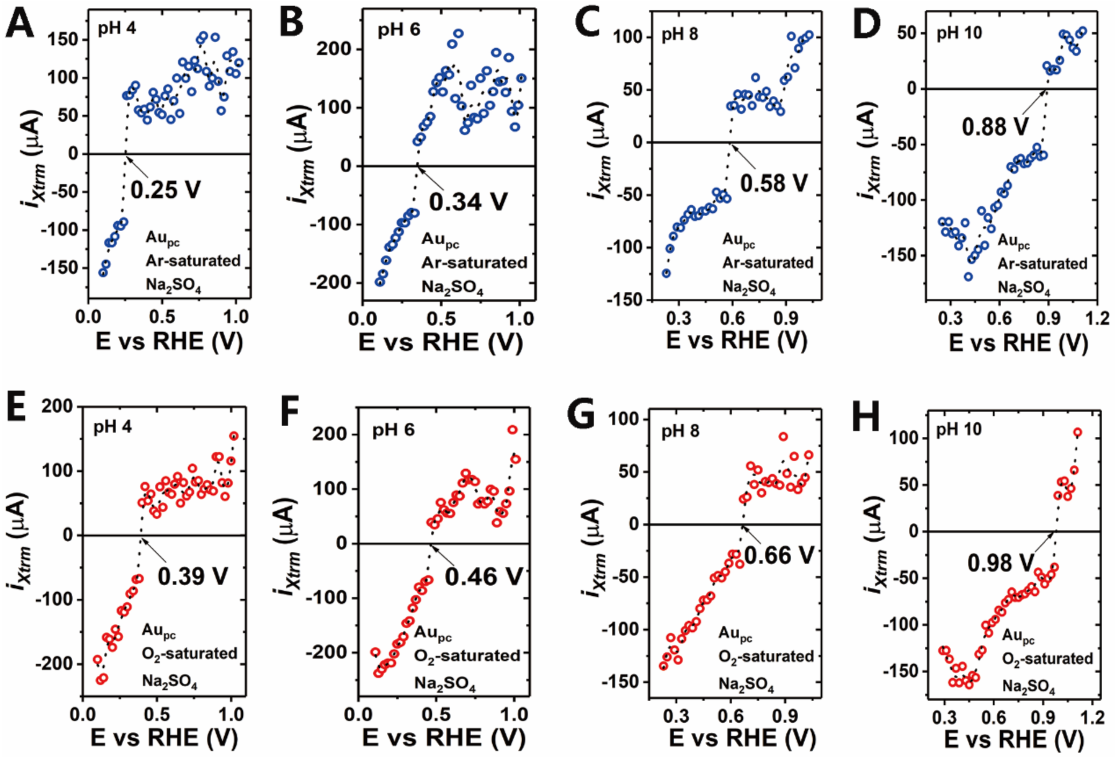

Figure 6.9. (A to D) Extreme current values of the laser-induced transients for Au$_{pc}$ submerged into Ar-saturated 0.5 M Na_2SO_4 solutions of different pHs (4, 6, 8, and 10). (E to H) The analogous extreme current values collected for the Au$_{pc}$ immersed into the O_2-saturated 0.5 M Na_2SO_4 solutions. Reproduced with permission from reference.[130,161] *Copyright © (2021), The Authors. Published by Wiley-VCH GmbH. Open access, published under a CC-BY license.*

Admittedly, the pH dependence of the PME, in this case, involves the effect of adsorption processes on the free charge distribution at the interface.[301,308] The PME is theorized to be independent of the electrolyte pH on the SHE scale when it is located within the potential range with no adsorption influence.[471] Nonetheless, the PME depends on the electrolyte pH when the PME lies at the potentials where adsorption processes affect the free charge.[301]

Figure 6.10 showcases a shift of the PME values towards more positive potentials arising from the pH increase for the Au$_{pc}$ electrode in both Ar-saturated and O_2-saturated 0.5 M Na_2SO_4 solutions. Even more intriguing is that in O_2-saturated Na_2SO_4 solutions, the evaluated PMEs are more positive than those measured in Ar-saturated electrolytes for all the investigated pH ranges. As such, the reduced O_2 can consume local protons at the electrode interface during the LICT experiments. Accordingly, changes in the local pH emanate and consequently shift the corresponding PMEs' location, which concords with the Au$_{pc}$ electrode in $HClO_4$ solutions at different pHs (see **section 6.1**). In this regard, determining the PME provides an avenue for estimating the local pH at the interface.

Another spotlight worth mentioning is the drastic elevation of the PME for the Au_{pc} electrode in both Ar-saturated and O_2-saturated 0.5 M Na_2SO_4 solutions when the pH varies from 6 to higher values. Subsequently, the PME became more sensitive to any pH alteration. A cursory look at **Figure 6.10** also reveals a gradual decrease in the influence of O_2 on the PME of the Au_{pc} electrode as the pH increase, especially when comparing the difference of the PME values in the Ar-saturated and O_2-saturated 0.5 M Na_2SO_4 solutions at pH 2 (~0.16 V_{RHE}) and pH 10 (~0.10 V_{RHE}).

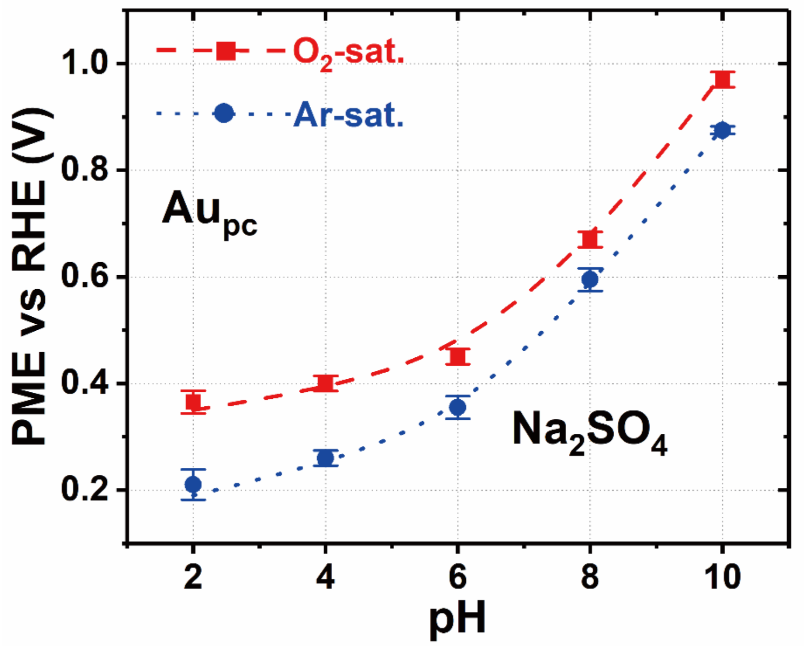

Figure 6.10*. The PME values chronicled for Au_{pc} in Ar-saturated (blue) and O_2-saturated (red) 0.5 M Na_2SO_4 solutions plotted as a function of the electrolyte pH. Reproduced from reference.*[161]

In the same vein, measurements on the Au_{pc} electrodes at various pHs (2, 4, 6, 8, and 10) in Ar-saturated and O_2-saturated 0.5 M K_2SO_4 solutions were conducted to probe the role of the alkali metal cation. **Figures 6.11A** to **E** reveal the potentials where the sign of the current transients flip for the Au_{pc} electrode in the Ar-saturated 0.5 M K_2SO_4 solutions. These potentials are ~0.13 V, ~0.27 V, ~1.26 V, ~1.30 V, and ~1.43 V *vs*. RHE for pHs 2, 4, 6, 8, and 10, respectively. The various potentials at which the water molecules turn over in the O_2-saturated 0.5 M K_2SO_4 electrolytes for the Au_{pc} electrode shift towards more positive values. These are ~0.27 V, ~0.37

V, ~1.40 V, ~1.38 V, and ~1.49 V *vs*. RHE for pHs 2, 4, 6, 8, and 10, respectively (*cf.* **Figures 6.11F** to **J**).

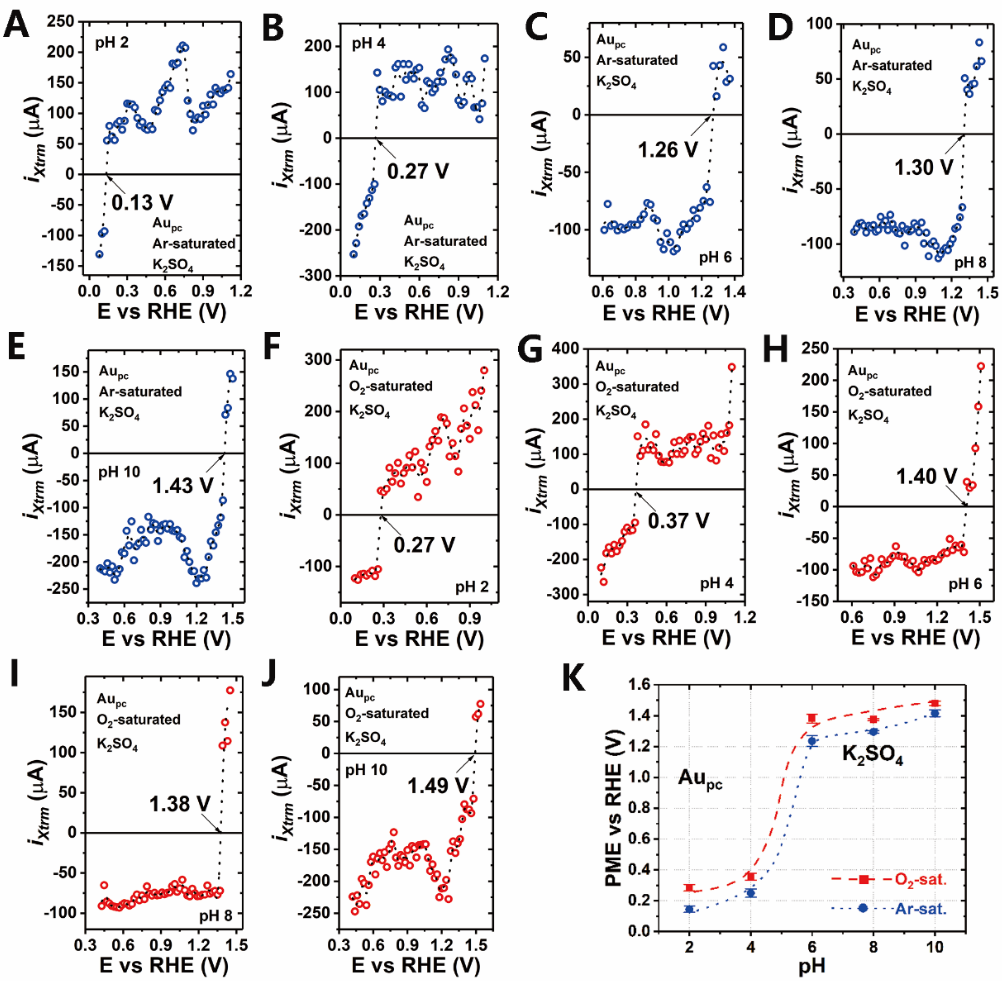

***Figure 6.11**. (**A** to **E**) Extreme values of laser-induced current transients estimated for Au$_{pc}$ immersed into the Ar-saturated 0.5 M K_2SO_4 solutions of different pHs (2, 4, 6, 8, and 10). (**F** to **J**) Analogous extreme current values collected for Au$_{pc}$ submerged into the O_2-saturated 0.5 M K_2SO_4 solutions of the corresponding pH values. **K**) The PME values plotted versus pH values for Au$_{pc}$ in Ar-saturated (blue) and O_2-saturated (red) 0.5 M K_2SO_4 solutions. Reproduced from reference.*[161]

In the case of the Au$_{pc}$ electrode in the 0.5 M Na_2SO_4 solutions, pH increase and oxygen involvement can reposition the PME values to more positive potentials. The only exception to this trend was the case of the Au$_{pc}$ electrode in the O_2-saturated 0.5 M K_2SO_4 electrolytes from pH 6 to 8. It is worth remarking that the PME value was tremendously shifted from pH 4 to 6 for the Au$_{pc}$ electrode in both Ar-saturated and O_2-saturated 0.5 M K_2SO_4 solutions (*cf.* **Figure 6.11K**). This implies that a slight modification in pH within this pH region can vary the EDL structure substantially. A possible explanation for the observation stems from the specific adsorption, such as *OH (* representing the adsorbed species) and sulfate adsorption resulting in a phase transition coupled with interfacial water rearrangements in the double layer,[472] which ultimately shifts the location of the PME. Surprisingly, the outcome differed from the case of the Au_{pc} electrode in the Na_2SO_4 electrolyte. The PME did not exhibit higher sensitivity to the pH change for higher pH (pH > 6), despite a rapid PME change from pH 4 to 6. Furthermore, like the case of the Au_{pc} electrode in the 0.5 M Na_2SO_4 electrolytes, the influence of O_2 on the PME of Au_{pc} became smaller with the pH increase (except in the case of pH 6) when comparing the difference of the PME values for the Au_{pc} electrode in the Ar-saturated and O_2-saturated 0.5 M K_2SO_4 solutions at pH 2 (~0.14 V) and pH 10 (~0.06 V).

Although the PME values for the Au_{pc} electrode in Ar-saturated 0.5 M K_2SO_4 solutions at pHs 6, 8, and 10 already exceed the thermodynamic equilibrium potential of the ORR (1.23 V *vs.* RHE), introducing oxygen further moves the PME to more positive potentials. Therefore, it can be envisaged that the water layer structure at the interface between the electrode and electrolyte is not solely influenced by dissolved O_2 but also by H^+, OH^-, and SO_4^{2-} ions adsorbed on the electrode surface.

What's more, **Figure 6.12** demonstrates that the location of the PME shows higher sensitivity to the pH in the presence of K^+ than Na^+ on the Au_{pc} electrode when the effect of the two cations on the Au_{pc} electrodes is compared. Particularly, when the pH of the electrolyte reaches 6 or higher, the difference in the PME value for the systems containing these two cations becomes large (around 0.92 V). Consequently, Na_2SO_4 and K_2SO_4 cannot be considered equal supporting electrolytes. Hence, the EDL properties in the presence of these two cations are significantly different at the same pH. From a combined CV of **Figures 6.5** and **6.6**, it can be suggested that an intense phase transition occurs at the electrode surface in the case of a K_2SO_4 solution.

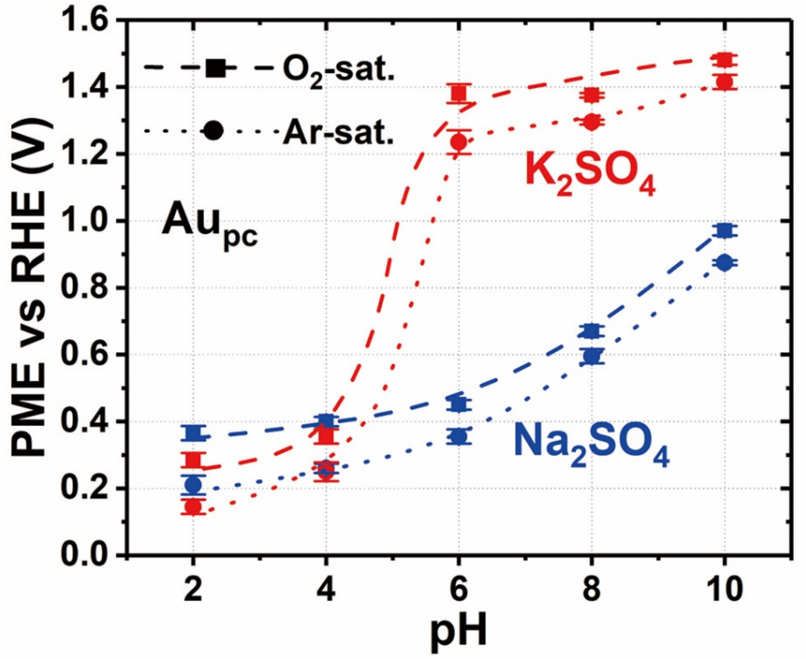

Figure 6.12. *The PME values for Au$_{pc}$ in Ar-saturated (dot) and O$_2$-saturated (dash) 0.5 M Na$_2$SO$_4$ (blue) and K$_2$SO$_4$ (red) solutions depicted as a function of the electrolyte pH. Reproduced with permission from reference.*[130,161] *Copyright © (2021), The Authors. Published by Wiley-VCH GmbH. Open access, published under a CC-BY license.*

Based on the PME values from pH 6 to 10 in Ar- and O$_2$-saturated 0.5 M Na$_2$SO$_4$ and K$_2$SO$_4$ electrolytes (*cf.* **Figure 6.12**), it is evident that the PMEs of the Na$^+$-containing electrolytes were consistently below the thermodynamic equilibrium potential of the ORR, whereas the K$^+$-containing electrolytes moved beyond the onset potential of the ORR. In this vein, the two cations were mixed to tailor the PME values toward the thermodynamic equilibrium potential of the ORR. This was necessary to establish the assertion that the PME is a valuable parameter for catalysis, as it can be tuned toward various targeted electrochemical reactions and systems. In realizing this, laser experiments were conducted in a mixed solution (60 mL 0.5 M Na$_2$SO$_4$ and 60 mL 0.5 M K$_2$SO$_4$) at pH 8 (*cf.* **Figure 6.13**). The evaluated PMEs for the Au$_{pc}$ electrode in the Ar-saturated and O$_2$-saturated mixed solutions were found to be ~0.96 V and ~1.08 V *vs.* RHE, respectively. Impressively, the PME values for the Au$_{pc}$ electrode in this hybrid electrolyte are located between the PMEs of the Au$_{pc}$ electrode in Na$_2$SO$_4$ and K$_2$SO$_4$ solutions at the same pH value.

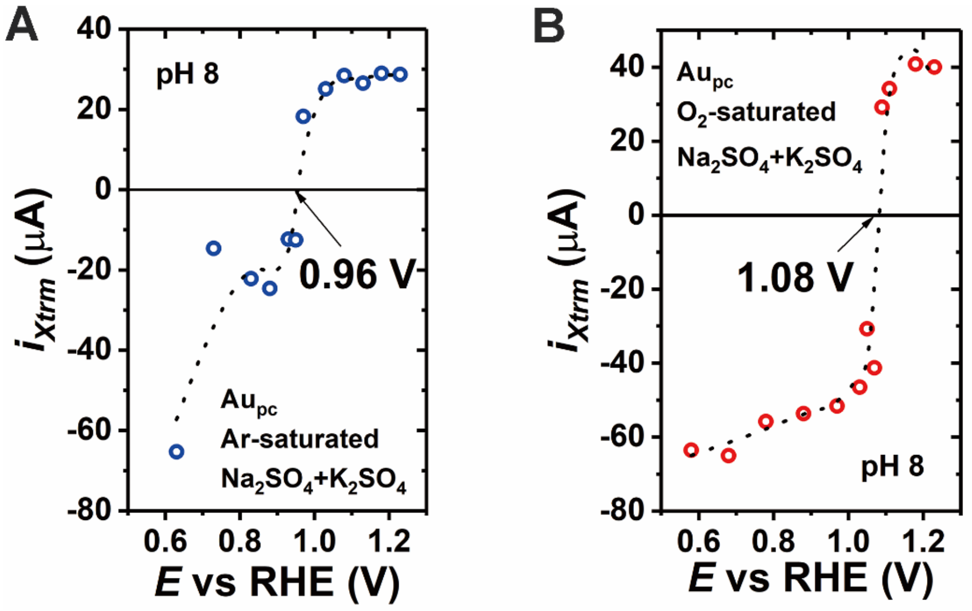

***Figure 6.13**. Plots of the PME determined on the Au_{pc} electrode in **A)** Ar-saturated and **B)** O_2-saturated mixed solution of 60 mL 0.5 M Na_2SO_4 and 60 mL 0.5 M K_2SO_4 at pH 8. Reproduced with permission from reference.[130,161] Copyright © (2021), The Authors. Published by Wiley-VCH GmbH. Open access, published under a CC-BY license.*

Broadly, the investigated electrocatalytic activities (HER and ORR) for the Au_{pc} electrode are highly related to the electrochemical interface order (*cf.* **Sections 6.1** and **6.2**). In this respect, it is possible to foretell the electrocatalytic activity with the PME change, resulting from the influence of electrolyte species (concentration and their nature). Therefore, the impact of the electrolyte component can be described quantitatively, owing to the linear trend observed for the electrocatalytic activity *versus* the PME in all investigated systems. If there exist several PMEs, the others that do not coincide with the PZC arise from specific adsorption effects. PME is a function of specific adsorption for certain systems. Note that one cannot generalize it to include PME is not a function of non-specific adsorption.

The degree of order of the interface between the electrode and electrolyte can be associated with the polarizability of the electrolyte, which the relative dielectric constant, ε_r, can quantify.[473,474,475] The relative dielectric constant depends on the nature and concentration of the ions. Within a particular concentration range (C < 2 M), this fundamental characteristic becomes a linear function of the nature and concentration of ions present in the solution,[475] as depicted by the following equation:

$$\varepsilon_r = \varepsilon_{pure\,H_2O} - \alpha(C_{ion}) \qquad 6.1$$

where $\varepsilon_{pure\,H_2O}$ denotes the dielectric constant of pure water ($\varepsilon_{pure\,H_2O}$ ~ 82 at room temperature), α stands for the proportionality coefficient describing the relative ion contribution, and C_{ion} is the ion concentration. Remarkably, previous scientific reports and **Figure 6.3F** performed within a narrow concentration range all portray a linear relationship for the value of the PME.[308,471] Analogous to **Equation (6.1)**, could be valid for some range of concentrations:

$$E_{PME} = E_{PME}^{at\ \varepsilon=\varepsilon_{pure\,H_2O}} \pm \beta C_{ion} \qquad 6.2$$

where E_{PME} represents the PME value under study while $E_{PME}^{at\ \varepsilon=\varepsilon_{pure\,H_2O}}$ depicts the corresponding value acquired for the system containing pure water and the function β stands for the relative contribution of the ion concentration.

As mentioned above, the electrocatalytic activity and the PME value correlate linearly in all the investigated systems. Rearranging **Equation (6.1)** in terms of C_{ion}, combining it with **Equation (6.2)**, and taking the electrode activity in pure water, A_{H_2O}, as the reference, one can express the electrode activity, A, as follows:

$$A \propto A_{H_2O} \pm \breve{\varphi}\left[\varepsilon_{pure\,H_2O} - \varepsilon_r^{electrolyte}\right] \qquad 6.3$$

where $\breve{\varphi}$ describes the proportionality coefficient or even function/operator dependent on the nature of the reaction.

Sections 6.1 and **6.2** show the systematic studies on the impact of the electrolyte composition on the interfacial process. The presented results and analyses qualitatively and quantitatively clarify the strong influence of the electrolyte composition on the performance of electrocatalytic systems. Associating the PME with the corresponding changes in the electrocatalytic reactions reflects how the interface structure can control the related electrocatalytic processes. Therefore, determining the PME can be a formidable method to comprehend better the electrochemical processes occurring at the electrode/electrolyte interface.

The results indicate that the alkali metal cations' nature strongly influences the EDL properties. Increasing the electrolyte pH in the presence of Na^+ and K^+ can shift the PME to more positive potentials for the Au_{pc} electrode. Nonetheless, the PME exhibits a higher sensitivity to the pH in the presence of K^+ than Na^+. Especially for the Au_{pc} electrode in 0.5 M Na_2SO_4 and K_2SO_4 solutions at pH 6, the difference in the PME values for these two electrolytes is *ca.* 0.92 V, indicating the EDL structure is significantly different for the Au_{pc} electrode in the solution containing Na^+ and K^+ ions. In this case, Na_2SO_4 and K_2SO_4 cannot be regarded as electrolytes of the same strength under the same conditions. As for the case in $HClO_4$ solutions, oxygen can move the PME to more positive potentials in the presence of Na^+ and K^+.

Interestingly, although the PME values for the Au_{pc} electrode in Ar-saturated 0.5 M K_2SO_4 solutions of pHs 6, 8, and 10 surpass the thermodynamic equilibrium potential of the ORR, introducing oxygen further moves the PME to more positive potentials. Moreover, the PME exhibits a linear trend with the hydration energies of the corresponding alkali metal cations. All the presented results demonstrate that the nature of the cation significantly sways the electrode processes. Consequently, determining the PME is a powerful approach to optimizing electrochemical devices *via,* for example, the electrolyte composition.

6.3 Cation Effect on Surface-Mounted Metal-Organic Framework Derivatives

Metal-organic frameworks, also known as porous coordination polymers, are a class of ordered, crystalline materials designed by coordinating organic ligands/linkers with metal ions/clusters.[476,477,478,479] Owing to their unique properties, including tunable pore structure, ultrahigh porosity, diversified framework architectures, ligand designability, and high specific surface areas, MOFs and MOF-derived materials have gained considerable research interest and are exploited for various applications in heterogeneous catalysis,[480,481,482,483,484] drug delivery,[485,486] gas separation and storage,[487,488,489,490] biomedical imaging,[491] and sensing,[492] in the last 20 years.

Recently, our groups developed a multipurpose and facile approach to synthesize mixed metal hydroxide electrocatalysts derived from surface-mounted MOFs with exceptional OER performance in alkaline media.[493,494] As such, this section elaborates on the cation effect on the SURMOF derivatives investigated *via* the LICT technique. The experiments were conducted for the Ni|Fe-[TA]-SURMOF derivatives in 0.1 M *AM*OH (*AM* = Li^+, Na^+, K^+, and

Cs$^+$) solutions. Here, [TA] represents deprotonated terephthalic acid. **Figure 6.14** depicts the OER performance of these derivatives assessed in the alkaline electrolytes containing different alkali metal cations. A decrease in the OER activity in the order of Cs$^+$ > K$^+$ > Na$^+$ > Li$^+$ is observed, which concords excellently with the previous research accounts.[495]

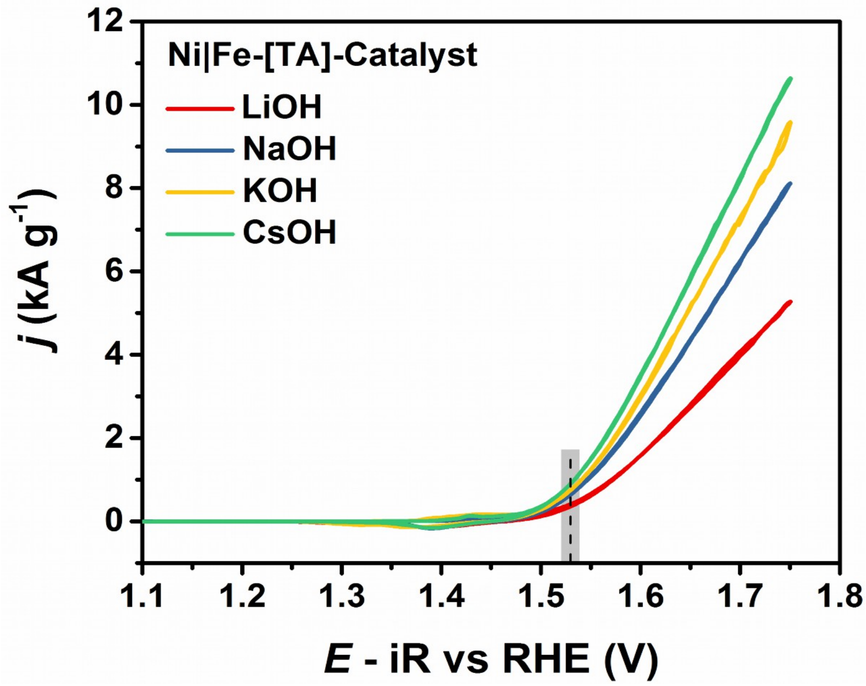

Figure 6.14. *OER polarization curves of Ni|Fe-[TA]-Catalysts recorded in* O_2*-saturated 0.1 M LiOH (pH 13.1), 0.1 M NaOH (pH 13.4), 0.1 M KOH (pH 13.4), and 0.1 M CsOH (pH 13.5) electrolytes. Scan rate: 5 mV* s^{-1}*. Note, the SURMOFs derivatives are denoted as Catalyst after electrochemical cycling here. Reproduced with permission from references.*[131,161] *Copyright © (2022), The Authors. Angewandte Chemie International Edition published by Wiley-VCH GmbH. Open access, Creative Commons Attribution Non-Commercial NoDerivs License.*

To check the interfacial water layer structure effect on the OER activity of the SURMOF-derived NiFe(OOH) electrocatalysts, the LICT measurements were performed in the corresponding systems containing different alkali metal cations (*cf.* **Figure 6.15**). Accordingly, the PMEs were evaluated to be *ca*. 0.96 V, 0.98 V, 1.00 V, and 1.04 V *vs*. RHE for 0.1 M LiOH, 0.1 M NaOH, 0.1 M KOH, and 0.1 M CsOH electrolytes, respectively. Evidently, the PME increases with the decrease of the alkali metal cation hydration energy. This trend was further affirmed using the *in-situ* Raman spectroscopy measurements.

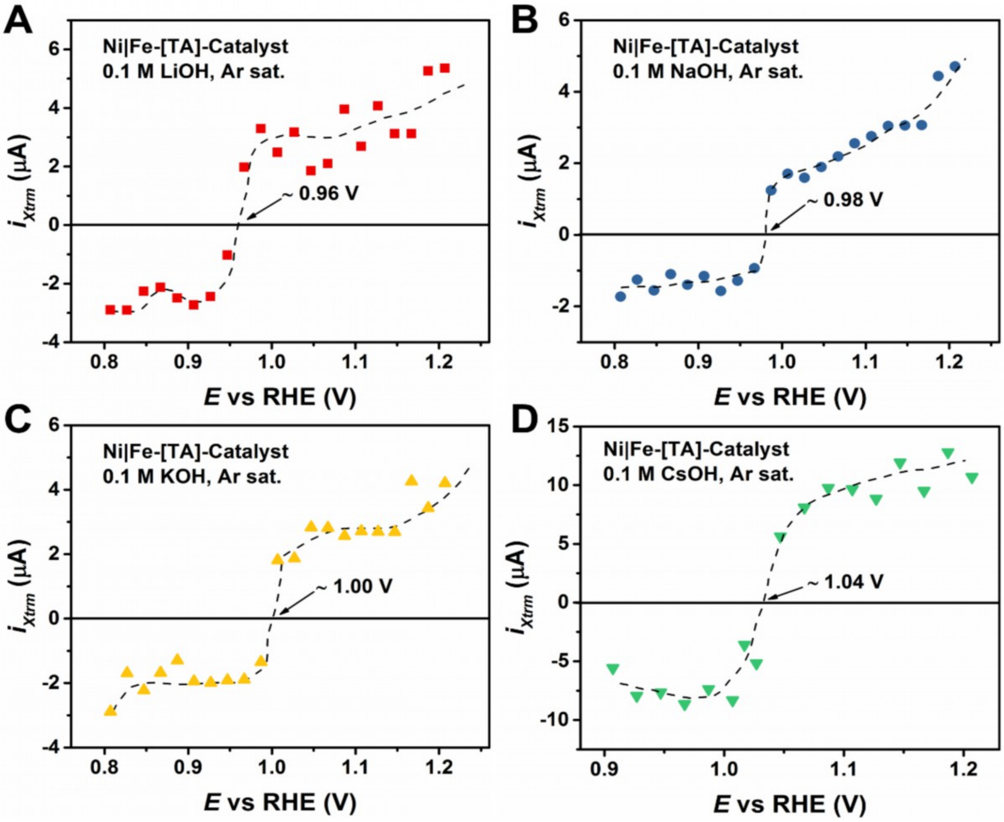

***Figure 6.15**. (**A** to **D**) The maximum current transient values plotted as a function of the applied potential for 0.1 M LiOH (pH 13.1), 0.1 M NaOH (pH 13.4), 0.1 M KOH (pH 13.4), and 0.1 M CsOH (pH 13.5) electrolytes, respectively. One can find the PME values at the point when the current transient changes its sign, i.e., i_{Xtrm} ~ 0. Reproduced with permission from references.[131,161] Copyright © (2022), The Authors. Angewandte Chemie International Edition published by Wiley-VCH GmbH. Open access, Creative Commons Attribution Non-Commercial NoDerivs License.*

According to the discussion in **section 6.2**, hypothetically, the closer the PME is to the thermodynamic equilibrium potential of the OER, the better the OER activity should be. In this regard, as the PME for the Ni|Fe-[TA]-Catalyst in the presence of Cs^+ is closer to the onset potential of the OER, its interfacial order at the onset potential of the OER will be more chaotic. Consequently, the Ni|Fe-[TA]-Catalyst would exhibit better OER performance in the presence of Cs^+. The observed OER activity results confirm these hypothetical expectations (*cf.* **Figure 6.14**). Additionally, the OER activity scales almost linearly with the PME (*cf.* **Figure 6.16**), indicating that the OER performance of the Ni|Fe-[TA]-Catalyst has a strong correlation with the interface structure influenced by the alkali metal cations in the electrolyte.

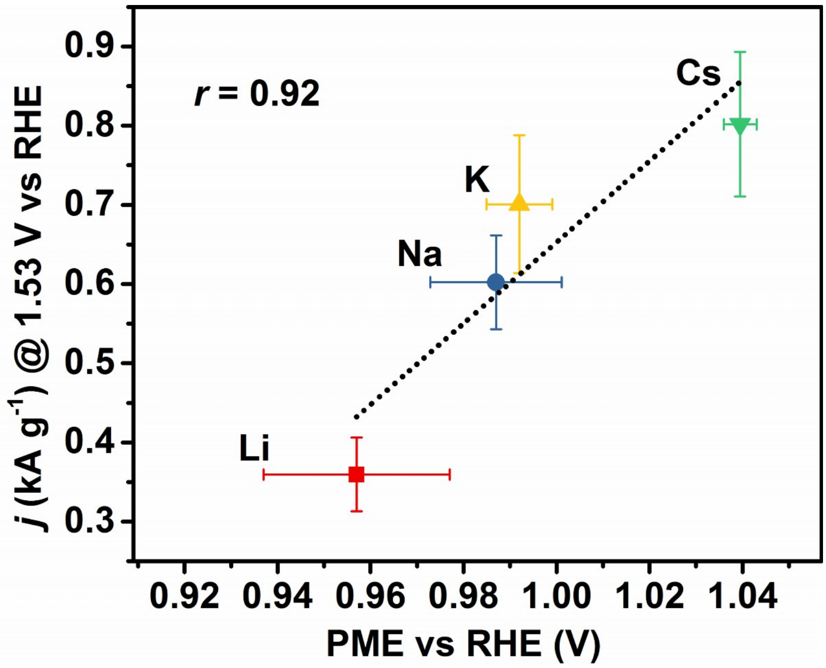

***Figure 6.16**. Graphical representation of the current density at the potential of 1.53 V versus the PMEs of Ni|Fe-[TA]-Catalyst in electrolytes containing alkali metal cations. The Pearson correlation coefficient (r) is 0.92, according to the linear fitting. Reproduced with permission from references.*[131,161] *Copyright © (2022), The Authors. Angewandte Chemie International Edition published by Wiley-VCH GmbH. Open access, Creative Commons Attribution Non-Commercial NoDerivs License.*

In summary, the cation effect on the OER activity of the SURMOF-derived NiFe(OOH) electrocatalysts follows the order of $Cs^+ > K^+ > Na^+ > Li^+$. Employing the LICT technique, the correlation between the OER performance and the PME was established. The obtained results further reinforce the proposition that the closer the PME is to the thermodynamic equilibrium potential of a certain reaction, the faster this reaction should be. Thus, the PME determination with the LICT can be considered a powerful method for investigating the electrochemical processes at the electrode/electrolyte interface.

6.4 Anion Effect on Prussian Blue Analog Battery Electrodes

Chapter 1 established the blueprint for the so-called hydrogen economy. Batteries are essential in achieving a carbon-free or green environment based mainly on renewable energy technologies.[496,497] Rechargeable aqueous alkali-ion batteries have recently attracted great interest due to their natural abundance, cost efficiency, environmental friendliness, safety, moderate to high capacity, and operation within the electrochemical stability window.[498] Therefore, Prussian blue (PB) and its analogs (PBAs) have been extensively explored as electrode materials for aqueous alkali metal-ion battery applications.[499] Investigating and understanding the mechanism of intercalation and de-intercalation (charge state of the surface) provides leeway to enhance the specific capacities and working potential and, by extension, facilitate efficiency.[497,498,499] Our group has demonstrated that one way to accomplish this is by employing the LICT technique.[154,155,157]

Motivated by the previous studies on the PBA electrodes, pH, and cation effect on electrode processes, the LICT method was deployed to probe the role of anions in the electrode/electrolyte interface of the NiHCF cathodes for aqueous sodium-ion batteries. Five different anions, namely, ClO_4^-, NO_3^-, Cl^-, OAc^-, and SO_4^{2-}, were chosen to understand the proton-driven degradation at low pH and obtain insights into the charge state of the interface. **Figure 6.17A** portrays the CVs recorded in Ar-saturated 0.25 M $NaClO_4$, 0.25 M $NaNO_3$, 0.25 M NaCl, 0.25 M NaOAc, and 0.25 M Na_2SO_4 electrolytes. The potential window for each CV measurement ranged from 0.1 V to 0.8 V *vs*. SSC at a scan rate of 50 mV s^{-1}. Only two CV cycles were conducted before and after the LICT measurements to avoid the thin films' possible degradation (stability issues) in the investigated electrolytes. Essentially, the CVs before and after the LICT measurements overlapped perfectly, meaning they all pursued the same paths. The CVs conform to reports in the literature.[500] For the LICT probing to obtain the PME, the potential range of -1.00 V to 0.8 V *vs*. SSC at 50 mV potential steps in Ar-saturated 0.25 M NaX (X = NO_3^-, ClO_4^-, Cl^-, OAc^-, and SO_4^{2-}) solutions was adopted.

Figure 6.17B presents the obtained PME values for the system containing NO_3^- anion at ~-0.68 V, ~0.38 V, and ~0.70 V *vs*. SSC. There exist multiple PMEs in every electrolyte. The electrolyte containing OAc^- anion shows only two PMEs, ~0.25 V and ~0.57 V *vs*. SSC (see **Figure 6.17E**). Specifically, the NiHCF electrode in Ar-saturated 0.25 M $NaClO_4$, NaCl, and Na_2SO_4 electrolytes portrays five PMEs (*cf*. **Figures 6.17C, D**, and **F**). Although every system possesses only one PZC[501] that is related to the PME, obtaining several PMEs is familiar, especially for battery electrodes.[154,155,157] The existence of three or more PMEs or the non-existence of any PME is supposed to be in harmony with the theory on the mass and charge influence from the interfacial water layer structure.[155] However, these findings make explaining the anion effect on the intercalation/deintercalation and activity much more difficult.

Furthermore, unlike the case in the cation effect study, a few of the hydration energy of the investigated anions, such as Cl^- (-381 kJ mol^{-1}), NO_3^- (-314 kJ mol^{-1}), and CH_3COO^- (-300 kJ mol^{-1}), is very close to the employed cation, Na^+ (-406 kJ mol^{-1}). Despite the hydration energies of SO_4^{2-} (1059 kJ mol^{-1}) and ClO_4^- (229 kJ mol^{-1}) being distant from the cation, Na^+ (-406 kJ mol^{-1}), it is unavoidable for some of the obtained results to be affected by the competition of the cations in the electrolyte. More so, the anions known to specifically adsorb (Cl^-, SO_4^{2-}) could introduce other effects to the LICT and activity measurements.[374,375,376,377]

In general, the hydration energy affects the ion's mobility. The lower the hydration or solvation energy, the faster the mobility of the ionic species. An increase in the hydration energy decreases the order of the water layer structure, a crucial factor for the LICT measurements. Notably, there is no clear link between the PME and the hydration energies of the various anions (*cf.* **Figure 6.17G**). However, from a thorough look at the degradation performance of the various anions from best to worst ($NO_3^- > ClO_4^- > Cl^- > OAc^- > SO_4^{2-}$),[500] one can suggest that the hydration energy performance pursues a similar trend, *i.e.*, from best to worst or low to high solvation energy. Different behavioral patterns of the interfacial intercalation/deintercalation processes modify the PMEs for the corresponding hydration energy of the various anions. Hence, the anions in the electrolyte solution account for the impact on the solvation energy and activity.

A)

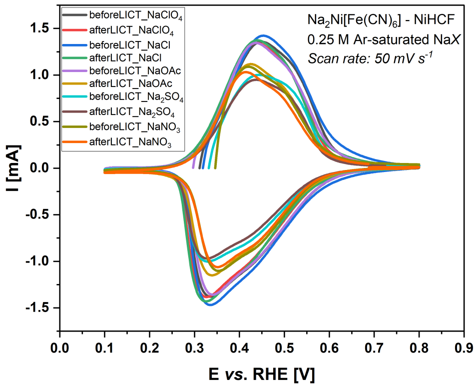

B) **C)**

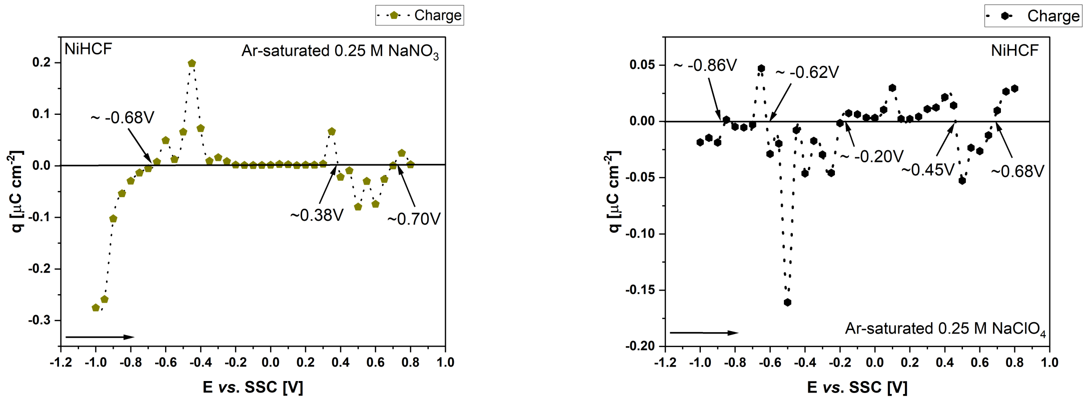

D) **E)**

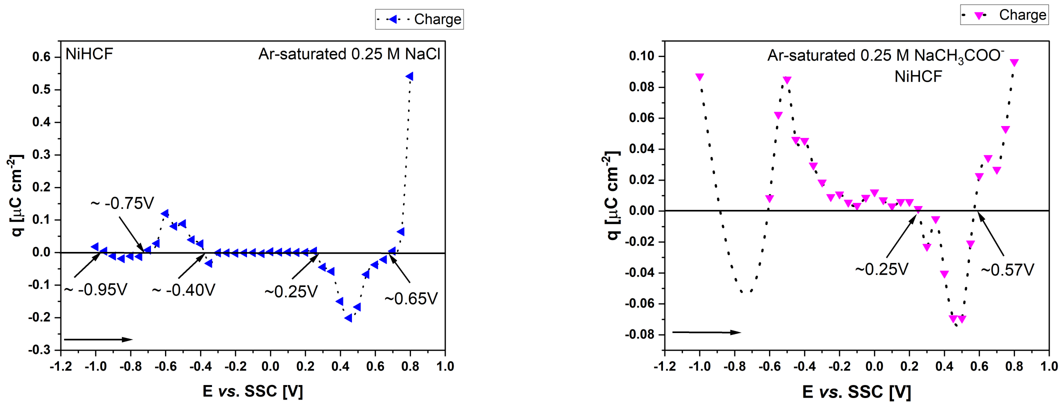

F) **G)**

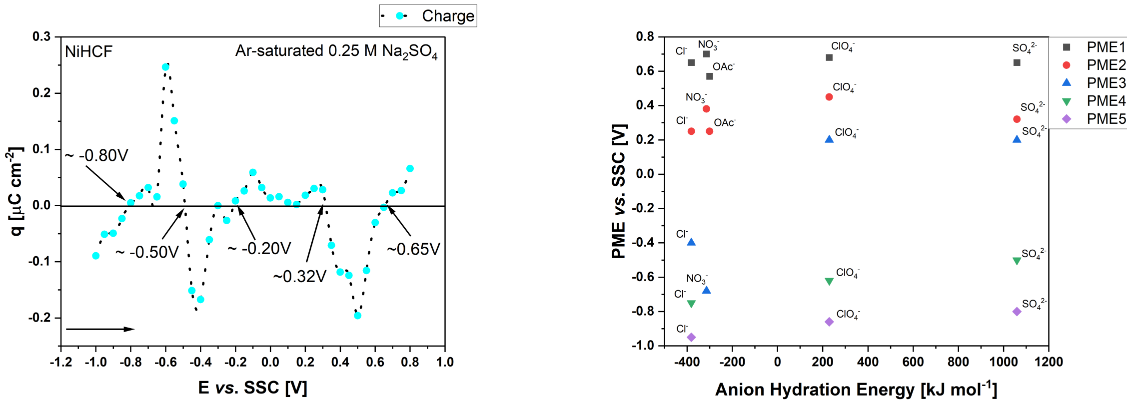

***Figure 6.17**. **A)** CVs of $Na_2Ni[Fe(CN)_6]$- NiHCF thin films before and after the LICT measurement conducted in Ar-saturated 0.25 M NaX (where X = NO_3^-, ClO_4^-, Cl^-, OAc^-, and SO_4^{2-}). Two CV cycles were performed for each case. Scan rate: 50 mV s^{-1} **B)** to **F)** PME vs. potential on the SSC RE scale in Ar-saturated 0.25 M $NaNO_3$, $NaClO_4$, NaCl, NaOAc, and Na_2SO_4 electrolytes. **G)** Graphical representation of the PMEs vs. anion hydration energies of the various electrolytes.*

6.5 pH Effect on Pd Monolayers Deposited on Au QCM Electrodes

Following fabricating the Pd MLs *via* ALD on the Au QCM chips, the pH effect of various concentrations of Ar-saturated perchloric acid was probed using CV, LICT, and EIS methods. Studies report that the Pd(*hkl*) and Pd MLs on the Au QCM electrodes provide close to optimum electrode and catalyst activity toward the HER, especially in acidic media.[243,379,502] In contrast, Pt is claimed to be the most active electrode and catalyst in alkaline media.[135,357,370,376,381,383] As such, the reaction of interest was the HER in acidic media.

The CVs in the various electrolytes (varying pH or concentrations of $HClO_4$) all follow the trend in the literature (primarily, the shape and features).[432] The corresponding CVs were compared before and after the laser measurements to check further that the CVs and, by extension, the structure, shape, and features of the electrode material remained the same before and after the laser experiments. As displayed in **Figures 6.18A**, **C**, and **E**, the CVs before and after the LICT measurements do not depart from the initial path or behavior, confirming the fact that the nature of the electrode remained intact throughout the experiment.

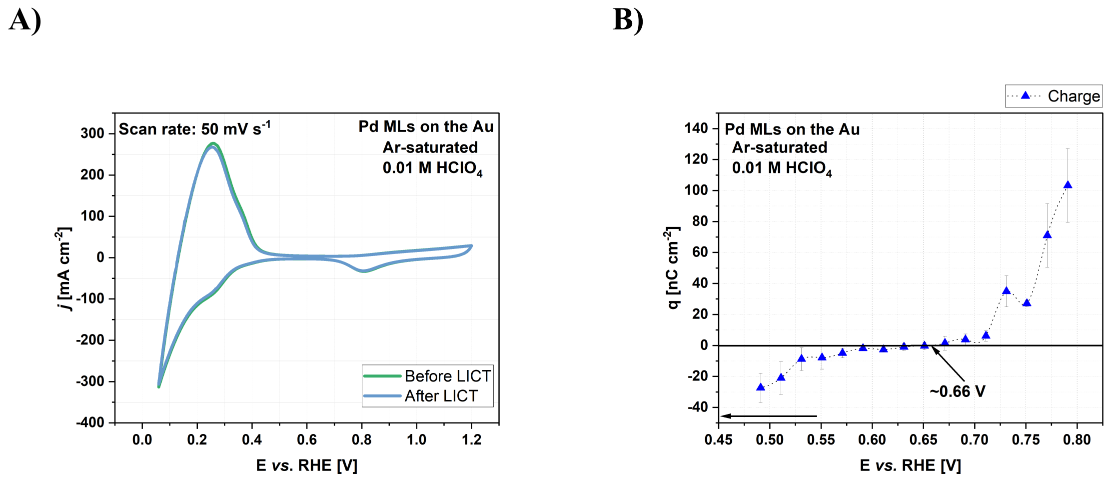

C) **D)**

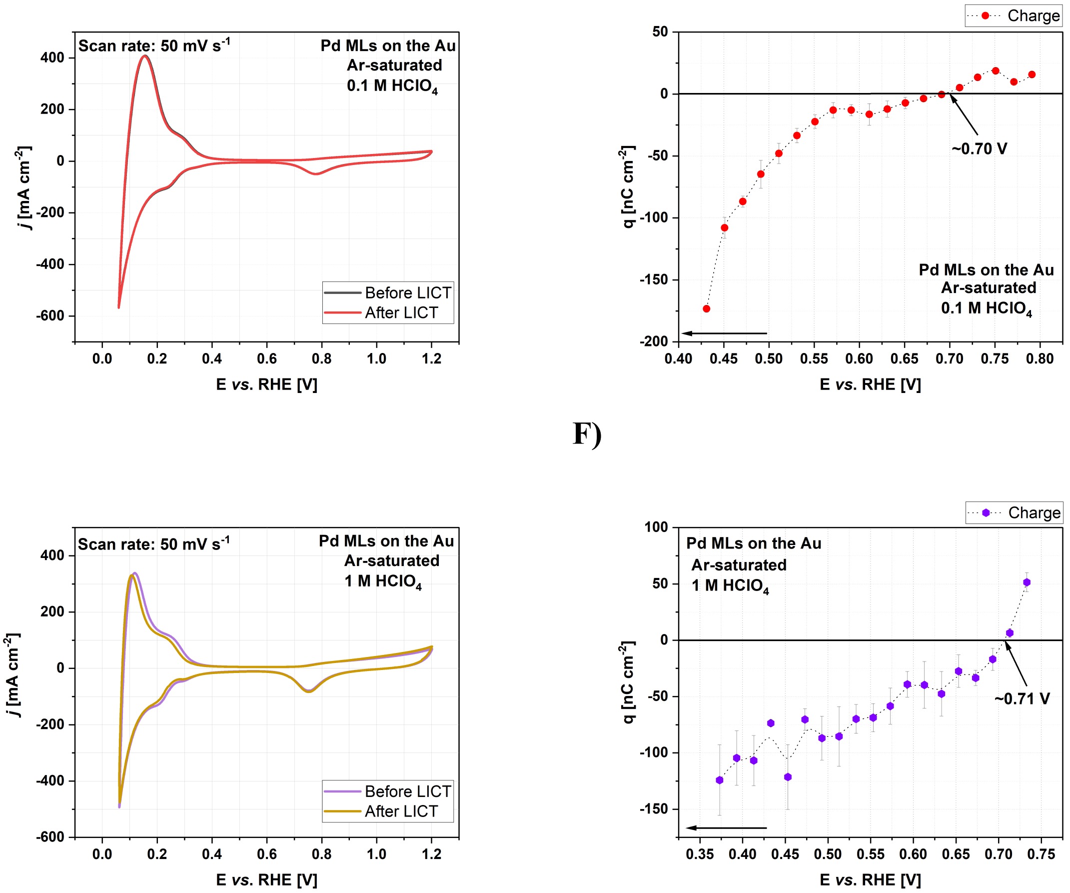

Figure 6.18*. Voltammograms conducted on the atomic layer deposition deposited Pd monolayers on an Au QCM electrode and an Ar-saturated* ***A)*** *0.01 M HClO$_4$ (pH = 2),* ***C)*** *0.1 M HClO$_4$ (pH = 1), and* ***E)*** *1 M HClO$_4$ (pH = 0) electrolyte, respectively. Scan rate: 50 mV s^{-1}. CVs conducted before and after the LICT are depicted in* ***A)*** *green and blue,* ***C)*** *black and red, and* ***E)*** *purple and orange colors, respectively. Plots of the evaluated charge densities emanating from the current transients as a function of the applied potential for* ***B)*** *0.01 M HClO$_4$,* ***D)*** *0.1 M HClO$_4$, and* ***F)*** *1 M HClO$_4$ electrolyte, respectively. The laser measurements were conducted from higher to lower potentials. The zero crossing of the charge density signifies the position of the PME.*

Since Au is featureless, no specific adsorption of anions is extensively visible. However, PGMs, particularly Pd and Pt, are very sensitive and exhibit specific anions adsorption. Also, Pd has many phases. To minimize and/or bypass this, perchloric acid (ClO_4^-) which shows no specific adsorption, was used as the electrolyte on the sensitive electrode, Pd MLs on the Au. It is worth remarking from the CVs at varying pHs that the lower part of the current densities (UPD region) moves to more negative values with increasing pH. The same assertion is repeated at the upper part of the CV (UPD region), where the current densities shift to more positive values with increasing pH.

In the presence of adsorption, there are better techniques (*e.g.*, the double-layer capacitance method could be more reliable) than the LICT method since history must be considered. The influence of H emanating from the Pd absorption/adsorption and the temperature influence (*ca.* 20-40 K) must all be incorporated. From deploying the LICT methodology, the PME value obtained for the system recorded in perchloric acid solution (at pH = 2) was ~0.66 V *vs*. RHE (*cf.* **Figure 6.18B**). The PME values in perchloric acid solutions at pHs 1 and 0 were evaluated as ~0.70 V and ~0.71 *vs*. RHE, respectively (*cf.* **Figure 6.18D**, **F**).

It is evident from the results that the PME shifts to more positive values when pH decreases (concentration increases). Hence, proton reduction is facilitated with 0.01 M $HClO_4$.[385] Therefore, it can be anticipated that the HER activity will be best promoted in 0.01 M $HClO_4$ at a pH of 2, according to the hypothesis (as it is closest to the thermodynamic equilibrium potential of the HER) and from the literature.[384,386] A linear trend is observed from the plot of PME *vs*. pH, revealing a relationship between the investigated parameters (*cf.* **Figure A2.1A**). Accordingly, one can infer that the PME is sensitive to pH, which is in harmony with the previous studies by Ding *et al.*[160,161]

***Table 6.1**. Comparison of the evaluated PME and C_{dl} values at different concentrations and pHs of perchloric acid solutions*

Concentration [M]	pH	PME *vs*. RHE [V]	C_{dl} [μF s^{1-n} cm^{-2}]
1	0	0.71	0.77
0.1	1	0.70	0.70
0.01	2	0.66	0.45

Table 6.1 showcases the PMEs and the minimum double-layer capacitances obtained in varying concentrations or pHs of perchloric acid solutions. EIS was performed in the system to get the C_{dl} values, and the equivalent electric circuit (*cf.* **Figure 6.19A**) was adopted to fit the data. The EEC used to fit the obtained impedance results primarily represents the modeling of real electronic systems. For instance, the uncompensated resistance due to impurities in the

electrolyte and the wires used for the connections are modeled by a resistor (*i.e.*, R_u). The charge transfer resistance (R_{ct}) represents any high or low resistance occurring because of the movement of hydrogen or oxygen in the system, leading to other reactions. C_{ad} and R_{ad} epitomize the pathway for specific adsorption at the double layer arising from additional anions/cations (*i.e.*, the adsorption capacitance and resistance). Real capacitors and resistors model the aforelisted electrical components. However, a constant phase element was deployed to model the capacitive behavior of the double layer.

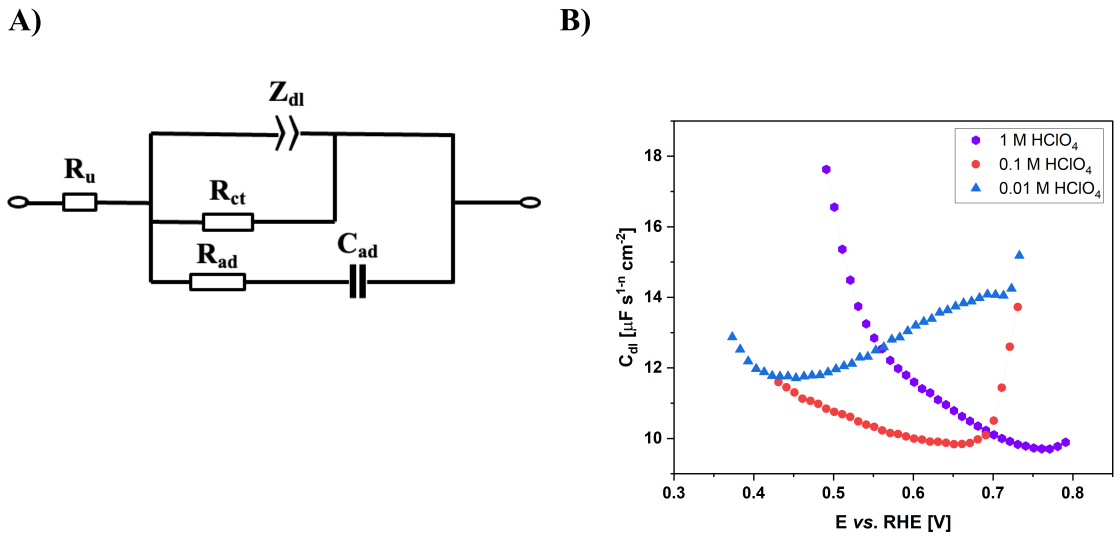

***Figure 6.19**. **A)** The equivalent electric circuit used to give meaning to the electrochemical system's reactions, mechanisms, and occurrences. **B)** Graphical representation of the plot of the capacitance of the double layer as a function of the applied potential in three different (1 M $HClO_4$, 0.1 $HClO_4$, and 0.01 M $HClO_4$) electrolytes for Pd MLs on the Au QCM electrode.*

As was observed for the plot of PME against pH, the minimum double-layer capacitance scales linearly with the electrolyte pH (see **Figure A2.1B**). Therefore, it is unsurprising that one principally notices that the PME and minimum double-layer capacitance values for the different electrolyte pHs are very close or nearly coincide. The two parameters (PME and $C_{dl,minimum}$) are not the same, as the $C_{dl,minimum}$ strictly coincides with the PZC of the material under study. Since it has been established that the PZC tends to shift to higher or more positive potential values than the PME, one can infer that the obtained results largely concur with the theory.[157] The outlier in this study is the $C_{dl,minimum}$ value obtained at pH = 2, which was significantly lower than its corresponding estimated PME.

Remarkably, one should note that the absence of an ordered arrangement (chaotic movement) implies that the equilibrium position of the double layer has been distorted and hence signifies the vicinity of the PME. The momentary disturbance of the double layer also suggests that the double layer or capacitor is uncharged; therefore, no current transfer is anticipated. The *n* values (CPE exponents) plotted for **Figure 6.19B** show no direct correlation with the PME (*cf.* **Figure A2.1C**). On the contrary, the CPE exponents were always maximum at the location of the $C_{dl,minimum}$.

In summary, the pH effect cannot be downplayed in electrocatalytic reactions and systems as it influences electrode processes' performance (activity and selectivity). By merging the LICT, CV, and EIS methods, valuable information about the interfacial properties and structure has permitted in-depth characterization and a better understanding of solvation effects in the investigated electrochemical system. The deployed approach can be extended to probing other electrochemical reactions and systems.

6.6 Cation Effect on Pd Monolayers Deposited on Au QCM Electrodes in Alkaline Media

As the Pd MLs on the Au QCM or Pd electrodes are generally high-performing electrodes and catalysts toward the HER, especially in acidic media, the former was employed to investigate the cation effect in alkaline media. The CVs in all the various 0.1 M *AM*OH electrolytes, *AM* = (Li^+, Na^+, K^+, Cs^+) did not reveal any significant modifications or departure from the CVs in the literature in terms of structure, shape, and features before and after the laser measurements (*cf.* **Figure 5.5**).[432]

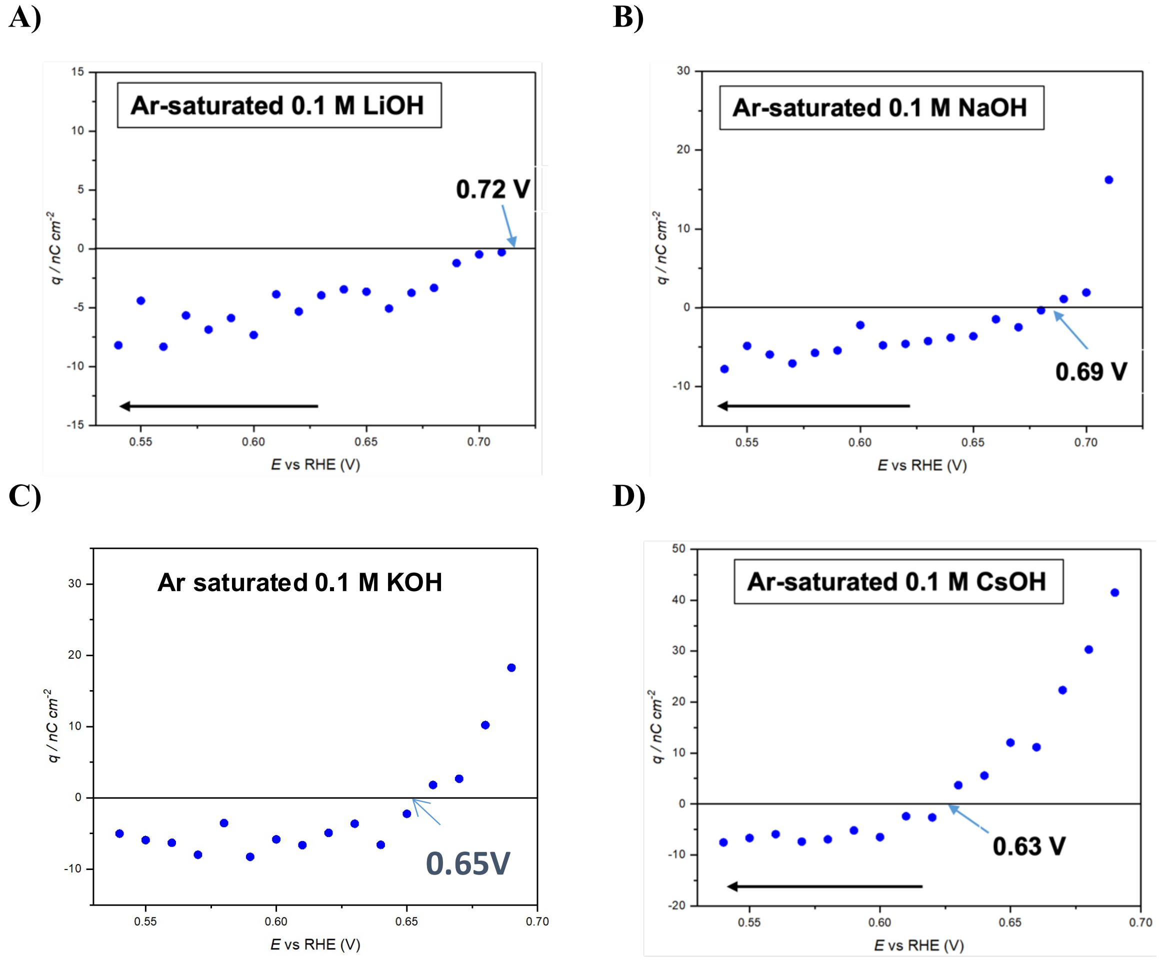

***Figure 6.20**. (**A** to **D**) The evaluated charge density from the current transients plotted as a function of the applied potential for the Pd MLs on the Au electrodes in Ar-saturated 0.1 M LiOH, 0.1 M NaOH, 0.1 M KOH, and 0.1 M CsOH electrolytes. The pHs of the various electrolytes were ca. 13. The PME value is indicated with an arrow, which occurs at the zero crossing of the charge density. The sweep direction of the laser measurements is marked with an arrow moving from right to left (higher to lower applied potentials).*

The PME values decreased in the order of $Li^+ > Na^+ > K^+ > Cs^+$. Specifically, the PME values of the Pd MLs on the Au QCM electrode in Ar-saturated 0.1 M LiOH, 0.1 M NaOH, 0.1 M KOH, and 0.1 M CsOH were ~0.72 V, ~0.69 V, ~0.65 V, and ~0.63 V *vs*. RHE, respectively (*cf*. **Figure 6.20**). Admittedly, the PME for the system containing the Li^+ cation was identified beyond the initial probed potential window. Therefore, an extension of the potential range was employed for that system, with the caution to stay within the double-layer region. The obtained PME results signify that LiOH would show poor activity performance toward the HER while CsOH would show optimum activity toward the HER, with the reverse scenarios for LiOH and CsOH true toward the ORR. These inferences are corroborated by previous HER experiments performed on Pt in alkaline media.[357,370,373] Stemming from this, one can forecast that the activity measurement toward both the HER and ORR would follow the same trend as predicted from the estimated PME in accordance with the hypothesis: the closer the PME is to the thermodynamic equilibrium potential of a specific electrocatalytic reaction, the faster the kinetics of that reaction becomes. In essence, the PME correlates with the electrocatalytic activity and, by extension, the selectivity of reactions.

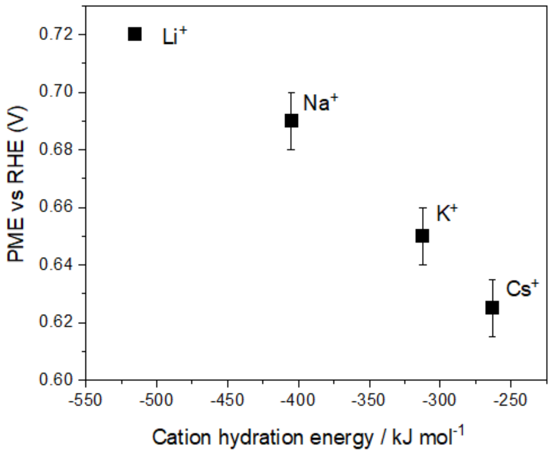

Figure 6.21. *Graphical representation of the PME plotted as a function of the cation hydration energy. The measurements were conducted on Pd MLs on the Au electrode in AMOH, where AM = (Li^+, Na^+, K^+, Cs^+). An almost linear trend is observed.*

Interestingly, the PME scales almost linearly with the hydration energy of the various alkali metal cations (*cf*. **Figure 6.21**), which is also in agreement with an earlier cation effect study on the SURMOF electrodes toward the OER.[131]

In a nutshell, the PME is a reliable parameter to predict the activity of electrocatalytic reactions correctly; hence, it is more essential for catalysis than the PZC. Electrolyte components, namely cations, contribute significantly toward the overall performance of electrocatalytic reactions and systems.

6.7 Electron Paramagnetic Resonance Spectroscopy

6.7.1 Hydrogen Adsorption on Pt

Despite the unambiguity in the usefulness of EPR spectroscopy in electrochemistry, the application of solvents (especially water) is particularly problematic due to their high relative permittivity, as revealed in the reference.[503] The consequence of this bottleneck is evinced through the weakening of the obtained signal occasioned by the solvent's ability to absorb electromagnetic (microwave) radiation. To circumvent this challenge, immense significance must be placed on designing suitable miniature cells with specific dimensions.

Methodology. It is essential to remark that Pt was chosen as the working electrode for these investigations because of its conventional nature, popularity, and broad scope of use in the electrochemistry community. It is classified as a model electrode and/or catalyst with already-known features, properties, etc. Moreover, several *in-situ* EC-EPR studies have already been performed using Pt as the working and counter electrodes (*cf.* **Figures 5.8** and **5.9**).[142,143,146,149] It must be, however, stated that these research works conducted in the recent past mainly focused on the *in-situ* generation of organic radicals[142,143,146,149] and a few on the *in-situ* generation of paramagnetic metal complexes.[504,505] The main target of this section is to investigate the hydrogen adsorption process in the H_{upd} region in the presence of liquid electrolytes. In other words, the aim is to detect atomic hydrogen species with one unpaired electron and should therefore be EPR active/visible. Whether it is detectable at room temperature at all is a question this study tries to answer. To realize this, the potentials in the H_{upd} region (adsorption and desorption) were held for several minutes while measuring the EPR response. However, before this, the cyclic voltammogram is performed to ensure the surface purity of the working electrode.

The as-received *in-situ* EC-EPR cell from LINEV ADANI (Belarus) (*cf.* **Figure 5.10**) was used for the experiments, except for a change from graphite to Pt as the working electrode and the counter electrode from Ag to Pt. The initial CVs performed using different reference electrodes (Pt, and Pd, respectively) are shown in **Figures 5.11A** and **B**. Nearly the entire length of the RE (Pd wire) was placed in a Teflon (PTFE) tube (AWG 32, ZEUS, USA) of inner and outer diameters, 0.25 mm and 0.33 mm, respectively, to insulate it from the counter electrode (Pt). This was essential to avoid any short circuit possibility. About 3 to 5 mm of the RE was left uninsulated. All three electrodes were introduced into the *ca*. 2 mm outer diameter EPR tube with an inner diameter of *ca*. 0.8 mm. A labeled pictorial representation of the various *in-situ* EC-EPR cell components, including the cell holder/protector, is displayed in **Figure 6.22A**. A good appreciation of the different electrode lengths used in the implementation can be seen. It is essential to remark that the part of the *in-situ* cell that goes into the cavity is from the center of the distance between the reference and working electrodes to about 10 mm of the working electrode's length. The gap ensures that at least 10 mm of the working electrode and electrolyte lies within the EPR cavity. More importantly, the arrangement prevents the reference and counter electrodes from electromagnetic interactions. A pictorial and schematic depiction of the fully assembled *in-situ* EC-EPR cell without its holder/protector is shown in **Figure 6.22B**. A complete representation of the fully assembled *in-situ* EC-EPR cell is provided in **Figure 6.22C**. Herein, the electrodes were of dimensions *ca*. 0.20 mm. Electrochemistry (CV), EPR tuning, and subsequent measurements were all possible with this configuration.

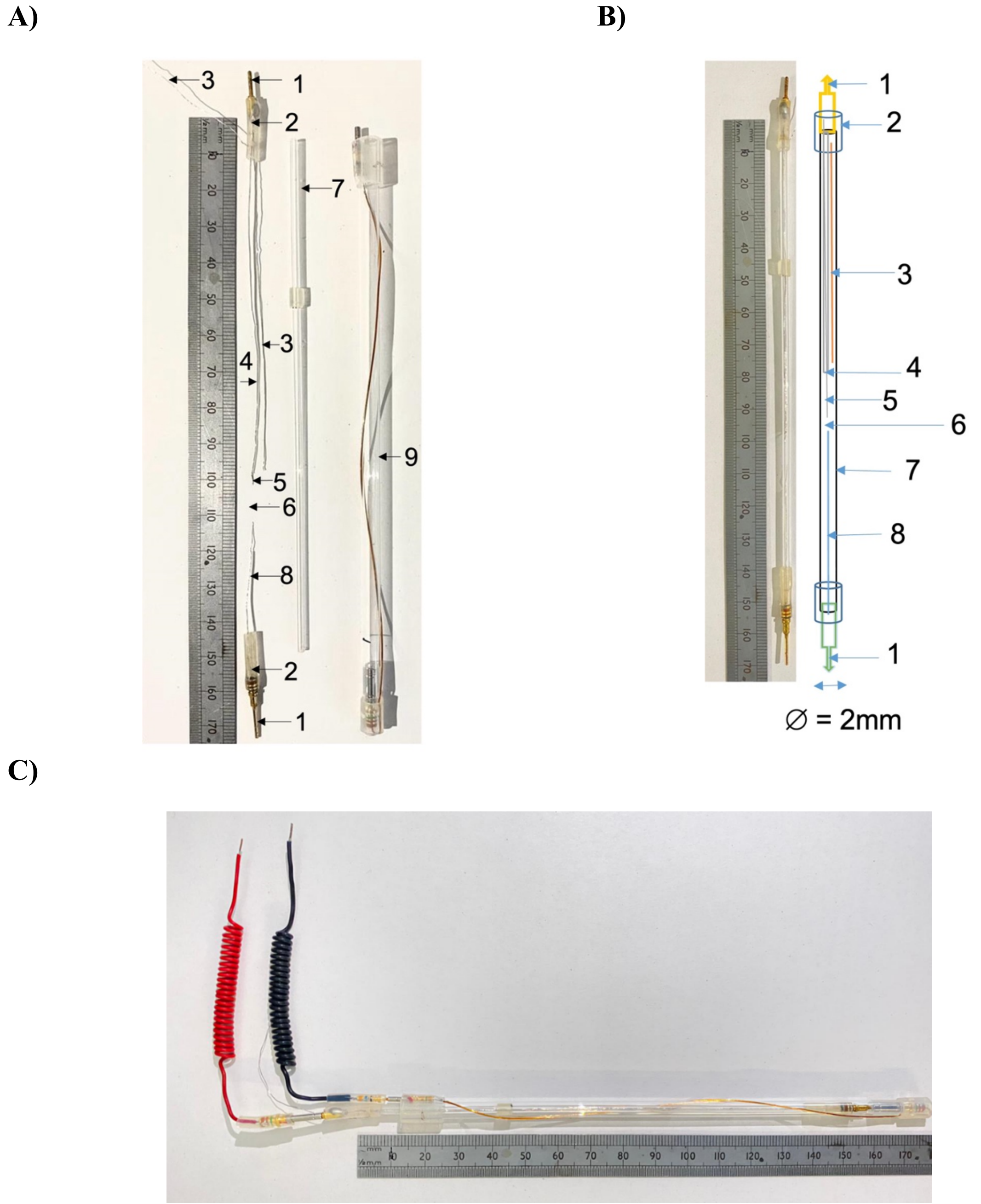

Figure 6.22. ***A)*** *Labeled pictorial depiction of the various components of the in-situ EC-EPR cell. The labeled parts are as follows: 1 - connecting pin, 2 - silicon connecting tube, 3 - counter electrode (Pt), 4 - Teflon tube, which insulates the reference almost the entire length of the reference electrode from the counter electrode to prevent the possibility of short circuit, 5 - reference electrode (PdH), 6 - the distance between the reference and working electrode (maximum of 10 mm was used), 7 - capillary tube, 8 - working electrode (Pt), and 9 - the holder/protector for the EPR capillary cell. The reference, counter, and working electrodes length are 100 mm, 96 mm, and 44 mm, respectively. About 3 mm of the reference electrode is left uninsulated in this case.* ***B)*** *Pictorial representation (left) and labeled schematic diagram (right) of the fully assembled quartz EPR capillary cell. The capillary tube has an outer diameter (∅) of 2 mm and an inner diameter of 0.8 mm.* ***C)*** *Fully assembled in-situ EC-EPR cell. This incorporates the quartz EPR capillary cell in its holder/protector, with a red wire connecting the reference electrode to the potentiostat and a black wire*

connecting the working electrode to the potentiostat. In contrast, a Pt wire connects the counter electrode to the potentiostat.

Figures 6.23A and **B** show the voltammetric measurements performed in the H_{upd} and the entire potential regions in an Argon-saturated 0.1 M $HClO_4$ medium using a mercury-mercurous sulfate reference electrode. It is essential to remark that the CV measurements in **Figures 6.23A** and **B** were obtained using the *in-situ* EC-EPR cell outside of the EPR spectrometer. Subsequently, the *in-situ* EC-EPR cell was placed inside the EPR spectrometer to record another voltammetric measurement conducted in an Ar-saturated electrolyte atmosphere (*cf.* **Figure 6.23C).** Due to the compactness of the *in-situ* EC-EPR cell and the EPR spectrometer, a PdH reference electrode was used in this configuration. After optimizing the CV, the EPR was tuned. The *in-situ* EC-EPR investigations were performed by holding the potentials for 25 minutes at the H_{upd} region to ensure that a sufficient quantity of atomic hydrogen is formed on the surface of Pt WE for being detected by EPR.

Before the *in-situ* measurements, the 2 mm outer diameter quartz EPR tube was inserted into the EPR device to obtain its response toward the EPR signal. Generally, relatively weak signals were obtained with low signal-to-noise ratios (*cf.* **Figure 6.24)**. Its corresponding integrated spectrum is also portrayed in the upper part of **Figure 6.23D**. It is essential to remark that the reference quartz EPR tube signals are weakened due to the introduction of the electrolyte. From the information obtained from the reference EPR signal, any slight modification could mean a possibility to detect adsorbed hydrogen or other paramagnetic species produced during the electrochemistry since Pt is by itself non-paramagnetic and, therefore, EPR inactive. The as-obtained EPR spectra after holding desorption potentials for 25 minutes at 0.25 V and 0.30 V *vs*. PdH RE are plotted in **Figure 6.24**. One can observe the appearance of additional EPR spikes/peaks for the two held potentials when compared to the reference, indicating a successful caging of atomic hydrogen on the surface of the working electrode. The EPR signal at 0.25 V appears more pronounced and generates a few more spikes than at 0.30 V *vs*. PdH RE. Similar results can be observed in the integrated EPR spectra (*cf.* **Figure 6.23D**). This indicates the presence of some intermediate paramagnetic radical species, *e.g.*, adsorbed hydrogen, which appeared at 0.25 V *vs*. PdH but was less evident at 0.30 V *vs*. PdH. Despite the long potential holding time, the obtained EPR signal needs to be stronger (seems very weak). This could be due to the constant quantity of paramagnetic species, which supports the hypothesis that this signal is due to H_{upd}, the limitation of the EPR sensitivity, or the electrolyte's dampening of the microwave radiation.

A)

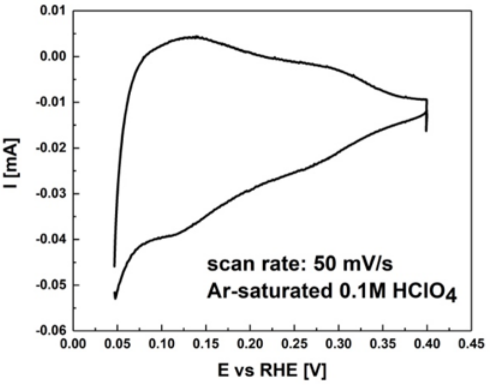
0.01
0.00
-0.01
-0.02
-0.03
-0.04
-0.05
-0.06
I [mA]
0.00
0.05
0.10
0.15
0.20
0.25
0.30
0.35
0.40
0.45
E vs RHE [V]
scan rate: 50 mV/s
Ar-saturated 0.1M $HClO_4$

B)

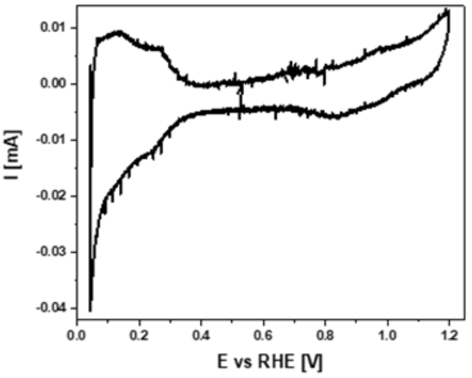
0.01
0.00
-0.01
-0.02
-0.03
-0.04
I [mA]
0.0
0.2
0.4
0.6
0.8
1.0
1.2
E vs RHE [V]

C)

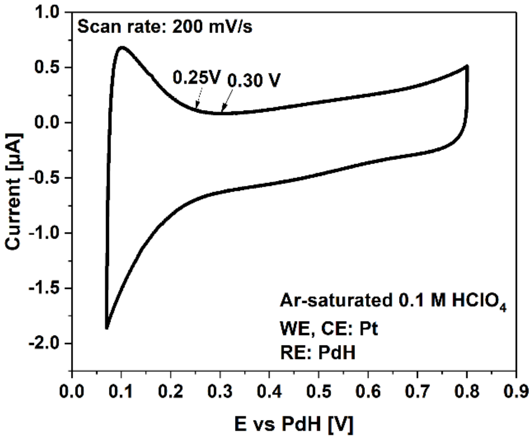
1.0
0.5
0.0
-0.5
-1.0
-1.5
-2.0
Current [µA]
Scan rate: 200 mV/s
0.25V
0.30 V
Ar-saturated 0.1 M $HClO_4$
WE, CE: Pt
RE: PdH
0.0
0.1
0.2
0.3
0.4
0.5
0.6
0.7
0.8
0.9
E vs PdH [V]

D)

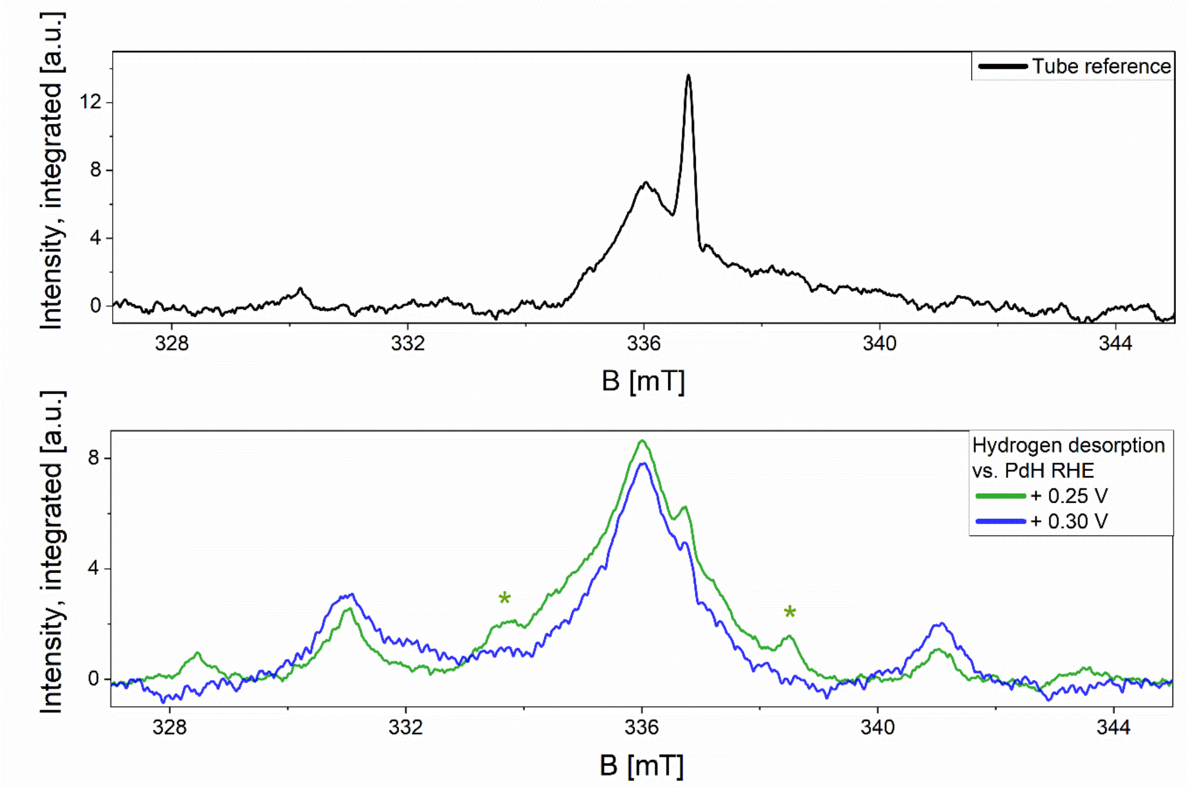

***Figure 6.23**. Cyclic voltammogram of Pt as the working electrode in **A)** narrow potential range, i.e., hydrogen under potential deposition region, and **B)** broad potential in an Ar-saturated 0.1 M $HClO_4$ with a scan rate of 50 mV s^{-1} **C)** Cyclic voltammogram performed in an Ar-saturated 0.1 M $HClO_4$ environment using a scan rate of 200 mV s^{-1} **D)** Integrated spectra of the capillary cell. Top: Integrated reference spectrum obtained with two visible EPR signals (336.1 mT, 336.7 mT) stemming from the tubes. Bottom: Integrated EPR spectra of the whole in-situ cell at desorption potentials 0.25 V and 0.30 V vs. PdH RE. Asterixes: Additional EPR signals around magnetic field values of 333.8 mT (g = 2.023) and 338.5 mT (g = 1.995) for +0.25 V vs. PdH. The parameters used for the measurements are as follows: Sweep time: 1500 s, modulation amplitude: 200 µT, power: 0.1 mW, microwave frequency: 9.452 GHz.*

EPR Spectra of the Pt-$HClO_4$-PdH In-situ Cell

The EPR spectrum of the quartz EPR capillary tube was recorded to serve as the reference (*cf.* upper part of **Figure 6.24**). The as-recorded EPR spectra conducted *in-situ* by holding the potentials at 0.25 V and 0.30 V *vs*. PdH, respectively, are also displayed with a magnification factor of 4 compared to the reference spectra (center and bottom part of **Figure 6.24**).

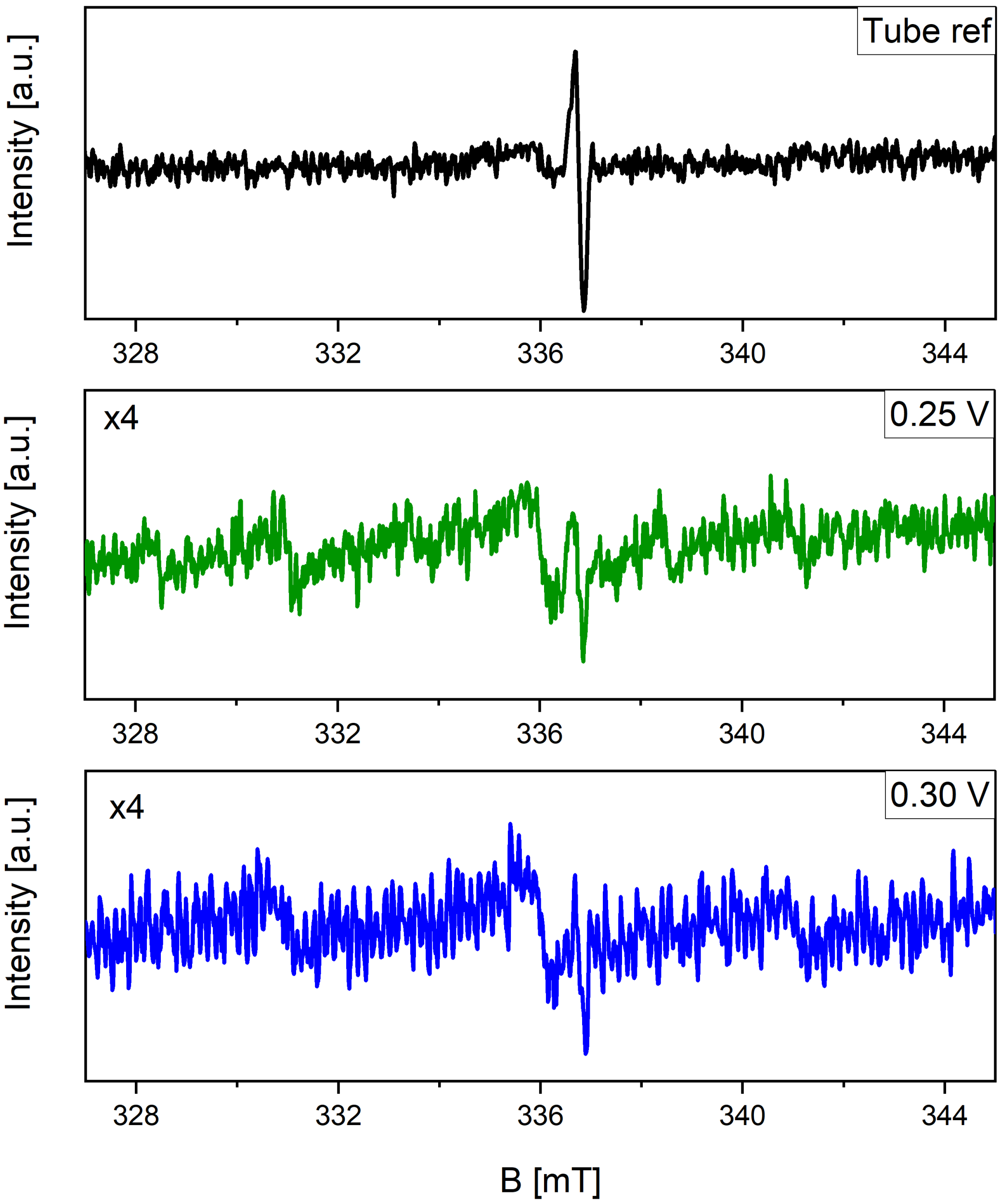

Figure 6.24. As-obtained EPR signals for the quartz EPR tube (reference) and the in-situ cell at hydrogen underpotential deposition potentials of 0.25 V and 0.30 V vs. PdH RE. Each spectrum is an average of three recordings. The spectra of the in-situ cell are multiplied by a factor of four with respect to the reference signal.

7.0 Concluding Remarks and Perspectives

This work aimed to study the influence of the electrolyte composition on the properties of the electric double layer and the electrode activity. In this respect, the unique laser-induced current transient technique was applied in the investigation of various electrochemical reactions and systems. The effects of electrolyte pH, alkali metal cation, and anion were systematically investigated. In particular, the hydrogen evolution, oxygen reduction, and oxygen evolution reactions were selected. Based on the obtained results, it can be inferred that the reaction under study proceeds at a fast rate when the potential of maximum entropy is closer to the thermodynamic equilibrium potential of that specific reaction, in line with our hypothesis. Another target of this dissertation was to develop and build a functional *in-situ* EC-EPR cell to probe the reaction mechanism of electrocatalytic reactions.

In **sections 6.1** and **6.2**, the measurements were conducted for the polycrystalline gold electrodes in electrolytes of various compositions. The LICT technique experiments with cyclic voltammetry confirmed electrolyte composition's influence on the EDL's properties. For the Au_{pc} in $HClO_4$ solutions at different pH values, higher H^+ concentrations of electrolytes lead to the enhancement of both electrode activities towards the HER. By contrast, lower H^+ concentrations of electrolytes lead to the enhancement of the activities towards the ORR. This is because the PME for lower pH values was closer to the thermodynamic equilibrium potential of the HER. In comparison, the PME is closer to the ORR for electrolyte compositions with lower concentrations of H^+. The introduction of oxygen can also alter the EDL properties because the local protons at the electrode/electrolyte interface can be consumed by reducing O_2 during the LICT measurements; this, in turn, leads to a change in the local pH.

Regarding the alkali metal cations, the PME showed a higher sensitivity to the pH in the presence of K^+ than Na^+. The PME increased with the rise of the electrolyte pH. However, it is worth noting that the PME can be altered sharply at some point (for instance, from pH 4 to 6 for the Au_{pc} electrode in 0.5 M K_2SO_4 solution). Besides, the interfacial structure for the Au_{pc} electrode in the electrolyte containing Na^+ and K^+ ions can be hugely different because of the enormous PME difference for these two cations, for instance, at pH 6. In this case, Na_2SO_4 and K_2SO_4 cannot be considered equal supporting electrolytes. As for the case in $HClO_4$ solutions, oxygen can also move the PME to more positive potentials in the alkali metal cations electrolyte. When fixing pH at 6, there was a linear relationship between the PME and the HER and ORR activities for the Au_{pc} electrodes in the presence of alkali metal cations. The PME increased with the decrease of hydration energy in the following order: $Li^+ < Na^+ < K^+ < Cs^+$. The rate of the HER increased in the Li^+-containing solutions, while the activity toward the ORR became higher in the presence of Cs^+. One can deduce that the electrode activity depends on the nature of the alkali metal cation since the HER and ORR activities presented a linear trend with the hydration energies of the corresponding alkali metal cations. The results of this part demonstrated that the different H^+ concentrations and the presence of alkali metal cations influence the interfacial structure, which can be further seen in electrocatalytic reactions.

Section 6.3 investigated the alkali metal cation effect on the OER activity of the surface-mounted metal-organic framework (SURMOF)-derived NiFe(OOH) electrocatalysts in alkaline media. It was established that the activity of the SURMOF-derivatives towards the OER shows a decreasing order, *i.e.*, $Cs^+ > K^+ > Na^+ > Li^+$. The LICT measurements revealed that the PME of the SURMOF derivatives was closer to the thermodynamic equilibrium potential of the OER in the presence of Cs^+. Furthermore, the obtained PME showed an approximately linear relationship with the OER activity, which evidences a clear correlation between the OER performance of the SURMOF-derivatives and the nature of the alkali metal cation. The observed results in this part further confirm our expectation that the closer the PME is to the thermodynamic equilibrium potential of a particular reaction, the faster that reaction would be.

Section 6.4 dealt with the impact of anions on the NiHCF PBA battery cathode electrode. The electrolytes deployed for this purpose were 0.25 M Ar-saturated sodium-based anions Na*X* (*X* = ClO_4^-, NO_3^-, Cl^-, SO_4^{2-}, CH_3COO^-). Multiple PMEs were obtained for every electrolyte. Apart from NaOAc and $NaNO_3$, showing two and three PMEs, respectively, the remaining exhibited five PMEs. Moreover, the plot of PME against hydration energy did not particularly follow any trend. Therefore, the data interpretation took a lot of work. Nonetheless, one can observe the influence of anions in the ongoing PME and intercalation and deintercalation processes.

In **sections 6.5** and **6.6**, the LICT assessments on atomic layer deposition deposited Pd monolayers on the Au QCM electrodes and electrochemically deposited Pd monolayers on the Au electrodes were performed. The ALD-deposited Pd monolayers on the Au QCM electrode system were investigated for the pH effect of varying concentrations or pHs of Ar-saturated perchloric acid solutions. Three principal methods were deployed: the LICT, CV, and EIS methodologies. The PMEs followed the order of 1 M $HClO_4$ > 0.1 M $HClO_4$ > 0.01 M $HClO_4$. The PME scaled linearly with the electrolyte pH, implying that locally reducing protons in the solution will significantly improve the system's performance toward the HER, and the opposite is true for the ORR. The minimum double-layer capacitance showed the same trend as the PME and hence correlated nicely. Using the electrochemically deposited Pd MLs on the Au QCM electrodes, the impact of cations in 0.1 M *AM*OH (*AM* = Li^+, Na^+, K^+, Cs^+) was studied. Principally, the evaluated PME results followed the order of $Cs^+ < K^+ < Na^+ < Li^+$. The results suggest that to enhance the HER significantly, Cs^+ will be preferred since it is closest to the thermodynamic equilibrium potential of that reaction. Meanwhile, Li^+, with the highest PME value, will promote the ORR. The hydration energy plot *versus* the applied potential reveals a linear relationship. Electrolyte components radically impact electrode processes.

Overall, the LICT technique shows great potential to be a powerful tool for investigating various electrochemical systems, thanks to its relative simplicity and the ease of combining it with other techniques. Determining the PME with the LICT method provides information on the EDL structure, which is helpful for better understanding the mechanisms of the electrochemical processes at the electrode/electrolyte interface. The LICT technique has been successfully employed to study noble metal electrodes, non-noble metal electrodes, metal oxides, and polymers. The obtained information about the EDL structure is significant for optimizing the studied systems. Excitingly, the role of the electrolyte composition in the electrochemical system requires highlighting due to its importance in characterizing the electrode performance. The presented results in this thesis demonstrate the ability of the LICT technique to improve the fundamental understanding of electrolyte effects in different simple or complex electrochemical systems. Therefore, this method can be utilized for other electrochemical systems: for instance, in the presence of organic and solid electrolytes. In addition, it can be applied to investigate the electrochemical interface reconstruction of other soft coinage metals. Ultimately, this precious and unique method can be a powerful tool for studying the mechanism of the interfacial processes and further optimizing several electrochemical systems.

In **section 6.7**, after relentlessly trying various configurations, a functional and unique *in-situ* EC-EPR cell setup was designed, constructed, and tested for a liquid electrocatalytic system. To our knowledge, this is the first report on successfully caging adsorbed hydrogen atomic species *via in-situ* EC-EPR methodology using either hydrogen or an Ar-saturated 0.1 M $HClO_4$ aqueous electrolyte to study the hydrogen adsorption process. Mainly, this study revealed that the modification in the paramagnetic species from the obtained EPR signals at 0.25 V to 0.3 V *vs*. PdH reference electrode could be linked to the formation of atomic hydrogen species.

Therefore, the developed methodology of combining a liquid electrocatalytic system with CV and EPR spectroscopy opens a leeway to probe further the selectivity and/or reaction pathway of other reactions through similar approaches to investigate the radical intermediates consumed or produced. The methodologies used in this dissertation could unlock numerous elusive processes and bring clarity to several electrochemical theories.

8.0 Appendix /Annex

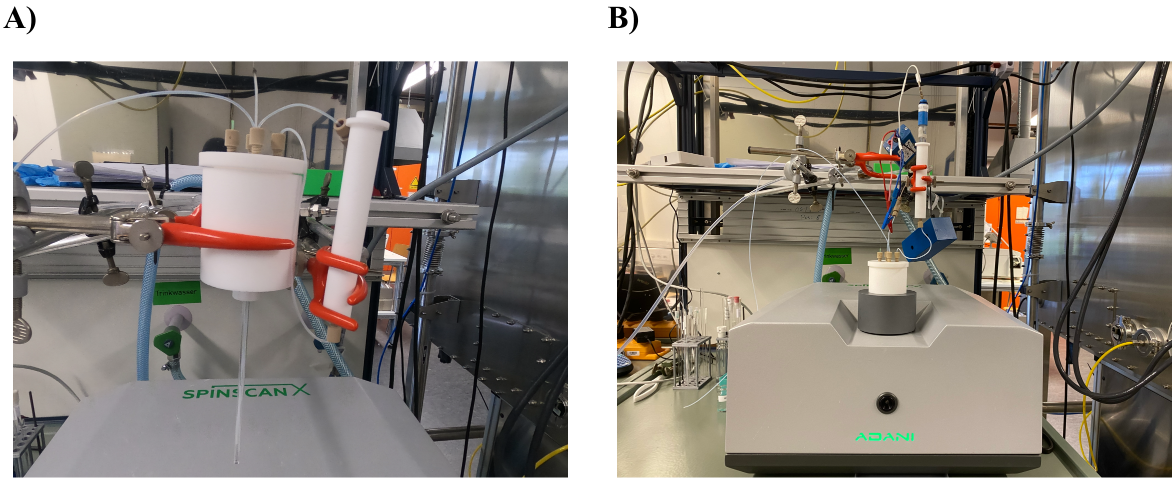

Figure A1.1. *Labeled pictorial representation of* ***A)*** *The main cell compartment housing the electrolyte, the gas inlet and outlet, and the three electrodes, working, counter and reference electrodes.* ***B)*** *the fully assembled in-situ EC-EPR cell setup placed in the EPR device with a Teflon support and the various electrodes connected to the potentiostat.*

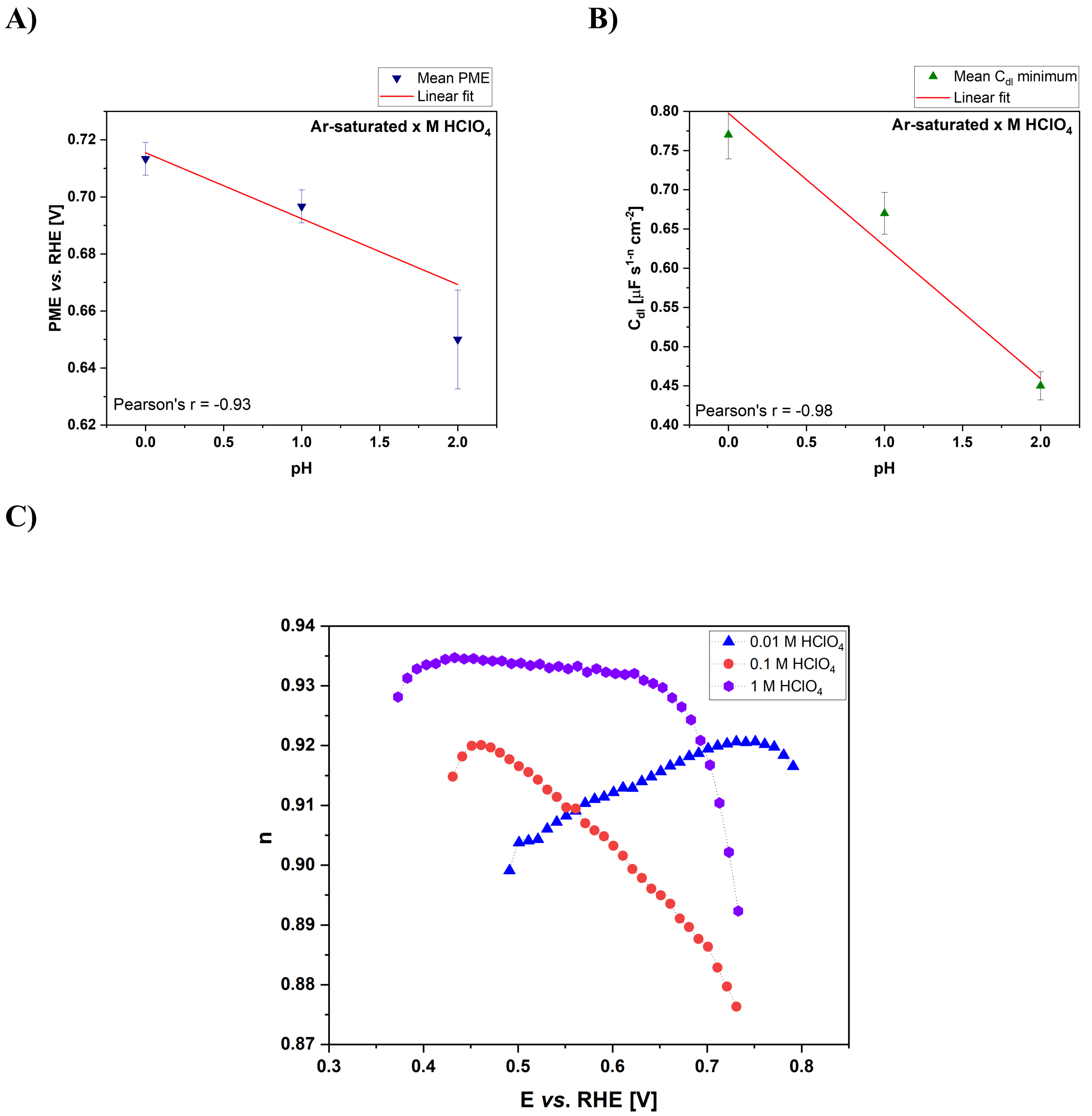

***Figure A2.1**. **A)** Graphical depiction of the relation between PME and pH **B)** A plot of double-layer capacitance as a function of electrolyte pH. The electrolyte employed was Ar-saturated perchloric acid and the electrode was Pd MLs on the Au. **C)** Graphical representation of the n values (CPE exponents) of the CPE plotted as a function of the applied potential in various concentrations of Ar-saturated perchloric acid. The electrode used was Pd MLs on the Au.*

8.1 List of Figures

***Figure 1.1**. A clear depiction of the accelerated growth in the global population from 1700 to the present time (2022). The statistical data for the plot was obtained from reference.[1]* 2

***Figure 1.2**. Graphical depiction of the eminent global warming. It is important to remark that most of the data relate to the fifth assessment report (AR5) released in 2013-2014. The AR5 data originated from 15 Earth system models (ESMs) and 5 Earth system models of Intermediate Complexity (EMICs). Displayed in black are the historical observations, the representative concentration pathway (RCP)8.5 scenario is in red, and the red-shaded plume portrays the range across the models. The solid line with dots depicts the globally averaged near-surface air temperature response to cumulative carbon dioxide (CO_2) emissions in addition to non-CO_2 forcers. The purple-shaded plume and the line signify the temperature response to cumulative CO_2 emissions and the non-CO_2 warming transient climate response to cumulative CO_2 emission (TCRE) distribution. The filled purple diamond represents the 2010 observation of surface temperature change (0.97°C based on the 2006-2015 mean compared to 1850-1900) and cumulative carbon dioxide emissions from 1876 to the end of 2010 of 1,930 GtCO_2. Shown as a hollow purple diamond is the value for 2017 based on the latest cumulative carbon emissions up to the end of 2017 of 2,220 GtCO_2 and a surface temperature anomaly of 1.1°C based on an assumed temperature increase of 0.2°C per decade. The thin blue line reveals the annual observations, with CO_2 emissions and estimated globally averaged near-surface temperature from scaling the incomplete coverage and blended HadCRUT4 dataset. The thin black line shows the coupled model intercomparison project (CMIP)5 multimodel mean estimate with CO_2 emissions. The thin black line portrays the global mean surface temperature (GMST) historical temperature trends, displaying lower temperature changes (0.87°C) up to 2006-2015, consequently leading to a larger balance in the carbon budget. The dotted black lines illustrate the remaining carbon budget estimates for 1.5°C. It is important to note that these remaining budgets exclude possible Earth system feedbacks that could reduce the budget, such as CO_2 and CH_4 release from permafrost thawing and tropical wetlands. Reproduced from reference.[24] Open access, permission of unrestricted use.* 6

***Figure 1.3**. The gradual global shift from the over-reliance on fossils to clean, green, low-carbon emission replacements. In 2020, oil contributed over 30%, coal ca. 30%, and natural gas over 20%, indicating ca. 80% of the global energy generation was based on high-carbon emission fossil fuel sources. The narrative in 2050 will be substantially the opposite as the reliance on fossils is predicted to dwindle while renewables, nuclear, and other sources will dominate. Adapted from reference.[36] Open access, permission of unrestricted use.* 8

***Figure 1.4**. **A)** Transport emissions in the European Union (EU) in 2019. **B)** Schematic depiction of the enormous potential of electricity and a hydrogen-powered universe. Herein, the numerous ways hydrogen can be generated and its scope of use are highlighted. The goal is to produce hydrogen utilizing a "green" and clean methodology, i.e., via electrolysis from a renewable energy source. Hydrogen is mainly employed in the production of ammonia. It is believed that eventually, the application of hydrogen will be dominant in the chemical production, metal refining, and fuel cell industries as the oil refining and synthetic gas production industries take the backstage. Reproduced from reference.[109] Open access, permission of unrestricted use.* 16

***Figure 2.1**. Modified schematic demonstration of the electric double-layer model on a negatively charged metal electrode. The inner and outer Helmholtz planes, as well as the diffuse layer, are exhibited. Water molecules are shown as blue spheres with arrows, whereas the hydrated cations are depicted in green, with the specifically adsorbed anion species in red. Figure adapted from reference.[189]* 29

***Figure 2.2**. Equivalent electric circuit model of the electrode/electrolyte interface.* 30

Figure 2.3. *Typical schematic representation of the potential energy profile of a chemical reaction.* 36

Figure 2.4. *A plot of current density as a function of the calculated overpotential from the Butler-Volmer equation. As calculated via the Nernst equation, the equilibrium potential herein is termed the Zero overpotential. The red curve indicates the total current density calculated using the Butler-Volmer equation. The blue curves depict the anodic and cathodic current densities corresponding to one electrode's oxidation and reduction currents.* 38

Figure 2.5. *Volcano plot for the oxygen reduction reaction. Herein, the activity is plotted as a function of the binding energy of adsorbed oxygen for different metal electrode surfaces. Pt exhibits close to optimum binding energy as well as activity. Reprinted with permission from reference.*[206] *Copyright © (2018), Royal Society of Chemistry.* 44

Figure 2.6. *Theoretical predictions of the free energies of adsorption of* $HOO_{(ads)}$ *(HOO*),* $HO_{(ads)}$ *(HO*) and* $O_{(ads)}$ *(O*). A plot of* ΔG_{HOO^*}, ΔG_{HO^*}, *and* ΔG_{O^*}, *respectively against* ΔG_{HO^*} *for (111), (100), and (211) for pure metal surfaces (filled squares) and Pt overlayers on Pt-alloy surfaces (open circles). Reprinted with permission from reference.*[207] *Copyright © (2005), Elsevier B. V.* 46

Figure 2.7. ***A)** Schematic depiction of a typical water electrolyzer, with the HER taking place at the cathode and the OER occurring at the anode. **B)** Schematic representation of the water splitting process, which has its source of electricity to decompose water into its gas components from renewables. Reproduced from reference*[232] *with permission from the Royal Society of Chemistry. Open access, published under a CC-BY license.* 49

Figure 2.8. *Schematic representation of a typical PEMFC. The anode has the source fuel* H_2 *where the HOR occurs, whereas the cathode with the oxidant (atmospheric oxygen) exhibits the ORR. Reproduced with permission from reference.*[250] *Copyright © (2000), WILEY-VCH Verlag GmbH, Weinheim, Fed. Rep. of Germany.* 56

Figure 3.1. *Schematic depiction of the orientation of water molecules at the electrode surface for **A)** a negatively charged and **B)** a positively charged electrode surface, respectively. For the water layer structure, oxygen is shown in red, whereas hydrogen is represented in silver/grey.* 64

Figure 3.2. *AIMD simulation results showing the calculated* N_{donor} *of interfacial water molecules as a function of the potential. Potential-dependent structures of the interfacial water layer are shown in the inset, labeled i to vi. The dynamics of interfacial water layer structure reveal constantly evolving patterns of the hydrogen molecules, from (i) two-H-sideways, (ii) to (v) one-H-down, and (vi) two-H-down. Reproduced with permission from reference.* [286] *Copyright © (2021), The Author(s), under exclusive license to Springer Nature Limited.* 65

Figure 3.3. ***A)** The double layer structure of a negatively charged electrode surface and the arrangement of the water layer structure around it. The PME is depicted as the potential with the most chaos and where the flipping of the signs of the water dipole occurs, whereas at the PZC, no net charge exists on the electrode surface. Figure reprinted from reference.*[157] ***B)** A schematic explanation of the arrangement of interfacial water dipoles and net electrode surface charges for key interfacial parameters like the potentials of zero charge and maximum entropy. Figure modified from reference.*[161] ***C)** Schematic depiction of a possible expectation at the potential of maximum entropy. Thanks to the enormous degree of chaos at the PME, species can be exchanged rapidly, which leads to faster kinetics and enhanced performance. Meanwhile, for the other instances showing either positive or negative electrode surface charge, the water layer structure is well ordered; hence the exchange of species proceeds rather slowly. Figure reproduced with permission from*

reference.[160] Copyright © (2021), The Authors. ChemElectroChem published by Wiley-VCH GmbH. Open access, published under a CC-BY license. 70

***Figure 3.4**. Schematic depiction of a typical electrocapillary curve. In other words, the surface tension of an electrode is plotted as a function of the applied potential. The PZC is indicated with a dot and arrow, corresponding to the apex of the surface tension.* 72

***Figure 3.5**. Typical graphical representation of the double layer capacitance (Cdl), which depicts the capacitance plotted as a function of the potential. The minimum of the capacitance-potential curve is known to be the minimum of the differential double-layer capacitance and corresponds to the PZC.* 74

***Figure 3.6**. Graphical representation of the total charge plotted as a function of the electrode potential. The PZC is captured as the potential corresponding to a total electrode charge (charge density) of zero.* 75

***Figure 3.7**. Graphical representation of an N_2O reduction plot conducted on Pt(111) in 0.1 M $HClO_4$. The maximum current peak of N_2O reduction, which is also the PZC, was found to be 0.34 V. Scan rate: 50 mV s^{-1}. Reprinted with permission from reference.[326] Copyright © (1995), Published by Elsevier B. V.* 77

***Figure 3.8**. **A)** An example of a 3D plotted current transients recorded during the laser measurement at various electrochemical potentials. The potential at which the current transients flip its sign corresponds to the PME, and the sign of the current transients coincides with the sign of the electrode surface charge. The figure was obtained from measurements conducted on polycrystalline gold in 0.5 M O_2-saturated Na_2SO_4 solution (pH 2) and was reprinted with permission from references.[161,130] Copyright © (2021), The Authors. Published by Wiley-VCH GmbH. Open access, published under a CC-BY license. **B)** An instance of a 2D current transient diagram with the extreme current transients plotted as a function of the applied potential on the reversible hydrogen electrode (RHE) scale. The data for plotting B was obtained from **A**). It is necessary to note that only some of the current transients are presented in this illustration. Reproduced from reference.[161]* 85

***Figure 3.9**. Representative scheme of the laser-induced current transient (LICT) technique setup. The laser head is shown on the left, with the three-electrode configuration electrochemical working cell on the right. The various numerically labeled parts are described as follows: 1 - electrolyte inlet, 2 - hot-water outlet, 3 - gas outlet, 4 - counter electrode (CE), 5 - electrolyte inlet/preconditioning chamber, 6 - gas inlet, 7 - reference electrode (RE), 8 - working electrode (WE), and 9 - hot-water inlet. Essentially, the relative positions of the electrodes, as portrayed in **Figure 3.9**, do not precisely correspond to the real measurement configuration, where the RE is located in between the WE and CE instead. Figure modified with permission from references.[161,162] Copyright © (2023), Elsevier Inc. All rights reserved.* 87

***Figure 3.10**. A bar chart plot depicting a comparison of the hydrogen evolution reaction activities of **A)** Pt(111), Pt(221), and Pt_{pc} electrodes in H_2-saturated 0.1 M MeOH electrolytes ($Me^+ = Li^+$, Na^+, K^+, Rb^+, Cs^+), **B)** Ir(111), **C)** Au(111) and Ag_{pc} electrodes.[356] **D)** OER activities of Ir-oxide thin films in $HClO_4$ and H_2SO_4 at pH = 1 (the curves have been iR-corrected).[357] The conditions and electrolyte components for each measurement are provided in the respective Figures. The so-called spectator species significantly impacts the hydrogen and oxygen evolution reactions, i.e., water electrolysis. Reproduced with permission from references.[356,357] Copyright © (2018), Wiley-VCH Verlag GmbH & Co. KGaA, Weinheim; Copyright © (2015), Royal Society of Chemistry.* 88

***Figure 3.11**. **A)** A plot of the activity trend of the HER for Pt(pc) electrodes in 0.1 M AMOH electrolytes (AM = Li^+, Na^+, K^+, Cs^+). Insert: Information on the Tafel slopes for the different electrolytes. **B)** Bar chart depicting the reaction-free energies computed for the Volmer, Tafel, and Heyrovsky steps of the HER on the pristine Pt(111) surface and in the presence of alkali metal cations. The results for bare and solvated cations are presented on the left and right sides, respectively, with the exemplary atomic-structure snapshots for the Li^+ case. Only the most energetically favorable reaction pathways obtained for each step are displayed for*

clarity. Reproduced from reference.[369] Copyright © (2022), Chongqing University. Production and hosting by Elsevier B.V. on behalf of KeAi. Open access, CC-BY-NC-ND 4.0... 90

***Figure 3.12**. **A)** Graphical representation of cyclic voltammograms (—) and concurrently recorded mass change (...) of a quartz-supported Pt electrode in the various electrolytes indicated in the figures. Scan rate: 100 mV s^{-1}. **B)** Absolute values of Δm versus Δq obtained from **Figure 3.12A**. The mass variations and charge densities correspond to the electrochemical area of the Pt electrode. Reproduced with permission from reference.[375] Copyright © (2000), Elsevier Science S. A. All rights reserved. 92*

***Figure 3.13**. **A)** A graphical representation of the exchange current density of HOR/HER plotted as a function of electrolyte pH on Pd/C nanocatalyst. The HOR/HER polarization curves were recorded via the rotating disk electrode (RDE) method in H_2-saturated electrolytes at 293 K. Scan rate: 1 mV s^{-1}, rotation speed: 1600 rpm. **B)** H_{upd} desorption peak potentials obtained from cyclic voltammograms of Pd/C plotted against electrolyte pH. From reference.[385] Reprinted with permission from AAAS. Copyright © (2016), The Authors. Open access, Creative Commons Attribution-NonCommercial license... 94*

***Figure 4.1**. Simplified scheme of a typical three-electrode setup. The reference, working, and counter electrodes are denoted by RE, WE, and CE, respectively. The electrolyte is depicted as blue color, whereas the voltmeter and ammeter are represented by V and A, respectively.. 96*

***Figure 4.2**. **A)** A model cyclic voltammetric plot indicating the time dependence relative to the applied electrode potential. E_1 and E_2 represent the minimum initial and maximum final electrode potentials. Essentially, parameters like the potential range and scan rate immensely influence the shape of the CV. **B)** A recorded typical stable cyclic voltammetric profile of a well-ordered Pt(111) electrode in 0.1 M $HClO_4$ electrolyte at a scan rate of 50 mV s^{-1}. Three distinguished regions can be observed: the hydrogen regime, the double-layer region, and the oxygen region. These separate regions are labeled I, II, and III, respectively. Figure reproduced with permission from reference.[] Copyright © (2014), Royal Society of Chemistry..... 98*

***Figure 4.3**. **A)** Prototypical Nyquist plot representation of EIS data and the insert is the electrochemical equivalent circuit depicting the type of reaction ongoing. **B)** Standard Bode plot representation for the EIS data corresponding to the Nyquist plot. Figures reproduced with permission from reference.[] Copyright © 1994 IUPAC... 104*

***Figure 4.4**. Energy state diagram of an element with spin S = ½ interacting with a nuclear spin of I = 3/2 .... 107*

***Figure 5.1**. Schematic depiction of the specially designed electrochemical cell for realizing several measurements, including CV, EIS, and LICT. Two compartments, namely, the preconditioning chamber, labeled (1), and the main compartment, named (2), make up the electrochemical cell. For completion, it is essential to mention that the three electrodes, the working electrode (WE), the counter electrode (CE), and the reference electrode (RE), are all placed in the main compartment. A distinct feature worth mentioning is the flat, light (laser, in this case) transmittable glass window, specially designed on the main compartment, named (2), permitting the laser beam to directly irradiate the working electrode surface. As represented in this figure, the relative positions of the various electrodes in the setup do not precisely correspond to their appearance in actual experimental measurements. Figure reprinted with permission from reference.[130,161] Copyright © (2021), The Authors. Published by Wiley-VCH GmbH. Open access, published under a CC-BY license. 109*

***Figure 5.2**. AT-cut EQCM electrode **A)** Au **B)** Electrochemically deposited Pd MLs on the Au electrode **C)** Atomic layer deposition deposited Pd MLs on the Au electrode **D)** Graphical illustration of the CVs of the*

Au QCM electrode before (red-labeled CV_{bd}) and after (blue-labeled CV_{ad}) the electrochemical deposition in 0.1 M H_2SO_4 and 0.1 mM H_2PdCl_4. The CVs were conducted in an Ar-saturated 0.1 M H_2SO_4 at a scan rate of 50 mV s^{-1}. ***E)*** *Scanning electron microscope image showing the topology of the freshly electrochemically deposited Pd MLs on the Au electrode. Almost the entire surface is homogeneously covered with Pd MLs. The few dark spots represent the Au electrodes that were not adequately covered due to mechanical failure and other defects. 112*

Figure 5.3*. CV (cleaning and surface probing) obtained on the* ***A)*** *ALD Pd ML on the Au QCM electrode using Ar-saturated 0.1 M $HClO_4$* ***B)*** *electrochemically deposited Pd ML on the Au QCM electrode using an Ar-saturated 0.1 M KOH. Only 3 CV cycles were performed at a scan rate of 50 mV s^{-1} for* ***A)*** *and* ***B)****. However, before the LICT, 10 CV cycles were done at a scan rate of* ***A)*** *50 mV s^{-1} and* ***B)*** *10 mV s^{-1}. The arrows indicate the direction of potential application for the laser measurements. 114*

Figure 5 4*. Graphical representation of the stable cyclic voltammogram recorded using Au_{pc} QCM electrode and 0.1 M H_2SO_4 electrolyte following electrochemical cleaning of several cycles. Scan rate: 50 mV s^{-1}. 116*

Figure 5.5*. Various CVs performed on the electrochemically deposited Pd MLs on the Au QCM electrode in Ar-saturated* ***A)*** *0.1 M LiOH,* ***B)*** *0.1 M NaOH,* ***C)*** *0.1 M KOH, and* ***D)*** *0.1 M CsOH. A scan rate of 50 mV s^{-1} was used for all the measurements. The red curve represents the starting or initial CV before the laser measurements, while the blue curve indicates the final CV or CV after the laser measurements. 117*

Figure 5.6*. Pictorial representation of the laser-induced current transient setup. The laser is depicted on the rear or furthest left part, with the attenuator placed a few centimeters away. The front or far right part is the position of the electrochemical cell, incorporating the three-electrode configuration. The working, counter, and reference electrodes are inserted at designated positions and connected to the potentiostat via clamps and wires. In detail, the WE is placed in the EQCM holder, and a clamp is inserted into the holder's head. The reference electrode is connected to the main cell, and by extension, the electrolyte via a Luggin capillary. 118*

Figure 5.7*. An example of the LICT measurements performed on the electrochemically deposited Pd MLs on the Au QCM electrode in an Ar-saturated 0.1 M KOH electrolyte. The potential range used lies within the double-layer region, and the PME (signaled by the zero-charge crossing) was found to be 0.65 V vs. RHE, as depicted with the arrow. 121*

Figure 5.8*.* ***A)*** *A pictorial (left) and schematic (right) representation of the in-situ electrochemical cell employed by reference in their investigation. Adapted from reference.[448] Copyright © (2022), American Chemical Society.* ***B)*** *Schematic representation of the in-situ EPR cell comprising a three-electrode configuration in the EPR capillary. Labeled a to k are: (a) Supporting Pt wire (diameter 0.5 mm); (b) WE, GO membrane coated onto Pt wire, with a length of ~2 cm; (c) intertwined Pt wire (diameter 0.05 mm); (d) sealant epoxy, prevents the short circuit, not in the EPR detecting area; (e) RE, insulated Ag wire (diameter 0.2 mm, coated with PTFE) with one end oxidized; (f) insulated Ag wire (diameter 0.2 mm, coated with PTFE) to connect the WE and the potentiostat; (g) CE, Pt mesh; (h) quartz capillary (diameter 1 mm); (i) aqueous electrolytes, e.g., Na_2SO_4/KOH; (j) sealant epoxy; (k) in-situ cell introduced into the EPR cavity. Adapted from reference.[449] Copyright © (2018), Royal Society of Chemistry.* ***C)*** *Schematic depiction of the in-situ EPR cell design used by reference[439] with a three-electrode configuration. Activated Carbon, Pt, and Ag|AgCl were the working, counter, and reference electrodes. Reprinted from reference.[439] Copyright © (2022), American Chemical Society.* ***D)*** *Schematic illustration of the entire EC-EPR cell design and construction as implemented by reference.[437] Reproduced with permission from reference.[437] Copyright © (2015), Elsevier. All rights reserved.* ***E)*** *A schematic example of typical EC-EPR cell designs implemented for use in Q- and W-band EPR range as reported by reference.[451] Adapted from reference.[451] Copyright © (2011), Elsevier. All rights reserved. 126*

Figure 5.9. ***A)*** *Pictorial representation of the interior of the EPR device, particularly highlighting the LGR attached to the constructed EC-EPR cell.* ***B)*** *The EC-EPR cell specifically developed to fit into the LGR. Labeled 1 to 6 are: 1, 3 - capillary supports, 2a - EPR sample tube specifically for use in the Q-band regime, 2b - X-band EPR tube for structural support, 4 - an adaptor for electrodes and sample flow, 5 - pegs for electrode attachment, 6 - capillary aiding the insertion of the working electrode to the resonator's sensitive part. WE, CE, and RE stand for working, counter, and reference electrodes, respectively.* ***C)*** *The output signal intensity plotted as a function of the magnetic field. Enhanced EPR signal sensitivity is realized using the LGR relative to the typical* TE_{011} *resonator used in most resonator cavities. Reproduced from reference*[435]*with permission from the Royal Society of Chemistry. Copyright © (2015), Royal Society of Chemistry.* *127*

Figure 5.10. ***A)*** *The in-situ EC-EPR cell components as-received from LINEV ADANI. Labeled 1 is the syringe, 2 - represents the working electrode, graphite in this case, 3 - is the counter/reference electrode; the tail end of the Ag wire has been coated with a mixture of* $FeCl_3$ *and* H_2SO_4 *to produce Ag/AgCl as the reference electrode, and the uncoated Ag parts represent the counter electrode, 4 - quartz EPR capillary tube of outer diameter 2 mm, inner diameter ca. 0.8-0.9 mm, 5 - tube holder/protector for the quartz EPR capillary tube, 6 -* $FeCl_3$ *solution, and 7 - ketoconazole solution in* H_2SO_4*.* ***B)*** *Pictorial depiction of the electrodes placed in the quartz EPR capillary tube. Particularly interesting is the display of the region where the center of the resonator is marked.* ***C)*** *Fully assembled EC-EPR cell* ***D)*** *The fully assembled EC-EPR cell in contact with their respective connecting pins.* ***E)*** *The connecting pins linked to the potentiostat.* *130*

Figure 5.11. ***A)*** *Cyclic voltammogram of Pt working electrode with Pt as CE and RE in an argon-saturated 0.1 M* $HClO_4$ *at a scan rate of 50 mV* s^{-1}*.* ***B)*** *CV implemented on Pt WE and CE with Pd as the RE in an argon-saturated 0.1 M* $HClO_4$ *at a scan rate of 200 mV* s^{-1}*.* ***C)*** *Graphical illustration of the hydrogen evolution reaction region performed using Pd as the working electrode and Pt as both counter and reference electrodes in 0.1 M* $HClO_4$ *in an open-air environment.* ***D)*** *Current held at -1 mA in the HER region for 300 seconds to further cause hydrogen adsorption in the bulk of Pd to produce a PdH reference electrode.* .. *131*

Figure 6.1. *Typical cyclic voltammograms of* Au_{pc} *measured at different pH values (0, 1, and 2) of the* $HClO_4$ *electrolytes. Scan rate: 50 mV* s^{-1}*. It is important to note that the CVs before and after the LICT measurements are almost indistinguishable. Reproduced from reference.*[161] *133*

Figure 6.2. *Model LICTs measured for* Au_{pc} *in an Ar-saturated* $HClO_4$ *at* ***A)*** *pH 1 and* ***B)*** *pH 2. It should be noted that all initial current values of the obtained transient peaks have been normalized to zero to ease comparison. The PME is located between the two potentials where the sign of the current transient varies. Reproduced from reference.*[161] *134*

Figure 6.3. *(****A*** *to* ***E****) Current extrema of the LICT results attained for the* Au_{pc} *electrode at different pH values (0, 0.5, 1.0, 1.5, and 2.0) of Ar-saturated* $HClO_4$ *electrolytes.* ***F)*** *The PME of* Au_{pc} *plotted as a function of the electrolyte pH. The PME of* Au_{pc} *shifts towards more positive values because of the pH rise. Reproduced from reference.* [161] *135*

Figure 6.4. *Characteristic* ***A)*** *HER and* ***B)*** *ORR polarization curves for* Au_{pc} *electrodes recorded at several pH values (0, 1.0, and 2.0) of* H_2*-saturated or* O_2*-saturated* $HClO_4$ *electrolytes. To augment the visibility, only the region dominated by the four-electron ORR kinetics is shown in* ***B)****.* ***C)*** *The HER activities of* Au_{pc}*, expressed as the exchange current density* j_0*, plotted as a function of the PME. A linear trend is observed between the PME and activity. Reproduced from reference.*[161] *136*

Figure 6.5. *Representative cyclic voltammograms of* Au_{pc} *at various pHs (2, 4, 6, 8, and 10) in 0.5 M Ar-saturated* ***A)*** Na_2SO_4 *and* ***B)*** K_2SO_4 *electrolytes. The scan rate used was 50 mV* s^{-1}*. Reproduced with*

permission from reference.[130,161] Copyright © (2021), The Authors. Published by Wiley-VCH GmbH. Open access, published under a CC-BY license. 138

Figure 6.6. Examples of cyclic voltammograms of the Au_{pc} electrode in 0.5 M Ar-saturated Na_2SO_4 (blue) and K_2SO_4 (red) electrolytes at pH 6. Scan rate: 50 mV s^{-1}. Reproduced with permission from reference.[130,161] Copyright © (2021), The Authors. Published by Wiley-VCH GmbH. Open access, published under a CC-BY license. 138

Figure 6.7. Typical cyclic voltammograms of the Au_{pc} electrode in 0.5 M Ar-saturated K_2SO_4 electrolytes at different scan rates. Reproduced from reference.[161] 139

Figure 6.8. 3D schemes of the LICT results acquired for Au_{pc} at pH 2 in **A)** an Ar-saturated and **B)** an O_2-saturated 0.5 M Na_2SO_4 electrolytes, respectively. (**C** and **D**) The corresponding 2D LICT graphs of the collected current extrema plotted as a function of the working electrode potential. Reproduced with permission from reference.[130,161] Copyright © (2021), The Authors. Published by Wiley-VCH GmbH. Open access, published under a CC-BY license. 140

Figure 6.9. (**A** to **D**) Extreme current values of the laser-induced transients for Au_{pc} submerged into Ar-saturated 0.5 M Na_2SO_4 solutions of different pHs (4, 6, 8, and 10). (**E** to **H**) The analogous extreme current values collected for the Au_{pc} immersed into the O_2-saturated 0.5 M Na_2SO_4 solutions. Reproduced with permission from reference.[130,161] Copyright © (2021), The Authors. Published by Wiley-VCH GmbH. Open access, published under a CC-BY license. 141

Figure 6.10. The PME values chronicled for Au_{pc} in Ar-saturated (blue) and O_2-saturated (red) 0.5 M Na_2SO_4 solutions plotted as a function of the electrolyte pH. Reproduced from reference.[161] 142

Figure 6.11. (**A** to **E**) Extreme values of laser-induced current transients estimated for Au_{pc} immersed into the Ar-saturated 0.5 M K_2SO_4 solutions of different pHs (2, 4, 6, 8, and 10). (**F** to **J**) Analogous extreme current values collected for Au_{pc} submerged into the O_2-saturated 0.5 M K_2SO_4 solutions of the corresponding pH values. **K**) The PME values plotted versus pH values for Au_{pc} in Ar-saturated (blue) and O_2-saturated (red) 0.5 M K_2SO_4 solutions. Reproduced from reference.[161] 143

Figure 6.12. The PME values for Au_{pc} in Ar-saturated (dot) and O_2-saturated (dash) 0.5 M Na_2SO_4 (blue) and K_2SO_4 (red) solutions depicted as a function of the electrolyte pH. Reproduced with permission from reference.[130,161] Copyright © (2021), The Authors. Published by Wiley-VCH GmbH. Open access, published under a CC-BY license. 145

Figure 6.13. Plots of the PME determined on the Au_{pc} electrode in **A)** Ar-saturated and **B)** O_2-saturated mixed solution of 60 mL 0.5 M Na_2SO_4 and 60 mL 0.5 M K_2SO_4 at pH 8. Reproduced with permission from reference.[130,161] Copyright © (2021), The Authors. Published by Wiley-VCH GmbH. Open access, published under a CC-BY license. 146

Figure 6.14. OER polarization curves of Ni|Fe-[TA]-Catalysts recorded in O_2-saturated 0.1 M LiOH (pH 13.1), 0.1 M NaOH (pH 13.4), 0.1 M KOH (pH 13.4), and 0.1 M CsOH (pH 13.5) electrolytes. Scan rate: 5 mV s^{-1}. Note, the SURMOFs derivatives are denoted as Catalyst after electrochemical cycling here. Reproduced with permission from references.[131,161] Copyright © (2022), The Authors. Angewandte Chemie International Edition published by Wiley-VCH GmbH. Open access, Creative Commons Attribution Non-Commercial NoDerivs License. 149

Figure 6.15. (**A** to **D**) The maximum current transient values plotted as a function of the applied potential for 0.1 M LiOH (pH 13.1), 0.1 M NaOH (pH 13.4), 0.1 M KOH (pH 13.4), and 0.1 M CsOH (pH 13.5) electrolytes, respectively. One can find the PME values at the point when the current transient changes its sign, i.e., $i_{Xtrm} \sim 0$. Reproduced with permission from references.[131,161] Copyright © (2022), The Authors.

Angewandte Chemie International Edition published by Wiley-VCH GmbH. Open access, Creative Commons Attribution Non-Commercial NoDerivs License. 150

***Figure 6.16**. Graphical representation of the current density at the potential of 1.53 V versus the PMEs of Ni|Fe-[TA]-Catalyst in electrolytes containing alkali metal cations. The Pearson correlation coefficient (r) is 0.92, according to the linear fitting. Reproduced with permission from references.*[131,161] *Copyright © (2022), The Authors. Angewandte Chemie International Edition published by Wiley-VCH GmbH. Open access, Creative Commons Attribution Non-Commercial NoDerivs License.* 151

***Figure 6.17**. **A)** CVs of* $Na_2Ni\square Fe(CN)_6\square$*- NiHCF thin films before and after the LICT measurement conducted in Ar-saturated 0.25 M NaX (where X =* NO_3^-, ClO_4^-, Cl^-, OAc^-, *and* SO_4^{2-}*). Two CV cycles were performed for each case. Scan rate: 50 mV* s^{-1} ***B)** to **F)** PME vs. potential on the SSC RE scale in Ar-saturated 0.25 M* $NaNO_3$, $NaClO_4$, *NaCl, NaOAc, and* Na_2SO_4 *electrolytes. **G)** Graphical representation of the PMEs vs. anion hydration energies of the various electrolytes* 154

***Figure 6.18**. Voltammograms conducted on the atomic layer deposition deposited Pd monolayers on an Au QCM electrode and an Ar-saturated **A)** 0.01 M* $HClO_4$ *(pH = 2), **C)** 0.1 M* $HClO_4$ *(pH = 1), and **E)** 1 M* $HClO_4$ *(pH = 0) electrolyte, respectively. Scan rate: 50 mV* s^{-1}*. CVs conducted before and after the LICT are depicted in **A)** green and blue, **C)** black and red, and **E)** purple and orange colors, respectively. Plots of the evaluated charge densities emanating from the current transients as a function of the applied potential for **B)** 0.01 M* $HClO_4$*, **D)** 0.1 M* $HClO_4$*, and **F)** 1 M* $HClO_4$ *electrolyte, respectively. The laser measurements were conducted from higher to lower potentials. The zero crossing of the charge density signifies the position of the PME.* 156

***Figure 6.19**. **A)** The equivalent electric circuit used to give meaning to the electrochemical system's reactions, mechanisms, and occurrences. **B)** Graphical representation of the plot of the capacitance of the double layer as a function of the applied potential in three different (1 M* $HClO_4$*, 0.1* $HClO_4$*, and 0.01 M* $HClO_4$*) electrolytes for Pd MLs on the Au QCM electrode.* 158

***Figure 6.20**. (**A** to **D**) The evaluated charge density from the current transients plotted as a function of the applied potential for the Pd MLs on the Au electrodes in Ar-saturated 0.1 M LiOH, 0.1 M NaOH, 0.1 M KOH, and 0.1 M CsOH electrolytes. The pHs of the various electrolytes were ca. 13. The PME value is indicated with an arrow, which occurs at the zero crossing of the charge density. The sweep direction of the laser measurements is marked with an arrow moving from right to left (higher to lower applied potentials).* ... 160

***Figure 6.21**. Graphical representation of the PME plotted as a function of the cation hydration energy. The measurements were conducted on Pd MLs on the Au electrode in AMOH, where AM = (*Li^+, Na^+, K^+, Cs^+*). An almost linear trend is observed.* 161

***Figure 6.22**. **A)** Labeled pictorial depiction of the various components of the in-situ EC-EPR cell. The labeled parts are as follows: 1 - connecting pin, 2 - silicon connecting tube, 3 - counter electrode (Pt), 4 - Teflon tube, which insulates the reference almost the entire length of the reference electrode from the counter electrode to prevent the possibility of short circuit, 5 - reference electrode (PdH), 6 - the distance between the reference and working electrode (maximum of 10 mm was used), 7 - capillary tube, 8 - working electrode (Pt), and 9 - the holder/protector for the EPR capillary cell. The reference, counter, and working electrodes length are 100 mm, 96 mm, and 44 mm, respectively. About 3 mm of the reference electrode is left uninsulated in this case. **B)** Pictorial representation (left) and labeled schematic diagram (right) of the fully assembled quartz EPR capillary cell. The capillary tube has an outer diameter (∅) of 2 mm and an inner diameter of 0.8 mm. **C)** Fully assembled in-situ EC-EPR cell. This incorporates the quartz EPR capillary cell in its holder/protector, with a red wire connecting the reference electrode to the potentiostat and a black wire connecting the working electrode to the potentiostat. In contrast, a Pt wire connects the counter electrode to the potentiostat.* 164

***Figure 6.23**. Cyclic voltammogram of Pt as the working electrode in **A)** narrow potential range, i.e., hydrogen under potential deposition region, and **B)** broad potential in an Ar-saturated 0.1 M $HClO_4$ with a scan rate of 50 mV s^{-1} **C)** Cyclic voltammogram performed in an Ar-saturated 0.1 M $HClO_4$ environment using a scan rate of 200 mV s^{-1} **D)** Integrated spectra of the capillary cell. Top: Integrated reference spectrum obtained with two visible EPR signals (336.1 mT, 336.7 mT) stemming from the tubes. Bottom: Integrated EPR spectra of the whole in-situ cell at desorption potentials 0.25 V and 0.30 V vs. PdH RE. Asterixes: Additional EPR signals around magnetic field values of 333.8 mT (g = 2.023) and 338.5 mT (g = 1.995) for +0.25 V vs. PdH. The parameters used for the measurements are as follows: Sweep time: 1500 s, modulation amplitude: 200 µT, power: 0.1 mW, microwave frequency: 9.452 GHz. 167*

***Figure 6.24**. As-obtained EPR signals for the quartz EPR tube (reference) and the in-situ cell at hydrogen underpotential deposition potentials of 0.25 V and 0.30 V vs. PdH RE. Each spectrum is an average of three recordings. The spectra of the in-situ cell are multiplied by a factor of four with respect to the reference signal. 168*

***Figure A1.1**. Labeled pictorial representation of **A)** The main cell compartment housing the electrolyte, the gas inlet and outlet, and the three electrodes, working, counter and reference electrodes. **B)** the fully assembled in-situ EC-EPR cell setup placed in the EPR device with a Teflon support and the various electrodes connected to the potentiostat. 173*

***Figure A2.1**. **A)** Graphical depiction of the relation between PME and pH **B)** A plot of double-layer capacitance as a function of electrolyte pH. The electrolyte employed was Ar-saturated perchloric acid and the electrode was Pd MLs on the Au. **C)** Graphical representation of the n values (CPE exponents) of the CPE plotted as a function of the applied potential in various concentrations of Ar-saturated perchloric acid. The electrode used was Pd MLs on the Au. 174*

8.2 List of Tables

***Table 5.1**. Potential ranges and potential steps applied during the LICT measurements for the polycrystalline Au electrode.* *119*

***Table 6.1**. Comparison of the evaluated PME and C_{dl} values at different concentrations and pHs of perchloric acid solutions* *157*

8.3 Related Publications

The two manuscripts reproduced in this section have the following acknowledged copyright permission:

- Reprinted from reference[163] with permission. *Copyright © (2021), The Authors. Published by Wiley-VCH GmbH. Open access, published under a CC-BY license.*

- Reprinted from reference[162] with permission. *Copyright © (2023), Elsevier Books, Elsevier.*

ChemElectroChem
Minireviews
doi.org/10.1002/celc.202101175
Chemistry Europe
European Chemical Societies Publishing
www.chemelectrochem.org

Prospects of Using the Laser-Induced Temperature Jump Techniques for Characterisation of Electrochemical Systems

Xing Ding+,[a] Theophilus Kobina Sarpey+,[a] Shujin Hou,[a, b] Batyr Garlyyev,[a] Weijin Li,[b, c]
Roland A. Fischer,*[b, c] and Aliaksandr S. Bandarenka*[a, b]

Understanding the processes, phenomena, and mechanisms occurring at the electrode/electrolyte interface is a prerequisite and significant for optimizing electrochemical systems. To this end, the advent of sub-microsecond laser pulses has paved the way and eased the investigations of the electrochemical interface (*e.g.*, electric double layer), which hitherto is difficult. The laser-induced current transient (LICT) and laser-induced potential transient (LIPT) techniques have proven to be valuable and unique tools for measuring key parameters of the electrified interface, such as the potential of maximum entropy (PME) and the potential of zero charge (PZC). Herein, we present a summary of studies performed in recent years using laser-induced temperature jump techniques. The relation between the PME/PZC and the electrocatalytic properties of various electrochemical interfaces are particularly highlighted. Special attention is given to its applications in investigating different systems and analyzing the influence of the electrolyte components, electrode composition and structure on the PME/PZC and various electrochemical processes. Moreover, possible applications of the LICT/LIPT techniques to investigate the interfacial properties of a myriad of materials, including surface-mounted metal-organic frameworks and metal oxides, are elaborated.

1. Introduction

A fundamental understanding of the various electrochemical processes taking place at the interface between the electrode and electrolyte is of crucial importance for several renewable energy provision systems. The often-applied solvent in most electrolytes is water. The interfacial water plays a pivotal role in electrochemical processes and often determines the rate of charge and mass transfer.[1] Therefore, the investigation of the interfacial water layer structure is necessary to optimize the studied systems.

A key parameter in the description of the electrochemical interface is the potential of zero charge (PZC).[2] It can be defined as the potential at which the excess charge equals zero on the electrode's surface. This simple definition has, however, a specific shortcoming. Particularly, the evaluation of this parameter in more complex systems characterized by adsorption processes at the electrified interface is problematic. As such, two types of PZCs have been introduced to circumvent this issue: the potential of zero free charge (PZFC) and the potential of zero total charge (PZTC).[3] As the names suggest, the PZFC is a type of PZC at which the excess free electronic charge density at the electrode surface is zero. In turn, the PZTC is a potential at which the sum of the free, electronic net charge density and the charge density transferred in adsorption (Faradaic) processes equals zero. Despite the clear difference between the PZFC and PZTC, the two parameters are the same in processes and/or materials that do not exhibit specific adsorption. Under these conditions, one can safely access the values of the PZFC *via* the determination of the PZTC.[4] Moreover, another essential parameter, the potential of maximum entropy (PME), is closely related to the PZFC.[5] It is commonly defined as the potential at which the entropy of the double layer formation maximizes. The introduction of the PME is particularly useful when assessing the "stiffness" of the water layer structure at the interface.[1b] When approaching the PME, the degree of order of the interfacial water molecules decreases. Consequently, the charge and mass transfer through the electric double layer (EDL) should proceed much more easily. In contrast, at potentials far from the PME, the interfacial water layer structure is more rigid, and this slows down the transfer of charge and mass through the EDL. Therefore, the determination of the PME is significant to understanding the processes taking place at the interface.

The PZC can be measured by the electrocapillary method, capacitance method, CO charge displacement, N_2O reduction and, so on.[6] However, the application of these methods is limited for various specific conditions. The capacitance method can only be used for dilute solutions and in the absence of

---

[a] *X. Ding,+ T. K. Sarpey,+ S. Hou, Dr. B. Garlyyev, Prof. Dr. A. S. Bandarenka*
Physics of Energy Conversion and Storage
Technical University of Munich
James-Franck-Straße 1, 85748 Garching b. München, Germany
E-mail: bandarenka@ph.tum.de
[b] *S. Hou, Dr. W. Li, Prof. R. A. Fischer, Prof. Dr. A. S. Bandarenka*
Catalysis Research Center TUM
Technical University of Munich
Ernst-Otto-Fischer-Straße 1, 85748 Garching b. München, Germany
E-mail: roland.fischer@tum.de
[c] *Dr. W. Li, Prof. R. A. Fischer*
Department of Chemistry
Technical University of Munich
Lichtenbergstraße 4, 85748 Garching b. München, Germany

[+] *These authors contributed equally to this work.*

An invited contribution to the Wolfgang Schuhmann Festschrift specific adsorption. The CO charge displacement method cannot be applied at high anodic potentials to avoid CO oxidation, while the N_2O reduction method is limited for the interfacial structure, which is sensitive to the N_2O reduction reaction. It must be emphasized that the N_2O reduction method helps to characterize distinctively between local PZTCs present in a particular sample.[6] Based on the aforementioned limitations, there is a compelling need to elaborate more versatile techniques. One of such approaches is the laser-induced temperature jump method. A short description of the techniques will be discussed in Section 2.

This short review highlights some recent works that have utilized the LICT/LIPT techniques to investigate the interfacial fundamentals of electrodes in various electrochemical systems. Additionally, an outlook regarding the application of the LICT/LIPT techniques on other non-noble metal-based electrodes, such as metal oxides (e.g., MnO_x) and metal-organic frameworks (MOFs), is discussed.

2. The LICT/LIPT Techniques

The method of probing the electrode/electrolyte interface with short, powerful laser pulses was developed by Benderskii *et al.* in the 1980s.[7] It utilizes the so-called temperature jump effect to probe the EDL for analyzing the electrochemical systems. Generally, two different methods are applied: the laser-induced potential transient (LIPT) and the laser-induced current transient (LICT) techniques. The former is performed under coulostatic conditions to measure the change of the open-circuit potential. By contrast, the LICT technique is conducted under potentiostatic conditions to record the current transients (Figure 1a).[8] In brief, the rapid increase in the electrode/electrolyte interface temperature caused by the laser pulse randomizes the ions and water molecules at the interface. The perturbed electric double layer returns almost rapidly to its initial state since the duration of the applied laser pulse is in the scale of nanosecond (5–10 ns).[8a] The system's answer is recorded as current transients,[9] the orientation of which coincides with the sign of the excess charge on the electrode surface. Namely, if the electrode is negatively charged, negative current transients are observed and *vice versa*. The potential at which the current transient changes its sign can be correlated with the PME (as illustrated in Figure 1b).

3. Applications of LICT/LIPT to Characterise Electrocatalytic Systems

The utilization of the LICT/LIPT techniques has successfully promoted the understanding of interfacial processes, especially in various electrocatalytic systems.[10] The determination of the PZC/PME gives the information of the double layer order/disorder status. Besides, these parameters are believed to be closely associated with the work function of the metal electrode.[11]

3.1. PME/PZC Determination of Various Electrode Materials

Interestingly, the PME of Pt(111) in alkaline media was found to be located at the onset potential of the OH-adsorption.[12] Recently, Sebastián-Pascual *et al.* also demonstrated that the location of the PME was related to the onset potential of the OH-adsorption on both Cu(111) and Cu(100) in 0.1 M NaOH solutions.[13] Similar results were observed for Cu(111) at the same pH level in our recent work.[8a] The PME of Cu(111) portrays a linear relationship with the electrolyte pH on the standard hydrogen electrode (SHE) scale. However, the decrease in the electrolyte pH shifts the PME towards the potential within the OH-adsorption region. Moreover, combining with electrochemical scanning tunneling microscopy imaging, it was found that the Cu(111) surface slowly starts to restructure at the PME in the electrolytes at pH = 11 and pH = 13. It should be noted that the pH dependency of the PME varies for the same electrode material with different surface structures.[11] Besides using noble metal electrodes for the laser-induced temperature jump measurements, the PZC of Mn_2O_3 was also successfully investigated.[14] The PZC, which is closely related to the PME,

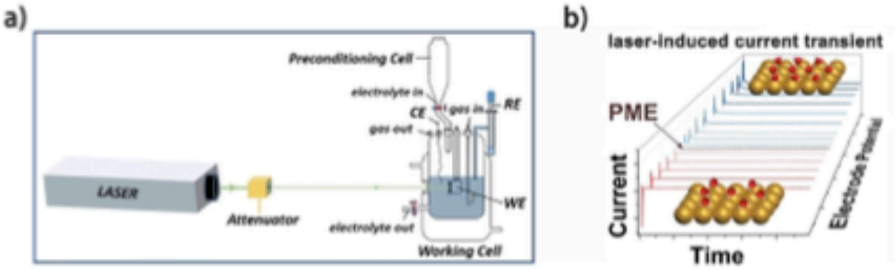

Figure 1. (a) Schematic illustration for the application of the laser-induced temperature jump technique. WE, RE, and CE correspond to working, reference, and counter electrode, respectively. (b) Typical current transients recorded during the laser measurement at various electrochemical potentials *via* the LICT. The potential at which the current transient changes its sign corresponds to the PME. (a, b) Reproduced with permission from Ref. [8b]. Copyright (2021) Wiley-VCH.

was located at 1.09 V *vs* RHE, thus, supporting the notion that Mn_2O_3 should catalyze the oxygen reduction reaction (ORR) well since the obtained PZC is quite close to the thermodynamic equilibrium potential of the ORR. This work demystified and further confirmed the reasons for the good ORR performance of Mn_2O_3 in this kind of electrolytes. Hence, investigating the actual EDL status obtained *via* illuminating the electrode with short laser pulses presents a leeway to investigating other metal oxide materials by employing the LICT/LIPT techniques.

3.2. Effects of Electrode Composition and Structure on the PME/PZC

Due to their great stability, noble metal-based catalysts are used in various electrocatalytic systems.[15] However, the performance of these metals in electrocatalysis still needs to be improved. To enhance the electrocatalytic performance of the electrodes, one can incorporate certain facets or defects to change the electrode surface structure or create alloys to change the electrode surface composition.[16] It is believed that this can finally increase the number of active sites at the electrode surface and improve the electrode activity. Thus, tuning the electrode composition and structure changes the performance of the electrode. However, change(s) in the properties of the EDL should also be considered. For instance, Pt single crystals show good performance for the ORR,[17] while the activity varies for different orientations of the Pt single crystals.[12] The difference in activity for different structures of Pt single crystals is due to the difference in the heat of adsorption of intermediates at different active centers and their different abundance.[16b,18] Interestingly, with the LIPT technique, García-Aráez *et al.* revealed that the locations of the PME for Pt single crystals in acidic solution differ with the surface structure.[11] Subsequently, Sarabia *et al.* also found a similar influence in the case of alkaline media.[12] Therefore, the interfacial water layer structure is heavily related to the electrode structure, further affecting the electrode activity. It can be noted that the PME increases in the order of Pt(110) < Pt(100) < Pt(111) in alkaline solutions (see Figure 2a–c), which is in line with the observed results for the ORR.[18] Namely, the PME for Pt(111) is closer to the thermodynamic equilibrium potential of the ORR. Thus, the interfacial water structure for Pt(111) is more loose and easy to reorganize during the charge and mass transfer through the electric double layer. This could also contribute to the observed situation that Pt(111) presents the best ORR activity among the three crystal orientations.

Although pure noble metals manifest good performance on electrocatalytic activities, modifying the electrode surface with certain transition metal hydroxides enhances the reaction activity.[20] For instance, adding nickel hydroxides to the Pt(111) surface promotes the rate of the hydrogen evolution reaction (HER).[21] Traditionally, the effect of the modification on the electrode is believed to correlate with the change in the interaction between the electrode surface and the relevant intermediates.[22] On that score, Ledezma-Yanez *et al.* demon-

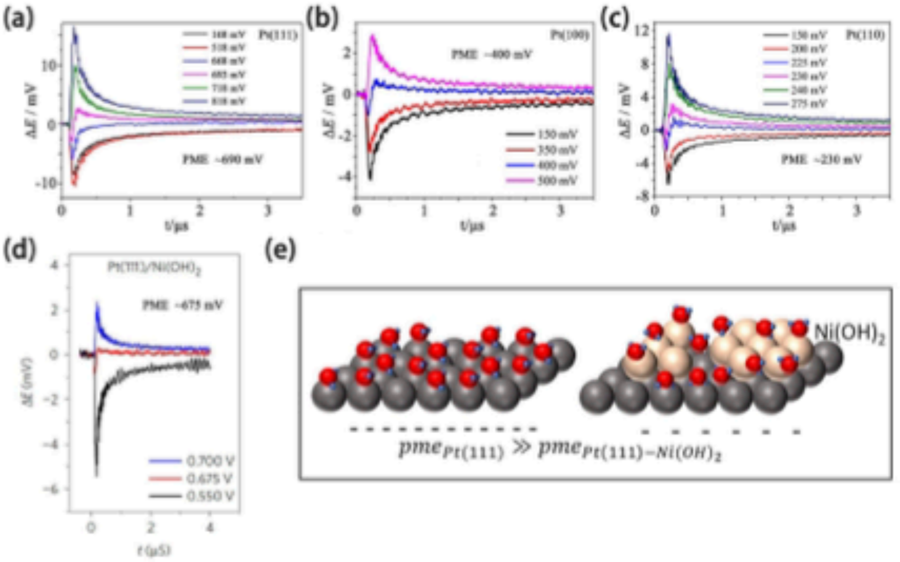

Figure 2. Laser-induced potential transients recorded at different potentials for (a) Pt(111), (b) Pt(100), (c) Pt(110), and (d) Pt(111)/$Ni(OH)_2$ in 0.1 M NaOH solution. The estimated PMEs are shown. (a–c) Reproduced with permission from Ref. [12]. Copyright (2020) Elsevier. (d) Reproduced with permission from Ref. [1b]. Copyright (2017) Springer Nature. (e) Scheme of the network of water dipoles on Pt(111) and the unstructured network on Pt(111)-$Ni(OH)_2$. Increasing the nickel coverage shifts the PME to the potentials closer to the thermodynamic equilibrium potential of the HER. Reproduced with permission from Ref. [23]. Copyright (2018) American Chemical Society.

strated that adding $Ni(OH)_2$ shifts the PME closer to the thermodynamic equilibrium potential of the HER by the LIPT experiments (Figure 2d).[1b] This means the presence of $Ni(OH)_2$ lowers the order of the interfacial water layer structure at the onset potential of the HER, which promotes the charge transfer and the kinetics of the reaction. Based on this proposal, Sarabia *et al.* used the LIPT to study further the influence of the coverage of $Ni(OH)_2$ on Pt(111) on the HER.[23a] They observed that increasing the $Ni(OH)_2$ coverage moves the PME to the potential where the HER takes place (Figure 2e). Again, this decreases the order of the electric double layer structure at the potential of the HER and improves the HER activity. Extending the studies on Cu(111), Auer *et al.* recently modified the surface of pristine Cu(111) with 0.1 and 0.2 monolayers (ML) of $Ni(OH)_2$.[23b] They reported a non-linear activity behavior when the $Ni(OH)_2$ coverage was increased, a deviation from the earlier study conducted on Pt(111) surface.[23a] Further probing using electrochemical scanning tunneling microscopy and the laser-induced temperature jump technique revealed that only the Cu(111) with 0.2 ML of $Ni(OH)_2$ exhibited high water layer structure disorder at the interface. This observation of the PME was noticed close to the thermodynamic equilibrium potential of the HER and was attributed to reaching the peak of surface roughness while increasing the monolayers of nickel hydroxide on the Cu(111) surface. This therefore induced an increase in disorder of the interfacial water layer structure.

3.3. Effect of Electrolyte Composition on the PME/PZC

In the past decades, most studies have focused on the compositional and structural modification of electrode materials to optimize electrocatalytic systems. Nevertheless, the role of electrolytes is gradually considered valuable.[24] For instance, it has been widely reported that the electrolyte pH can drastically influence the rate of the HER.[25] Several hypotheses have been developed to address this issue.[26] Climent *et al.* discovered that the PME value for Au changes upon variation of the electrolyte pH by using the LIPT technique.[10d] Similarly, comparable observations were made using Pt as the electrode material and varying the electrolyte pH.[27] Besides, Martinez-Hincapié *et al.* demonstrated that there is a variation in pH dependences for the PMEs of Pt(111), Pt(100), and Pt(110) electrodes (Figure 3a).[28] This finding clarifies the fact that PMEs of different crystallographic orientations of the same electrode might not necessarily show the same behavior with varying electrolyte pH. Ganassin *et al.* also observed the pH dependence of the PME for Ir(111) in acidic media (Figure 3b).[29] However, hydrogen and specific anion adsorption effect should be considered in the cases which occur on more electroactive materials (Pt and Ir). Because, in the double layer region where there is no specific adsorption, the PME is supposed to be independent of the electrolyte pH on the SHE scale or shift approximately 59 mV per pH unit on the RHE scale.[5,11,28] Interestingly, the pH dependence of the HER activity has been correlated to the effect of pH on the location of the PME.[1b]

Apart from the electrolyte pH, the presence of alkali metal cations can also drastically alter the electrocatalytic activity of the electrodes. Their influence on the electrode processes has been investigated in some previous works.[24b,30] Particularly, Strmcnik *et al.* demonstrated that the activities towards the ORR and hydrogen oxidation reaction on Pt linearly correlate with the hydration energies of the corresponding alkali metal cations.[24c] Besides, the pH influence can be considerably different in the presence of alkali metal cations. In our recent work, polycrystalline Au in Ar- and O_2-saturated 0.5 M Na_2SO_4 or K_2SO_4 solution was examined using the LICT technique.[8b] As shown in Figure 3c, it was found that the PME shifts towards more positive potentials as a result of increasing the electrolyte pH and introducing oxygen. This could be due to the variation in the local pH at the interface. Moreover, the PME difference becomes enormous when the electrolyte pH reaches 6, which means, in this case, the electric double layer structures for Au in Na^+- and K^+-containing electrolytes are significantly different. Thus, different electrode processes can be expected in electrolytes containing these two cations. Therefore, the utilization of the LICT/LIPT techniques is believed to help promote the fundamental understanding regarding the electrode processes happening in various electrocatalytic systems.

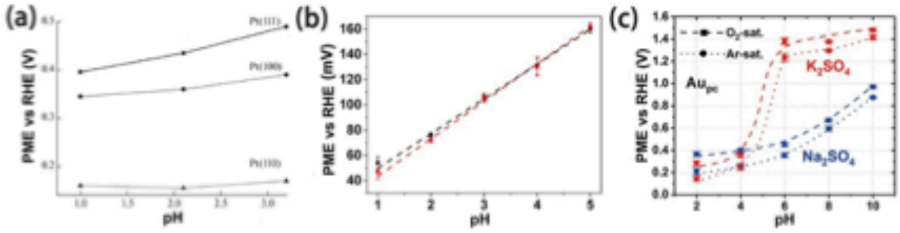

Figure 3. (a) Dependence of the PMEs on the pH for Pt(111), Pt(100), and Pt(110). Reproduced with permission from Ref. [28]. Copyright (2017) Springer Nature. (b) The PMEs plotted as a function of the pH for Ir(111) with (red symbols) and without (black) the thermodiffusion correction. Reproduced with permission from Ref. [29]. Copyright (2017) Springer Nature. (c) The values of the PME for polycrystalline gold in Ar-saturated (dot) and O_2-saturated (dash) 0.5 M Na_2SO_4 (blue) and K_2SO_4 (red) solutions depicted as a function of the electrolyte pH. Reproduced with permission from Ref. [8b]. Copyright (2021) Wiley-VCH.

4. Applications of LICT/LIPT for the Investigation of Aqueous Battery Systems

Batteries have been widely used for renewable energy storage applications.[31] Especially, aqueous metal-ion batteries have attracted considerable attention owing to their safety, low cost, and wide availability. However, a better understanding of intercalation and de-intercalation processes is still required to improve and optimize the investigated systems.[32] The LICT methodology could be a powerful tool to research the field of aqueous metal-ion batteries because the PME of the systems can easily reveal the interfacial charge status during different processes. As the hydration energy of cations and anions could influence the stiffness of the water layer structure at the interface, the resulting PME of the investigated system can be affected by different ions.[9a,33] For instance, promising electrode material used in aqueous Na-ion batteries, $Na_2Ni[Fe(CN)_6]$, were investigated with the LICT technique.[9b] The position of the PME for thin films of $Na_2Ni[Fe(CN)_6]$ in 0.25 M Na_2SO_4 was around −0.13 V *vs* Ag/AgCl (SSC), while the current transients stayed positive for the case of 0.25 M K_2SO_4 at the same investigated potential region. Interestingly, the obtained results showed that the electrodes were positively charged for both systems during the intercalation processes (Figure 4a, b). Moreover, the LICT measurements showed the presence of three different PMEs as shown in Figure 4c. This observation could be explained from the different hydration energies hence different ion mobilities occasioned by the different electrolyte compositions (Na_2SO_4, NaCl, and $NaClO_4$) used for electrodepositing the $Na_2Co[Fe(CN)_6]$ films. It is envisaged that the aforementioned differences influence the interfacial processes, thus, leading to different relaxation times.[9,33] As mentioned earlier, the PME is associated with the interfacial water layer structure. One can, therefore, correlate the PMEs with the processes taking place at the interface. For this system, the locations of the PMEs are close to the onset potential range of the (de)intercalation of Na^+, which lies between 0.1 V and 0.9 V *vs* SSC. The stiffness of the EDL reaches its minimum at the PMEs, which is significant for the (de)intercalation process. These results show that the LICT/LIPT methods are promising techniques for studying the electrode/electrolyte interfacial phenomena for various electrode materials for aqueous metal-ion batteries.

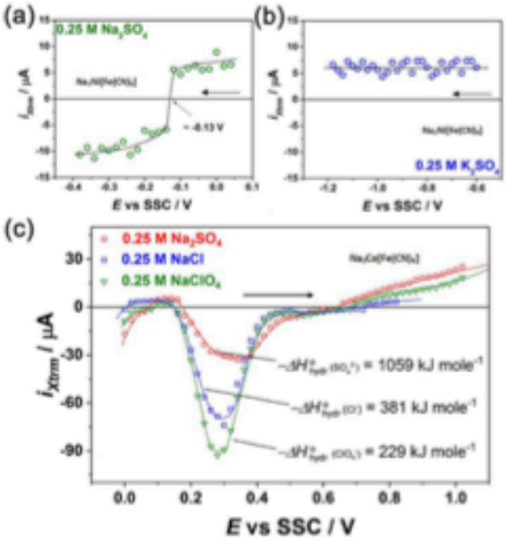

Figure 4. The maximal current transients collected for $Na_2Ni[Fe(CN)_6]$ in (a) 0.25 M Na_2SO_4, and (b) 0.25 M K_2SO_4, and for (c) $Na_2Co[Fe(CN)_6]$ in 0.25 M Na_2SO_4, 0.25 M NaCl, and 0.25 M $NaClO_4$. (a,b) Reproduced with permission from Ref. [9b]. Copyright (2017) American Chemical Society. (c) Reproduced with permission from Ref. [9a]. Copyright (2018) American Chemical Society.

5. Summary and Perspective

To conclude, we have analyzed recent research articles that employed the LICT/LIPT techniques to investigate various electrocatalytic and aqueous metal-ion battery systems. From the numerous literature presented, one can vividly establish and confirm the value and uniqueness of these techniques in characterizing the electrode/electrolyte interface as they permit the determination of the PME/PZC of various systems. These parameters help to elucidate the processes occurring at the interface as a function of, for example, electrolyte composition. As a result of its relative simplicity and ease of combining it with other techniques, the LICT/LIPT methodologies can be applied to various electrocatalytic or aqueous metal-ion battery systems.

As is evident from the works highlighted herein, there is an excellent opportunity to apply LICT/LIPT techniques to explore other systems containing non-noble metal electrodes, metal oxides, metal-organic frameworks (MOFs), conductive polymers, metal alloys (Figure 5). For instance, our group has recently developed a versatile and facile strategy to synthesize mixed metal hydroxide electrocatalysts derived from surface-mounted

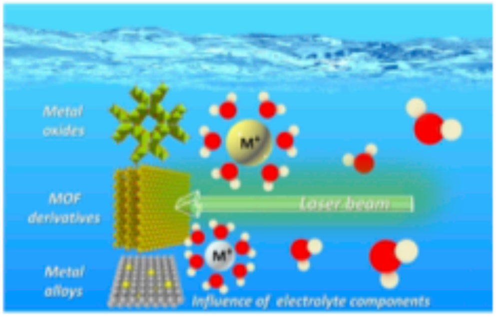

Figure 5. Schematic of the LICT/LIPT techniques for the investigation of the influence of electrolyte components. Herein, several promising electrocatalyst materials such as metal oxides, MOF derivatives and metal alloys are presented. The LICT/LIPT techniques provide a unique approach to elucidate the EDL structure-performance relationships in electrochemical systems.

MOFs (SURMOFs) with excellent OER performance in alkaline media.[34] However, the investigation of the electrolyte effect on MOFs-based systems has rarely been reported since most studies focus on the design of the electrode materials. Therefore, rational electrolyte engineering in MOFs-based systems is required to improve the performance of materials in electrocatalytic systems.

Owing to the presented ability of the LICT/LIPT techniques for improving the fundamental understanding of the electric double layer properties in various simple or complicated electrochemical systems, we envisage these methods can be further applied to other aforementioned systems to investigate the mechanism of the interfacial processes and finally optimize the studied systems.

Acknowledgements

We are grateful for the financial support from Deutsche Forschungsgemeinschaft under Germany's excellence strategy – EXC 2089/1 – 390776260, Germany's excellence cluster "e-conversion", DFG project BA 5795/5-1 and BA 5795/6-1 and DFG research group 2982 under UNusual anODE (UNODE). X.D. and S. J. H acknowledge financial support from the China Scholarship Council. Open Access funding enabled and organized by Projekt DEAL.

Conflict of Interest

The authors declare no conflict of interest.

Keywords: potential of maximum entropy · laser-induced current/potential transient · electric double layer · electrolyte influence · metal-organic frameworks

[1] a) J.-J. Velasco-Velez, C. H. Wu, T. A. Pascal, L. F. Wan, J. Guo, D. Prendergast, M. Salmeron, *Science* **2014**, *346*, 831–834; b) I. Ledezma-Yanez, W. D. Z. Wallace, P. Sebastián-Pascual, V. Climent, J. M. Feliu, M. T. Koper, *Nat. Energy* **2017**, *2*, 17031.
[2] A. S. Shatla, M. Landstorfer, H. Baltruschat, *ChemElectroChem* **2021**, *8*, 1817–1835.
[3] a) V. Climent, N. García-Araez, E. Herrero, J. M. Feliu, *Russ. J. Electrochem.* **2006**, *42*, 1145–1160; b) A. Frumkin, O. Petrii, *Electrochim. Acta* **1975**, *20*, 347–359.
[4] T. Pajkossy, D. Kolb, *Electrochem. Commun.* **2003**, *5*, 283–285.
[5] P. Sebastián, R. Martínez-Hincapié, V. Climent, J. M. Feliu, *Electrochim. Acta* **2017**, *228*, 667–676.
[6] a) G. Lippmann, Relations entre les phénomènes électriques et capillaires. Gauthier-Villars Paris, France **1875**; b) P. Horsman, B. E. Conway, E. Yeager, *Comprehensive Treatise of Electrochemistry: The Double Layer*, Springer Science & Business Media **2013**; c) S. Trasatti, *J. Electroanal. Chem. Interfacial Electrochem.* **1974**, *54*, 437–441; d) C. D. Silva, G. Cabello, W. A. Christinelli, E. C. Pereira, A. Cuesta, *J. Electroanal. Chem.* **2017**, *800*, 25–31; e) H. Ebert, R. Parsons, G. Ritzoulis, T. VanderNoot, *J. Electroanal. Chem. Interfacial Electrochem.* **1989**, *264*, 181–193; f) V. Climent, G. A. Attard, J. M. Feliu, *J. Electroanal. Chem.* **2002**, 532, 67–74; g) G. A. Attard, O. Hazzazi, P. B. Wells, V. Climent, E. Herrero, J. M. Feliu, *J. Electroanal. Chem.* **2004**, 568, 329–342.
[7] a) V. Benderskii, S. Babenko, A. Krivenko, *J. Electroanal. Chem. Interfacial Electrochem.* **1978**, *86*, 223–225; b) V. Benderskii, G. Velichko, I. Kreitus, *J. Electroanal. Chem. Interfacial Electrochem.* **1984**, *181*, 1–20.
[8] a) A. Auer, X. Ding, A. S. Bandarenka, J. Kunze-Liebhäuser, *J. Phys. Chem. C* **2021**, *125*, 5020–5028; b) X. Ding, B. Garlyyev, S. Watzele, T. K. Sarpey, A. S. Bandarenka, *Chem. Eur. J.* **2021** *27*, 10016–10020.
[9] a) D. Scieszka, C. Sohr, P. Scheibenbogen, P. Marzak, J. Yun, Y. Liang, J. Fichtner, A. S. Bandarenka, *ACS Appl. Mater. Interfaces* **2018**, *10*, 21688–21695; b) D. Scieszka, J. Yun, A. S. Bandarenka, *ACS Appl. Mater. Interfaces* **2017**, *9*, 20213–20222.
[10] a) P. Sebastián, E. Gómez, V. Climent, J. M. Feliu, *Electrochim. Acta* **2019**, *311*, 30–40; b) P. Sebastián, A. P. Sandoval, V. Climent, J. M. Feliu, *Electrochem. Commun.* **2015**, *55*, 39–42; c) V. Climent, B. A. Coles, R. G. Compton, J. M. Feliu, *J. Electroanal. Chem.* **2004**, *561*, 157–165; d) V. Climent, B. A. Coles, R. G. Compton, *J. Phys. Chem. B* **2001**, *105*, 10669–10673.
[11] N. Garcia-Araez, V. Climent, J. M. Feliu, *J. Phys. Chem. C* **2009**, *113*, 9290–9304.
[12] F. J. Sarabia, P. Sebastián, V. Climent, J. M. Feliu, *J. Electroanal. Chem.* **2020**, *872*, 114068.
[13] P. Sebastian-Pascual, F. J. Sarabia, V. Climent, J. M. Feliu, M. Escudero-Escribano, *J. Phys. Chem. C* **2020**, *124*, 23253–23259.
[14] T. C. Nagaiah, A. Tiwari, M. Kumar, D. Scieszka, A. S. Bandarenka, *ACS Appl. Energ. Mater.* **2020**, 3, 9, 9151–9157.
[15] a) Q. Lenne, Y. R. Leroux, C. Lagrost, *ChemElectroChem* **2020**, *7*, 2345; b) M. Shao, Q. Chang, J.-P. Dodelet, R. Chenitz, *Chem. Rev.* **2016**, *116*, 3594–3657.
[16] a) C. V. Rao, C. R. Cabrera, Y. Ishikawa, *J. Phys. Chem. Lett.* **2010**, *1*, 2622–2627; b) V. Colic, A. S. Bandarenka, *ACS Catal.* **2016**, *6*, 5378–5385; c) D. M. Morales, M. A. Kazakova, M. Purcel, J. Masa, W. Schuhmann, *J. Solid State Electrochem.* **2020**, *24*, 2901–2906; d) A. Alinezhad, L. Gloag, T. M. Benedetti, S. Cheong, R. F. Webster, M. Roelsgaard, B. B. Iversen, W. Schuhmann, J. J. Gooding, R. D. Tilley, *J. Am. Chem. Soc.* **2019**, *141*, 16202–16207; e) H. B. Aiyappa, J. Masa, C. Andronescu, M. Muhler, R. A. Fischer, W. Schuhmann, *Small Methods* **2019**, *3*, 1800415.
[17] A. M. Gómez-Marín, R. Rizo, J. M. Feliu, *Catal. Sci. Technol.* **2014**, *4*, 1685–1698.
[18] J.-C. Dong, M. Su, V. Briega-Martos, L. Li, J.-B. Le, P. Radjenovic, X.-S. Zhou, J. M. Feliu, Z.-Q. Tian, J.-F. Li, *J. Am. Chem. Soc.* **2019**, *142*, 715–719.
[19] T. Schmidt, V. Stamenkovic, M. Arenz, N. Markovic, P. Ross Jr, *Electrochim. Acta* **2002**, *47*, 3765–3776.
[20] a) S. Xue, R. W. Haid, R. M. Kluge, X. Ding, B. Garlyyev, J. Fichtner, S. Watzele, S. Hou, A. S. Bandarenka, *Angew. Chem. Int. Ed.* **2020**, *59*, 10934–10938; *Angew. Chem.* **2020**, *132*, 11026–11031; b) I. T. McCrum, M. T. Koper, *Nat. Energy* **2020**, *5*, 891–899; c) K. Elumeeva, J. Masa, J. Sierau, F. Tietz, M. Muhler, W. Schuhmann, *Electrochim. Acta* **2016**, *208*, 25–32.
[21] R. Subbaraman, D. Tripkovic, D. Strmcnik, K.-C. Chang, M. Uchimura, A. P. Paulikas, V. Stamenkovic, N. M. Markovic, *Science* **2011**, *334*, 1256–1260.
[22] N. Danilovic, R. Subbaraman, D. Strmcnik, K. C. Chang, A. Paulikas, V. Stamenkovic, N. M. Markovic, *Angew. Chem. Int. Ed.* **2012**, *51*, 12495–12498; *Angew. Chem.* **2012**, *124*, 12663–12666.
[23] a) F. J. Sarabia, P. Sebastián-Pascual, M. T. Koper, V. Climent, J. M. Feliu, *ACS Appl. Mater. Interfaces* **2018**, *11*, 613–623; b) A. Auer, F. J. Sarabia, D. Winkler, C. Griesser, V. Climent, J. M. Feliu, J. Kunze-Liebhäuser, *ACS Catal.* **2021**, 11, 10324–10332.
[24] a) V. Colic, M. D. Pohl, D. Scieszka, A. S. Bandarenka, *Catal. Today* **2016**, *262*, 24–35; b) S. Xue, B. Garlyyev, S. Watzele, Y. Liang, J. Fichtner, M. D. Pohl, A. S. Bandarenka, *ChemElectroChem* **2018**, *5*, 2326–2329; c) D. Strmcnik, K. Kodama, D. van der Vliet, J. Greeley, V. R. Stamenkovic, N. Marković, *Nat. Chem.* **2009**, *1*, 466.
[25] a) J. Zheng, W. Sheng, Z. Zhuang, B. Xu, Y. Yan, *Sci. Adv.* **2016**, *2*, e1501602; b) D. Strmcnik, P. P. Lopes, B. Genorio, V. R. Stamenkovic, N. M. Markovic, *Nano Energy* **2016**, *29*, 29–36.
[26] P. S. Lamoureux, A. R. Singh, K. Chan, *ACS Catal.* **2019**, *9*, 6194–6201.
[27] a) V. Climent, B. A. Coles, R. G. Compton, *J. Phys. Chem. B* **2002**, *106*, 5988–5996; b) V. Climent, B. A. Coles, R. G. Compton, *J. Phys. Chem. B* **2002**, *106*, 5258–5265.
[28] R. Martínez-Hincapié, P. Sebastián-Pascual, V. Climent, J. M. Feliu, *Russ. J. Electrochem.* **2017**, *53*, 227–236.
[29] A. Ganassin, P. Sebastián, V. Climent, W. Schuhmann, A. S. Bandarenka, J. M. Feliu, *Sci. Rep.* **2017**, *7*, 1246.
[30] a) B. Garlyyev, S. Xue, S. Watzele, D. Scieszka, A. S. Bandarenka, *J. Phys. Chem. Lett.* **2018**, *9*, 1927–1930; b) S. Xue, B. Garlyyev, A. Auer, J. Kunze-Liebhauser, A. S. Bandarenka, *J. Phys. Chem. C* **2020**, *124*, 12442–12447; c) B. Garlyyev, S. Xue, M. D. Pohl, D. Reinisch, A. S. Bandarenka, *ACS*

Omega **2018**, *3*, 15325–15331; d) V. Briega-Martos, F. J. Sarabia, V. Climent, E. Herrero, J. M. Feliu, *ACS Meas. Sci. Au* **2021**, 10.1021/acsmeasuresciau.1c00004.
[31] A. Rabis, P. Rodriguez, T. J. Schmidt, *ACS Catal.* **2012**, *2*, 864.
[32] R. M. Dell, *Solid State Ionics* **2000**, *134*, 139.
[33] S. Pratihar, A. Chandra, *J. Chem. Phys.* **2011**, *134*, 024519.
[34] a) W. Li, S. Xue, S. Watzele, S. Hou, J. Fichtner, A. L. Semrau, L. Zhou, A. Welle, A. S. Bandarenka, R. A. Fischer, *Angew. Chem. Int. Ed.* **2020**, *59*, 5837–5843; *Angew. Chem.* **2020**, *132*, 5886–5892; b) W. Li, S. Watzele, H. A. El-Sayed, Y. Liang, G. Kieslich, A. S. Bandarenka, K. Rodewald, B. Rieger, R. A. Fischer, *J. Am. Chem. Soc.* **2019**, *141*, 5926–5933; c) S. Hou, W. Li, S. Watzele, R. M. Kluge, S. Xue, S. Yin, X. Jiang, M. Döblinger, A. Welle, B. Garlyyev, P. Müller-Buschbaum, C. Wöll, A. S. Bandarenka, R. A. Fischer, *Adv. Mater.* **2021**, 10.1002/adma.202103218.

Manuscript received: August 31, 2021
Revised manuscript received: December 9, 2021
Accepted manuscript online: December 15, 2021

Probing the electrified solid–liquid interfaces with laser-induced transient techniques

Theophilus Kobina Sarpey[a], **Emre Keles**[a], **Elena L. Gubanova**[a], **and Aliaksandr S. Bandarenka**[a,b], [a] Physics of Energy Conversion and Storage, Physik-Department, Technische Universität München, Garching bei München, Germany; and [b] Catalysis Research Center TUM, Garching bei München, Germany

Introduction	**2**
Techniques for measuring the PZC and PME	**3**
Capacitance method	4
Electrocapillary method	4
CO charge displacement method	4
N_2O reduction method	4
The laser-induced transient techniques	**5**
Fundamental concepts of the laser-induced transient techniques	5
Origin of a system response during a laser-induced current transient experiment	7
Measurement schemes	7
Description of the main laser parameters and specifications	7
Realization of the laser-induced current transient experiment	9
Application of the laser-induced transient techniques	**9**
Electrocatalysis	9
Effects of electrode structure on the PME/PZC	9
Effect of electrolyte composition (cations, pH) on the PME/PZC	10
PME/PZC determination of various electrode materials	10
Investigation of aqueous rechargeable metal-ion batteries by the LICT technique	12
Summary	**14**
Acknowledgments	**14**
References	**14**

Key points

- To clarify the significance of the electrified electrode/electrolyte interface, particularly the electric double layer in electrochemical systems, reactions, and processes.
- To elucidate and identify the importance in fully knowing the role interfacial water and dipoles play in enhancing electrochemical activities of several electrochemical systems.
- To explain in detail the relevance of the potentials of zero charge and maximum entropy, and how they can be measured more effectively and efficiently.
- The laser-induced transient techniques are introduced with a special focus on the theoretical background of the methods, and the experimental realization is particularly broadly elaborated with the experimental setup and the corresponding stepwise measurement scheme.
- Emphasis on the usefulness and wide scope of applicability of the methods (LICT, LIPT) for several electrochemical systems, reactions, processes, materials, etc. are proven with specific examples from the literature.
- To point out that the intentional and purposeful use of the methodology will lead to realizing the rational design of efficient and optimized electrochemical systems.

Abstract

The crucial role and significance of the electrified electrode/electrolyte interface in optimizing electrochemical systems cannot be underestimated. The net orientation of dipoles and solvent layer structure at the electrode/electrolyte interface can immensely impact electrochemical processes such as the electrode catalytic activity and the charge and mass transfer. The so-called temperature jump effect is refreshingly triggered by employing sub-microsecond laser pulses to irradiate various electrodes. The laser-induced transient techniques are valuable, reliable, and unique tools for determining critical parameters of the electrified interface, such as the potential of maximum entropy (PME) and the potential of zero charge (PZC). Herein, we accentuate the theory behind the techniques and provide relevant information about the experimental setup and design.

https://doi.org/10.1016/B978-0-323-85669-0.00045-3

A detailed summary of recent studies using the laser-induced transient techniques is discussed, with particular emphasis on the relation between the PME/PZC and the electrocatalytic properties of various electrochemical systems.

Introduction

The undisputed prerequisite in successfully designing efficient electrochemical systems includes having full knowledge and understanding of the electric double layer (EDL) properties as it plays a crucial role in several electrochemical systems, particularly electrolyzers, fuel cells, batteries, supercapacitors, and many more. The EDL structure (*see* **Fig. 1**) plays an inherent role in interfacial processes, particularly in optimizing various electrocatalytic reactions. The first known attempt to characterize the EDL structure was published in 1853 when Hermann L. F. von Helmholtz[2] proposed a simplified EDL structure to describe the charge and potential arrangement at the solid/liquid interface. In this so-called Helmholtz model, the charged/electrified electrode (electron conductor) surface (i.e., when submerged in an electrolyte) attracts counter-ions in the electrolyte (ionic conductor) to its surface and repels similarly charged ions, and consequently, a double layer of ions forms on the electrode surface. The resulting charge layers act like a conventional capacitor with two planar parallel electrodes separated by a dielectric material upon the application of a potential. It is important to add that the two formed charge layers in the Helmholtz model are separated by a distance, say H.

Since the influence of the thermal motion of ions in the double layer is not negligible, Gouy[3] and Chapman[4] accounted for that through the extension of the Helmholtz model by proposing a diffuse layer at the interface. These two models, namely, Helmholtz and Gouy-Chapman models, were subsequently merged by Stern[5] to describe the ion distribution in the Helmholtz and diffuse layers. In a while, Grahame[6] modified the Stern model, intimating that the Helmholtz layer can be further divided into two planes, the inner and the outer Helmholtz planes. In brief detail (*cf.* Fig. 1), specifically adsorbed species lose aspects of their solvation shell and therefore mainly attach to the electrode surface, together with the water molecules, and from their center to the electrode surface is termed the inner Helmholtz plane (IHP). In turn, the outer Helmholtz plane (OHP) comprises the non-specifically adsorbed species known to retain their full solvation shells and hence cannot approach closer to the electrode surface. Therefore, they are a bit distant and eventually form another layer called the outer Helmholtz plane. As already mentioned, another layer comprising the bulk electrolyte and some fully solvated/hydrated species forms outside the outer Helmholtz plane due to thermal agitation. This region is known as the diffuse layer.

Although the models have been refined endlessly, they remain the basis of today's research concerning the double layer structure at the solid/liquid interface. It is therefore not surprising that besides the electrode structure and composition,[7–15] the electrolyte components play a crucial role regarding the electrocatalytic performance (most especially, activity and selectivity) of the electrode[16–21] upon exploring the concepts of the EDL.

The net orientation of solvent, i.e., the water layer structure (as the often-applied solvent in most electrolytes is water) at the electrified electrochemical interface, one of the essential interfacial properties, can tremendously influence the electrochemical processes such as the electrode activity and the charge and mass transfer at the interface. Therefore, it is refreshing to know that using robust methodologies like the laser-induced transient techniques, important parameters (potentials of maximum entropy and zero charge) can be determined in the vicinity of the electrified electrode/electrolyte interface. Their knowledge supplies the relevant information required to comprehend the electrode/electrolyte interface structure better, and by extension, the electrochemical processes taking place in a structure (i.e., adsorption of charged and uncharged species at the surface) and their kinetics.

The first reported concept of the potential of zero charge (PZC) was initiated in 1928 by A. Frumkin.[22] The PZC corresponds to the potential where there is apparently no net accumulation of excess charge on the electrode surface. Simply put, it represents the potential where the excess charge on the electrode surface vanishes as the applied potential is varied. As a first approximation, the PZC is related to the work function for transition metals and can be described by the following equation:

$$E_{PZC} = \Phi/_{e_0} + K_s \tag{1}$$

Here, Φ stands for the metal's work function, e_0 represents the electron charge and K_s is a constant depicting the influence of the solvent on E_{PZC} of the electrode.

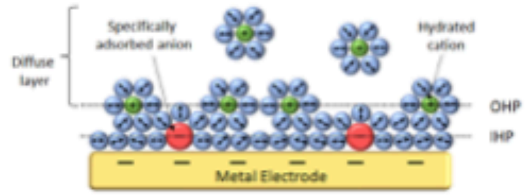

Fig. 1 Modified schematic demonstration of the electric double layer model on a negatively charged metal electrode. The inner and outer Helmholtz planes, as well as the diffuse layer, are exhibited. Water molecules are shown as blue spheres with arrows, whereas the hydrated cations are depicted in green with the specifically adsorbed anion species in red. Figure adapted from Ref. 1.

It is essential to distinguish between two types of PZCs depending on the nature of the electrode material as the PZC is not a unique property of the metal but relies on the detailed composition of the whole system. Namely, one that considers adsorption processes at the electrified interface and hence depends on the pH of the electrolyte and the other, which is independent of adsorption processes. The latter is usually referred to as the potential of zero free charge (PZFC) and is defined as a type of PZC which occurs when the free, electronic net charge of the electrode surface is zero in applied potential.[23–25] By contrast, the former is termed the potential of zero total charge (PZTC) and results when the sum of the free, electronic net charge density and the charge density transferred throughout reversible adsorption (Faradaic) processes are zero in applied potential. However, for ideally polarizable electrode materials that do not exhibit specific adsorption (hydrogen, OH^-, and anions) processes occasioned by charge transfer, the PZFC and PZTC remain the same. In the likelihood of this scenario, the value of the PZFC can also be known once the PZTC is measured since it is the only parameter accessible experimentally.

The potential of maximum entropy (PME) is the potential at which the disorder of the water molecules close to the electrode surface is maximal. Put differently, the entropy of the double layer formation peaks at the PME. On that basis, the PME is significant in assessing the rigidity or looseness of the interfacial water layer and is closely related to the PZC, specifically, the PZFC. This close association is due to the electrostatic interactions of the water dipoles with the electric field at the interface. More precisely, the PME is located at a slightly negative potential compared to the PZC because of the strong directional bond that exists between the oxygen of the water molecule and the (unoccupied) d-orbitals of the (uncharged) transition metal electrode surface.[26] Since relatively huge energy is required to break the bond from the PZC to the PME, the latter tends to occur at a more negative potential compared to the former. Fig. 2A and B elucidate the positioning of some vital parameters significant in describing the properties of the electrified electrode/electrolyte interface.

It is worth noting that other terms like the potential of turn-over of the water molecules or potential of water reorientation and the potential of zero transient (PZT) are sometimes justifiably used to depict the PME. These are evinced from the fact that at the PME, the flipping (upwards or downwards) of the hydrogen and oxygen in the water molecules is uniquely realized. Consequently, electrochemical reactions proceed with alacrity (faster reaction kinetics) in the vicinity of the PME as species (charge, mass, etc.) can easily move through the EDL due to the lowering of the energy barrier[30] occasioned by loose water layer structure. On the contrary, at potentials far away from the PME, the solvent (mostly water) layer structure becomes stiff, elevating the energy barrier and eventually slowing down the reaction kinetics. In this condition, the transfer of mass and charge through the EDL proceeds slower. Fig. 2C further elaborates the concept and significance of the PME.

Techniques for measuring the PZC and PME

Having established what the PZC and PME really are, let us quickly look at the various techniques that can help in measuring these vital parameters. Despite their importance, the determination of the PZC and PME has never been straightforward. However, there

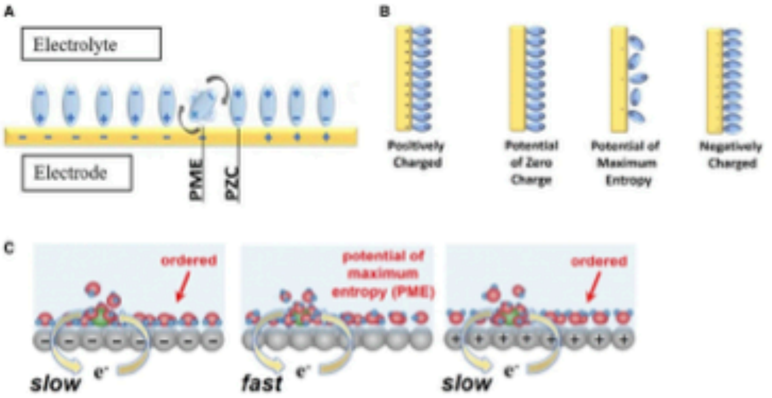

Fig. 2 (A) The double layer structure of a negatively charged electrode surface and the arrangement of the water layer structure around it. The PME is depicted as the potential with the most chaos and where the flipping of the signs of the water dipole occurs, whereas at the PZC, there exists no net charge on the electrode surface. (B) A schematic explanation of the arrangement of interfacial water dipoles and net electrode surface charges for key interfacial parameters like the potentials of zero charge and maximum entropy. (C) Schematic depiction of a possible expectation at the potential of maximum entropy. Thanks to the enormous degree of chaos at the PME, species can be exchanged rapidly, which leads to faster kinetics and enhanced performance. Meanwhile, for the other instances showing either positive or negative electrode surface charge, the water layer structure is well ordered; hence the exchange of species proceeds rather slowly. (A) Figure reprinted from Ref. 27, (B) Figure modified from Ref. 28, (C) Figure reproduced with permission from Ref. 29. Copyright (2021), Wiley-VCH GmbH.

are certain techniques used in determining the PZC (PZTC in most cases since PZFC cannot be currently determined experimentally), which include the capacitance method, electrocapillary method, CO charge displacement, and the N_2O reduction methods. As the role of interfacial water molecules is crucial in realizing significant improvements in the engineering and optimization of electrocatalytic systems, decoupling the possible interference of its response from the water in the bulk of the solution is pivotal in the established techniques.

Capacitance method

The double layer capacitance (C_{dl}) is an essential descriptor of the electrode/electrolyte interface, and since the PZC is one of the parameters that lie at the electrified interface, it can be correlated to the C_{dl}. Namely, the PZC is basically the potential where the C_{dl} is minimum. In principle, the PZC should be located at the minimum of the differential capacitance C_d. Remarkably, this method of PZC determination first originated from Vorsina and Frumkin.[31] Although the capacitance method is very useful, it comes with its own limitations and hence can only be employed for dilute solutions and in the absence of specific adsorption. This stems from the inner double layer C_i typically dominating the C_{dl} at high electrolyte concentrations, as shown in Eq. (2), obtained from the Gouy-Chapman-Stern model of the EDL.

$$\frac{1}{C_{dl}}=\frac{1}{C_i}+\frac{1}{C_d} \tag{2}$$

Here, C_i and C_d are the capacitance of the inner double layer and the differential capacitance of the diffuse layer, respectively.

Therefore, the capacitance method can scarcely be employed for the PZC determination in the case of high electrolyte concentrations.[32]

Electrocapillary method

Electrocapillarity simply designates the relationship between the interfacial tension or stress and the electrode potential. Therefore, this method employs the electrocapillary equation,[33,34] which also incorporates the so-called Lippmann equation.[35] In this method, the PZC is evaluated as the potential where the electrocapillary curve reaches its peak. Several authors have reported accurate measurements of the interfacial tensions for liquid–liquid interfaces.[6,36,37] The electrocapillary method has also been successfully applied to determine the PZC of some special materials, including liquid metals (mercury, gallium, and its alloys).[38] Recently, this method has been applied to determine the PZC of certain metal-free electrodes like carbon aerogel.[39] However, the scope of use of electrocapillarity is limited, as the dependency of surface tension on the electrode potential is explored in this method. Simply put, it is experimentally impossible to access the absolute interfacial tension at the solid/liquid interface due to several complexities involved in estimating the interfacial stress of solid electrodes. What's more, solids generally do not exhibit surfaces that are in equilibrium, which is a prerequisite for employing this method.

CO charge displacement method

Using the CO charge displacement method, the PZC of some notable noble metal electrodes can be determined.[40,41] This method functions by the complete adsorption of CO until saturation is reached onto the surface of noble metals of mainly Pt group metals (Pt, Pd, Rh, Ir) and is governed by the equation:

$$q_{dis}=q_f-q_i \tag{3}$$

Where q_{dis}, is the charge measured during the CO adsorption process, q_i, the total electrode charge before the CO adsorption and q_f denotes the total electrode charge after the CO adsorption.

During the CO adsorption process, the oxidation states of the noble metal are expected to remain the same. In other words, the charge measured during the CO adsorption process, q_{dis}, should equate to the difference between the total electrode charge before (q_i) and after (q_f) CO adsorption. Eq. (3) further approximates to:

$$q_{dis}=-q_i \tag{4}$$

Since q_f cannot be directly determined but is assumed to be negligible when compared to q_i. Following several measurements for different potentials, the PZC can be evaluated as the potential where q_i is zero.[42,43] Although the CO displacement method can also be used to evaluate the dependence of the PZC on stepped single crystal surface[42] and electrolyte pH,[41] its benefits mainly lie in noble metal electrodes. Furthermore, at high anodic potentials, this method becomes redundant as CO oxidation must be prevented.

N_2O reduction method

After initial works by Ebert et al.[44] Attard et al.[45] opined in their research that the N_2O reduction method can be considered as a surface probe to determine the PZC premised on N_2O's sensitivity to the local total charge. For instance, the N_2O reduction method is utilized to uniquely characterize the difference between local PZTCs existing in a specific sample under study.[44]

So far, this method has been applied on only noble metals such as Ir, Rh, Pd, and Pt electrodes,[44] which is a limitation to its broad applicability. Another limitation hinges on the structural type this method applies. As an example, the N_2O reduction method is limited to just interfacial structures that are sensitive to N_2O reduction reaction.[43]

Other approaches such as vibrational properties of water molecules in the interface,[46,47] scrapping method,[48] and even laser ablation voltammetry method[49] have all been equally used to determine the surface charge of electrode materials. However, all these methods have some limitations like the ones earlier mentioned. Due to the ostensibly destructive nature of the latter two approaches, they cannot be applied to single crystals. For instance, in the scrapping method,[47] the electrode charge is extracted through the regeneration of the metallic surface. Meanwhile, for the laser ablation voltammetry method,[48] the surface of electrode materials can be completely destroyed, and this approach was first employed on a molybdenum electrode.

In brief, all the various methods so far enumerated here have numerous limitations in their broad applicability to several material types. Therefore, it is imperative to find alternative techniques that are robust, versatile and can be employed for many different materials without/with little restrictions. In that regard, the laser-induced transient techniques can be quite helpful in realizing and circumventing most of the limitations the already discussed methods pose.

The laser-induced transient techniques

It has already been established that the electrified electrode/electrolyte interface is vital in optimizing electrode processes or electrocatalytic reactions and plays a crucial role in their design. As such, determining parameters like the PZC and PME that are at the forefront of the electrified interface is essential and hence cannot be undermined. The critical question remains: How can these parameters be measured effectively and help close the gap between simplified theoretical models and dynamic actual electrocatalytic systems? More so, resolving and bringing clarity to the role interfacial water plays in these reactions and electrochemical systems is needful.

In our opinion, the answer lies (most, if not all) with the laser-induced transient techniques through which the sign or the charge on the electrode can be directly measured. The first known use of this methodology was reported by Benderskii and co-workers[50] in 1978, when short, powerful laser pulses were employed to investigate the electrode/electrolyte interface. Subsequently, the kinetics of electrochemical processes occurring on platinum electrodes were studied using an analogous technique by Benderskii's group and others.[51–54] Following these successes, the technique continues to be explored in probing the electrified interface of various electrochemical reactions and systems. Popular among the wide scope application of the method in recent years include investigating the surface charge of gold,[55–57] platinum[29,58–60], and iridium[61] electrodes. Our group has also contributed to further extending the scope of usage of this technique to materials, such as aqueous metal-ion battery,[62,63] manganese oxide,[64] copper,[65] and surface-mounted metal-organic framework[66] electrodes, with the prospects of investigating other electrodes in sight.

The laser-induced transient techniques utilize the so-called temperature jump effect. In that regard, when the surface of a non-transparent electrode is irradiated with a laser source (powerful and short), a sudden surge (ca. 20–40 K) in the temperature of the interfacial region is triggered. Indeed, the working electrode and the electrolyte (the majority being water) create a double layer when a constant potential is applied to the system. This system initially attains an equilibrium state. Upon introduction of the laser pulses at the interfacial region, i.e., the double layer, the equilibrium becomes distorted for a brief period. Interestingly, the response of the system is displayed as current or potential transients and corresponds to the electrode surface charge. More precisely, the system's response mainly highlights the influence of the brief temperature hike on the structure of the inner Helmholtz plane.

The technique is applicable in assessing parameters like the PZC, closely associated with the PME, where water molecules reorient more easily. Thus, independent, and valuable information about the interfacial properties and structure can be obtained. Hence, one direct application of the technique is the determination of the kinetics and mechanism of various electrode processes. This assertion is realized on the condition that the only influence of the laser illumination is the heating of the electrode surface. Hence, fast processes occurring at the electrode/electrolyte interface can be investigated. Depending on the significant difference between the rate of the temperature change and the relaxation time, either thermodynamic or kinetic information can be separately obtained.[55] The former is achieved if the temperature change rate is slower than the relaxation time, with the opposite being true for the latter. Combining results from the laser technique with data obtained from methods like electrochemical impedance spectroscopy and electrochemical quartz crystal microbalance, in-depth characterization, and better understanding of solvation effects in electrochemical systems can be realized. In effect, the behavior of interfacial water molecules on several electrodes, especially on the surfaces of metal and metal oxides, under in-situ conditions can be determined with high selectivity.

Fundamental concepts of the laser-induced transient techniques

Following briefly introducing the technique, its benefits, and scope, it is essential to now delve deeper into the theoretical principles underpinning it.

Assuming that the penetration depth of the light (laser, in this case) is negligible, then the temperature change after a laser pulse can be described as:

$$\Delta T(t) = \frac{1}{\sqrt{\pi \kappa c d} + \sqrt{\pi \kappa_s c_s d_s}} \int_0^t q(t - t') \frac{1}{\sqrt{t'}} dt' \tag{5a}$$

Here, κ, c, and d and κ_s, c_s, and d_s represent the thermal conductivity, thermal capacity, and density of the metal and the aqueous electrolyte (solution), respectively.

Alternatively, the temperature change of the electrode surface due to the laser light absorption just after the end of the laser pulse can be calculated as follows:

$$\Delta T(t) = \frac{I(1-R)}{\sqrt{\pi \kappa c d}} \left(1 + \sqrt{\frac{\kappa_s c_s d_s}{\kappa c d}}\right)^{-1} \sqrt{t_0} \tag{6b}$$

With I being the intensity of the laser light, R denoting the reflectivity of the surface, and t_0 representing the duration of the laser pulse.

The function q designates the power density adsorbed at the metal surface and is dependent on the temporal shape of the laser pulse via the following equation:

$$q(t) = (1-R)I(t) \tag{7}$$

Where $I(t)$ denotes the intensity or the time-dependent energy flux per unit area.

More importantly, for a uniform laser pulse, integrating Eq. (5a) produces the following key formulas:

$$\Delta T(t) = \frac{2(1-R)I}{\sqrt{\pi \kappa c d} + \sqrt{\pi \kappa_s c_s d_s}} \sqrt{t} \ \ (t \le t_0) \quad \textit{Heating} \tag{8}$$

$$\Delta T(t) = \frac{2(1-R)I}{\sqrt{\pi \kappa c d} + \sqrt{\pi \kappa_s c_s d_s}} \left[\sqrt{t} - \sqrt{t - t_0}\right] \ \ (t > t_0) \quad \textit{Cooling} \tag{9}$$

Notably, a long duration of the laser pulse results in the expansion of the term $\sqrt{t - t_0}$. In this respect, only the lower terms in the series remain relevant, and therefore the temperature change decreases with time as:

$$\Delta T(t) = \frac{1}{2} \Delta T_m \sqrt{\frac{t_0}{t}} \tag{10}$$

Where $\Delta T(t)$ designates the rate of decay of the current after the laser pulse or the temperature of the metallic surface fall. ΔT_m represents the maximum temperature change achieved at the end of the pulse.

A linear relationship between the temperature and the potential change can be obtained in scenarios where the temperature change is small enough, as shown below:

$$\Delta E = \left(\frac{\partial E}{\partial T}\right) \Delta T = \left(\frac{\partial E}{\partial T}\right)_q \frac{1}{2} \Delta T_m \sqrt{\frac{t_0}{t}} \tag{11}$$

In essence, the temperature coefficient of the open circuit potential can be evaluated from the slope after plotting ΔE vs. $1/\sqrt{t}$. Noteworthy, from the electrocapillary equation, the following equation can be invariably obtained:

$$\left(\frac{\partial E}{\partial T}\right)_q = -\left(\frac{\partial \Delta S}{\partial q}\right)_T \tag{12}$$

With ΔS denoting the interfacial entropy of formation. Through the integration of the slopes obtained from plotting ΔE vs $1/\sqrt{t}$ as a function of the double layer charge, a graphical illustration of ΔS can be produced. Following that, one can safely predict that $\left(\frac{\partial \Delta S}{\partial q}\right)_T$ will be zero when the curve ΔS vs. q reaches its maximum. In this accord, deducing from Eq. (12), it is prudent to make the inference that the change of the electrochemical potential occasioned by the sudden but brief temperature rise via laser illumination will equally be zero. As such, it is evident that this technique allows the identification of the PME of double layer formation.

It must be quickly pointed out that the equations derived so far did not consider all the possible contributions accompanying the irradiation of an electrode surface with laser pulses. In principle, the response of the potential to the sudden increase of the temperature due to the laser illumination can be partitioned into three categories, namely, the temperature coefficient of the potential drop through the electric double layer $\left(\frac{\partial E}{\partial T}\right)_q$, which is the main contributor, the thermodiffusion potential caused by the difference in the temperature between the solution in contact with the working and reference electrodes, and the temperature gradient in the metal electrode. Generally, the temperature coefficient of the metal/solution potential (E^{M-S}) drop through the EDL can be further split into three contributions and is given as follows:

$$\left(\frac{\partial E^{M-S}}{\partial T}\right)_{q,M} = \frac{1}{e}\left(\frac{\partial \Phi}{\partial T}\right)_q + \left(\frac{\partial E^2}{\partial T}\right)_q + \left(\frac{\partial E^W}{\partial T}\right)_q \tag{13}$$

Where Φ is the work function at the given charge q, E^W is the potential drop due to solvent (re)structuring, E^2 defines the potential drop at the diffuse layer.

As the discussion above does not account for the influence of thermodiffusion potential on the open circuit potential after laser illumination heating, it is worth mentioning that it can be estimated from the so-called Eastman entropy of transfer from the ions involved. This is given as:

$$\frac{\Delta E_{Thermodiffusion}}{\Delta T} = -\frac{1}{F}\sum \frac{t_i}{z_i}\widehat{S}_i \tag{14}$$

With t_i, z_i, and $\widehat{S}_i$ being the transport number, the charge, and the Eastman entropy of the ion i, respectively. It is explicitly implied following a quick glance at **Eq. (14)** that the thermodiffusion potential relies heavily on the nature of the electrolyte. However, the applied electrode potential does not influence this potential contribution. Therefore, in accounting for the highly significant responses from the EDL, the thermodiffusion effect is often neglected.[59,67] An analogous argument can be pursued for the temperature gradient in the metal electrode. In effect, the temperature coefficient of the potential drop through the electric double layer is at the core of this technique.

Origin of a system response during a laser-induced current transient experiment

With the theoretical principles governing the laser-induced transient technique explained, it is worth recapping some vital aspects of the discussions so far. When the surface of a non-transparent electrode is irradiated with a laser source, a sudden increase in the temperature (ca. 20–40 K) of the interfacial region occurs. This alteration in temperature induces the occurrence of a series of transients, and with this change in effect, it is possible to extract valuable information regarding the interface by monitoring the current or potential transients, which hitherto is not available in in-situ techniques.

One significant hallmark of the technique is that the high-power laser illumination results in a sudden temperature change, which is very fast, and decoupling the double layer response from the charge transfer processes is possible.

According to the commonly acknowledged model, in the absence of specifically adsorbed ions, the innermost plane of the solid/liquid interface termed, the inner Helmholtz plane, is composed of a solvent monolayer.[1] The actual system response to the brief laser irradiation reveals the influence of the electrode temperature on the structure of the inner Helmholtz plane of the electric double layer. In aqueous electrolytes systems, one can expect that the polarized water molecules will alter their average orientation according to the sign of the excess surface charge resulting from the applied potential.[67,68] How the solvent molecules orient themselves depends on the interactions between their dipole moment and the electric field produced by the electrode surface charge (E_{Charge}). As a result of the relatively large dipole moment of the electrode surface charge, the potential drop of the electrode emanates to a great extent from the water dipoles E_{dipole}.[67] Therefore, the potential established between the electrode surface and the electrolyte E_{M-S} can be shown as:

$$E_{M-S} = E_{Charge} + E_{dipole} \tag{15}$$

A quick temperature jump resulting from the laser illumination randomizes the solvent adlayer for a brief period, altering E_{dipole} and, as a consequence, E_{M-S} (**Eq. 15**). This leads to the exposure of the excess charge accumulated at the electrode surface, generating potential drops. Upon the relaxation of the double layer interface, the current or potential transients can be observed.

The potential jumps can be observed as current or potential transients, with their sign corresponding to the sign of the electrode surface charge. Based on this phenomenon, the so-called laser-induced current transient (LICT) and laser-induced potential transient (LIPT) methods, or more generally, the laser-induced transient techniques (LITT), or laser-induced temperature jump techniques (LITJT), can be applied to check the electrode surface charge. With the LIPT technique, a change is induced at the open circuit potential, which indicates the orientation of the water dipoles depending on their sign. The LICT technique is performed potentiostatically. During the measurement, the reorganization of the EDL caused by the laser illumination can be recorded as the current transient. A positively charged electrode is expected to reveal positive current transients, whereas a known negatively charged electrode will yield negative current transients from the laser pulse results. The PME is assigned to the potential where the sign of the current transient flips, as shown in **Fig. 3**A and B. The 3D graphical representation (**Fig. 3**A) of the current spikes paints a picture of increasing magnitudes of the current transients in both negative and positive directions and an almost zero point, the PME. As indicated in **Fig. 3**A, the orientation of water dipoles is depicted as oxygen (red color) down when the electrode excess surface charge is positive (positive current transient) and hydrogen (gray/silver color) down for a negatively charged electrode (negative current transient). It is essential to remark that **Fig. 3**B was carved out of **Fig. 3**A. This was plotted by extracting the peak (extreme/maximal) current transient values to simplify and clearly depict the location of the PME in the 2D plot. The zero-crossing point represents the PME, as is evident in **Fig. 3**B.

Measurement schemes

Description of the main laser parameters and specifications

The laser measurements in our laboratory are conducted using a Quanta-Ray INDI pulsed Nd:YAG laser (Spectra-Physics Lasers, USA) with a repetition rate of 10 Hz and 5–8 ns pulse duration. Essentially, a suitable selection of the laser illumination wavelength is key in avoiding side effects, such as photoemission of electrons. Basically, the photoemission threshold for typical metal electrodes is around 200–300 nm (i.e., representing a work function of ca. 4–5 eV).[57] Another critical parameter of the laser that

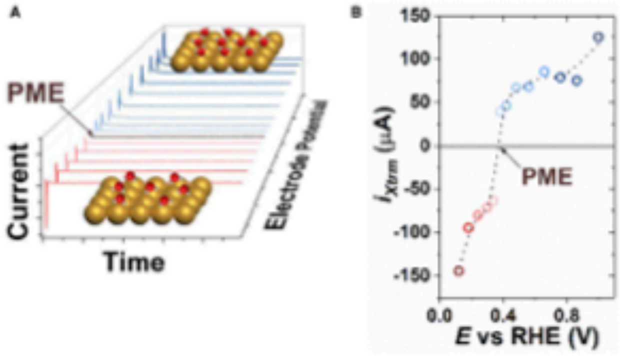

Fig. 3 (A) 3D plotted current transients recorded during the laser measurement at various electrochemical potentials. The potential at which the current transients flip its sign corresponds to the PME, and the sign of the current transients coincide with the sign of the electrode surface charge. (B) 2D current transient diagram with the extreme current transients plotted as a function of the applied potential on the reversible hydrogen electrode (RHE) scale. The data for plotting (B) was obtained from (A). It is necessary to note that not all the current transients are presented in this illustration. (A) The figure was obtained from measurements conducted on polycrystalline gold in 0.5 M O_2-saturated Na_2SO_4 solution (pH 2) and was reprinted with permission from Refs. 28,55. Copyright (2021), Wiley-VCH GmbH, (B) Reproduced from Ref. 28.

must be chosen carefully is its energy, power, or intensity. Apparently, the intensity of the laser beam varies depending on the nature of the electrode and electrolyte under study. Hence, an appropriate laser beam intensity should allow a rapid increase in temperature without causing any destruction to the metallic electrode surface. The wavelength of the laser device applied in all our experiments is 532 nm (i.e., double the frequency of the fundamental frequency of this laser), which is obviously above the photoemission of electrons and therefore prevents that effect. The diameter of the laser beam is maintained at 9 mm for all the laser measurements. Essentially, because the energy emanating directly from the laser beam can reach 200 mJ, constituting a fluence of ca. 314 mJcm^{-2}, which is excessively high and can destroy the working electrode, a motorized beam splitter (VA-CB-532-CONEX, Newport Corp.) serves as an attenuator. This is used to control the energy of the laser pulses that will eventually reach the working electrode. The laser can be operated by either a table-top controller or a GCR control software (Spectra Physics Lasers, USA). The attenuator is manipulated by a Variable Attenuator software (model: CCVA-PR-CD, Spectra-Physics Lasers, USA) to adjust the energy of the laser beam.

It is essential to point out that the laser-induced transient techniques can be mainly categorized into two, namely, LICT and LIPT techniques. The former is implemented under coulostatic conditions to monitor the change of the open-circuit potential, i.e., potential transients. On the contrary, the LICT technique is executed under potentiostatic conditions (keeping the electrode potential constant) to record the current transients flowing through the external circuit after the laser pulse (*see* Fig. 4).

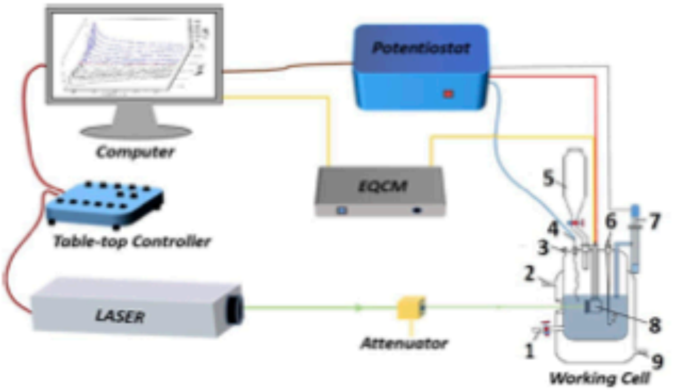

Fig. 4 Schematic representation of the laser-induced current transient (LICT) technique setup. The laser head is shown on the left with the three-electrode configuration electrochemical working cell on the right. The various numerically labeled parts are described as follows: 1—electrolyte inlet, 2—hot-water outlet, 3—gas outlet, 4—counter electrode (CE), 5—electrolyte inlet/preconditioning chamber, 6—gas inlet, 7—reference electrode (RE), 8—working electrode (WE), and 9—hot-water inlet. It is essential to mention that the relative positions of the electrodes as portrayed in the figure do not correspond to the actual measurement configuration, where the RE is located in between the WE and CE instead. Figure reproduced with permission from Refs. 28,55. Copyright (2021), Wiley-VCH GmbH.

Realization of the laser-induced current transient experiment

The working procedure of the laser-induced transient techniques, specifically, the laser-induced current transient technique is described as follows.

The distance between the laser source and the working electrode is kept constant all through the experiments. The electrochemical cell employed for the laser measurements uses the popular three-electrode configuration. Additionally, the three-electrode electrochemical cell for the LICT measurement is equipped with a preconditioning compartment beside its main compartment (*cf.* Fig. 4). After preparing the electrolyte solution, it is preconditioned by purging it with a suitable gas (usually, argon to obtain an inert atmosphere) in the preconditioning compartment, and after saturation is achieved, it is then introduced into the main compartment. Before introducing the electrolyte solution, the whole electrochemical cell must be cleaned severally to ensure the complete cleanliness of the experiment.

A flat but circular, laser light transmittable glass window is designed on the main compartment of the electrochemical cell to ensure that the laser beam reaches the working electrode surface directly. During the experiments, the inside atmosphere can be controlled with a gas inlet and outlet located in the main compartment. The temperature of the investigated electrolytes can also be adjusted by a water thermostat, particularly for this electrochemical cell. Usually, an AT-cut quartz crystal wafer electrochemical quartz crystal microbalance (EQCM) electrode with a surface area of 1.37 cm^2 from Stanford Research Systems, USA, is used as the working electrode (WE) for the LICT measurements. Of course, other forms and shapes of electrode materials can also be used. In terms of reference electrodes (REs), typically, a mercury-mercurous sulfate electrode (MMS) (SI Analytics, Germany) serves this purpose, and it is connected to the electrolyte through a luggin capillary. Frequently, a platinum wire is used as the counter electrode (CE). Of course, the three electrodes must be connected to a potentiostat, and the VSP-300 potentiostat, Bio-Logic, France, is employed for such measurements in our laboratory. As mentioned in The laser-induced transient techniques section, the EQCM can also be connected between the WE and the computer to collect useful data regarding the mass changes of the WE. The experiments begin by first assessing the surface quality or purity of the WE by conducting a cyclic voltammogram. Following that, the laser is activated for a relatively short time for each potential. The LICT measurements are performed in the potentiostatic mode to monitor the change of the current as a function of time. It is significant to mention that the laser measurements are performed for several potentials in a defined potential window dependent on the reaction or system being investigated. The current transients can be recorded from the response of the system following the laser illumination. The extreme values of the current transients (more recently, the charge obtained from estimating the area under the current transients, or simply put, the integration of the current transients) can be plotted as a function of the applied potential to find the PME.

Application of the laser-induced transient techniques

Under this section, various examples of experiments reported in the literature utilizing the laser-induced transient techniques are elaborated to further clarify its benefits and wide scope of use. Therefore, this section is subdivided into two main parts, namely, electrocatalysis and batteries. For electrocatalysis, three categories are targeted, entailing effects of electrode composition and structure on the PME/PZC, effects of electrolyte components on the PME/PZC, and lastly, PME/PZC determination of various electrode materials are also discussed. For battery systems, scenarios ranging from situations where no PME was found to multiple PMEs will be expounded.

Electrocatalysis

Applying the LICT technique in electrocatalysis can help to get valuable information regarding the properties of the EDL, which forms between the electrode and electrolyte. For instance, knowing the effect of the electrode structure and electrode/electrolyte composition on the PME/PZC can significantly improve the development of an effective catalytic material for a defined catalytic reaction. To be more precise, the closer the PME value is to the thermodynamic equilibrium potential of a particular electrocatalytic reaction, the faster the kinetics of this reaction should be. Specific examples of LICT application in electrocatalysis will be discussed in the following.

Effects of electrode structure on the PME/PZC

It is well known that the electrode structure can play an essential role in electrocatalysis, especially in the case of structure-sensitive reactions. For instance, the oxygen reduction reaction (ORR) can be promoted on Pt electrocatalyst by introducing surface defects such as steps and concavities.[69–71] Understanding the structure-activity relation can assist the rational usage of active materials by developing effective catalyst design. Thus, applying the LICT technique can provide valuable information about the PME values depending on the electrode structure, which could, in turn, be used for identifying the most preferred surface for an investigated reaction.

One of the pioneering studies of the impact electrode structures have on the electrified interfacial properties of electrochemical systems was performed by Climent et al.[57] in the early 2000s. The electrode of concern was Au(111) single crystal electrode as well as polycrystalline gold. Perchloric and sulfuric acid were used as electrolytes to ease comparison regarding the influence of specifically adsorbed anions. It is worth noting that the concentration used for the $HClO_4$ acid solution was dilute, namely, 0.01 M, whereas a high concentration of 0.1 M was used for H_2SO_4. This was critical in comparing the results obtained from utilizing the laser technique to the results obtained using the capacitance method (minimum of the double layer), which is only applicable to dilute solutions. The PZC values obtained for Au(111) single crystal and polycrystalline gold electrodes were 0.5 V and 0.25 V, respectively.

Thanks to their impeccable stability, Pt-group metal catalysts are usually used in various electrocatalytic systems.[72,73] One obvious solution to improving the electrocatalytic performance involves incorporating certain facets or defects to alter the electrode surface structure or the creation of alloys to modify the electrode surface composition.[71,74,75] This process will lead to an upsurge in the number of active sites at the electrode surface and eventually enhance the electrode activity. Simply put, electrocatalytic performance can be modified by tuning the electrode composition and structure. It is significant to add that change(s) in the properties of the EDL results in massive changes in electrocatalytic performances and must be considered. Pt single crystals portray good performance toward the ORR,[69–71] while the activity varies for different orientations of the Pt single crystals.[76,77] The difference in activity for different structures of Pt single crystals is due to the difference in the heat of adsorption of intermediates at different active centers and their different abundance.[77]

Another investigation of the electrode structure effect on the PME was performed at the Pt single-crystal surfaces in both alkaline and acidic solutions.[76,77] Interestingly, the locations of the PMEs vary in accordance with their respective surface structures. An analogous trend was found for both media for the Pt(110) < Pt(100) < Pt(111) single crystals, which corresponds to activity results for ORR.[78] In other words, the PME value of Pt(111) is closer to the thermodynamic potential of the ORR compared to the Pt(100) and Pt(110) surfaces. Essentially, the interfacial water structure for the Pt(111) surface is looser, and therefore, easily reorganizes during the charge and mass transfer through the electric double layer.

Effect of electrolyte composition (cations, pH) on the PME/PZC

Besides the electrode structure, the role of electrolytes in electrocatalytic systems should not be underestimated. In the last years, increasing attention has been dedicated to investigating the effects of electrolyte pH as well as alkali metal cations, anions, and even the impact that certain ionic liquids have on the activity of the catalytic system.[79–82] Apart from standard techniques, such as rotating disk electrode voltammetry, infra-red spectroscopy, scanning probe techniques, etc., the LICT has been successfully applied for investigating some of these phenomena as well.

Keeping the electrode material fixed, the electrolyte composition (anions, cations, etc.) was tailored by constantly modifying certain specific components. In that regard, the PME was correlated with the hydration/solvation energy or even pH of the various electrolytes investigated. Besides always using conventional electrolytes, Sebastian et al.[83] employed several components of room temperature ionic liquids (RTILs) in contact with Au(111), Au(100), Au(110), and Pt(111) to probe the solid/liquid interface via the laser-induced transient technique. The three RTILs ($[E_{mmim}][Tf_2N]$, $[E_{mim}][Tf_2N]$, and $[B_{mmim}][Tf_2N]$) comprised three different imidazolium cations while the same $[Tf_2N]$ anion was maintained. The laser measurements indicated that the highest values of the PME in RTIL media correspond to the atomically closest packet surface structures, following the order of Au(111) > Au(100) > Au(110), in agreement with work function values. Results from the laser experiments portrayed that solvent restructuring as a function of both the value and direction of the applied potential depends essentially on the type of cation. The cyclic voltammograms in Fig. 5A–C show minor surface sensitive features compared to the behavior of the same Au(hkl) surfaces in contact with the other electrolytes, namely, $[E_{mmim}][Tf_2N]$ and $[B_{mmim}][Tf_2N]$. In fact, for the $[E_{mim}][Tf_2N]$ electrolyte, there is an increase in the capacitive current spanning the potential region between 0.0 V and −1.0 V vs. Ag. The PME values for each Au basal plane in contact with $[E_{mim}][Tf_2N]$ are shown in both 3D LIPT plots and blank voltammograms for Au(111) (Fig. 5A), Au(100) (Fig. 5B), and Au(110) (Fig. 5C). Interestingly, for the basal plane Au(hkl)/Choline chloride:urea Deep Eutetic Solvent (DES) interface, no PME was found via the laser-induced transient technique. The authors ascribed this finding to the complex chemical structure of the DES as well as DES adsorbing strongly on Au(hkl) electrodes.

It is worth stating that anions can likewise be tailored or tuned in an analogous fashion to the cations to measure their impact on various electrocatalytic electrodes or even on battery materials. A clear trend between the PME values and the anions can be plotted as a function of parameters, such as the hydration energy.

PME/PZC determination of various electrode materials

Recent measurements of the PME and PZC values employing the laser-induced transient technique have focused mainly on using Pt group metals. Our group has expanded the scope of applicability of the technique to include other electrode materials, especially non-precious material surfaces such as metal oxides (specifically, manganese oxide). This section will examine and discuss the electrified interfacial properties of some of these non-precious electrodes.

For instance, laser-induced transient investigations were performed on Cu surfaces in alkaline electrolytes.84 It was found that Cu(111) (see Fig. 6B and D) exhibits a higher PME than Cu(100) (*cf.* Fig. 6A and C) at the studied conditions with estimated values of 0.060 ± 0.019 V vs. RHE and −0.170 ± 0.005 V vs. RHE, respectively. Interestingly, the PME values, in this case for both surfaces were located at the onset potential of the OH-voltammetric feature (Fig. 6C and D). In a separate work, Auer et al.[85] investigated the surface of Cu(111) in alkaline media and demonstrated the influence of pH on the PZFC. Eventually, the pH dependency of the PME was shown to vary for the same electrode material but with different surface structures. To further corroborate the findings on a different material, the PME of Pt(111) in alkaline media was conducted. Again, the PME was found to be at the onset potential of the OH-adsorption feature.[77]

For the first time, Hou et al.[86] employed the in-situ laser-induced transient technique together with another in-situ technique, namely, Raman spectroscopy on surface-mounted metal-organic framework (SURMOF) derivatives. It was observed that the nature of alkali metal cations strongly impacts the oxygen evolution reaction (OER) performance. Moreover, the PME followed the trend of $Cs^+ > K^+ > Na^+ > Li^+$ (*cf.* Fig. 7A) and this concords with the OER activity measurements and the in-situ Raman spectroscopy measurements (*cf.* Fig. 7B and C).

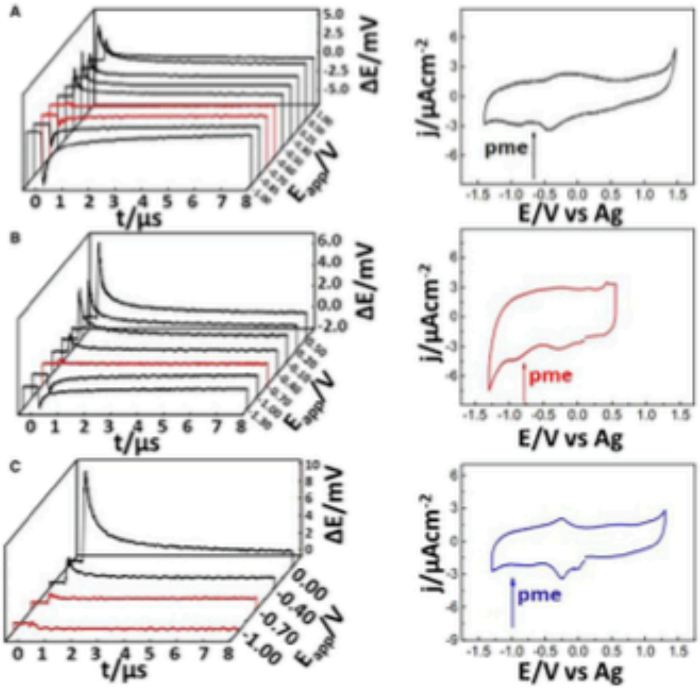

Fig. 5 3D representation of the LIPT results and their corresponding PME location in the cyclic voltammogram for the interface between (A) Au(111)/[E_{mim}][Tf_2N], (B) Au(100)/[E_{mim}][Tf_2N], and (C) Au(110)/[E_{mim}][Tf_2N]. Figure reproduced with permission from Ref. 83. Copyright (2019), Elsevier.

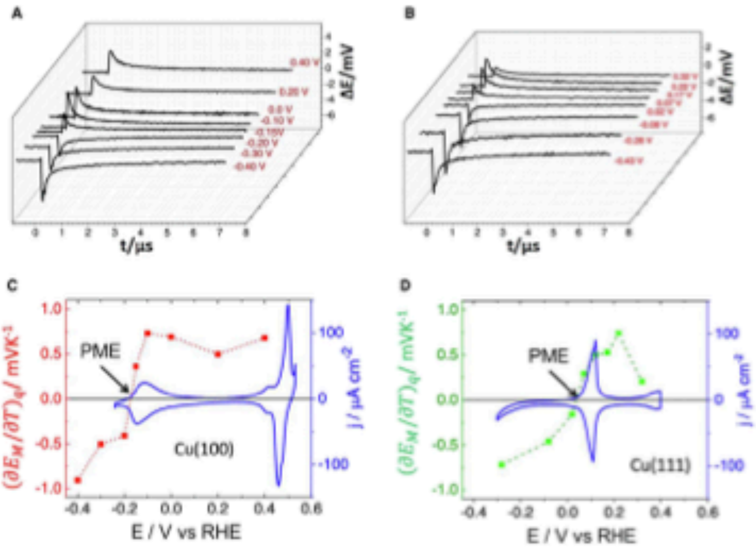

Fig. 6 3D plots of the LIPTs recorded at different applied potentials for (A) Cu(100)|0.1 M NaOH and (B) Cu(111)|0.1 M NaOH. Blank cyclic voltammograms with their corresponding thermal coefficient ($\partial E_M/\partial T$) representation at various applied potentials of (C) Cu(100)|0.1 M NaOH and (D) Cu(111)|0.1 M NaOH. Scan rate: 50 mV/s^{-1}. Adapted with permission from Ref. 84. Copyright (2020), American Chemical Society.

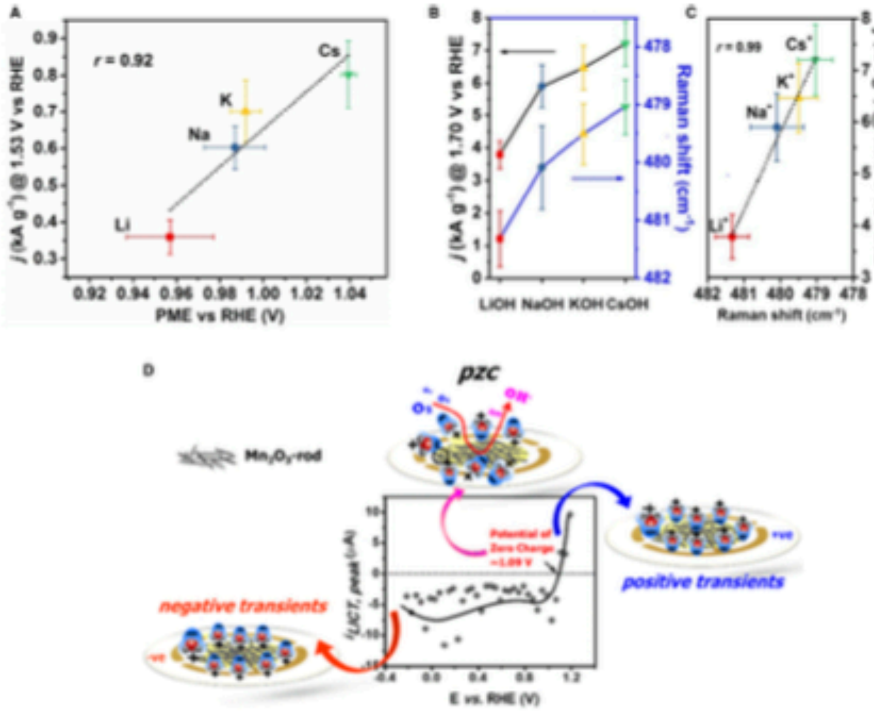

Fig. 7 (A) A plot of the electrocatalytic activities at 1.53 V vs. RHE as a function of the potential of maximum entropy for Ni|Fe-[TA]-Catalyst electrode in the presence of different alkali metal cations. The LICT measurements were performed in Ar-saturated 0.1 M MOH electrolytes, with M representing the various cations, namely, Li$^+$, Na$^+$, K$^+$, and Cs$^+$. The Pearson correlation coefficient (r) obtained from the linear fit was 0.92. (B,C) Correlation of the electrocatalytic activities acquired at 1.70 V vs. RHE (solid black line in B) and the Raman peaks at approximately 480 cm^{-1} (the solid blue line in B) in various electrolytes. The Pearson correlation coefficient (r) obtained from the linear fit of C was 0.99, *Wiley-VCH GmbH*. (D) 2D graphical representation of the dependence of the extreme current values of all the measured transients (black) on the applied potential (scanned anodically, and the dotted line serves as a guide for the eye). The resulting PZC was 1.09 V vs. RHE. Schematic representation of the negative and positive current transients, corresponding to the negative and positive excess surface charges, respectively, on the electrode are nicely displayed and the location of PZC is also portrayed. The LICT study was conducted using manganese oxide electrode toward the ORR. (A–C) A, B, and C were adapted with permission from Ref. 66. Copyright (2022), (D) D reproduced with permission from Ref. 64. Copyright (2020), American Chemical Society

The PZC of the manganese oxide (Mn_2O_3) electrode was also investigated using the laser-induced current transient technique and was found to be ca. 1.09 V vs. RHE (see Fig. 7D), which is close to the thermodynamic equilibrium potential of the oxygen reduction reaction (ORR).[64] This finding validated and deciphered the strong performance that accompanies Mn_2O_3 for the ORR.

Investigation of aqueous rechargeable metal-ion batteries by the LICT technique

In our days, various conventional and unconventional energy sources are utilized. For instance, solar and wind power technologies have already emerged as key components of providing sustainable energy with negligible greenhouse gas emissions. However, because solar and wind resources are stochastic, there may be problems with intermittent energy production.[63,85] Therefore, it is crucial to create energy storage systems in order to provide consumers with consistent, inexpensive energy, which will all lead to strengthening the security of the energy supply. Batteries are considered to be essential embodiments in arriving at the goal of a carbon-free or green environment based mainly on renewable energy technologies.[86] Recently, the aqueous rechargeable metal-ion batteries have attracted great interest due to their cost efficiency, safety, environmental friendliness, natural abundance, and high capacity.[87] In that vein, it is prudent to fathom the mechanism of intercalation and de-intercalation to ameliorate the efficiency of these systems, and eventually optimize their effectiveness. Thus, the use of the LICT technique may create new opportunities for research of the electrode/electrolyte interface, which should help to better appreciate the intercalation/deintercalation mechanisms, and subsequently improve battery performance. For the first time, Scieszka et al. applied the LICT methodology to investigate the interface between $Na_2Ni[Fe(CN)_6]$ model battery electrodes and aqueous solutions.[62,63] In order to investigate the effect of hydration energy on the PME, 0.25 M Na_2SO_4 and 0.25 M K_2SO_4 electrolytes were used in the study. It was demonstrated that the electrode surfaces were positively charged during intercalation/deintercalation of sodium and potassium cations, pointing to the complexity of the intercalation process of the alkali metal cations. Interestingly, tripolar shapes were observed for the obtained current transients (Fig. 8A–D). Such shape of transients was attributed to the interfacial processes of intercalation/

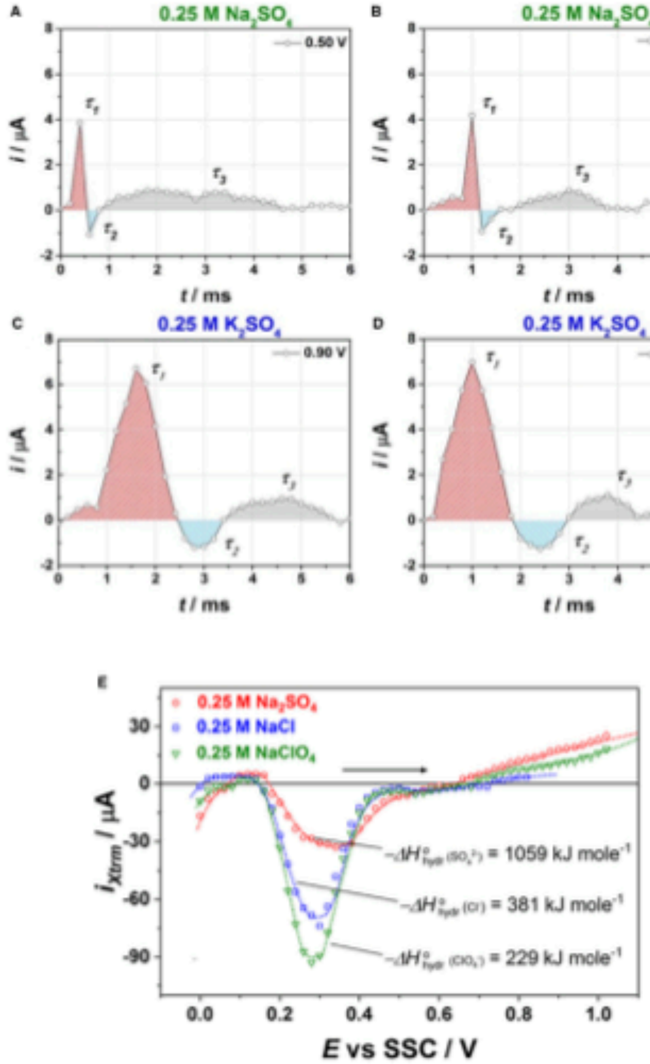

Fig. 8 Representation of the relaxation times for the current transients obtained from $Na_2Ni[Fe(CN)_6]$ thin films in 0.25 M Na_2SO_4 at potential values of (A) 0.50 V and (B) 0.68 V, as well as in 0.25 M K_2SO_4 at potential values of (C) 0.90 V and (D) 0.96 V. All the presented potentials were referenced vs. the silver-silver chloride (SSC) electrode. Three clearly distinguishable peaks associated with the interfacial processes corresponding to three different time constants (designated as $\tau1$, $\tau2$, and $\tau3$) can be observed. (E) Graphical depiction of the extreme current transients obtained for $Na_2Co[Fe(CN)_6]$ in three different electrolytes, namely, 0.25 M Na_2SO_4, 0.25 M NaCl, and 0.25 M $NaClO_4$. A clear dependence of the potential of maximum entropy on the hydration energy of the various anions are exhibited, with each showing up to three PMEs. (A–D) Figures reproduced with permission from Ref. 62. Copyright (2017), American Chemical Society, (E) Figure reproduced with permission from Ref. 63. Copyright (2018), American Chemical Society.

deintercalation, which have three different relaxation time constants. In addition, it was shown that the relaxation behavior is affected by the nature of the alkali metal cations, most likely, due to their different solvation energy.[62] Further investigations of the electrode/electrolyte interface formed between electrodeposited $Na_2Co[Fe(CN)_6]$ films and aqueous solutions revealed that the PME depends on the anions' properties as well. Moreover, Na-ion battery model systems show up to three PMEs in all investigated electrolytes, such as 0.25 M Na_2SO_4, 0.25 M NaCl, and 0.25 M $NaClO_4$ (Fig. 8E).[63] To summarize the above-mentioned studies on aqueous metal-ion batteries, the use of the LICT technique demonstrated significant utility in the investigation of interfacial processes for such systems. Therefore, the consistent application of this technique can significantly contribute to the development of efficient battery systems.

Summary

In summary, the electric double layer has been elucidated, and the crucial role of interfacial water in optimizing electrochemical systems and reactions has also been discussed. Key parameters like the potentials of zero charge and maximum entropy, which are vital to the electrified interface have been explained in detail. The various techniques employed in determining the PZC and PME were also elaborated with a special highlight on the limitations of each method. Remarkably, the laser-induced transient techniques were presented, beginning from a general overview of the techniques, and then the fundamentals governing them were proven and expounded. Delightfully, the origin of the sign flipping of interfacial water dipoles was further explained with mathematical proofs. Additionally, the source of system feedback following the brief laser illumination was also elaborated. Subsequently, the experimental details, including the need to employ certain laser specifications were also highlighted. Moreover, several examples from the literature that apply the techniques to various electrochemical systems, from electrocatalysis to battery, were discussed to establish the point that these techniques are valuable and possess a wide scope of applicability.

It has been vividly established from the carefully chosen literature discussed herein that an excellent opportunity exists to employ LITJ techniques on other systems comprising several material types. More precisely, besides using noble metals, non-noble metals have also been measured using these methods. Metal oxides (manganese oxide, as an example) and metal-organic frameworks (MOFs) have also been investigated with these techniques. As such, it is our considered opinion that materials such as conductive polymers, metal alloys, and even more sophisticated and/or complicated compositions and structures of materials can eventually be probed with the laser-induced transient techniques.

Based on the fundamentals and the numerous pieces of literature presented, one can infer that, indeed, these approaches really help in characterizing the electrified electrode/electrolyte interface and, therefore, a better understanding of the processes, mechanisms, and phenomena occurring at the interface can be obtained. This will surely open avenues for the rational design of efficient, effective, and optimized electrochemical systems.

Acknowledgments

We gratefully thank the Deutsche Forschungsgemeinschaft (DFG) under Germany's excellence strategy—EXC 2089/1 – 390776260, Germany's excellence cluster "e-conversion", DFG project BA 5795/4-1, and BA 5795/5-1 for the financial support. Likewise, we appreciate the financial support from DFG research group 2982 under UNusual anODE (UNODE).

References

1. Hamann, C. H.; Hamnett, A.; Vielstich, W. *Electrochemistry*, second, completely revised and updated ed.; Wiley-Vch Verlag GmbH & Co. KGaA: Weinheim, 2007.
2. Helmholtz, H. Ueber Einige Gesetze der Vertheilung Elektrischer Ströme in Körperlichen Leitern, mit Anwendung auf die Thierisch-Elektrischen Versuche. *Ann. Phys.* **1853,** *165*, 353–377.
3. Gouy, M. Sur la Constitution de la Charge Électrique à la Surface d'un Électrolyte. *Phys. Theor. Appl.* **1910,** *9*, 457–468.
4. Chapman, D. L. A Contribution to the Theory of Electrocapillarity. *Mag. J. Sci.* **1913,** *25*, 475–481.
5. Stern, O. Zur Theorie der Elektrolytischen Doppelschicht. *Z. Elektrochem. Angew. Phys. Chem.* **1924,** *30*, 508–516.
6. Grahame, D. C. The Electrical Double Layer and the Theory of Electrocapillarity. *Chem. Rev.* **1947,** *41*, 441–501.
7. Garlyyev, B.; Watzele, S.; Fichtner, J.; Michalička, J.; Schökel, A.; Senyshyn, A.; Perego, A.; Pan, D.; El-Sayed, H. A.; Macak, J. M.; Atanassov, P.; Zenyuk, I. V.; Bandarenka, A. S. Electrochemical Top-Down Synthesis of C-Supported Pt Nano-Particles With Controllable Shape and Size. Mechanistic Insights and Application. *Nano Res.* **2020,** *14*, 2762–2769.
8. Hou, J.; Wu, Y.; Zhang, B.; Cao, S.; Li, Z.; Sun, L. Rational Design of Nanoarray Architectures for Electrocatalytic Water Splitting. *Adv. Funct. Mater.* **2019,** *29*, 1808367.
9. Xue, S.; Haid, R. W.; Kluge, R. M.; Ding, X.; Garlyyev, B.; Fichtner, J.; Watzele, S.; Hou, S.; Bandarenka, A. S. Enhancing the Hydrogen Evolution Reaction Activity of Platinum Electrodes in Alkaline Media Using Nickel–Iron Clusters. *Angew. Chem. Int. Ed.* **2020,** *59*, 10934–10938.
10. Ling, T.; Jaroniec, M.; Qiao, S. Z. Recent Progress in Engineering the Atomic and Electronic Structure of Electrocatalysts Via Cation Exchange Reactions. *Adv. Mater.* **2020,** *32*, e2001866.
11. Yang, S.; Li, S.; Lv, Y.; Duan, Z.; Li, C.; Praeg, R. F.; Gao, D.; Chen, G. Defect-Density Control of Platinum-Based Nanoframes With High-Index Facets for Enhanced Electrochemical Properties. *Nano Res.* **2019,** *12*, 2881–2888.
12. Zhang, L.; Doyle-Davis, K.; Sun, X. Pt-Based Electrocatalysts With High Atom Utilization Efficiency: From Nanostructures to Single Atoms. *Energy Environ. Sci.* **2019,** *12*, 492–517.

13. Li, H.; Han, Y.; Zhao, H.; Qi, W.; Zhang, D.; Yu, Y.; Cai, W.; Li, S.; Lai, J.; Huang, B. Fast Site-to-Site Electron Transfer of High-entropy Alloy Nanocatalyst Driving Redox Electrocatalysis. *Nat. Commun.* **2020,** *11,* 1–9.
14. Kani, K.; Lim, H.; Whitten, A. E.; Wood, K.; Yago, A. J. E.; Hossain, M. S. A.; Heinzie, J.; Na, J.; Yamauchi, Y. First Electrochemical Synthesis of Mesoporous RhNi Alloy Films for an Alkali-Mediated Hydrogen Evolution Reaction. *J. Mater. Chem. A* **2021,** *9,* 2754–2763.
15. Cao, D.; Xu, H.; Cheng, D. Construction of Defect-Rich RhCu Nanotubes With Highly Active Rh_3Cu_1 Alloy Phase for Overall Water Splitting in all pH Values. *Adv. Energy Mater.* **2020,** *10,* 1903038.
16. Arminio-Ravelo, J. A.; Jensen, A. W.; Jensen, K. D.; Quinson, J.; Escudero-Escribano, M. Electrolyte Effects on the Electrocatalytic Performance of Iridium-Based Nanoparticles for Oxygen Evolution in Rotating Disc Electrodes. *ChemPhysChem* **2019,** *20,* 2956–2963.
17. König, M.; Vaes, J.; Klemm, E.; Pant, D. Solvents and Supporting Electrolytes in the Electrocatalytic Reduction of CO_2. *iScience* **2019,** *19,* 135–160.
18. Birdja, Y. Y.; Pérez-Gallent, E.; Figueiredo, M. C.; Göttle, A. J.; Calle-Vallejo, F.; Koper, M. T. M. Advances and Challenges in Understanding the Electrocatalytic Conversion of Carbon Dioxide to Fuels. *Nat. Energy* **2019,** *4,* 732–745.
19. Li, G.-F.; Divinagracia, M.; Labata, M. F.; Ocon, J. D.; Abel-Chuang, P.-Y. Electrolyte-Dependent Oxygen Evolution Reactions in Alkaline Media: Electrical Double Layer and Interfacial Interactions. *ACS Appl. Mater. Inter.* **2019,** *11,* 33748–33758.
20. Gao, D.; Arán-Ais, R. M.; Jeon, H. S.; Cuenya, B. R. Rational Catalyst and Electrolyte Design for CO_2 Electroreduction Towards Multicarbon Products. *Nat. Catal.* **2019,** *2,* 198–210.
21. Sa, Y. J.; Lee, C. W.; Lee, S. Y.; Na, J.; Lee, U.; Hwang, Y. J. Catalyst–Electrolyte Interface Chemistry for Electrochemical CO_2 Reduction. *Chem. Soc. Rev.* **2020,** *49,* 6632–6665.
22. Frumkin, A.; Gorodetzkaya, A. Capillary Electric Phenomena in Amalgams. I Thallium Amalgams. *Z. Phys. Chem.* **1928,** *136,* 451–472.
23. Ding, X.; Sarpey, T. K.; Hou, S.; Garlyyev, B.; Li, W.; Fischer, R. A.; Bandarenka, A. S. Prospects of Using the Laser-Induced Temperature Jump Techniques for Characterisation of Electrochemical Systems. *ChemElectroChem* **2022,** *9,* e20210117.
24. Climent, V.; García-Araez, N.; Herrero, E.; Feliu, J. M. Potential of Zero Total Charge of Platinum Single Crystals: A Local Approach to Stepped Surfaces Vicinal to Pt(111). *Russ. J. Electrochem.* **2006,** *42,* 1145–1160.
25. Frumkin, A. N.; Petrii, O. A. Potentials of Zero Total and Zero Free Charge of Platinum Group Metals. *Electrochim. Acta* **1975,** *20,* 347–359.
26. Trasatti, S. J. Interaction of Water With Metal Surfaces. A Theory on the Role of the Solid Substrate. *J. Electroanal. Chem. Interfacial Electrochem.* **1974,** *54,* 437–441.
27. Scieszka, D. *In-Depth Characterization of Electrified Solid/Liquid Interfaces With the Laser-Induced Current Transient Technique.* Ph. D. thesis, TUM, September 2019.
28. Ding, X. *LASER-Assisted Determination of the Potential of Maximum Entropy. Applications in Electrocatalysis.* Ph. D. thesis, TUM, September 2021.
29. Ding, X.; Scieszka, D.; Watzele, S.; Xue, S.; Garlyyev, B.; Haid, R. W.; Bandarenka, A. S. A Systematic Study of the Influence of Electrolyte Ions on the Electrode Activity. *ChemElectroChem* **2022,** *9,* e202101088.
30. Ledezma-Yanez, I.; Wallace, W. D. Z.; Sebastián-Pascual, P.; Climent, V.; Feliu, J. M.; Koper, M. T. M. Interfacial Water Reorganization as a pH-Dependent Descriptor of the Hydrogen Evolution Rate on Platinum Electrodes. *Nat. Energy* **2017,** *2,* 17031.
31. Vorsina, M.; Frumkin, A. Capacity of the Double Layer of the Mercury Electrode in Dilute Solutions of Hydrochloric Acid and of Potassium Chloride. *Doklady Akad. Nauk SSSR* **1939,** *24,* 918–921.
32. Ojha, K.; Arulmozhi, N.; Aranzales, D.; Koper, M. T. M. Double Layer at the Pt(111)–Aqueous Electrolyte Interface: Potential of Zero Charge and Anomalous Gouy–Chapman Screening. *Angew. Chem. Int. Ed.* **2020,** *59,* 711–715.
33. Plieth, W. J. On the Derivation and Formulation of the Electrocapillary Equation of Ideally Polarizable Electrodes. *J. Electroanal. Chem.* **1970,** *27,* 468–471.
34. Harrison, J. A.; Randles, J. E. B.; Schiffrin, D. J. The Entropy of Formation of the Mercury-Aqueous Solution Interface and the Structure of the Inner Layer. *J. Electroanal. Chem. Interfacial Electrochem.* **1973,** *48,* 359–381.
35. Lippmann, G. Relations Entre Les Phénomènes Électriques et Capillaires. *Ann. Chim. Phys.* **1875,** *5,* 494–549.
36. Parsons, R.; Bockris, J. O.'M.; Conway, B. E. Equilibrium Properties of Electrified Interfaces. In *Modern Aspects of Electrochemistry,* vol 1; Academic Press: New York, 1954.
37. Girault, H.; Schiffrin, D.; Bard, A. J.; *Electrochemistry of Liquid-Liquid Interfaces. Electroanalytical Chemistry,* vol 15; Marcel Dekker: New York, 1989.
38. Horsman, P.; Conway, B. E.; Yeager, E. *Comprehensive Treatise of Electrochemistry: The Double Layer,* Springer Science & Business Media, 2013.
39. Shao, L.-H.; Biener, J.; Kramer, D.; Viswanath, R. N.; Baumann, T. F.; Hamza, A. V.; Weissmüller, J. Electrocapillary Maximum and Potential of Zero Charge of Carbon Aerogel. *J. Phys. Chem. Chem. Phys.* **2010,** *12,* 7580–7587.
40. Silva, C. D.; Cabello, G.; Christinelli, W. A.; Pereira, E. C.; Cuesta, A. Simultaneous Time-Resolved ATR-SEIRAS and CO-Charge Displacement Experiments: The Dynamics of CO Adsorption on Polycrystalline Pt. *J. Electroanal. Chem.* **2017,** *800,* 25–31.
41. Clavilier, J.; Albalat, R.; Gomez, R.; Orts, J.; Feliu, J. M.; Aldaz, A. Study of the Charge Displacement at Constant Potential During CO Adsorption on Pt(110) and Pt(111) Electrodes in Contact With a Perchloric Acid Solution. *J. Electroanal. Chem.* **1992,** *330,* 489–497.
42. Climent, V.; Attard, G.; Feliu, J. M. Potential of Zero Charge of Platinum Stepped Surfaces: A Combined Approach of CO Charge Displacement and N_2O Reduction. *J. Electroanal. Chem.* **2002,** *532,* 67–74.
43. Climent, V.; Gómez, R.; Feliu, J. M. Effect of Increasing Amount of Steps on the Potential of Zero Total Charge of Pt(111) Electrodes. *Electrochim. Acta* **1999,** *45,* 629–637.
44. Ebert, H.; Parsons, R.; Ritzoulis, G.; VanderNoot, T. The Reduction of Nitrous Oxide on Platinum Electrodes in Acid Solution. *J. Electroanal. Chem. Interfacial Electrochem.* **1989,** *264,* 181–193.
45. Attard, G.; Ahmadi, A. Anion-Surface Interactions Part 3. N_2O Reduction as a Chemical Probe of the Local Potential of Zero Total Charge. *J. Electroanal. Chem.* **1995,** *389,* 175–190.
46. Ataka, K.-. I.; Yotsuyanagi, T.; Osawa, M. Potential-Dependent Reorientation of Water Molecules at an Electrode/Electrolyte Interface Studied by Surface-Enhanced Infrared Absorption Spectroscopy. *J. Phys. Chem.* **1996,** *100,* 10664–10672.
47. Iwasita, T.; Xia, X. H. Adsorption of Water at Pt (111) Electrode in $HClO_4$ Solutions. The Potential of Zero Charge. *J. Electroanal. Chem.* **1996,** *411,* 95–102.
48. Andersen, T. N.; Perkins, R. S.; Eyring, H. Zero-Charge Potentials of Solid Metals. *J. Am. Chem. Soc.* **1964,** *86,* 4496.
49. Nakamura, K.; Ohno, M.; Umemoto, K.; Hinoue, T. Potential of Zero Charge of a Molybdenum Electrode by Laser Ablation Voltammetry. *Chem. Lett.* **2000,** 1050–1051.
50. Benderskii, V. A.; Babenko, S. D.; Krivenko, A. G. Investigation of the Charge Relaxation in the Double Layer by a Thermal Jump. *J. Electroanal. Chem. Interfacial Electrochem.* **1978,** *86,* 223–225.
51. Benderskii, V. A.; Velichko, G. I. Temperature Jump in Electric Double-Layer Study: Part I. Method of Measurements. *J. Electroanal. Chem. Interfacial Electrochem.* **1982,** *140,* 1–22.
52. Benderskii, V. A.; Velichko, G. I.; Kreitus, I. Temperature Jump in Electric Double-Layer Study: Part II. Excess Entropy of EDL Formation at the Interface of Mercury and Electrolyte Solutions of Various Concentrations. *J. Electroanal. Chem. Interfacial Electrochem.* **1984,** *181,* 1–20.
53. Smalley, J. F.; Krishnan, C. V.; Goldman, M.; Feldberg, S. W.; Ruzic, I. Laser-Induced Temperature-Jump Coulostatics for the Investigation of Heterogeneous Rate Processes: Theory and Application. *J. Electroanal. Chem.* **1988,** *248,* 255–282.
54. Smalley, J. F.; Newton, M. D.; Feldberg, S. W. An Informative Subtlety of temperature-Jump or Coulostatic Responses for Surface-Attached Species. *Electrochem. Commun.* **2000,** *2,* 832–838.
55. Ding, X.; Garlyyev, B.; Watzele, S. A.; Sarpey, T. K.; Bandarenka, A. S. Spotlight on the Effect of Electrolyte Composition on the Potential of Maximum Entropy. Supporting Electrolytes are not Always Inert. *Chemistry* **2021,** *27,* 10016–10020.
56. Climent, V.; Coles, B. A.; Compton, R. G. Laser-Induced Potential Transients on a Au(111) Single-Crystal Electrode. Determination of the Potential of Maximum Entropy of Double-Layer Formation. *J. Phys. Chem. B* **2002,** *106,* 5258–5265.

57. Climent, V.; Coles, B. A.; Compton, R. G. Laser Induced Current Transients Applied to a Au(111) Single Crystal Electrode. A General Method for the Measurement of Potentials of Zero Charge of Solid Electrodes. *J. Phys. Chem. B* **2001,** *105*, 10669–10673.
58. Climent, V.; Coles, B. A.; Compton, R. G. Laser-Induced Potential Transients on a Au(111) Single-Crystal Electrode. Determination of the Potential of Maximum Entropy of Double-Layer Formation. *J. Phys. Chem. B* **2002,** *106*, 5988–5996.
59. Climent, V.; Garcia-Araez, N.; Compton, R. G.; Feliu, J. M. Effect of Deposited Bismuth on the Potential of Maximum Entropy of Pt(111) Single-Crystal Electrodes. *J. Phys. Chem. B* **2006,** *110*, 21092–21100.
60. Garcia-Aráez, N.; Climent, V.; Feliu, J. M. Evidence of Water Reorientation on Model Electrocatalytic Surfaces From Nanosecond-Laser-Pulsed Experiments. *J. Am. Chem. Soc.* **2008,** *130*, 3824–3833.
61. Ganassin, A.; Sebastián, P.; Climent, V.; Schuhmann, W.; Bandarenka, A. S.; Feliu, J. M. On the pH Dependence of the Potential of Maximum Entropy of Ir(111) Electrodes. *Sci. Rep.* **2017,** *7*, 1–14.
62. Scieszka, D.; Yun, J.; Bandarenka, A. S. What do Laser-Induced Transient Techniques Reveal for Batteries? Na- and K- Intercalation From Aqueous Electrolytes as an Example. *ACS Appl. Mater. Inter.* **2017,** *9*, 20213–20222.
63. Scieszka, D.; Sohr, C.; Scheibenbogen, P.; Marzak, P.; Yun, J.; Liang, Y.; Fichtner, J.; Bandarenka, A. S. Multiple Potentials of Maximum Entropy of a $Na_2Co[Fe(CN)_6]$ Battery Electrode Material: Does the Electrolyte Composition Control the Interface? *ACS Appl. Mater. Inter.* **2018,** *10*, 21688–21695.
64. Nagaiah, T. C.; Tiwari, A.; Kumar, M.; Scieszka, D.; Bandarenka, A. S. In-Situ Probing of Mn2O3 Activation Towards Oxygen Electroreduction by Laser-Induced Current Transient Technique. *ACS Appl. Energy Mater.* **2020,** *3*, 9151–9157.
65. Auer, A.; Ding, X.; Bandarenka, A. S.; Kunze-Liebhäuser, J. The Potential of Zero Charge and the Electrochemical Interface Structure of Cu(111) in Alkaline Solutions. *J. Phys. Chem. C* **2021,** *125*, 5020–5028.
66. Hou, S.; Xu, L.; Ding, X.; Kluge, R. M.; Sarpey, T. K.; Haid, R. W.; Garlyyev, B.; Mukherjee, S.; Warnan, J.; Koch, M.; Zhang, S.; Li, W.; Bandarenka, A. S.; Fischer, R. A. Dual In-Situ Laser Techniques Underpin the Role of Cations in Impacting Electrocatalysts. *Angew. Chemie Int. Ed.* **2022,** *61*, e20221610.
67. Yamakata, A.; Osawa, M. Dynamics of Double-Layer Restructuring on a Platinum Electrode Covered by CO: Laser-Induced Potential Transient Measurement. *J. Phys. Chem. C* **2008,** *112*, 11427–11432.
68. Toney, M. F.; Howard, J. N.; Richer, J.; Borges, G. L.; Gordon, J. G.; Melroy, O. R.; Wiesler, D. G.; Yee, D.; Sorensen, L. B. Voltage-Dependent Ordering of Water Molecules at an Electrode–Electrolyte Interface. *Nature* **1994,** *368*, 444–446.
69. Gómez-Marín, A. M.; Feliu, J. M. Oxygen Reduction on Nanostructured Platinum Surfaces in Acidic Media: Promoting Effect of Surface Steps and Ideal Response of Pt(111). *Catal. Today* **2015,** *244*, 172–1769.
70. Kuzume, A.; Herrero, E.; Feliu, J. M. Oxygen Reduction on Stepped Platinum Surfaces in Acidic Media. *J. Electroanal. Chem.* **2007,** *599*, 333–343.
71. Čolić, V.; Bandarenka, A. S. Pt Alloy Electrocatalysts for the Oxygen Reduction Reaction: From Model Surfaces to Nanostructured Systems. *ACS Catal.* **2016,** *6*, 5378–5385.
72. Lenne, Q.; Leroux, Y. R.; Lagrost, C. Surface Modification for Promoting Durable, Efficient, and Selective Electrocatalysts. *ChemElectroChem* **2020,** *7*, 2345–2363, 4501.
73. Shao, M.; Chang, Q.; Dodelet, J.-P.; Chenitz, R. Recent Advances in Electrocatalysts for Oxygen Reduction Reaction. *Chem. Rev.* **2016,** *116*, 3594–3657.
74. Morales, D. M.; Kazakova, M. A.; Purcel, M.; Masa, J.; Schuhmann, W. The Sum is More Than Its Parts: Stability of MnFe Oxide Nanoparticles Supported on Oxygen-Functionalized Multi-Walled Carbon Nanotubes at Alternating Oxygen Reduction Reaction and Oxygen Evolution Reaction Conditions. *J. Solid State Electrochem.* **2020,** *24*, 2901–2906.
75. Aiyappa, H. B.; Masa, J.; Andronescu, C.; Muhler, M.; Fischer, R. A.; Schuhmann, W. MOFs for Electrocatalysis: From Serendipity to Design Strategies. *Small Methods* **2019,** *3*, 1800415.
76. Garcia-Araez, N.; Climent, V.; Feliu, J. M. Potential-Dependent Water Orientation on Pt(111), Pt(100), and Pt(110), as Inferred From Laser-Pulsed Experiments. Electrostatic and Chemical Effects. *J. Phys. Chem. C* **2009,** *113*, 9290–9304.
77. Sarabia, F. J.; Sebastián, P.; Climent, V.; Feliu, J. M. New Insights into the Pt(hkl)-Alkaline Solution Interphases From the Laser Induced Temperature Jump Method. *J. Electroanal. Chem.* **2020,** *872*, 114068.
78. Schmidt, T. J.; Stamenkovic, V.; Arenz, M.; Markovic, N. M.; Ross, P. N. Oxygen Electrocatalysis in Alkaline Electrolyte: Pt(hkl), Au(hkl) and the Effect of Pd-Modification. *J. Electrochim. Acta* **2002,** *47*, 3765–3776.
79. Mitchell, J. B.; Shen, M.; Twight, L.; Boettcher, S. W. Hydrogen-Evolution-Reaction Kinetics pH Dependence: Is It Covered? *Chem. Catal.* **2022,** *2*, 236–238.
80. Colic, V.; Pohl, M. D.; Scieszka, D.; Bandarenka, A. S. Influence of the Electrolyte Composition on the Activity and Selectivity of Electrocatalytic Centers. *Catal. Today* **2016,** *262*, 24–35.
81. Garlyyev, B.; Xue, S.; Watzele, S.; Scieszka, D.; Bandarenka, A. S. Influence of the Nature of the Alkali Metal Cations on the Electrical Double-Layer Capacitance of Model Pt(111) and Au(111) Electrodes. *J. Phys. Chem. Lett.* **2018,** *9*, 1927–1930.
82. Goyal, A.; Koper, M. T. M. The Interrelated Effect of Cations and Electrolyte pH on the Hydrogen Evolution Reaction on Gold Electrodes in Alkaline Media. *Angew. Chem. Int. Ed.* **2021,** *60*, 13452–13462.
83. Sebastián, P.; Gómez, E.; Climent, V.; Feliu, J. M. Investigating the M(hkl)|Ionic Liquid Interface by Using Laser Induced Temperature Jump Technique. *Electrochimica Acta* **2019,** *311*, 30–40.
84. Sebastián-Pascual, P.; Sarabia, F. J.; Climent, V.; Feliu, J. M.; Escudero-Escribano, M. Elucidating the Structure of the Cu-Alkaline Electrochemical Interface With the Laser-Induced Temperature Jump Method. *J. Phys. Chem. C* **2020,** *124*, 23253–23259.
85. Khare, V.; Nema, S.; Baredar, P. Solar-Wind Hybrid Renewable Energy System: A Review. *Renew. Sust. Energy Rev.* **2016,** *58*, 23–33.
86. Goikolea, E.; Palomares, V.; Wang, S.; Larramendi, I. R.; Guo, X.; Wang, G.; Rojo, T. Na-Ion Batteries—Approaching Old and New Challenges. *Adv. Energy Mater.* **2020,** *10*, 2002055.
87. Pan, Z.; Liu, X.; Yang, J.; Li, X.; Liu, Z.; Loh, X. J.; Wang, J. Aqueous Rechargeable Multivalent Metal-Ion Batteries: Advances and Challenges. *Adv. Energy Mater.* **2021,** *11*, 2100608.

9.0 Bibliography

---

[1] World population. Worldometer. https://www.worldometers.info/world-population/. (Date Accessed Online: 6. October 2022).

[2] (Nations, 2022) United Nations. https://news.un.org/en/story/2022/07/1122272 (Date Accessed Online: 15. December 2022).

[3] (Agency, International Energy Agency, 2022) Agency, I. E. (02. 12 2022). *International Energy Agency*. Von https://www.iea.org/commentaries/for-the-first-time-in-decades-the-number-of-people-without-access-to-electricity-is-set-to-increase-in-2022 (Date Accessed Online: 15. December 2022).

[4] (Agency, https://www.iea.org/data-and-statistics/data-product/electricity-information, 2022) Agency, I. E. (03. 12 2022). *https://www.iea.org/data-and-statistics/data-product/electricity-information*. (Date Accessed Online: 15. December 2022).

[5] (BP, 2022) BP. (03. 12 2022). *BP Energy Outlook 2022*. Von https://www.bp.com/content/dam/bp/business-sites/en/global/corporate/pdfs/energy-economics/energy-outlook/bp-energy-outlook-2022.pdf (Date Accessed Online: 15. December 2022).

[6] (BloombergNEF, 2022) BloombergNEF. (03. 12 2022). *https://assets.bbhub.io/professional/sites/24/BNEF-Power-Transition-Trends-2022_FINAL.pdf*. Von https://assets.bbhub.io/professional/sites/24/BNEF-Power-Transition-Trends-2022_FINAL.pdf (Date Accessed Online: 15. December 2022).

[7] (Outlook, 2022) Outlook, I. E. (02. 12 2022). *EIA*. Von https://www.eia.gov/outlooks/ieo/pdf/ieo2019.pdf (Date Accessed Online: 15. December 2022).

[8] Smalley, R. E., *Future Global Energy Prosperity: The Terawatt Challenge*, MRS Bulletin, 2005, **30**, *6*, 412-417.

[9] (www.bp.com/, 2019) Bp statistical review – www.bp.com/ (Date Accessed Online: 08. August, 2019).

[10] (Technische Universität Darmstadt, 2019) Technische Universität Darmstadt, Universität Duisburg-Essen Unabhängiges Institut für Umweltfragen:http://de.statista.com/statistik/daten/studie/246112/umfrage/weltweitesangebot-von-primaerenergie-nach-energietraeger.

[11] (Agency, IEA- http://www.eia.gov/forecasts/ieo/, 2019) IEA- http://www.eia.gov/forecasts/ieo/ (Date Accessed Online: December 2022).

[12] (Agency, International Energy Agency – Energy and Climate Change, 2015; https://www.iea.org/reports/energy-and-climate-change, 2022). (Date Accessed Online: December 2022).

[13] (Schönwiese, 2022) Christian D. Schönwiese http://www.fze.uni-saarland.de/AKE_Archiv/DPG2002_undfrueher/DPG2001_Buch/DPG2001_01Schoenwiese.pdf (Date Accessed Online: December 2022).

---

[14] (2016, 2022) IEA (2016), *CO_2 Emissions from Fuel Combustion 2016*, OECD Publishing, Paris, https://doi.org/10.1787/co2_fuel-2016-en (Date Accessed Online: December 2022).

[15] (Figueres, et al., 2018, 564) Figueres, C., Le Quéré, C., Mahindra, A., Bäte, O., Whiteman, G., Peters, G., & Guan, D., *Emissions are Still Rising: Ramp Up the Cuts*, Nature, 2018, **564**, *7734*, 27-30.

[16] (BLÖSCHL, et al., 2017) Blöschl, G., Hall, J., Parajka, J., Perdigão, R. A. P., Merz, B., Arheimer, B., Aronica, G. T., Bilibashi, A., Bonacci, O., Borga, M., Čanjevac, I., Castellarin, A., Chirico, G. B., Claps, P., Fiala, K., Frolova, N., Gorbachova, L., Gül, A., Hannaford, J., Harrigan, S., Kireeva, M., Kiss, A., Kjeldsen, T. R., Kohnová, S., Koskela, J. J., Ledvinka, O., Macdonald, N., Mavrova-Guirguinova, M., Mediero, L., Merz, R., Molnar, P., Montanari, A., Murphy, C., Osuch, M., Ovcharuk, V., Radevski, I., Rogger, M., Salinas, J. L., Sauquet, E., Šraj, M., Szolgay, J., Viglione, A., Volpi, E., Wilson, D., Zaimi, K., & Živković N., *Changing Climate Shifts Timing of European Floods*, Science, 2017, **357**, *6351*, 588-590.

[17] (V. Masson-Delmotte, 2018) Masson-Delmotte, V., Zhai, P., Pörtner, H. -O., Roberts, D., Skea, J., Shukla, P. R., Pirani, A., Moufouma-Okia, W., Péan, C., Pidcock, R., Connors, S., Matthews, J. B. R., Chen, Y., Zhou, X., Gomis, M. I., Lonnoy, E., Maycock, T., Tignor, M., & Waterfield, T., *IPCC, 2018: Global warming of 1.5°C. An IPCC Special Report on the Impacts of Global Warming of 1.5°C Above Pre-Industrial Levels and Related Global Greenhouse Gas Emission Pathways, in the Context of Strengthening the Global Response to the Threat of Climate Change*, *Sustainable Development, and Efforts to Eradicate Poverty*, 2019.

[18] (https://www.prognos.com/sites/default/files/2022-07/Prognos_KlimawandelfolgenDeutschland_Detailuntersuchung%20Flut_AP2_3b_.pdf, 2022). Kosten durch Klimawandelfolgen in Deutschland. *https://www.prognos.com/sites/default/files/2022.07/Prognos_KlimawandelfolgenDeutschland_Detailuntersuchung%20Flut_AP2_3b_.pdf* (Date Accessed Online: 22. July 2022).

[19] (transition., 2022) Hydrogen Council. How Hydrogen Empowers the Energy Transition. https://hydrogencouncil.com/wp-content/uploads/2017/06/Hydrogen-Council-Vision-Document-pdf (Date Accessed Online: December 2022).

[20] (UNFCCC, 2022) UNFCCC. Adoption of the Paris Agreement. Report No. FCCC/CP/2015/L.9/Rev.1, http://unfccc.int/resource/docs/2015/cop21/eng/109r01.pdf (Date Accessed Online: December 2022).

[21] (International Energy Agency, Key Trends in CO2 Emissions from Fuel Combustion 2015, International Energy Agency, IEA Publications, Paris, France, 2015, 2022) Key Trends in CO2 Emissions from Fuel Combustion 2015, https://www.pbl.nl/sites/default/files/downloads/pbl-2015-iea-co2-emissions-from-fuel-combustion-1971-2013-part-3-total-greenhouse-gas-emissions.pdf (Date Accessed Online: December 2022).

[22] (hE. Dlugokencky, 2022) https://gml.noaa.gov/ccgg/trends/index.html (Date Accessed Online: 06. December 2022).

[23] (International Energy Agency, Energy Technology Perspectives 2015, International Energy Agency, IEA/OECD, IEA Publications, Paris, France, 2015; https://www.iea.org/reports/energy-technology-perspectives-2015, 2022) Energy Technology Perspectives 2015, International Energy Agency, IEA/OECD, IEA Publications, Paris, France, 2015; https://www.iea.org/reports/energy-technology-perspectives-2015 (Date Accessed Online: December 2022).

---

[24] (Rogelj, 2018) Rogelj, J., D. Shindell, K. Jiang, S. Fifita, P. Forster, V. Ginzburg, C. Handa, H. Kheshgi, S. Kobayashi, E. Kriegler, L. Mundaca, R. Séférian, & M. V. Vilariño, 2018: Mitigation Pathways Compatible with 1.5°C in the Context of Sustainable Development. In: *Global Warming of 1.5°C. An IPCC Special Report on the impacts of global warming of 1.5°C above pre-industrial levels and related global greenhouse gas emission pathways, in the context of strengthening the global response to the threat of climate change, sustainable development, and efforts to eradicate poverty* [Masson-Delmotte, V., P. Zhai, H.-O. Pörtner, D. Roberts, J. Skea, P.R. Shukla, A. Pirani, W. Moufouma-Okia, C. Péan, R. Pidcock, S. Connors, J.B.R. Matthews, Y. Chen, X. Zhou, M.I. Gomis, E. Lonnoy, T. Maycock, M. Tignor, & T. Waterfield (eds.)]. Cambridge University Press, Cambridge, UK and New York, NY, USA, 93-174.

[25] (M. Z. Jacobson, 2017) Jacobson, M. Z., Delucchi, M. A., Bauer, Z. A. F., Goodman, S. C., Chapman, W. E., Cameron, M. A., Bozonnat, C., Chobadi, L., Clonts, H. A., Enevoldsen, P., Erwin, J. R., Fobi, S. N., Goldstrom, O. K., Hennessy, E. M., Liu, J., Lo, J., Meyer, C. B., Morris, S. B., Moy, K. R., O'Neill, P. L., & Yachanin, A. S., *100% Clean and Renewable Wind, Water, and Sunlight All-Sector Energy Roadmaps for 139 Countries of the World*, Joule, 2017, **1**, *1*, 108-121.

[26] (Schwieterman, 2019, 878, 19) Schwieterman, E. W., Reinhard, C. T., Olson, S. L., Harman, C. E., & Lyons, T. W., *A Limited Habitable Zone for Complex Life*, Astrophys. J., 2019, **878**, *1*, 19.

[27] (NASA Exoplanet Archive, kein Datum) NASA Exoplanet Archive, NASA Exoplanet Science Institute, https://exoplanetarchive.ipac.caltech.edu/docs/counts_detail.html (Date Accessed Online: 6. October 2020).

[28] (The habitable exoplanets catalog, 2022) (https://phl.upr.edu/projects/habitable-exoplanets-catalog, kein Datum) The Habitable Exoplanet Catalog. (Date Accessed Online: 6. October 2022).

[29] Seh, Z. W., Kibsgaard, J., Dickens, C. F., Chorkendorff, I., Nørskov, J. K., & Jaramillo, T. F., *Combining Theory and Experiment in Electrocatalysis: Insights into Materials Design*, Science, 2017, **355**, eaad4998.

[30] Net Zero by 2050 – Analysis – IEA. https://www.iea.org/reports/net-zero-by-2050 (Date Accessed Online: February 2022).

[31] Höök, M., & Tang, X., *Depletion of Fossil Fuels and Anthropogenic Climate Change - A Review*, Energy Policy, 2013, **52**, 797-809.

[32] Grubler, A., Wilson, C., Bento, N., Boza-Kiss, B., Krey, V., McCollum, D. L., Rao, N. D., Riahi, K., Rogelj, J., De Stercke, S., Cullen, J., Frank, S., Fricko, O., Guo, F., Gidden, M., Havlík, P., Huppmann, D., Kiesewetter, G., Rafaj, P., Schoepp, W., & Valin, H., *A Low Energy Demand Scenario for Meeting the 1.5 °C Target and Sustainable Development Goals Without Negative Emission Technologies*, Nature Energy, 2018, **3**, 515-527.

[33] Renewable Energy: The Clean Facts. https://www.nrdc.org/stories/renewable-energy-clean-facts (Date Accessed Online: February 2022).

[34] Hussain, A., Arif, S. M., & Aslam, M., *Emerging Renewable and Sustainable Energy Technologies: State of the Art*, Renew. & Sustainable Energy Rev., 2017, **71**, 12-28.

---

[35] Moriarty, P. & Honnery, D., *Global Renewable Energy Resources and Use in 2050*, In: T. M. Letcher, (Ed.), *Managing Global Warming: An Interface of Technology and Human Issues*, Academic Press, 2019, 221-235.

[36] (Bp, 2022) https://www.bp.com/content/dam/bp/business-sites/en/global/corporate/pdfs/energy-economics/energy-outlook/bp-energy-outlook-2022.pdf (Date Accessed Online: December 2022).

[37] (reports, 2022) https://archive.ipcc.ch/pdf/special-reports/srren/SRREN_FD_SPM_final.pdf (Date Accessed Online: December 2022).

[38] (IPCC, 2022) https://www.ipcc.ch/report/renewable-energy-sources-and-climate-change-mitigation/ (Date Accessed Online: December 2022).

[39] (Zervos, 2022) Zervos, A., Renewables 2022 Global Status Report, 2022. https://www.ren21.net/wp-content/uploads/2019/05/GSR2022_Full_Report.pdf (Date Accessed Online: December 2022).

[40] (Wind in power, 2022) Wind in Power, European Statistics 2014, EWEA 2015, https://windeurope.org/wp-content/uploads/files/about-wind/statistics/EWEA-Annual-Statistics-2015.pdf (Date Accessed Online: December 2022).

[41] (Providing all global energy with wind, 2011) Jacobson, M. Z., & Delucchi, M. A., *Providing all Global Energy with Wind, Water, and Solar Power, Part I: Technologies, Energy Resources, Quantities and Areas of Infrastructure, and Materials*, Energy Policy, 2011, **39**, *3*, 1154-1169.

[42] Agrawal, S., & Soni, R., *Renewable Energy: Sources, Importance and Prospects for Sustainable Future*, Energy: Crises, Challenges and Solutions, 2021, 131-150.

[43] Neto, P. B. L., Saavedra, O. R., & Oliveira, D. Q., *Renewable Sources Complementarity*, In: A.C. Zambroni de Souza, B. Venkatesh, (Eds.), *Planning and Operation of Active Distribution Networks: Technical, Social and Environmental Aspects*, Springer Int. Publishing, Cham, 2022, 353-376.

[44] (Kiriyama, 2004) Kiriyama, E., & Suzuki, A., *Use of Real Options in Nuclear Power Plant Valuation in the Presence of Uncertainty with* CO_2 *Emission Credit*, J. Nuclear Sci. & Tech., 2004, **41**, *7*, 756-764.

[45] (Sailor, 2000) Sailor, W. C., Bodansky, D., Braun, C., Fetter, S., & van der Zwaan, B., *A Nuclear Solution to Climate Change?*, Science, 2000, **288**, *5469*, 1177-1178.

[46] (Eichholz, 1976) Eichholz, G. G., *Environmental Aspects of Nuclear Power*, Ann Arbor Science Publishers, Inc., 1976.

[47] (Baker, 1999) Baker, J. N., & Collinson, A., *Electrical Energy Storage at the Turn of the Millennium*, Power Eng J., 1999, **13**, *3*, 107-112.

[48] (Connolly, 2007) Connolly, D., *An Investigation into the Energy Storage Technologies Available for the Integration of Alternative Generation Techniques*, 2007, Limerick, Ireland, University of Limerick.

---

[49] (Zakeri, 2015) Zakeri, B., & Syri, S., *Electrical Energy Storage Systems: A Comparative Life Cycle Cost Analysis*, Renew. & Sustainable Energy Rev., 2015, **42**, 569-596.

[50] (Larcher, 2015) Larcher, D., & Tarascon, J. -M., *Towards Greener and More Sustainable Batteries for Electrical Energy Storage*, Nat. Chem., 2015, **7**, *1*, 19-29.

[51] (Zhao, 2015) Zhao, H., Wu, Q., Hu, S., Xu, H., & Rasmussen, C. N., *Review of Energy Storage System for Wind Power Integration Support*, Appl. Energy, 2015, **137**, *C*, 545-553.

[52] (Walawalkar, 2007) Walawalkar, R., Apt, J., & Mancini, R., *Economics of Electric Energy Storage for Energy Arbitrage and Regulation in New York*, Energy Policy, 2007, **35**, *4*, 2558-2568.

[53] (Guney, 2017) Guney, M. S., & Tepe, Y., *Classification and Assessment of Energy Storage Systems*, Renew. & Sustainable Energy Rev., 2017, **75**, 1187-1197.

[54] (Cabeza, 2015) Cabeza, L., Martorell, I., Miró, L., Fernández, A., & Barreneche, C., *Introduction to Thermal Energy Storage (TES) Systems*, (Ed: Cabeza, L. F.), Woodhead Publishing, Cambridge, UK, 2015.

[55] ((IEC), 2011) International Electrotechnical Commission (IEC), Electrical Energy Storage, Geneva, Switzerland, 2011.

[56] (Peng, 2013) Peng, Q., Yang, X., Ding, J., Wei, X., & Yang, J., *Design of New Molten Salt Thermal Energy Storage Material for Solar Thermal Power Plant*, Appl. Energy, 2013, **112**, 682-689.

[57] (Herrmann, 2004) Herrmann, U., Kelly, B., & Price, H., *Two-Tank Molten Salt Storage for Parabolic Trough Solar Power Plants*, Energy, 2004, **29**, *5-6*, 883-893.

[58] (Chen, Progress in electrical energy storage system: A critical review, 2009) Chen, H., Cong, T. N., Yang, W., Tan, C., Li, Y., & Ding, Y., *Progress in Electrical Energy Storage System: A Critical Review*, Progress in Natural Science, 2009, **19**, *3*, 291-312.

[59] (Letcher, 2016) Letcher, T. M., Law, R., & Reay, D., *Storing Energy: With Special Reference to Renewable Energy Sources* (Vol. 86). Oxford: Elsevier, 2016.

[60] (Lewis, 2007) Lewis, N. S., *Powering the Planet*, MRS Bull., 2007, **32**, *10*, 808-820.

[61] (Zafirakis, 2013) Zafirakis, D., Chalvatzis, K. J., Baiocchi, G., & Daskalakis, G., *Modeling of Financial Incentives for Investments in Energy Storage Systems that Promote the Large-Scale Integration of Wind Energy*, Appl. Energy, 2013, **105**, 138-154.

[62] (Studies, 2022) GIS ASIE – French Academic Network on Asian Studies, http://www.gis-reseau-asie.org/en/relocated-people-three-gorges (Date Accessed Online: December 2022).

[63] (Williams, 2008) Succar, S. & Williams, R. H., *Compressed Air Energy Storage: Theory, Resources, And Applications for Wind Power*, Princeton Environmental Institute, 08. April 2008. Princeton Environmental Institute, Princeton University.

[64] (Auer, 2012) Auer, J., & Keil, J., *State-of-the-Art Electricity Storage Systems: Indispensable Elements of the Energy Revolution*, Deutsche Bank Research, Frankfurt, Germany, 2012.

---

[65] (Sebastián, 2012) Sebastián, R. & Peña Alzola, R., *Flywheel Energy Storage Systems: Review and Simulation for an Isolated Wind Power System*, Renew. & Sustainable Energy Rev., Elsevier, 2012,**16**, *9*, 6803-6813.

[66] (Jossen, 2018) Prof. Dr.-Ing. Andreas Jossen, Lecture, Energy Storage - Flywheels, 17. May 2018, Page 4.

[67] (Swierczynski, 2010) Swierczynski, M., Teodorescu, R., Rasmussen, C. N., Rodriguez, P., & Vikelgaard, H., In: *Overview of the Energy Storage Systems for Wind Power Integration Enhancement*, 2010 IEEE International Symposium on Industrial Electronics, Bari, Italy, 2010, 3749-3756.

[68] (Abedini, 2008) Abedini, A., & Nasiri, A., *Applications of Super Capacitors for PMSG Wind Turbine Power Smoothing*. In: *2008 34th Annual Conference of IEEE Industrial Electronics*, IEEE, 2008, 3347-3351.

[69] (Banerjee, 1990) Banerjee, S., Chatterjee, J. K., & Tripathy, S. C., *Application of Magnetic Energy Storage Unit as Load-Frequency Stabilizer*, IEEE Transactions on Energy Conversion, 1990, **5**, *1*, 46-51.

[70] (Molina, 2012) Molina, M. G., *Distributed Energy Storage Systems for Applications in Future Smart Grids*. In: 2012 Sixth IEEE/PES Transmission and Distribution: Latin America Conference and Exposition (T&D-LA), IEEE, 2012, 1-7.

[71] (Li, 2008) Li, X., Hu, C., Liu, C., & Xu, D., *Modeling and Control of Aggregated Super-Capacitor Energy Storage System for Wind Power Generation*. In: 2008 34th Annual Conference of IEEE Industrial Electronics, IEEE, 2008, 3370-3375.

[72] (Kiehne, 2003) Kiehne, H. A., *Battery Technology Handbook*, Vol. 118, CRC Press, Florida, FL, 2003.

[73] (Liu J. Z., 2013) Liu, J., Zhang, J. G., Yang, Z., Lemmon, J. P., Imhoff, C., Graff, G. L., Li, L., Hu, J., Wang, C., Xiao, J., Xia, G., Viswanathan, V. V., Baskaran, S., Sprenkle, V., Li, X., Shao, Y., & Schwenzer, B., *Materials Science and Materials Chemistry for Large Scale Electrochemical Energy Storage: from Transportation to Electrical Grid*, Adv. Functional Mater., 2013, **23**, *8*, 929-946.

[74] (Yang, 2011) Yang, Z., Zhang, J., Kintner-Meyer, M. C., Lu, X., Choi, D., Lemmon, J. P., & Liu, J., *Electrochemical Energy Storage for Green Grid*, Chem. Rev., 2011, **111**, *5*, 3577-3613.

[75] (Kempener, 2015) Kempener, R., & Borden, E., *Battery Storage for Renewables: Market Status and Technology Outlook*, Int. Renew. Energy Agency, Abu Dhabi, 2015.

[76] (Poullikkas, 2013) Poullikkas, A., *A Comparative Overview of Large-Scale Battery Systems for Electricity Storage*, Renew. & Sustainable Energy Rev., 2013, **27**, 778-788.

[77] (Amrouche, 2016) Amrouche, S. O., Rekioua, D., Rekioua, T., & Bacha, S., *Overview of Energy Storage in Renewable Energy Systems*, Int. J. Hydrogen Energy, 2016, **41**, *45*, 20914-20927.

---

[78] (Hall, 2008) Hall, P. J., & Bain, E. J., *Energy-Storage Technologies and Electricity Generation*, Energy Policy, 2008, **36**, *12*, 4352-4355.

[79] (Valøen, 2007) Valøen, L. O., & Shoesmith, M. I., *The Effect of PHEV and HEV Duty Cycles on Battery and Battery Pack Performance*. In: PHEV 2007 Conference, 2007, 4-5.

[80] (Armand, 2008) Armand, M., & Tarascon, J. -M., *Building Better Batteries*, Nature, 2008, **451**, *7179*, 652-657.

[81] (Grosjean, 2012) Grosjean, C., Miranda, P. H., Perrin, M., & Poggi, P., *Assessment of World Lithium Resources and Consequences of their Geographic Distribution on the Expected Development of the Electric Vehicle Industry*, Renew. & Sustainable Energy Rev., 2012, **16**, *3*, 1735-1744.

[82] (Tarascon, 2010) Tarascon, J.-M., *Is Lithium the New Gold?*, Nat. Chem., 2010, **2***, 6*, 510.

[83] (Vesborg, 2012) Vesborg, P. C. K., & Jaramillo, T. F., *Addressing the Terawatt Challenge: Scalability in the Supply of Chemical Elements for Renewable Energy*, RSC Adv., 2012, **2***, 21*, 7933-7947.

[84] (Posada, 2017) Posada, J. O. G., Rennie, A. J., Villar, S. P., Martins, V. L., Marinaccio, J., Barnes, A., Glover, C. F., Worsley, D. A., & Hall, P. J., *Aqueous Batteries as Grid-Scale Energy Storage Solutions*, Renew. & Sustainable Energy Rev., 2017, **68***,* 1174-1182.

[85] (Palomares, 2012) Palomares, V., Serras, P., Villaluenga, I., Hueso, K. B., Carretero-González, J., & Rojo, T., *Na-Ion Batteries, Recent Advances & Present Challenges to Become Low-Cost Energy Storage Systems*, Energy Environ. Sci., 2012, **5**, *3*, 5884-5901.

[86] (exploded., 2023) Why those Samsung Batteries Exploded? https://www.washingtonpost.com/news/the-switch/wp/2016/09/12/why-those-samsung batteries-exploded/ (Date Accessed Online: 21. January 2023).

[87] (Tesla investigates video of model s car exploding, 2019) *Tesla Investigates Video of Model s Car Exploding, https://www.theguardian.com/technology/2019/apr/22/tesla-investigates-video-of-model- s-car-exploding* (Date Accessed Online: 21. January 2023).

[88] (http://english.etnews.com/20191023200001, 2019) ESS Equipped with LG Chem's Battery Produced from South Korea Causes Another Fire. http://english.etnews.com/20191023200001 (Date Accessed Online: 21. January 2023).

[89] (Dong, 2016) Dong, X., Chen, L., Liu, J., Haller, S., Wang, Y., & Xia, Y., *Environmentally-Friendly Aqueous Li (or Na)-Ion Battery with Fast Electrode Kinetics and Super-Long Life*, Sci. Adv., 2016, **2***, 1*, e1501038.

[90] (Hou Z. L., 2015) Hou, Z., Li, X., Liang, J., Zhu, Y., & Qian, Y., *An Aqueous Rechargeable Sodium Ion Battery Based on a* $NaMnO_2$-$NaTi_2(PO_4)_3$ *Hybrid System for Stationary Energy Storage*, J. Mater. Chem. A, 2015, **3**, *4*, 1400-1404.

[91] (Wu, 2015) Wu, X., Luo, Y., Sun, X., Qian, J., Cao, Y., Ai, X., & Yang, H., *Low-Defect Prussian Blue Nanocubes as High Capacity and Long Life Cathodes for Aqueous Na-Ion Batteries*, Nano Energy, 2015, **13**, *C*, 117-123.

---

[92] (Pan, 2013) Pan, H., Hu, Y. -S., & Chen, L., *Room-Temperature Stationary Sodium-Ion Batteries for Large-Scale Electric Energy Storage*, Energy Environ. Sci., 2013, **6**, *8*, 2338-2360.

[93] (George W. Crabtree, 2004) Crabtree, G. W., Dresselhaus, M. S., & Buchanan, M. V., *The Hydrogen Economy*, Phys. Today, 2004, **57**, *12*, 39-44.

[94] (X. Ren, 2020) Ren, X., Dong, L., Xu, D., & Hu, B., *Challenges Towards Hydrogen Economy in China*, Int. J. Hydrogen Energy, 2020, **45**, *59*, 34326-34345.

[95] (Mah, 2019) Mah, A. X. Y., Ho, W. S., Bong, C. P. C., Hassim, M. H., Liew, P. Y., Asli, U. A., Kamaruddin, M. J., & Chemmangattuvalappil, N. G., *Review of Hydrogen Economy in Malaysia and its Way Forward*, Int. J. Hydrogen Energy, 2019, **44**, *12*, 5661-5675.

[96] (Al Ghafri, 2022) Al Ghafri, S. Z. S., Munro, S., Cardella, U., Funke, T., Notardonato, W., Trusler, J. P. M., Leachman, J., Span, R., Kamiya, S., Pearce, G., Swanger, A., Rodriguez, E. D., Bajada, P., Jiao, F., Peng, K., Siahvashi, A., Johns, M. L., & May, E. F., *Hydrogen Liquefaction: A Review of the Fundamental Physics, Engineering Practice and Future Opportunities*, Energy Environ. Sci., 2022, **15**, 2690-2731.

[97] (Sherif, 2005) Sherif, S. A., Barbir, F., & Veziroglu, T. N., *Towards a Hydrogen Economy*, The Electricity J., 2005, **18**, *6*, 62-76.

[98] Stöckl, F., Schill, W. -P., & Zerrahn, A., *Optimal Supply Chains and Power Sector Benefits of Green Hydrogen*, Scientific Reports, 2021, **11**, 14191.

[99] Fasihi, M., & Breyer, C., *Baseload Electricity and Hydrogen Supply Based on Hybrid PV-Wind Power Plants*, J. Cleaner Production, 2020, **243**, 118466.

[100] (B. Tanç, 2020) Tanç, B., Arat, H. T., Conker, Ç., Baltacioğlu, E., & Aydin, K., *Energy Distribution Analyses of an Additional Traction Battery on Hydrogen Fuel Cell Hybrid Electric Vehicle*, Int. J. Hydrogen Energy, 2020, **45**, *49*, 26344-26356.

[101] (F. Dawood, 2020) Dawood, F., Anda, M., & Shafiullah, G., *Hydrogen Production for Energy: An Overview*, Int. J. Hydrogen Energy, 2020, **45**, *7*, 3847-3869.

[102] The German National Hydrogen Strategy. (Strategy. https://www.energypartnership.cn/fileadmin/user_upload/china/media_elements/Documents/German_National_Hydrogen_Strategy.pdf, 2020) (Date Accessed Online: January 2023).

[103] (UNFCCC. Adoption of the Paris Agreement. Report No. FCCC/CP/2015/L.9/Rev.1, 2015) UNFCCC. Adoption of the Paris Agreement. Report No. FCCC/CP/2015/L.9/Rev.1, http://unfccc.int/resource/docs/2015/cop21/eng/l09r01.pdf (Date Accessed Online: January 2023).

[104] (L. B. Weger, 2021) Weger, L. B., Leitão, J., & Lawrence, M. G., *Expected Impacts on Greenhouse Gas and Air Pollutant Emissions due to a Possible Transition towards a Hydrogen Economy in German Road Transport*, Int. J. Hydrogen Energy, 2021, **46**, *7*, 5875-5890.

[105] The Future of Hydrogen, IEA. https://www.iea.org/reports/the-future-of-hydrogen (Date Accessed Online: January 2023).

---

[106] (A. Ajanovic and R. Haas, 2021) Ajanovic, A., & Haas, R., *Prospects and Impediments for Hydrogen and Fuel Cell Vehicles in the Transport Sector*, Int. J. Hydrogen Energy, 2021, **46**, *16*, 10049-10058.

[107] Yu, M., Wang, K., & Vredenburg, H., *Insights into Low-Carbon Hydrogen Production Methods: Green, Blue and Aqua Hydrogen*, Int. J. Hydrogen Energy, 2021, **46**, 21261-21273.

[108] (2019., 2019) International Energy Agency (IEA) - The Future of Hydrogen: Seizing Today's Opportunities. 2019; https://www.iea.org/reports/the-future-of-hydrogen. (Date Accessed Online: January 2023).

[109] (Office of Energy Efficiency & Renewable Energy U. h.) Office of Energy Efficiency & Renewable Energy, US. https://www.energy.gov/eere/fuelcells/h2scale. (Date Accessed Online: January 2023).

[110] (Safari, 2020) Safari, F., & Dincer, I., *A Review and Comparative Evaluation of Thermochemical Water Splitting Cycles for Hydrogen Production*, Energy Conversion and Management, 2020, **205**, *1*, 112182.

[111] (Kiros, 2006) Kiros, Y., Pirjamali, M., & Bursell, M., *Oxygen Reduction Electrodes in Chlor-Alkali Cells*, Electrochim. Acta, 2006, **51**, *16*, 3346-3350.

[112] (Kothari, Comparison of environmental and economic aspects of various hydrogen production methods, 2008) Kothari, R., Buddhi, D., & Sawhney, R. L., *Comparison of Environmental and Economic Aspects of Various Hydrogen Production Methods*, Renew. & Sustainable Energy Rev., 2008, **12**, *2*, 553-563.

[113] (Darras, 2012) Darras, C., Muselli, M., Poggi, P., Voyant, C., Hoguet, J. C., & Montignac, F., *PV Output Power Fluctuations Smoothing: The MYRTE Platform Experience*, Int. J. Hydrogen Energy, 2012, **37**, *19*, 14015-14025.

[114] (Crabtree, 2004) Crabtree, G. W., Dresselhaus, M. S., & Buchanan, M. V., *The Hydrogen Economy*, Phys. Today, 2004, **57**, *12*, 39-44.

[115] (Zhang, 2020) Zhang, H., Maijenburg, A. W., Li, X., Schweizer, S. L. & Wehrspohn, R. B., *Bifunctional Heterostructured Transition Metal Phosphides for Efficient Electrochemical Water Splitting*, Adv. Funct. Mater., 2020, **30**, *34*, 2003261.

[116] (Miller, 2020) Miller, H. A., Bouzek, K., Hnat, J., Loos, S., Bernäcker, C. I., Weißgärber, T., Röntzsch, L., & Meier-Haack, J. M., *Green Hydrogen from Anion Exchange Membrane Water Electrolysis: A Review of Recent Developments in Critical Materials and Operating Conditions*, Sustain. Energy Fuels, 2020, **4**, *5*, 2114-2133.

[117] (Ahmadi, 2020) Ahmadi, P., Torabi, S. H., Afsaneh, H., Sadegheih, Y., Ganjehsarabi, H., & Ashjaee, M., *The Effects of Driving Patterns and PEM Fuel Cell Degradation on the Lifecycle Assessment of Hydrogen Fuel Cell Vehicles*, Int. J. Hydrogen Energy, 2020, **45**, *5*, 3595-3608.

[118] (Long, 2019) Long, Z., Axsen, J., Miller, I., & Kormos, C., *What Does Tesla Mean to Car Buyers? Exploring the Role of Automotive Brand in Perceptions of Battery Electric Vehicles*, Transp. Res. A, 2019, **129**, 185-204.

[119] (https://www.toyota.co.uk/new-cars/mirai, 2023) Toyota Homepage - https://www.toyota.co.uk/new-cars/mirai (Date Accessed Online: January 2023).

---

[120] (https://www.hyundaiusa.com/us/en/vehicles/nexo, 2023) Hyundai Homepage - https://www.hyundaiusa.com/us/en/vehicles/nexo (Date Accessed Online: January 2023).

[121] (https://www.bmwgroup.com/en/news/general/2022/FuelCell.html, 2023) BMW Homepage - https://www.bmwgroup.com/en/news/general/2022/FuelCell.html (Date Accessed Online: January 2023).

[122] (https://automobiles.honda.com/clarity-fuel-cell, 2023) https://automobiles.honda.com/clarity-fuel-cell (Date Accessed Online: January 2023).

[123] (https://media.daimlertruck.com/marsMediaSite/en/instance/ko/Development-milestone-Daimler-Truck-tests-fuel-cell-truck-with-liquid-hydrogen.xhtml?oid=51975637, 2023) https://media.daimlertruck.com/marsMediaSite/en/instance/ko/Development-milestone-Daimler-Truck-tests-fuel-cell-truck-with-liquid-hydrogen.xhtml?oid=51975637 (Date Accessed Online: January 2023).

[124] (https://teslamotorsclub.com/tmc/threads/is-tesla-launching-a-“new-hydrogen-car”.285819/, 2023) https://teslamotorsclub.com/tmc/threads/is-tesla-launching-a-“new-hydrogen-car”.285819/ (Date Accessed Online: January 2023).

[125] (https://www.tesla.com/en_gb/modelx, 2023) Tesla Homepage - https://www.tesla.com/en_gb/modelx (Date Accessed Online: January 2023).

[126] (Hydrogen Council. How hydrogen empowers the energy transition. https://hydrogencouncil.com/wp-content/uploads/2017/06/Hydrogen-Council-Vision-Document-pdf, 2023) Hydrogen Council. How Hydrogen Empowers the Energy Transition. (Hydrogen Council. How Hydrogen Empowers the Energy Transition. https://hydrogencouncil.com/wp-content/uploads/2017/06/Hydrogen-Council-Vision-Document-pdf (Date Accessed Online: January 2023).

[127] (Lund, Integration of renewable energy into the transport and electricity sectors through V2G, 2008) Lund, H. & Kempton, W., *Integration of Renewable Energy into the Transport and Electricity Sectors through V2G*, Energy Policy, 2008, **36**, *9*, 3578-3587.

[128] Office of Energy Efficiency & Renewable Energy, US. https://www.energy.gov/eere/fuelcells/hydrogen-production (Date Accessed Online: January 2023).

[129] (Ramachandran, 1998) Ramachandran, R., & Menon, R. K., *An Overview of Industrial Uses of Hydrogen*, Int. J. Hydrogen Energy, 1998, **23**, *7*, 593-598.

[130] Ding, X., Garlyyev, B., Watzele, S. A., Sarpey, T. K., & Bandarenka, A. S., *Spotlight on the Effect of Electrolyte Composition on the Potential of Maximum Entropy. Supporting Electrolytes are not Always Inert*, Chemistry - A European J., 2021, **27**, 10016-10020.

[131] Hou, S., Xu, L., Ding, X., Kluge, R. M., Sarpey, T. K., Haid, R. W., Garlyyev, B., Mukherjee, S., Warnan, J., Koch, M., Zhang, S., Li, W., Bandarenka, A. S., & Fischer, R. A., *Dual In-Situ Laser Techniques Underpin the Role of Cations in Impacting Electrocatalysts*, Angew. Chemie Int. Ed., 2022, **61**, *24*, e20221610.

[132] *A*rminio-Ravelo, J. A., Jensen, A. W., Jensen, K. D., Quinson, J., & Escudero-Escribano, M., *Electrolyte Effects on the Electrocatalytic Performance of Iridium-Based Nanoparticles for Oxygen Evolution in Rotating Disc Electrodes*, ChemPhysChem, 2019, **20**, 2956-2963.

[133] König, M., Vaes, J., Klemm, E., & Pant, D., *Solvents and Supporting Electrolytes in the Electrocatalytic Reduction of CO_2*, Iscience, 2019, **19**, 135-160.

[134] Kani, K., Lim, H., Whitten, A. E., Wood, K., Yago, A. J. E., Hossain, M. S. A., Henzie, J., Na, J., & Yamauchi, Y., *First Electrochemical Synthesis of Mesoporous RhNi Alloy Films for an Alkali-Mediated Hydrogen Evolution Reaction*, J. Mater. Chem. A, 2021, **9**, 2754-2763.

[135] Xue, S., Haid, R. W., Kluge, R. M., Ding, X., Garlyyev, B., Fichtner, J., Watzele, S., Hou, S., & Bandarenka, A. S., *Enhancing the Hydrogen Evolution Reaction Activity of Platinum Electrodes in Alkaline Media Using Nickel-Iron Clusters*, Angew. Chem., Int. Ed., 2020, **59**, 10934-10938.

[136] Cao, D., Xu, H., & Cheng, D., *Construction of Defect-Rich RhCu Nanotubes with Highly Active Rh_3Cu_1 Alloy Phase for Overall Water Splitting in all pH Values*, Adv. Energy Mater., 2020, **10**, 1903038.

[137] Garlyyev, B., Watzele, S., Fichtner, J., Michalička, J., Schökel, A., Senyshyn, A., Perego, A., Pan, D., El-Sayed, H. A., Macak, J. M., Atanassov, P., Zenyuk, I. V., & Bandarenka, A. S., *Electrochemical Top-Down Synthesis of C-Supported Pt Nano-Particles with Controllable Shape and Size. Mechanistic Insights and Application*, Nano Res., 2020, **14**, 2762-2769.

[138] Hartog S. D., Neukermans, S., Samanipour, M., Ching, H. Y. V., Breugelmans, T., Hubina, A., & Ustarroz, J., *Electrocatalysis under a Magnetic Lens: A Combined Electrochemistry and Electron Paramagnetic Resonance Review*, Electrochim. Acta, 2022, **407**, 139704.

[139] Geske, D. H., & Maki, A. H., *Electrochemical Generation of Free Radicals and their Study by Electron Spin Resonance Spectroscopy; the Nitrobenzene Anion Radical*, J. Am. Chem. Soc., 1960, **82**, 2671-2676.

[140] Maki, A. H., & Geske, D. H., *Electron Spin Resonance and Polarographic Investigation of Substituted Nitrobenzene Negative Ions*, J. Am. Chem. Soc., 1961, **83**, 1852-1860.

[141] Dunsch, L., *Recent Advances in In Situ Multi-Spectroelectrochemistry*, J. Solid State Electrochem., 2011, **15**, 1631-1646.

[142] Liu, Q., Sun, B., Liu, Z., Kao, Y., Dong, B. W. Jiang, S. D., Li, F., Liu, G., Yang, Y., & Mo, F., *A General Electrochemical Strategy for the Sandmeyer Reaction*, Chem. Sci., 2018, **9**, 8731-8737.

[143] Luspai, K., Barbieriková, Z., Malcek, M., Bucinsky, L., Stasko, A., Bella, M., Milata, V., Rapta, P., & Brezová, V., *Cathodic and Photocatalytic Reduction of Nitroquinolones Investigated by In Situ EPR/UV-Vis Spectroelectrochemistry and EPR Spectroscopy*, Current Organic Chem., 2013, **17**, *21*, 2427-2439.

[144] Pauwels, D., Ching, H. Y. V., Samanipour, M., Neukermans, S., Hereijgers, J., Doorslaer, S. V., Wael, K. D., & Breugelmans, T., *Identifying Intermediates in the Reductive Intramolecular Cyclisation of Allyl 2-bromobenzyl Ether by an Improved Electron Paramagnetic Resonance Spectroelectrochemical Electrode Design Combined with Density Functional Theory Calculations*, Electrochim. Acta, 2018, **271**,10-18.

---

[145] Neukermans, S., Samanipour, M., Ching, H. Y. V., Hereijgers, J., Doorslaer, S. V., Hubin, A., & Breugelmans, T., *A Versatile In-Situ Electron Paramagnetic Resonance Spectroelectrochemical Approach for Electrocatalyst Research*, ChemElectroChem, 2020, **7**, *22*, 4578-4586.

[146] Šimková, L., Dmitrieva, E., Klíma, J., Dunsch, L., & Ludvík, J., (Spectro) Electrochemical Investigation of Reduction Mechanism of a New Energetic Molecule 2,2-dinitroethene-1,1-diamine (FOX-7) in Aprotic Solvents, *J. Solid State Electrochem.*, 2015, **19**, 103-112.

[147] Tamski, M. A., Macpherson, J. V., Unwin, P. R., & Newton, P. R., *Electrochemical Electron Paramagnetic Resonance Utilizing Loop Gap Resonators and Micro-Electrochemical Cells*, Phys. Chem. Chem. Phys., 2015, **17**, 23438-23447.

[148] Tamski, M. A., Dale, M. W., Breeze, B. G., Macpherson, J. V., Unwin, P. R., & Newton, P. R., *Quantitative Measurements in Electrochemical Electron Paramagnetic Resonance*, Electrochim. Acta, 2016, **213**, 802-810.

[149] Murray, P. R., Collison, D., Daff, S., Austin, N., Edge, R., Flynn, B. W., Jack, L., Leroux, F., McInnes, E. J. L., Murray, A. F., Sells, D., Stevenson, T., Wolowska, J., & Yellowlees, L. J., *An In situ Electrochemical Cell for Q- and W-Band EPR Spectroscopy*, J. Mag. Resonance, 2011, **213**, *1*, 206-209.

[150] Yu, X., Roemmele, T. L., & Boeré, R. T., *Synthesis, Electronic Structures, and Electrochemistry of 3-Triarylphosphoraniminato-1,3,5-trithia-2,4,6,8-tetrazocines: Detection of Trithiatetrazocinyl Radical Anions*, ChemElectroChem, 2018, **5**, *6*, 968-978.

[151] Morsy, M. A., & Kawde, A. N. M., *Electron Paramagnetic Resonance Monitoring for On-Demand Electrochemically-Generated Radicals*, Electrochim. Acta, 2015, **160**, 22-27.

[152] Heinze, J., *Ultramicroelectrodes in Electrochemistry*, Angew. Chem. Int. Ed., 1993, **32**, *9*, 1268-1288.

[153] Aoki, K., *Theory of Ultramicroelectrodes*, Electroanalysis, 1993, **5**, 627-639.

[154] (Scieszka, Yun, & Bandarenka, 2017) Scieszka, D., Yun, J., & Bandarenka, A. S., *What do Laser-Induced Transient Techniques Reveal for Batteries? Na- and K-Intercalation from Aqueous Electrolytes as an Example*, ACS Appl. Mater. Interfaces, 2017, **9**, *23*, 20213-20222.

[155] (Scieszka, et al., 2018) Scieszka, D., Sohr, C., Scheibenbogen, P., Marzak, P., Yun, J., Liang, Y., Fichtner, J., & Bandarenka, A. S., *Multiple Potentials of Maximum Entropy of a* $Na_2Co[Fe(CN)_6]$ *Battery Electrode Material: Does the Electrolyte Composition Control the Interface?*, ACS Appl. Mater. Interfaces, 2018, **10**, *25*, 21688-21695.

[156] (Nagaiah, Tiwari, Kumar, Scieszka, & Bandarenka, 2020) Nagaiah, T. C., Tiwari, A., Kumar, M., Scieszka, D., & Bandarenka, A. S., *In-Situ Probing of* Mn_2O_3 *Activation Towards Oxygen Electroreduction by Laser-Induced Current Transient Technique*, ACS Appl. Energy Mater., 2020, **3**, *9*, 9151-9157.

[157] (Scieszka, In-Depth Characterization of Electrified Solid/Liquid Interfaces with the Laser-Induced Current Transient Technique, 2019) Scieszka, D., *In-Depth Characterization of Electrified Solid/Liquid Interfaces with the Laser-Induced Current Transient Technique*, **Ph. D. Thesis, Technical University of Munich**, September 2019.

---

[158] (Auer, Ding, Bandarenka, & Kunze-Liebhäuser, 2021) Auer, A., Ding, X., Bandarenka, A. S., & Kunze-Liebhäuser, J., *The Potential of Zero Charge and the Electrochemical Interface Structure of Cu(111) in Alkaline Solutions*, J. Phys. Chem. C, 2021, **125**, *9*, 5020-5028.

[159] (Ding, et al., Spotlight on the Effect of Electrolyte Composition on the Potential of Maximum Entropy. Supporting Electrolytes are not Always Inert, 2021) Ding, X., Garlyyev, B., Watzele, S. A., Sarpey, T. K., & Bandarenka, A. S., *Spotlight on the Effect of Electrolyte Composition on the Potential of Maximum Entropy. Supporting Electrolytes are not Always Inert*, Chemistry - A European J., 2021, **27**, *39*, 10016-10020.

[160] (Ding, et al., 2022) Ding, X., Scieszka, D., Watzele, S., Xue, S., Garlyyev, B., Haid, R. W., & Bandarenka, A. S., *A Systematic Study of the Influence of Electrolyte Ions on the Electrode Activity*, ChemElectroChem, 2022, **9**, *1*, e202101088.

[161] (Ding X. , LASER-Assisted Determination of the Potential of Maximum Entropy. Applications in Electrocatalysis , 2021) Ding, X., *LASER-Assisted Determination of the Potential of Maximum Entropy. Applications in Electrocatalysis*, **Ph. D. Thesis, Technical University of Munich**, September 2021.

[162] (Sarpey, 2023) Sarpey, T. K., Keleş, E., Gubanova, E. L., & Bandarenka, A. S., *Probing the electrified solid-liquid interfaces with laser-induced transient techniques*. In: Encyclopedia of Solid-Liquid Interfaces, K. Wandelt and G. Bussetti, Ed. Elsevier: Amsterdam, 2022.

[163] (Ding X. S.-I., 2022) Ding, X.,‡ Sarpey, T. K.,‡ Hou, S., Garlyyev, B., Li, W., Fischer, R. A., & Bandarenka, A. S., *Prospects of Using the Laser-Induced Temperature Jump Techniques for Characterisation of Electrochemical Systems*, ChemElectroChem, 2022, **9**, *4*, e202101175.

[164] (Haid, 2022) Haid(1), R., Ding(1), X., Sarpey, T. K., Bandarenka, A. S., & Garlyyev, B., *Exploration of the Electrical Double Layer Structure: Influence of Electrolyte Components on the Double Layer Capacitance and Potential of Maximum Entropy*, Current Opinion in Electrochem., 2022, **32**, 100882.

[165] (Brett, 1993) Brett, C. M. A., & Brett, A. M. O., *Electrochemistry: Principles, Methods, and Applications*, New York, Oxford University Press Inc., USA, 1993.

[166] (Ostwald, 1902) Ostwald, W., Catalysis 1, Nature, 1902, 65, 1692, 522-526.

[167] (Nørskov, 2014) Nørskov, J. K., Studt, F., Abild-Pedersen, F., & Bligaard, T., Fundamental Concepts in Heterogeneous Catalysis, NJ: John Wiley and Sons, Inc., Hoboken, New Jersey, USA, 2014, 2.

[168] Helmholtz, H., *Ueber Einige Gesetze der Vertheilung Elektrischer Ströme in Körperlichen Leitern, mit Anwendung auf die Thierisch-Elektrischen Versuche*, Ann. Phys. 1853, **165**, 353-377.

[169] Gouy, M., *Sur la Constitution de la Charge Électrique à la Surface d'un Électrolyte*, Phys. Theor. Appl., 1910, **9**, 457-468.

[170] Chapman, D. L., *A Contribution to the Theory of Electrocapillarity*, Mag. J. Sci., 1913, **25**, 475-481.

[171] (Butt, 2018) Butt, H. -J., & Kappl, M., *Surface and Interfacial Forces*, Wiley-VCH, Berlin, Germany, Second Edition, 2018, 99-131.

---

[172] Stern, O., *Zur Theorie der Elektrolytischen Doppelschicht*, Z. Elektrochem. Angew. Phys. Chem., 1924, **30**, 508-516.

[173] Grahame, D. C., *The Electrical Double Layer and the Theory of Electrocapillarity*, Chem. Rev., 1947, **41**, 441-501.

[174] Garlyyev, B., Watzele, S., Fichtner, J., Michalička, J., Schökel, A., Senyshyn, A., Perego, A., Pan, D., El-Sayed, H. A., Macak, J. M., Atanassov, P., Zenyuk, I. V., & Bandarenka, A. S., *Electrochemical Top-Down Synthesis of C-Supported Pt Nano-Particles with Controllable Shape and Size. Mechanistic Insights and Application*, Nano Res., 2020, **14**, 2762-2769.

[175] Hou, J., Wu, Y., Zhang, B., Cao, S., Li, Z., & Sun, L., *Rational Design of Nanoarray Architectures for Electrocatalytic Water Splitting*, Adv. Funct. Mater., 2019, **29**, 1808367.

[176] Xue, S., Haid, R. W., Kluge, R. M., Ding, X., Garlyyev, B., Fichtner, J., Watzele, S., Hou, S., Bandarenka, A. S., *Enhancing the Hydrogen Evolution Reaction Activity of Platinum Electrodes in Alkaline Media Using Nickel-Iron Clusters*, Angew. Chem., Int. Ed., 2020, **59**, 10934-10938.

[177] Ling, T., Jaroniec, M., & Qiao, S. Z., *Recent Progress in Engineering the Atomic and Electronic Structure of Electrocatalysts via Cation Exchange Reactions*, Adv. Mater., 2020, **32**, e2001866.

[178] Yang, S., Li, S., Lv, Y., Duan, Z., Li, C., Praeg, R. F., Gao, D., & Chen, G., *Defect-Density Control of Platinum-Based Nanoframes with High-Index Facets for Enhanced Electrochemical Properties*, Nano Res., 2019, **12**, 2881-2888.

[179] Zhang, L., Doyle-Davis, K., & Sun, X., *Pt-Based Electrocatalysts with High Atom Utilization Efficiency: from Nanostructures to Single Atoms*, Energy Environ. Sci., 2019, **12**, 492-517.

[180] Li, H., Han, Y., Zhao, H., Qi, W., Zhang, D., Yu, Y., Cai, W., Li, S., Lai, J., & Huang, B., *Fast Site-to-Site Electron Transfer of High-entropy Alloy Nanocatalyst Driving Redox Electrocatalysis*, Nat. Commun., 2020, **11**, 1-9.

[181] Kani, K., Lim, H., Whitten, A. E., Wood, K., Yago, A. J. E., Hossain, M. S. A., Heinzie, J., Na, J., & Yamauchi, Y., *First Electrochemical Synthesis of Mesoporous RhNi Alloy Films for an Alkali-Mediated Hydrogen Evolution Reaction*, J. Mater. Chem. A, 2021, **9**, 2754-2763.

[182] Cao, D., Xu, H., & Cheng, D., *Construction of Defect-Rich RhCu Nanotubes with Highly Active* Rh_3Cu_1 *Alloy Phase for Overall Water Splitting in all pH Values*, Adv. Energy Mater., 2020, **10**, 1903038.

[183] Arminio-Ravelo, J. A., Jensen, A. W., Jensen, K. D., Quinson, J., & Escudero-Escribano, M., *Electrolyte Effects on the Electrocatalytic Performance of Iridium-Based Nanoparticles for Oxygen Evolution in Rotating Disc Electrodes*, ChemPhysChem., 2019, **20**, 2956-2963.

[184] König, M., Vaes, J., Klemm, E., & Pant, D., *Solvents and Supporting Electrolytes in the Electrocatalytic Reduction of* CO_2, Iscience, 2019, **19**, 135-160.

[185] Birdja, Y. Y., Pérez-Gallent, E., Figueiredo, M. C., Göttle, A. J., Calle-Vallejo, F., & Koper, M. T. M., *Advances and Challenges in Understanding the Electrocatalytic Conversion of Carbon Dioxide to Fuels*, Nat. Energy, 2019, **4**, 732-745.

---

[186] Li, G. -F., Divinagracia, M., Labata, M. F., Ocon, J. D., & Abel-Chuang, P. -Y., *Electrolyte-Dependent Oxygen Evolution Reactions in Alkaline Media: Electrical Double Layer and Interfacial Interactions*, ACS Appl. Mater. Interfaces, 2019, **11**, 33748-33758.

[187] Gao, D., Arán-Ais, R. M., Jeon, H. S., & Cuenya, B. R., *Rational Catalyst and Electrolyte Design for CO_2 Electroreduction Towards Multicarbon Products*, Nar. Catal., 2019, **2**, 198-210.

[188] Sa, Y. J., Lee, C. W., Lee, S. Y., Na, J., Lee, U., & Hwang, Y. J., *Catalyst-Electrolyte Interface Chemistry for Electrochemical CO_2 Reduction*, Chem. Soc. Rev., 2020, **49**, 6632-6665.

[189] (Hamann, 2007) Hamann, C. H., Hamnett, A., & Vielstich, W., *Electrochemistry*; 2nd, Completely Revised and Updated Ed.; Wiley-Vch Verlag GmbH & Co. KGaA: Weinheim, 2007.

[190] (Schmickler, 2010) Schmickler, W., & Santos, E., *Electrolyte Solutions*. In: *Interfacial Electrochemistry*. Berlin: Springer, Second Edition, 2010, 19-27.

[191] (Bagotsky, 2006) Bagotsky, V. S., *Fundamentals of Electrochemistry*, Hoboken, NJ, USA: John Wiley and Sons. Inc., Second Edition, 2006, 51-68.

[192] (Colic, 2015) Colic, V., Tymoczko, J., Maljusch, A., Ganassin, A., Schuhmann, W., & Bandarenka, A. S., *Experimental Aspects in Benchmarking of the Electrocatalytic Activity*, ChemElectroChem, 2015, **2**, *1*, 143-149.

[193] (Cooper, 2006) Cooper, K., & Smith, M., *Electrical Test Methods for On-line Fuel Cell Ohmic Resistance Measurement*, J. Power Sources, 2006, **160**, *2*, 1088-1095.

[194] (Wojtowicz, 1968) Wojtowicz, J., Laliberté, L., & Conway, B. E., *Current Distribution and Potential Profile at a Linear Wire Electrode of Significant Ohmic Resistance*, Electrochim. Acta, 1968, **13**, *3*, 361-373.

[195] (Myland & Oldham, 2000) Myland, J. C., & Oldham, K. B., *Uncompensated Resistance. 1. The Effect of Cell Geometry*, Anal. Chem., 2000, **72**, *17*, 3972-3980.

[196] (Epelboin, Keddam, & Takenouti, 1972) Epelboin, I., Keddam, M., & Takenouti, H., *Use of Impedance Measurements for the Determination of the Instant Rate of Metal Corrosion*, J. Appl. Electrochem., 1972, 71-79.

[197] (Sabatier, 1902) Sabatier, P., & Senderens, J. B., *Hydrogénation Directe des Oxydes du Carbone en Présence de Divers Métaux Divisés, (The Direct Hydrogenation of Carbon Oxides in the Presence of Various Divided Metals.)*, Comptes Rendus des Séances de l'académie des Sciences (C. R. Hebd. Seances. Acad. Sci.), 1902, **134**, 689-691.

[198] (Sabatier P. , 1920) Sabatier, F., *La Catalyse en Chimie Organique*; Berauge: Paris, France, 1920.

[199] (Sabatier P. , Hydrogénations et déshydrogénations par catalyse, 1911) Sabatier, P., *Hydrogénations et Déshydrogénations par Catalyse,* Berichte Der Deutschen Chemischen Gesellschaft*,* 1911, **44***,* *3*, 1984-2001.

[200] (Ooka, 2021) Ooka, H., Huang, J., & Exner, K. S., *The Sabatier Principle in Electrocatalysis: Basics, Limitations, and Extensions*, Front. Energy Res., 2021, **9**, 654460.

---

[201] (Chorkendorff, 2017) Chorkendorff, I., & Niemantsverdriet, J. W., *Concepts of Modern Catalysis and Kinetics*, Wiley-VCH Verlag (John Wiley & Sons. Inc.), Weinheim, Third Edition, 2017.

[202] (Balandin, 1969) Balandin, A. A., *Modern State of the Multiplet Theory of Heterogeneous Catalysis 1*, Advances in Catalysis, Elsevier, 1969, **19**, 1-210.

[203] (Trasatti, 1972) Trasatti, S., *Work Function, Electronegativity, and Electrochemical Behaviour of Metals: III. Electrolytic Hydrogen Evolution in Acid Solutions*, J. Electroanal. Chem. Interfacial Electrochem., 1972, **39**, *1*, 163-184.

[204] (Calle-Vallejo, 2013) Calle-Vallejo, F., Koper, M. T. M., & Bandarenka, A. S., *Tailoring the Catalytic Activity of Electrodes with Monolayer Amounts of Foreign Metals*, Chemical Soc. Rev., 2013, **42**, *12*, 5210-5230.

[205] (Peterson, 2012) Peterson, A. A., & Nørskov, J. K., *Activity Descriptors for* CO_2 *Electroreduction to Methane on Transition-Metal Catalysts*, J. Phys. Chem. Lett., 2012, **3**, *2*, 251-258.

[206] (Parsons, 1958) Parsons, R., *The rate of Electrolytic Hydrogen Evolution and the Heat of Adsorption of Hydrogen*, Trans. Faraday Soc., 1958, **54**, 1053-1063.

[207] (Nørskov J. K.-C.–1., 2004) Nørskov, J. K., Rossmeisl, J., Logadottir, A., Lindqvist, L., Kitchin, J. R., Bligaard, T., & Jónsson, H., *Origin of the Overpotential for Oxygen Reduction at a Fuel-Cell Cathode*, J. Phys. Chem. B, 2004, **108**, *46*, 17886-17892.

[208] (I.E.L. Stephens, 2012) Stephens, I. E. L., Bondarenko, A. S., Grønbjerg, U., Rossmeisl, J., & Chorkendorff, I., *Understanding the Electrocatalysis of Oxygen Reduction on Platinum and its Alloys (Review)*, Energy & Environ. Sci., 2012, **5**, *5*, 6744-6762.

[209] (Rossmeisl, 2005) Rossmeisl, J., Logadottir, A., & Nørskov, J. K., *Electrolysis of Water on (Oxidized) Metal Surfaces*, J. Chem. Phys., 2005, **319**, *1-3*, 178-184.

[210] (Abild-Pedersen, 2007) Abild-Pedersen, F., Greeley, J., Studt, F., Rossmeisl, J., Munter, T. R., Moses, P. G., Skúlason, E., Bligaard, T., & Nørskov, J. K., *Scaling Properties of Adsorption Energies for Hydrogen-Containing Molecules on Transition-Metal Surfaces*, Phys. Rev. Lett., 2007, **99**, *1-6*, 016105.

[211] (Doyle, 2015) Doyle, A. D., Montoya, J. H., & Vojvodic, A., *Improving Oxygen Electrochemistry through Nanoscopic Confinement*, ChemCatChem, 2015, **7**, *5*, 738-742.

[212] (Darby, 2018) Darby, M. T., Stamatakis, M., Michaelides, A., & Sykes, E. C. H., *Lonely Atoms with Special Gifts: Breaking Linear Scaling Relationships in Heterogeneous Catalysis with Single-Atom Alloys*, J. Phys. Chem. Lett., 2018, **9**, *18*, 5636-5646.

[213] (Khorshidi, 2018) Khorshidi, A., Violet, J., Hashemi, J., & Petersen, A. A., *How Strain can Break the Scaling Relations of Catalysis*, Nat. Catal., 2018, **1**, *4*, 263-268.

[214] (Szécsényi, 2019) Szécsényi, Á., Khramenkova, E., Chernyshov, I. Y., Li, G., Gascon, J., & Pidko, E. A., *Breaking Linear Scaling Relationships with Secondary Interactions in Confined Space: A Case Study of Methane Oxidation by Fe/ZSM-5 Zeolite*, ACS Catal., 2019, **9**, *10*, 9276-9284.

---

[215] (Zheng, 2015) Zheng, Y., Jiao, Y., Jaroniec, M., & Qiao, S. Z., *Advancing the Electrochemistry of the Hydrogen Evolution Reaction through Combining Experiment and Theory*, Angew. Chem. Int. Ed., 2015, **54**, *1*, 52-65.

[216] (Nørskov J. K., 2009) Nørskov, J. K., Bligaard, T., Rossmeisl, J., & Christensen, C. H., *Towards the Computational Design of Solid Catalysts*, Nat. Chem., 2009, **1**, *1*, 37-46.

[217] (Jinnouchi, 2015) Jinnouchi, R., Nagoya, A., Kodama, K., & Morimoto, Y., *Solvation Effects on OH Adsorbates on Stepped Pt Surfaces*, J. Phys. Chem. C, 2015, **119**, *29*, 16743-16753.

[218] (innouchi, 2017) Jinnouchi, R., Nagoya, A., Kodama, K., & Morimoto, Y., *Simulated Volcano Plot of Oxygen Reduction Reaction on Stepped Pt Surfaces*, Electrochim. Acta, 2017, **230**, 470-478.

[219] (Langmuir, 1922) Langmuir, I., *The mechanism of the Catalytic Action of Platinum in the Reactions* $2Co + O_2 = 2Co_2$ *and* $2H_2 + O_2 = 2H_2O$, Trans. Faraday Soc., 1922, **17**, 621-654.

[220] (Taylor, 1925) Taylor, H. S., *A Theory of the Catalytic Surface,* Proc. R. Soc. Lond. Series A, Containing Papers of a Mathematical and Physical Character, 1925, **108**, *745*, 105-111.

[221] (A., 2009) Van Santen, R. A., *Complementary Structure Sensitive and Insensitive Catalytic Relationships*, Acc. Chem. Res., 2009, **42**, *1*, 57-66.

[222] (Hou S. K., 2021) Hou, S., Kluge, R. M., Haid, R. W., Gubanova, E. L., Watzele, S. A., Bandarenka, A. S. & Garlyyev, B., *A Review on Experimental Identification of Active Sites in Model Bifunctional Electrocatalytic Systems for Oxygen Reduction and Evolution Reactions*, ChemElectroChem., 2021, **8**, *18*, 3433-3456.

[223] (Calle-Vallejo F. T., 2015) Calle-Vallejo, F., Tymoczko, J., Colic, V., Vu, Q. H., Pohl, M. D., Morgenstern, K., Loffreda, D., Sautet, P., Schuhmann, W. & Bandarenka, A. S., *Finding Optimal Surface Sites on Heterogeneous Catalysts by Counting Nearest Neighbors*, Science 2015, **350**, *6257*, 185-189.

[224] (Schmidt, 2022) Schmidt, T. O., Ngoipala, A., Arevalo, R. L., Watzele, S. A., Lipin, R., Kluge, R. M., Hou, S., Haid, R. W., Senyshyn, A., Gubanova, E. L., Bandarenka, A. S., & Vandichel, M., *Elucidation of Structure-Activity Relations in Proton Electroreduction at Pd Surfaces, Theoretical and Experimental Study*, Small, 2022, **18**, *30*, 2202410.

[225] (Haid R. W., 2021) Haid, R. W., Kluge, R. M., Schmidt, T. O., & Bandarenka, A. S., *In-Situ Detection of Active Sites for Carbon-Based Bifunctional Oxygen Reduction and Evolution Catalysis*, Electrochim. Acta, 2021, **382**, 138285.

[226] (Liang, 2019) Liang, Y., Csoklich, C., McLaughlin, D. Schneider, O., & Bandarenka, A. S., *Revealing Active Sites for Hydrogen Evolution at Pt and Pd Atomic Layers on Au Surfaces*, ACS Appl. Mater. Interfaces, 2019, **11**, *13*, 12476-12480.

[227] (Pfisterer, 2017) Pfisterer, J. H. K., Liang, Y., Schneider, O., & Bandarenka, A. S., *Direct Instrumental Identification of Catalytically Active Surface Sites*, Nature, 2017, **549**, *7670*, 74-77.

[228] (Trasatti, Water electrolysis: who first?, 1999) Trasatti, S., *Water electrolysis: Who First?*, J. Electroanal. Chem., 1999, **476**, 90-91.

[229] (Nicholson, 2023) Nicholson W. & Carlisle, A., https://archive.org/details/journalofnatural05lond/page/186/mode/2up?view=theater (Date Accessed Online: February 2023).

[230] (Ritter, 1800) Magazin für den neuesten Zustand der Naturkunde mit Rücksicht auf die dazugehörigen Hülfswissenschaften, Volta's Galvanische Batterie: nebst Versuchen mit derselben angestellt / J[ohann] W[ilhelm] Ritter Beyträge zur nähern Kenntniß des Galvanismus [und der Resultate seiner Untersuchung] / hrsg. von J[ohann] W[ilhelm] Ritter. - Jena: Frommann, 1800. - Bd. 1, Stück 4., https://zs.thulb.uni-jena.de/rsc/viewer/jportal_derivate_00124781/MZN_1800_Bd02_d356.tif?logicalDiv=jportal_jparticle_00149748, https://zs.thulb.uni-jena.de/receive/jportal_jpvolume_00079148 (Date Accessed Online: February 2023).

[231] (Schellen, 1884) Schellen, H., *Magneto-Electric and Dynamo-Electric Machines*, 3rd Ed., Vol.1, D. Van Nostrand, New York, 1884, p. 218, fig. 124, Translated by Keith, N. S., & Neyman, P.

[232] (Kreuter, 1998) Kreuter, W., & Hofmann, H., *Electrolysis: The Important Energy Transformer in a World of Sustainable Energy*, Int. J. Hydrogen Energy, 1998, **23**, *8*, 661-666.

[233] (Yang M.-Q. W., 2018) Yang, M.-Q., Wang, J., Wu, H., & Ho, G. W., *Noble Metal-Free Nanocatalysts with Vacancies for Electrochemical Water Splitting*, Small, 2018, **14**, *15*, 1703323.

[234] (Zeradjanin, 2020) Zeradjanin, A. R., Polymeros, G., Toparli, C., Ledendecker, M., Hodnik, N., Erbe, A., Rohwerder, M., & La Mantia, F., *What is the Trigger for the Hydrogen Evolution Reaction? – Towards Electrocatalysis Beyond the Sabatier Principle*, Phys. Chem. Chem. Phys., 2020, **22**, *16*, 8768-8780.

[235] (Zeng, 2015) Zeng, M. & Li, Y., *Recent Advances in Heterogeneous Electrocatalysts for the Hydrogen Evolution Reaction*, J. Mater. Chem. A, 2015, **3**, *29*, 14942-14962.

[236] (Exner, 2021) Exner, K. S., *Hydrogen Electrocatalysis Revisited: Weak Bonding of Adsorbed Hydrogen as Design Principle for Active Electrode Materials*, Current Opinion in Electrochem., 2021, **26**, 100673.

[237] (Stühmeier, 2021) Stühmeier, B. M., Pietsch, M., Schwämmlein, J. N., & Gasteiger, H., *Pressure and Temperature Dependence of the Hydrogen Oxidation and Evolution Reaction Kinetics on Pt Electrocatalysts via PEMFC-based Hydrogen-Pump Measurements*, J. Electrochem. Soc., 2021, **168**, *6*, 064516.

[238] (Song, 2023) Song, K. -T, Schott, C. M., Schneider, P. M., Watzele, S. A., Kluge, R. M., Gubanova, E. L., & Bandarenka, A. S., *Combining Impedance and Hydrodynamic Methods in Electrocatalysis. Characterization of* $Pt_{(pc)}$*,* Pt_5Gd*, and Nanostructured Pd for the Hydrogen Evolution Reaction*, J. Phys. Energy, 2023, **5,** 014016.

[239] (Nørskov J. K., 2005) Nørskov, J. K., Bligaard, T., Logadóttir, A., Kitchin, J. R., Chen, J. G., Pandelov, S., & Stimming, U., *Trends in the Exchange Current for Hydrogen Evolution*, J. Electrochem. Soc., 2005, **152**, *3*, J23-J26.

[240] (Conway, 2002) Conway, B. E., & Tilak, B. V., *Interfacial Processes Involving Electrocatalytic Evolution and Oxidation of* H_2*, and the Role of Chemisorbed H*, Electrochim. Acta, 2002, **47**, *22-23*, 3571-3594.

---

[241] (Shinagawa, 2015) Shinagawa, T., Garcia-Esparza, A., & Takanabe, K., *Insight on Tafel Slopes from a Microkinetic Analysis of Aqueous Electrocatalysis for Energy Conversion*, Sci. Rep., 2015, **5**, 13801.

[242] (Seh, 2017) Seh, Z. W., Kibsgaard, J., Dickens, C. F., Chorkendorff, I., Nørskov, J. K., & Jaramillo, T. F., *Combining Theory and Experiment in Electrocatalysis: Insights into Materials Design*, Science, 2017, **355***,* 6321.

[243] (Li X. H., 2016) Li, X., Hao, X., Abudula, A., & Guan, G., *Nanostructured Catalysts for Electrochemical Water Splitting: Current State and Prospects*, J. Mater. Chem. A, 2016, **4**, *31*, 11973-12000.

[244] (hao, 2021) Zhao, J., Wang, J., Chen, Z., Ju, J., Han, X., & Deng, Y., *Metal Chalcogenides: An Emerging Material for Electrocatalysis*, APL Materials, 2021, **9**, *5*, 050902.

[245] (ang, 2020) Wang, Y., Li, X., Zhang, M., Zhou, Y., Rao, D., Zhong, C., Zhang, J., Han, X., Hu, W., Zhang, Y., Zaghib, K., Wang, Y., & Deng, Y., *Lattice-Strain Engineering of Homogeneous* $NiS_{0.5}Se_{0.5}$ *Core-Shell Nanostructure as a Highly Efficient and Robust Electrocatalyst for Overall Water Splitting*, Adv. Mater., 2020, **32**, *40*, 2000231.

[246] (Busch, 2016) Busch, M., Halck, N. B., Kramm, U. I., Siahrostami, S., Krtil, P., & Rossmeisl, J., *Beyond the Top of the Volcano? - A Unified Approach to Electrocatalytic Oxygen Reduction and Oxygen Evolution*, Nano Energy, 2016, **29**, 126-135.

[247] (Huang, 2019) Huang, Z, -F., Song, J., Du, Y., Xi, S., Dou, S., Nsanzimana, J. M. V., Wang, C., Xu, Z. J., & Wang, X., *Chemical and Structural Origin of Lattice Oxygen Oxidation in Co-Zn Oxyhydroxide Oxygen Evolution Electrocatalysts*, Nat. Energy, 2019, **4**, 329-338.

[248] (Liang C. Z., 2020) Liang, C., Zou, P., Nairan, A., Zhang, Y., Liu, J., Liu, K., Hu, S., Kang, F., Fan, H. J., & Yang, C., *Exceptional Performance of Hierarchical Ni-Fe Oxyhydroxide @ NiFe Alloy Nanowire Array Electrocatalysts for Large Current Density Water Splitting*, Energy Environ. Sci., 2020, **13**, *1*, 86-95.

[249] (Michael, 2015) Michael, J. D., Demeter, E. L., Illes, S. M., Fan, Q., Boes, J. R., & Kitchin, J. R., *Alkaline Electrolyte and Fe Impurity Effects on the Performance and Active-Phase Structure of NiOOH Thin Films for OER Catalysis Applications*, J. Phys. Chem. C, 2015, **119**, *21*, 11475-11481.

[250] (Garcia, 2019) Garcia, A. C., Touzalin, T., Nieuwland, C., Perini, N., & Koper, M. T. M., *Enhancement of Oxygen Evolution Activity of Nickel Oxyhydroxide by Electrolyte Alkali Cations*, Angew. Chem. Int. Ed., 2019, **58**, *37*, 12999-13003.

[251] (Abaspour, 2014) Abaspour, A., Parsa, N. T., & Sadeghi, M., *A New Feedback Linearization-NSGA-II Based Control Design for PEM Fuel Cell*, Int. J. Computer Applications, 2014, **97**, *10*, 25-32.

[252] (Carrette, 2000) Carrette, L., Friedrich, K. A., & Stimming, U., *Fuel cells: Principles, Types, Fuels, and Applications*, ChemPhysChem, 2000, **1**, *4*, 162-193.

[253] (Schönbein, 1837) Schönbein, C. F., *On the Odour Accompanying Electricity, and on the Probability of Its Dependence on the Presence of a New Substrate*, Proc. R. Soc., London, 1837, **4**, 226-226.

---

[254] (Schönbein, Neue Beobachtungen über die Volta'sche Polarisation fester und flüssiger Leiter, 1839) Schönbein, C. F., *Neue Beobachtungen über die Volta'sche Polarisation fester und flüssiger Leiter*, Ann. Phys. Chem., 1839, **123**, 101-123.

[255] (Grove, 1838) Grove, W. R., *On a New Voltaic Combination of Gases by Platinum*, London, Edinburgh, Dublin Philos. Mag. J. Sci., 1838, **13**, 430-431.

[256] (Grove, On Voltaic Series and the Combination of Gases by Platinum) Grove, W. R., *On Voltaic Series and the Combination of Gases by Platinum*, London, Edinburgh, Dublin Philos. Mag. J. Sci., 1839, **14**, 127-130.

[257] (Bacon, 1959) Bacon, F. T., *Hydrogen-Oxygen Energy Storage Cells*, World Sci. Rev*., 1959.*

[258] (Bacon F. T.-4.) Bacon, F. T., & Fry, T. M., *Review Lecture: The Development and Practical Application of Fuel Cells*, Proc. R. Soc. Long. A, 1973, **334**, *1599*, 427-452.

[259] (Adams A. M., 1963) Adams, A. M., Bacon, F. T., & Watson, R. G. H., Fuel Cells (Ed. Mitchell, W. Jr.), 1963, New York and London: Academic Press, 129-192.

[260] (Bacon F. T., Fuel Cells, Past, Present and Future, 1969) Bacon, F. T., *Fuel Cells, Past, Present and Future*, Electrochim. Acta, 1969, **14**, *7*, 569-585.

[261] (St-Pierre J., 2001) St-Pierre, J., & Wilkinson, D. P., *Fuel cells: A New, Efficient and Cleaner Power Source*, Am. Institute of Chemical Engineers (AIChE) J., 2001, **47**, *7*, 1482-1486.

[262] (St-Pierre, 2014) St-Pierre, J., Angelo, M., Bethune, K., Ge, J., Higgins, S., Reshetenko, T., Virji, M., & ZhaI, Y., *PEMFC Contamination - Fundamentals and Outlook*, ECS Transactions, 2014, **61**, *23*, 1-14.

[263] (J., 2009) St-Pierre, J., In: *Polymer Electrolyte Fuel Cell Durability*, Büchi, F. N., Inaba, M., Schmidt, T. J., Springer, New York, 2009, 289.

[264] (Mohammed, 2019) Mohammed, H., Al-Othman, A., Nancarrow, P., Tawalbeh, M., & El Haj, A. M., *Direct HydroCarbon Fuel Cells: A Promising Technology for Improving Energy Efficiency*, Energy, 2019, **172**, *C*, 207-219.

[265] (Mahajan, 2023) Mahajan, C., Hasannaeimi, V., Neuber, N., Wang, X., Busch, R., Gallino, I., & Mukherjee, S., *Model Metallic Glasses for Superior Electrocatalytic Performance in a Hydrogen Oxidation Reaction*, ACS Appl. Mater. Interfaces, 2023, **15**, *5*, 6697-6707.

[266] (An, 2021) An, L., Zhao, X., Zhao, T., & Wang, D., *Atomic-Level Insight into Reasonable Design of Metal-Based Catalysts for Hydrogen Oxidation in Alkaline Electrolytes*, Energy & Environ. Sci., 2021, **14***,* *5*, 2620-2638.

[267] (Ni, 2019) Ni, W., Krammer, A., Hsu, C. S., Chen, H. M., Schüler, A., & Hu, X., *$Ni_3 N$ as an Active Hydrogen Oxidation Reaction Catalyst in Alkaline Medium*, Angew. Chem. Int. Ed., 2019, **58**, *22*, 7445-7449.

[268] (Trogadas, 2020) Trogadas, P., & Coppens, M. -O., *Nature-Inspired Electrocatalysts and Devices for Energy Conversion*, Chem. Soc. Rev., 2020, **49**, 3107-3141.

---

[269] (Fu, 2020) Fu, L., Li, Y., Yao, N., Yang, F., Cheng, G., & Luo, W., *IrMo Nanocatalysts for Efficient Alkaline Hydrogen Electrocatalysis*, ACS Catal., 2020, **10**, *13*, 7322-7327.

[270] (Jin, 2023) Jin, Y., Su, L., Jia, H., Men, Y., & Luo, W., *Nickel-Based Electrocatalysts for Hydrogen Oxidation Reaction under Alkaline Electrolytes*, ChemCatChem, 2023, e202300056.

[271] (Wang, 2014) Wang, D. -W., & Su, D., *Heterogeneous Nanocarbon Materials for Oxygen Reduction Reaction*, Energy Environ. Sci., 2014, **7**, 576-591.

[272] (Song C. &., 2008) Song, C., & Zhang, J., In Electrocatalytic Oxygen Reduction Reaction, Edited by Zhang, J., PEM Fuel Cell Electrocatalysts and Catalyst Layers - Fundamentals and Applications, Springer, 2008, 89-134.

[273] (Harzer, 2018) Harzer, G. S., Orfanidi, A., El-Sayed, H., Madkikar, P., & Gasteiger, H. A., *Tailoring Catalyst Morphology towards High Performance for Low Pt Loaded PEMFC Cathodes*, J. Electrochem. Soc., 2018, **165**, *10*, F770-F779.

[274] (Harzer G. S., 2018) Harzer, G. S., Schwämmlein, J. N., Damjanović, A. M., Ghosh, S., & Gasteiger, H. A., *Cathode Loading Impact on Voltage Cycling Induced PEMFC Degradation: A Voltage Loss Analysis*, J. Electrochem. Soc., 2018, **165**, *6*, F3118-F3131.

[275] (Nesselberger, 2011) Nesselberger, M., Ashton, S., Meier, J. C., Katsounaros, I., Mayrhofer, K. J., & Arenz, M., *The Particle Size Effect on the Oxygen Reduction Reaction Activity of Pt Catalysts: Influence of Electrolyte and Relation to Single Crystal Models*, J. Am. Chem. Soc., 2011, **133**, *43*, 17428-17433.

[276] (Patniboon, 2023) Patniboon, T., & Hansen, H. A., *Effects of Electrolyte Anion Adsorption on the Activity and Stability of Single Atom Electrocatalysts*, Chem. Phys. Rev., 2023, **4**, *1*, 011401.

[277] (Wang W. M., 2019) Wang, W., Jia, Q., Mukerjee, S., & Chen, S., *Recent Insights into the Oxygen-Reduction Electrocatalysis of Fe/N/C Materials*, ACS Catal., 2019, **9**, *11*, 10126-10141.

[278] (Chen W. ,.-K.-Y.-X., 2022) Chen, W., Zhang, M. -K., Liu, B. -Y., Cai, J., & Chen, Y. -X., *Challenges and Recent Progress in Unraveling the Intrinsic pH Effect in Electrocatalysis*, Current Opinion in Electrochem., 2022, **34**, 101003.

[279] (Huang J. Z., 2023) Huang, J., Zhang, Y., Li, M., Groß, A., & Sakong, S., *Comparing Ab Initio Molecular Dynamics and a Semiclassical Grand Canonical Scheme for the Electric Double Layer of the Pt(111)/Water Interface*, J. Phys. Chem. Lett., 2023, **14**, *9*, 2354-2363.

[280] (Gomes-Filho, 2023) Gomes-Filho, M. S., Pereira, A. O., Feliciano, G. T., Pedroza, L. S., & Coutinho-Net, M. D., *Extending the Applicability of Popular Force Fields for Describing Water/Metal Interfaces: Application to Water/Pd(111)*, Phys. Scr., 2023, **98**, 015009.

[281] (Groß, 2014) Groß, A., Gossenberger, F., Lin, X., Naderian, M., Sakong, S., & Roman, T., *Water Structures at Metal Electrodes Studied by Ab Initio Molecular Dynamics Simulations*, J. Electrochem. Soc., 2014, **161**, *8*, E3015-E3020.

[282] (Chen G. L., 2022) Chen, G., Li, X., & Feng, X., *Upgrading Organic Compounds through the Coupling of Electrooxidation with Hydrogen Evolution*, Angew. Chem. Int. Ed., 2022, **61**, e202209014.

---

[283] (Adamu, 2022) Adamu, H., Yamani, Z. H., & Qamar, M., *Modulation to Favorable Surface Adsorption Energy for Oxygen Evolution Reaction Intermediates over Carbon-Tunable Alloys towards Sustainable Hydrogen Production*, Mater. Renew. & Sustain. Energy, 2022, **11**, 169-213.

[284] (Briega-Martos, 2019) Briega-Martos, V., Herrero, E., & Feliu, J. M., *Pt(hkl) Surface Charge and Reactivity*, Current Opinion in Electrochem., 2019, **17**, 97-105.

[285] (Briega-Martos V. H., 2017) Briega-Martos, V., Herrero, E., & Feliu, J. M., *Effect of pH and Water Structure on the Oxygen Reduction Reaction on Platinum Electrodes*, Electrochim. Acta, 2017, **241**, 497-509.

[286] (Wang Y. H.-Y.-J.-C.-L.-Q.-F., 2023) Wang, Y. H., Li, S., Zhou, R. -Y., Zheng, S., Zhang, Y. -J., Dong, J. -C., Yang, Z. -L., Pan, F., Tian, Z. -Q., & Li, J. -F., *In Situ Electrochemical Raman Spectroscopy and Ab Initio Molecular Dynamics Study of Interfacial Water on a Single-Crystal Surface*, Nat. Protoc., 2023, **18**, 883-901.

[287] (Wang Y. H.-M.-Y.-F.-C.-L.-Q.-F., 2021) Wang, Y. H., Zheng, S., Yang, W. -M., Zhou, R. -Y., He, Q. -F., Radienovic, P., Dong, J. -C., Li, S., Zheng, J., Yang, Z. -L., Attard, G., Pan, F., Tian, Z. -Q., & Li, J. -F., *In situ Raman Spectroscopy Reveals the Structure and Dissociation of Interfacial Water*, Nature, 2021, **600**, 81-85.

[288] (Tong) Tong, Y., Lapointe, F., Thämer, M., Wolf, M., & Campen, R. K., *Hydrophobic Water Probed Experimentally at the Gold Electrode/Aqueous Interface*, Angew. Chem. Int. Ed., 2017, **56**, *15*, 4211-4214.

[289] (Li C. -Y.-B.-H.-L.-F.-Q., 2019) Li, C. -Y., Le, J. -B., Wang, Y. -H., Chen, S., Yang, Z. -L., Li, J. -F., Cheng, J., & Tian, Z. -Q., *In situ Probing Electrified Interfacial Water Structures at Atomically Flat Surfaces*, Nat. Mater., 2019, **18**, 697-701.

[290] (Toney, 1994) Toney, M. F., Howard, J. N., Richer, J., Borges, G. L., Gordon, J. G., Melroy, O. W., Wiesler, D. G., Yee, D., & Sorensen, L. B., *Voltage-Dependent Ordering of Water Molecules at an Electrode-Electrolyte Interface*, Nature, 1994, **368**, 444-446.

[291] (Ataka K. -I., 1996) Ataka, K. -I., Yotsuyanagi, T., & Osawa, M., *Potential-Dependent Reorientation of Water Molecules at an Electrode/Electrolyte Interface Studied by Surface-Enhanced Infrared Absorption Spectroscopy*, J. Phys. Chem., 1996, **100**, *25*, 10664-10672.

[292] (Gragson, 1997) Gragson, D. E., McCarty, B. M., & Richmond, G. L., *Ordering of Interfacial Water Molecules at the Charged Air/Water Interface Observed by Vibrational Sum Frequency Generation*, J. Am. Chem. Soc., 1997, **119**, 6144-6152.

[293] (Fleischmann, 1981) Fleischmann, M., Hendra, P. J., Hill, I. R., & Pemble, M. E., *Enhanced Raman Spectra from Species Formed by the Coadsorption of Halide Ions and Water Molecules on Silver Electrodes*, J. Electroanal. Chem., 1981, **117**, 243-255.

[294] (Jiang, 2007) Jiang, Y. -X., Li, J. -F., Wu, D. -Y., Yang, Z. -L., Ren, B., Hu, J. -W., Chow, Y. L., & Tian, Z. -Q., *Characterization of Surface Water on Au Core Pt-Group Metal Shell Nanoparticles Coated Electrodes by Surface-Enhanced Raman Spectroscopy*, Chem. Commun., 2007, **28**, 4608-4610.

[295] (Velasco-Velez, 2014) Velasco-Velez, J. J., Wu, C. H., Pascal, T. A., Wan, L. F., Guo, J., Prendergast, D., & Salmeron, M., *Interfacial Water. The Structure of Interfacial Water on Gold Electrodes Studied by X-ray Absorption Spectroscopy*, Science, 2014, **346**, *6211*, 831-834.

---

[296] (Petit, 2015) Petit, T., Yuzawa, H., Nagasaka, M., Yamanoi, R., Osawa, E., Kosugi, N., & Aziz, E. F., *Probing Interfacial Water on Nanodiamonds in Colloidal Dispersion*, J. Phys. Chem. Lett., 2015, **6**, *15*, 2909-2912.

[297] (Gonella, 2021) Gonella, G., Backus, E. H. G., Nagata, Y., Bonthuis, D. J., Loche, P., Schlaich, A., Netz, R. R., Kühnle, A., McCrum, I. T., Koper, M. T. M., Wolf, M., Winter, B., Meijer, G., Campen, R. K., & Bonn, M., *Water at Charged Interfaces*, Nat. Rev. Chem., 2021, **5**, 466-485.

[298] (Dewan, 2014) Dewan, S., Carnevale, V., Bankura, A., Eftekhari-Bafrooei, A., Fiorin, G., Klein, M. L., & Bouguet, E., *Structure of Water at Charged Interfaces: A Molecular Dynamics Study*, Langmuir, 2014, **30**, *27*, 8056-8065.

[299] Frumkin, A., & Gorodetzkaya, A., *Capillary Electric Phenomena in Amalgams. I Thallium Amalgams*, Z. Phys. Chem., 1928, **136**, 451-472.

[300] Climent, V., García-Araez, N., Herrero, E., & Feliu, J. M., *Potential of Zero Total Charge of Platinum Single Crystals: A Local Approach to Stepped Surfaces Vicinal to Pt(111)*, Russ. J. Electrochem., 2006, **42**, 1145-116.

[301] Frumkin, A. N., & Petrii, O. A., *Potentials of Zero Total and Zero Free Charge of Platinum Group Metals*, Electrochim. Acta, 1975, **20**, 347-359.

[302] (Pajkossy, 2018) Pajkossy, T., Müller, C., & Jacob, T., *The Metal-Ionic Liquid Interface as Characterized by Impedance Spectroscopy and In Situ Scanning Tunneling Microscopy*, Phys. Chem. Chem. Phys., 2018, **20**, 21241.

[303] (Martínez-Hincapié, 2017) Martínez-Hincapié, R., Sebastián-Pascual, P., Climent, V., & Feliu J. M., *Investigating Interfacial Parameters with Platinum Single Crystal Electrodes*, Russ. J. Electrochem., 2017, **53**, 227-236.

[304] (Attard, 2017) Attard, G. A., Hunter, K., Wright, E., Sharman, J., Martínez-Hincapié, R., & Feliu, J. M., *The Voltammetry of Surfaces Vicinal to Pt{110}: Structural Complexity Simplified by CO Cooling*, J. Electroanal. Chem., 2017, **793**, 137-146.

[305] (Attard G. H., 2004) Attard, G. A., Hazzazi, O., Wells, P. B., Climent, V., Herrero, E., & Feliu, J. M., *On the Global and Local Values of the Potential of Zero Total Charge at Well-Defined Platinum Surfaces: Stepped and Adatom Modified Surfaces*, J. Electroanal. Chem., 2004, **568**, 329-342.

[306] (Pajkossy T. &., 2003) Pajkossy, T., & Kolb, D. M., *On the Origin of the Double Layer Capacitance Maximum of Pt(111) Single Crystal Electrodes*, Electrochem. Comm., 2003, **5**, *4*, 283-285.

[307] (Garcia-Araez, 2006) Garcia-Araez, N., Climent, V., Herrero, E., Feliu, J. M., & Lipkowski, J., *Thermodynamic Approach to the Double Layer Capacity of a Pt(111) Electrode in Perchloric Acid Solutions*, Electrochim. Acta, 2006, **51**, *18*, 3787-3793.

[308] (Ganassin, 2017) Ganassin, A., Sebastián, P., Climent, V., Schuhmann, W., Bandarenka, A. S., & Feliu, J. M., *On the pH Dependence of the Potential of Maximum Entropy of Ir(111) Electrodes*, Sci. Rep., 2017, **7**, 1-14.

[309] Trasatti, S. J., *Interaction of Water with Metal Surfaces. A Theory on the Role of the Solid Substrate*, J. Electroanal. Chem. Interfacial Electrochem., 1974, **54**, 437-441.

---

[310] (Ledezma-Yanez, 2017) Ledezma-Yanez, I., Wallace, W. D. Z., Sebastián-Pascual, P., Climent, V., Feliu, J. M., & Koper, M. T. M., *Interfacial Water Reorganization as a pH-Dependent Descriptor of the Hydrogen Evolution Rate on Platinum Electrodes*, Nat. Energy, 2017, **2**, 17031.

[311] Plieth, W. J., *On the Derivation and Formulation of the Electrocapillary Equation of Ideally Polarizable Electrodes*, J. Electroanal. Chem., 1970, **27**, 468-471.

[312] Harrison, J. A., Randles J. E. B., & Schiffrin, D. J., *The Entropy of Formation of the Mercury-Aqueous Solution Interface and the Structure of the Inner Layer*, J. Electroanal. Chem. Interfacial Electrochem., 1973, **48**, 359-381.

[313] Lippmann, G., *Relations Entre Les Phénomènes Électriques et Capillaires*, Ann. Chim. Phys., 1875, **5**, 494-549.

[314] Grahame, D. C., *The Electrical Double Layer and the Theory of Electrocapillarity*, Chem. Rev., 1947, **41**, 441-501.

[315] Parsons, R., In: Bockris, J. O.'M, Conway, B. E., *Equilibrium Properties of Electrified Interfaces, Modern Aspects of Electrochemistry*. Eds. New York: Academic Press, New York, Vol 1., 1954,

[316] Girault, H., & Schiffrin, D., In: Bard A. J., *Electrochemistry of Liquid-Liquid Interfaces*, Electroanalytical Chemistry, Ed. New York: Marcel Dekker, New York, Vol 15, 1989.

[317] Horsman, P., Conway, B. E., & Yeager, E., *Comprehensive Treatise of Electrochemistry: The Double Layer*. Ed. Springer Science & Business Media, 2013.

[318] Shao, L. -H., Biener, J., Kramer, D., Viswanath, R. N., Baumann, T. F., Hamza, A. V., & Weissmüller, J., *Electrocapillary Maximum and Potential of Zero Charge of Carbon Aerogel*, J. Phys. Chem. Chem. Phys., 2010, **12**, 7580-7587.

[319] Vorsina, M., & Frumkin, A., *Capacity of the Double Layer of the Mercury Electrode in Dilute Solutions of Hydrochloric Acid and of Potassium Chloride*, Doklady Akad. Nauk. SSSR., 1939, **24**, 918-921.

[320] (Jun, 2020) Jun, H., *Electrochemical Impedance Spectroscopy for Electrocatalytic Interfaces and Reactions: Classics Never Die*, J. Electrochem., 2020, **26**, *1*, 3-18.

[321] Ojha, K., Arulmozhi, N., Aranzales, D., & Koper, M. T. M., *Double Layer at the Pt(111)-Aqueous Electrolyte Interface: Potential of Zero Charge and Anomalous Gouy-Chapman Screening*, Angew. Chem., Int. Ed., 2020, **59**, 711-715.

[322] Silva, C. D., Cabello, G., Christinelli, W. A., Pereira, E. C., & Cuesta, A., *Simultaneous Time-Resolved ATR-SEIRAS and CO-Charge Displacement Experiments: The Dynamics of CO Adsorption on Polycrystalline Pt*, J. Electroanal. Chem., 2017, **800**, 25-31.

[323] Clavilier, J., Albalat, R., Gomez, R., Orts, J., Feliu, J. M., & Aldaz, A., *Study of the Charge Displacement at Constant Potential During CO Adsorption on Pt(110) and Pt(111) Electrodes in Contact with a Perchloric Acid Solution*, J. Electroanal. Chem., 1992, **330**, 489-497.

[324] Climent, V., Attard, G., & Feliu, J. M., *Potential of Zero Charge of Platinum Stepped Surfaces: A Combined Approach of CO Charge Displacement and* N_2O *Reduction*, J. Electroanal. Chem., 2002, **532**, 67-74.

---

[325] Climent, V., Gómez, R., & Feliu, J. M., *Effect of Increasing Amount of Steps on the Potential of Zero Total Charge of Pt(111) Electrodes*, Electrochim. Acta, 1999, **45**, 629-637.

[326] Ebert, H., Parsons, R., Ritzoulis, G., & VanderNoot, T., *The Reduction of Nitrous Oxide on Platinum Electrodes in Acid Solution*, J. Electroanal. Chem. Interfacial Electrochem., 1989, **264**, 181-193.

[327] Attard, G., & Ahmadi, A., *Anion-Surface Interactions, Part 3.* N_2O *Reduction as a Chemical Probe of the Local Potential of Zero Total Charge*, J. Electroanal. Chem., 1995, **389**, 175-190.

[328] (Ahmadi A. B., 1993) Ahmadi, A., Bracey, E., Evans, R. W., & Attard, G., *Anion-Surface Interactions: Part II. Nitrous Oxide Reduction as a Probe of Anion Adsorption on Transition Metal Surfaces*, J. Electroanal. Chem., 1993, **350**, *1-2*, 297-316.

[329] Iwasita, T., & Xia, X. H., *Adsorption of Water at Pt (111) Electrode in* $HClO_4$ *Solutions. The Potential of Zero Charge*, J. Electroanal. Chem., 1996, **411**, 95-102.

[330] Andersen, T. N., Perkins, R. S., & Eyring, H., *Zero-Charge Potentials of Solid Metals*, J. Am. Chem. Soc., 1964, **86**, 4496.

[331] Nakamura, K., Ohno, M., Umemoto, K., & Hinoue, T., *Potential of Zero Charge of a Molybdenum Electrode by Laser Ablation Voltammetry*, Chem. Lett., 2000, 1050-1051.

[332] (Xu, 2023) Xu, P., von Rueden, A. D., Schimmenti, R., Mavrikakis, M., & Suntivich, J., *Optical Method for Quantifying the Potential of Zero Charge at the Platinum-Water Electrochemical Interface*, Nat. Mater., 2023.

[333] (Huang J. L., 2020) Huang, J., Li, P., & Chen, S., *Potential of Zero Charge and Surface Charging Relation of Metal-Solution Interphases from a Constant-Potential Jellium-Poisson-Boltzmann Model*, Physical Rev. B, 2020, **101**, *12*, 125422.

[334] (Sundararaman, 2023) Sundararaman, R., & Schwarz, K., *Solvent Effects Determine the Sign of the Charges of Maximum Entropy and Capacitance at Silver Electrodes*, J. Chem. Phys., 2023, **158**, 121102.

[335] (Santos, 2023) Santos, E., & Schmickler, W., *The Potential of Zero Charge of a Metal Electrode and the Surface Potential of Water from Simulations*, Current Opinion in Electrochem., 2023, **38**, 101208.

[336] (Bramley, 2020) Bramley, G., Nguyen, M. -T., Glezakou, V. -A., Rousseau, R. & Skylaris, C. -K., *Reconciling Work Functions and Adsorption Enthalpies for Implicit Solvent Models: A Pt (111)/Water Interface Case Study*, J. Chemical Theory and Computation, 2020, **16**, *4*, 2703-2715.

[337] (Le, 2017) Le, J., Iannuzzi, M., Cuesta, A., & Cheng, J., *Determining Potentials of Zero Charge of Metal Electrodes versus the Standard Hydrogen Electrode from Density-Functional-Theory-Based Molecular Dynamics*, Phys. Rev. Lett., 2017, **119**, *1*, 016801.

[338] Benderskii, V. A., Babenko, S. D., & Krivenko, A. G., *Investigation of the Charge Relaxation in the Double Layer by a Thermal Jump*, J. Electroanal. Chem. Interfacial Electrochem., 1978, **86**, 223-225.

---

[339] Benderskii, V. A., & Velichko, G. I., *Temperature Jump in Electric Double-Layer Study: Part I. Method of Measurements*, J. Electroanal. Chem. Interfacial Electrochem., 1982, **140**, 1-22.

[340] Benderskii, V. A., Velichko, G. I., & Kreitus, I., *Temperature Jump in Electric Double-Layer Study: Part II. Excess Entropy of EDL Formation at the Interface of Mercury and Electrolyte Solutions of Various Concentrations*, J. Electroanal. Chem. Interfacial Electrochem., 1984, **181**, 1-20.

[341] Smalley, J. F., Krishnan, C.V., Goldman, M., Feldberg, S. W., & Ruzic, I., *Laser-Induced Temperature-Jump Coulostatics for the Investigation of Heterogeneous Rate Processes: Theory and Application*, J. Electroanal. Chem., 1988, **248**, 255-282.

[342] Smalley, J. F., Newton, M. D., & Feldberg, S. W., *An Informative Subtlety of Itemperature-Jump or Coulostatic Responses for Surface-Attached Species*, Electrochem. Commun., 2000, **2**, *12*, 832-838.

[343] Climent, V., Coles, B. A., & Compton, R. G., *Laser-Induced Potential Transients on a Au(111) Single-Crystal Electrode. Determination of the Potential of Maximum Entropy of Double-Layer Formation*, J. Phys. Chem. B, 2002, **106**, 5258-5265.

[344] Climent, V., Coles, B. A., & Compton, R. G., *Laser Induced Current Transients Applied to a Au(111) Single Crystal Electrode. A General Method for the Measurement of Potentials of Zero Charge of Solid Electrodes*, J. Phys. Chem. B, 2001, **105**, 10669-10673.

[345] Climent, V., Coles, B. A., & Compton, R. G., *Laser-Induced Potential Transients on a Au(111) Single-Crystal Electrode. Determination of the Potential of Maximum Entropy of Double-Layer Formation,* J. Phys. Chem. B, 2002, **106**, 5988-5996.

[346] Climent, V., Garcia-Araez, N., Compton, R. G., & Feliu, J. M., *Effect of Deposited Bismuth on the Potential of Maximum Entropy of Pt(111) Single-Crystal Electrodes*, J. Phys. Chem. B, 2006, **110**, 21092-21100.

[347] García-Aráez, N., Climent, V., & Feliu, J. M., *Evidence of Water Reorientation on Model Electrocatalytic Surfaces from Nanosecond-Laser-Pulsed Experiments*, J. Am. Chem. Soc. 2008, **130**, 3824-3833.

[348] (Harrison, 1973) Harrison, J. A., Randles, J. E. B., & Schiffrin, D. J., *The Entropy of Formation of the Mercury-Aqueous Solution Interface and the Structure of the Inner Layer*, J. Electroanal. Chem. lnterfacial Electrochem., 1973, **48**, 359-381.

[349] Yamakata, A., & Osawa, M., *Dynamics of Double-Layer Restructuring on a Platinum Electrode Covered by CO: Laser-Induced Potential Transient Measurement,* J. Phys. Chem. C, 2008, **112**, 11427-11432.

[350] Toney, M. F., Howard, J. N., Richer, J., Borges, G. L., Gordon, J. G., Melroy, O. R., Wiesler, D. G., Yee, D., & Sorensen, L. B., *Voltage-Dependent Ordering of Water Molecules at an Electrode-Electrolyte Interface*, Nature, 1994, **368**, 444-446.

[351] (Garlyyev B. K., Optimizing the Size of Platinum Nanoparticles for Enhanced Mass Activity in the Electrochemical Oxygen Reduction Reaction, 2019) Garlyyev, B., Kratzl, K., Rück, M., Michalička, J., Fichtner, J., Macak, J. M., Kratky, T., Günther, S., Cokoja, M., Bandarenka, A. S., Gagliardi, A., & Fischer, R. A., *Optimizing the Size of Platinum Nanoparticles for Enhanced Mass Activity in the Electrochemical Oxygen Reduction Reaction*, Angew. Chem. Int. Ed., 2019, **58**, *28*, 9596-9600.

---

[352] (Koper, 2011) Koper, M. T., *Structure Sensitivity and Nanoscale Effects in Electrocatalysis*, Nanoscale, 2011, **3**, *5*, 2054-2073.

[353] (Rück, 2019) Rück, M., Bandarenka, A. S., Calle-Vallejo, F., & Gagliardi, A., *Fast Identification of Optimal Pure Platinum Nanoparticle Shapes and Sizes for Efficient Oxygen Electroreduction*, Nanoscale Adv., 2019, **1**, *8*, 2901-2909.

[354] (Colic V. &., 2016) Colic, V., & Bandarenka, A. S., *Pt Alloy Electrocatalysts for the Oxygen Reduction Reaction: From Model Surfaces to Nanostructured Systems*, ACS Catal., 2016, **6**, *8*, 5378-5385.

[355] (Gómez-Marín, 2015) Gómez-Marín, A. M., & Feliu, J. M., *Oxygen Reduction on Nanostructured Platinum Surfaces in Acidic Media: Promoting Effect of Surface Steps and Ideal Response of Pt(111)*, Catal. Today, 2015, **244**, 172-176.

[356] (Garlyyev B. X., Influence of the Nature of the Alkali Metal Cations on the Electrical Double-Layer Capacitance of Model Pt(111) and Au(111) Electrodes, 2018) Garlyyev, B., Xue, S., Watzele, S., Scieszka, D., & Bandarenka, A. S., *Influence of the Nature of the Alkali Metal Cations on the Electrical Double-Layer Capacitance of Model Pt(111) and Au(111) Electrodes*, J. Phys. Chem. Lett., 2018, **9**, *8*, 1927-1930.

[357] (Xue S. G., 2018) Xue, S., Garlyyev, B., Watzele, S., Liang, Y., Fichtner, J., Pohl, M. D., & Bandarenka, A. S., *Influence of Alkali Metal Cations on the Hydrogen Evolution Reaction Activity of Pt, Ir, Au, and Ag Electrodes in Alkaline Electrolytes*, ChemElectroChem, 2018, **5**, *17*, 2326-2329.

[358] (Ganassin A. C., 2015) Ganassin, A., Colic, V., Tymoczko, J., Bandarenka, A. S., & Schuhmann, W., *Non-Covalent Interactions in Water Electrolysis: Influence on the Activity of Pt(111) and Iridium Oxide Catalysts in Acidic Media*, Phys. Chem. Chem. Phys. (PCCP), 2015, **17**, *13*, 8349-8355.

[359] (Mitchell, 2022) Mitchell, J. B., Shen, M., Twight, L., & Boettcher, S. W., *Hydrogen-Evolution-Reaction Kinetics pH Dependence: Is It Covered?*, Chem. Catal., 2022, **2**, *2*, 236-238.

[360] (Sebastián P. G., 2019) Sebastián, P., Gómez, E., Climent, V., & Feliu, J. M., *Investigating the M(hkl)|Ionic Liquid Interface by Using Laser Induced Temperature Jump Technique*, Electrochim. Acta, 2019, **311**, 30-40.

[361] (Deng, 2022) Deng, B., Huang, M., Zhao, X., Mou, S., & Dong, F., *Interfacial Electrolyte Effects on Electrocatalytic CO_2 Reduction*, ACS Catal., 2022, **12**, *1*, 331-362.

[362] (Ikeda, 1987) Ikeda, S., Takagi, T., & Ito, K., *Selective Formation of Formic Acid, Oxalic Acid, and Carbon Monoxide by Electrochemical Reduction of Carbon Dioxide*, Bulletin Chem. Soc., Japan, 1987, **60**, 2517-2522.

[363] (Amatore, 1981) Amatore, C., & Savéant, J., *Mechanism and Kinetic Characteristics of the Electrochemical Reduction of Carbon Dioxide in Media of Low Proton Availability*, J. Am. Chem. Soc., 1981, **103**, *17*, 5021-5023.

[364] (Lamy, 1977) Lamy, E., Nadjo, L., & Savéant, J., *Standard Potential and Kinetic Parameters of the Electrochemical Reduction of Carbon Dioxide in Dimethylformamide*, J. Electroanal. Chem., 1977, **78**, 403-407.

---

[365] (Gunathunge, 2017) Gunathunge, C. M., Ovalle, V. J., & Waegele, M. M., *Probing Promoting Effects of Alkali Cations on the Reduction of CO at the Aqueous Electrolyte/Copper Interface*, Phys. Chem. Chem. Phys., 2017, **19**, *44*, 30166-30172.

[366] (Waegele, 2019) Waegele, M. M., Gunathunge, C. M., Li, J., & Li, X., *How Cations Affect the Electric Double Layer and the Rates and Selectivity of Electrocatalytic Processes*, J. Chem. Phys., 2019, **151**, *16*, 160902-160922.

[367] (Briega-Martos V. S., 2021) Briega-Martos, V., Sarabia, F. J., Climent, V., Herrero, E., & Feliu, J. M., *Cation Effects on Interfacial Water Structure and Hydrogen Peroxide Reduction on Pt(111)*, ACS Meas. Sci. Au., 2021, **1**, *2*, 48-55.

[368] (Garcia, Enhancement of Oxygen Evolution Activity of Nickel Oxyhydroxide by Electrolyte Alkali Cations, 2019) Garcia, A. C., Touzalin, T., Nieuwland, C., Perini, N., & Koper, M. T. M., *Enhancement of Oxygen Evolution Activity of Nickel Oxyhydroxide by Electrolyte Alkali Cations*, Angew. Chem. Int. Ed., 2019, **58**, *37*, 12999-13003.

[369] (Bičáková, 2012) Bičáková, O., & Straka, P., *Production of Hydrogen from Renewable Resources and Its Effectiveness*, Int. J. Hydrogen Energy, 2012, **37**, *16*, 11563-11578.

[370] (Taji, Alkali Metal Cations Change the Hydrogen Evolution Reaction Mechanisms at Pt Electrodes in Alkaline Media, 2022) Taji, Y., Zagalskaya, A., Evazzade, I., Watzele, S., Song, K. -T., Xue, S., Schott, C., Garlyyev, B., Alexandrov, V., Gubanova, E., & Bandarenka, A. S., *Alkali Metal Cations Change the Hydrogen Evolution Reaction Mechanisms at Pt Electrodes in Alkaline Media*, Nano Mater. Sci., 2022, ISSN 2589-9651, https://doi.org/10.1016/j.nanoms.2022.09.003.

[371] (Goyal, 2021) Goyal, A., & Koper, M. T. M., *The Interrelated Effect of Cations and Electrolyte pH on the Hydrogen Evolution Reaction on Gold Electrodes in Alkaline Media*, Angew. Chem. Int. Ed., 2021, **60**, *24*, 13452-13462.

[372] (Huang B. R.-H., 2021) Huang, B., Rao, R. R., You, S., Hpone, Myint, K., Song, Y., Wang, Y., Ding, W., Giordano, L., Zhang, Y., Wang, T., Muy, S., Katayama, Y., Grossman, J. C., Willard, A. P., Xu, K., Jiang, Y., & Shao-Horn, Y., *Cation- and pH-Dependent Hydrogen Evolution and Oxidation Reaction Kinetics*, JACS Au., 2021, **1**, *10*, 1674-1687.

[373] (Strmcnik, 2009) Strmcnik, D., Kodama, K., van der Vliet, D., Greeley, J., Stamenkovic, V. R., & Marković, N. M., *The Role of Non-Covalent Interactions in Electrocatalytic Fuel-Cell Reactions on Platinum*, Nat. Chem., 2009, **1**, *6*, 466-472.

[374] (Diaz-Morales, 2014) Diaz-Morales, O., Hersbach, T. J., Hetterscheid, D. G., Reek, J. N., & Koper, M. T. M., *Electrochemical and Spectroelectrochemical Characterization of an Iridium-Based Molecular Catalyst for Water Splitting: Turnover Frequencies, Stability, and Electrolyte Effects*, J. Am. Chem. Soc., 2014, **136**, *29*, 10432-10439.

[375] (Krischer, 2008) Krischer, K., & Savinova, E. R., *Fundamentals of Electrocatalysis*, In: *Handbook of Heterogeneous Catalysis* (Eds G. Ertl, H. Knözinger, F. Schüth & J. Weitkamp) (2008).

[376] (Santos M. C., 2000) Santos, M. C., Miwa, D. W., & Machado, S. A. S., *Study of Anion Adsorption on Polycrystalline Pt by Electrochemical Quartz Crystal Microbalance*, Electrochem. Comm., 2000, **2**, *10*, 692-696.

---

[377] (Lamy-Pitara, 2000) Lamy-Pitara, E., El Mouahid, S., & Barbier, J., *Effect of Anions on Catalytic and Electrocatalytic Hydrogenations and on the Electrocatalytic Oxidation and Evolution of Hydrogen on Platinum*, Electrochim. Acta, 2000, **45**, *25-26*, 4299-4308.

[378] (Hunter, 2016) Hunter, B. M., Hieringer, W., Winkler, J. R., Gray, H. B., & Müller, A. M., *Effect of Interlayer Anions on [NiFe]-LDH Nanosheet Water Oxidation Activity*, Energy & Environ. Sci., 2016, **9**, 1734-1743.

[379] (Shin, 2011) Shin, J. Y., Kim, Y. S., Lee, Y., Shim, J. H., Lee, C., & Lee, S.-G., *Impact of Anions on Electrocatalytic Activity in Palladium Nanoparticles Supported on Ionic Liquid-Carbon Nanotube Hybrids for the Oxygen Reduction Reaction*, Asian J. Chem., 2011, **6**, *8*, 2016-2021.

[380] (Chen W. Z.-K.-Y.-X., 2022) Chen, W., Zhang, M. -K., Liu, B. -Y., Cai, J., & Chen, Y. -X., *Challenges and Recent Progress in Unraveling the Intrinsic pH Effect in Electrocatalysis*, Current Opinion in Electrochem., 2022, **34**, 101003.

[381] (Strmcnik D. U., 2013) Strmcnik, D., Uchimura, M., Wang, C., Subbaraman, R., Danilovic, N., Van Der Vliet, D., Paulikas, A. P., Stamenkovic, V. R., & Markovic, N. M., *Improving the Hydrogen Oxidation Reaction Rate by Promotion of Hydroxyl Adsorption*, Nat. Chem., 2013, **5**, *4*, 300-306.

[382] (Durst, 2014) Durst, J., Simon, C., Hasché, F., & Gasteiger, H. A., *Hydrogen Oxidation and Evolution Reaction Kinetics on Carbon Supported Pt, Ir, Rh, and Pd Electrocatalysts in Acidic Media*, J. Electrochem. Soc., 2014, **162**, *1*, F190-F203.

[383] (Zhong, 2015) Zhong, Y., Ueno, K., Mori, Y., Oshikiri, T., & Misawa, H., *Cocatalyst Effects on Hydrogen Evolution in a Plasmon-Induced Water-Splitting System*, J. Phys. Chem. C, 2015, **119**, *16*, 8889-8897.

[384] (Takashima, 2012) Takashima, T., Hashimoto, K., & Nakamura, R., *Mechanisms of pH-Dependent Activity for Water Oxidation to Molecular Oxygen by MnO2 Electrocatalysts*, J. Am. Chem. Soc., 2012, **134**, *3*, 1519-1527.

[385] (Strmcnik D. L., 2016) Strmcnik, D., Lopes, P. P., Genorio, B., Stamenkovic, V. R., & Markovic, N. M., *Design Principles for Hydrogen Evolution Reaction Catalyst Materials*, Nano Energy, 2016, **29**, 29-36.

[386] (Zheng J. S., 2016) Zheng, J., Sheng, W., Zhuang, Z., Xu, B., & Yan, Y., *Universal Dependence of Hydrogen Oxidation and Evolution Reaction Activity of Platinum-Group Metals on pH and Hydrogen Binding Energy*, Sci. Adv., 2016, **2**, *3*, e1501602.

[387] (McCrum, 2017) McCrum, I. T., *Understanding the Effects of Electrolyte pH and Spectator Ions on Electrocatalysis*, **Ph. D. Dissertation, The Pennsylvania State University**, 2017.

[388] (Blizanac, 2004) Blizanac, B. B., Lucas, C. A., Gallagher, M. E., Arenz, M., Ross, P. N., & Marković, N. M., *Anion Adsorption, CO Oxidation, and Oxygen Reduction Reaction on a Au (100) Surface: The pH Effect*, J. Phys. Chem. B, 2004, **108**, *2*, 625-634.

[389] (Bard, 2000) Bard, A. J., & Faulkner, R., *Electrochemical Methods. Fundamentals and Applications*, John Wiley & Sons, Inc., 2nd Edition, 2000.

[390] (Mabbott, 1983) Mabbott, G. A., *An Introduction to Cyclic Voltammetry*, J. Chem. Educ., 1983, **60**, *9*, 697-702.

---

[391] (Skoog, 1996) Skoog, D. A., & Leary, J. J., *Voltammetrie*. In: *Instrumentelle Analytik*, Springer-Lehrbuch, Springer, Berlin, Heidelberg, 1996, 576-610.

[392] (Kissinger, 1983) Kissinger, P. T., & Heineman, W. R., *Cyclic Voltammetry*, J. Chem. Educ., 1983, **60**, *9*, 702-706.

[393] (Aristo, 2015) Aristo, N., & Habekost, A., *Cyclic Voltammetry - A Versatile Electrochemical Method Investigating Electron Transfer Processes*, J. Chem. Educ., 2015, **3**, *5*, 115-119.

[394] (Van Benschoten, 1983) Van Benschoten, J. J., Lewis, J. Y., Heineman, W. R., Roston, D. A., & Kissinger, P. T., *Cyclic Voltammetry Experiment*, J. Chem. Educ., 1983, **60**, *9*, 772-776.

[395] (Gómez-Marín A. M., Oxygen Reduction Reaction at Pt Single Crystals: A Critical Overview, 2014) Gómez-Marín, A. M., Rizo, R., & Feliu, J. M., *Oxygen Reduction Reaction at Pt Single Crystals: A Critical Overview*, Catal. Sci. Technol., 2014, **4**, *6*, 1685-1698.

[396] (Lei, 2015) Lei, Y., Chen, F., Jin, Y., & Liu, Z., *Ag-Cu Nanoalloyed Film as a High-Performance Cathode Electrocatalytic Material for Zinc-Air Battery*, Nanoscale Research Lett., 2015, **10**, *197*, 1-8.

[397] (Tsai, 2014) Tsai, W. -Y., Taberna, P. -L., & Simon, P., *Electrochemical Quartz Crystal Microbalance (EQCM) Study of Ion Dynamics in Nanoporous Carbons*, J. Am. Chem. Soc., 2014, **136**, *24*, 8722-8728.

[398] (Kwon, 2006) Kwon, K. D., Green, H., Bjöörn, P., & Kubicki, J. D., *Model Bacterial Extracellular Polysaccharide Adsorption onto Silica and Alumina: Quartz Crystal Microbalance with Dissipation Monitoring of Dextran Adsorption*, Environ. Sci. Technol., 2006, **40**, *24*, 7739-7744.

[399] (Shouji, 2000) Shouji, E., & Buttry, D. A., *EQCM Measurements of Solvent Transport during* Li^+ *Intercalation in* V_2O_5 *Xerogel Films*, Electrochim. Acta, 2000, **45**, *22-23*, 3757-3764.

[400] (Zhang C. F.-R., 2009) Zhang, C., Fan, F. -R. F., & Bard, A. J., *Electrochemistry of Oxygen in Concentrated NaOH Solutions: Solubility, Diffusion Coefficients, and Superoxide Formation*, J. Am. Chem. Soc., 2009, **131**, *1*, 177-181.

[401] (Yuan, 2004) Yuan, Y., Wang, L., & Amemiya, S., *Chronoamperometry at Micropipet Electrodes for Determination of Diffusion Coefficients and Transferred Charges at Liquid/Liquid Interfaces*, Anal. Chem., 2004, **76**, *18*, 5570-5578.

[402] (Denuault, 1991) Denuault, G., Mirkin, M. V., & Bard, A. J., *Direct Determination of Diffusion Coefficients by Chronoamperometry at Microdisk Electrodes*, J. Electroanal. Chem. Interfacial Electrochem., 1991, **308**, *1-2*, 27-38.

[403] (Wang J. , 2012) Wang, J., *Advances in Electroanalytical Chemistry, Chapter 4 - Measurement of the Diffusion Coefficients of* $[Ru(NH_3)_6]^{3+}$ *and* $[Ru(NH_3)_6]^{2+}$ *in Aqueous Solution using Microelectrode Double Potential Step Chronoamperometry*, **Ph. D. Thesis, St. John's College, University of Oxford**, 2012.

[404] (Bahadori, 2015) Bahadori, L., Chakrabarti M. H., Manan, N. S. A., Hashim, M. A., Mjalli, F. S., AlNashef, I. M., & Brandon, N., *The Effect of Temperature on Kinetics and Diffusion Coefficients of Metallocene Derivatives in Polyol-Based Deep Eutectic Solvents,* PLoS One, 2015, **10**, *12*, e0144235.

---

[405] (Warburg, 1899) Warburg, E., *About the Behaviour of So-Called 'Impolarizable Electrodes' the Present Alternating Current*, Ann. Phys. Chem., 1899, **67**, *3*, 493-499.

[406] (Randles, 1947) Randles, J. E. B., *Kinetics of Rapid Electrode Reactions*, Discussi. Faraday Soc., 1947, **1**, 11-19.

[407] (Gerischer, 1951) Gerischer, H., *Wechselstrompolarisation von Elektroden mit einen Potentialbestimmenden Schritt beim Gleichgewichtspotential I.*, Z. Phys. Chem., 1951, **198**, 286-313.

[408] (Gerischer, Wechselstrompolarisation von Elektroden mit einem Potentialbestimmenden Schritt beim Gleichgewichtspotential. II., 1952) Gerischer, H., *Wechselstrompolarisation von Elektroden mit einem Potentialbestimmenden Schritt beim Gleichgewichtspotential II.*, Z. Phys. Chem., 1952, **201**, 55-67.

[409] (Gerischer, Elektrodenpolarisation bei Überlagerungen von Wechselstrom und Gleichstrom. I. Theorie , 1954) Gerischer, H., *Elektrodenpolarisation bei Überlagerungen von Wechselstrom und Gleichstrom. I. Theorie*, Z. Phys. Chem., 1954, Neue Folge 1, 278-299.

[410] (Gerischer H. &., 1955) Gerischer, H., & Vielstich, W., *Zur Elektrolyse bei konstantem Elektrodenpotential. I. Der Strom-Zeit-Verlauf bei gehemmter Entladung mit Nachlieferung durch Diffusion und Rückschlüsse auf die Kinetik*, Z. Phys. Chem., 1955, Neue Folge 3, 16-33.

[411] (Grahame, 1952) Grahame, D. C., *Mathematical Theory of the Faradaic Admittance (Pseudocapacity and Polarization Resistance)*, J. Electrochem. Soc., 1952, **99**, *12*, 370C-385C.

[412] (Macdonald, 2006) Macdonald, D. D., *Reflections on the History of Electrochemical Impedance Spectroscopy*, Electrochim. Acta, 2006, **51**, *8-9*, 1376-1388.

[413] (Macdonald, Review of Mechanistic Analysis by Electrochemical Impedance Spectroscopy, 1990) Macdonald, D. D., *Review of Mechanistic Analysis by Electrochemical Impedance Spectroscopy*, Electrochim. Acta, 1990, **35**, *10*, 1509-1525.

[414] (Macdonald D. D., 1882) Macdonald, D. D., & McKubre, M. C. H., *Impedance Measurements in Electrochemical Systems*, In: *Modern Aspects of Electrochemistry 14*, Bockris, J. O., Conway, & White, 1982, Springer, Plenum Press, New York, 61-150.

[415] (Brug, 1984) Brug, G. J., Eeden, A. V., Sluyters-Rehbach, M., & Sluyters, J. H., *The Analysis of Electrode Impedances Complicated by the Presence of a Constant Phase Element*, J. Electroanal. Chem., 1984, **176**, *1-2,* 275-295.

[416] (Lasia, 2002) Lasia, A., *Electrochemical Impedance Spectroscopy and Its Applications in Modern Aspects of Electrochemistry*, Vol. 32, Springer, New York, USA, 2002, 143-248.

[417] (Orazem, 2017) Orazem, M. E., & Tribollet, B., *Electrochemical Impedance Spectroscopy*, John Wiley & Sons, Inc., Hoboken, Second Edition, 2017.

[418] (Sluyters-Rehbach, Impedances of Electrochemical Systems: Terminology, Nomenclature and Representation - Part I: Cells with Metal Electrodes and Liquid Solutions (IUPAC Recommendations 1994), 1994) Sluyters-Rehbach, M., *Impedances of Electrochemical Systems: Terminology, Nomenclature and Representation - Part I: Cells with Metal Electrodes and Liquid Solutions (IUPAC Recommendations 1994)*, Pure & Appl. Chem., 1994, **66**, *9*, 1831-1891.

---

[419] Tresp, H., Hammer, M. U., Winter, J., Weltmann, K. D., & Reuter, S., *Quantitative Detection of Plasma-Generated Radicals in Liquids by Electron Paramagnetic Resonance Spectroscopy*, J. Phys. D, Appl. Phys., 2013, **46**, *43*, 435401.

[420] Hogg, N., *Detection of Nitric Oxide by Electron Paramagnetic Resonance Spectroscopy*, Free Radical Biology & Medicine, 2010, **49**, *2*, 122-129.

[421] Zweier, J. L., & Kuppusamy, P., *Electron Paramagnetic Resonance Measurements of Free Radicals in the Intact Beating Heart: A Technique for Detection and Characterization of Free Radicals in Whole Biological Tissues*, Proceedings of the National Academy of Sciences, 1988, **85**, *15*, 5703-5707.

[422] Yordanov, N. D., & Gancheva, V., *A New Approach for Extension of the Identification Period of Irradiated Cellulose-Containing Foodstuffs by EPR Spectroscopy*, Appl. Radiation & Isotopes, 2000, **52**, *2*, 195-198.

[423] Boizot, B., Petite, G., Ghaleb, D., & Calas, G., *Radiation Induced Paramagnetic Centres in Nuclear Glasses by EPR Spectroscopy. Nuclear Instruments and Methods in Physics Research Section B: Beam Interactions with Materials and Atoms*, 1998, **141**, *1-4*, 580-584.

[424] Bertrand, P., *Electron Paramagnetic Resonance Spectroscopy*, Springer, 2020.

[425] Weil, J. A., & Bolton, J. R., *Electron Paramagnetic Resonance: Elementary Theory and Practical Applications*, John Wiley & Sons, 2007.

[426] Shi, T., Schins, R. P., Knaapen, A. M., Kuhlbusch, T., Pitz, M., Heinrich, J., & Borm, P. J., *Hydroxyl Radical Generation by Electron Paramagnetic Resonance as a New Method to Monitor Ambient Particulate Matter Composition*, J. Environ. Monitoring, 2003, **5**, *4*, 550-556.

[427] (Tang J. P., 2005) Tang, J., Petri, M., Kibler, L. A., & Kolb, D. M., *Pd Deposition onto Au(111) Electrodes from Sulphuric Acid Solution*, Electrochim. Acta, 2005, **205**, *51*, 125-132.

[428] (Kibler, 2003) Kibler, L. A., El-Aziz, A. M., & Kolb, D. M., *Electrochemical Behaviour of Pseudomorphic Overlayers: Pd on Au(1 1 1)*, J. Molecular Catal. A: Chemical, 2003, **199**, *1-2*, 57-63.

[429] (Kibler L. A., 2000) Kibler, L. A., Kleinert, M., & Kolb, D. M., *Initial stages of Pd deposition on Au(hkl): Part II*, Surf. Sci., 2000, **461**, *1-3*, 155-167.

[430] (Kibler L. A., 1999) Kibler, L. A., Kleinert, M., Randler, R., & Kolb, D. M., *Initial Stages of Pd Deposition on Au(hkl) Part I: Pd on Au(111)*, Surf. Sci., 1999, **443**, *1-2*, 19-30.

[431] (Baldauf, 1996) Baldauf, M., & Kolb, D. M., *Formic Acid Oxidation on Ultrathin Pd Films on Au(hkl) and Pt(hkl) Electrodes*, J. Phys. Chem., 1996, **100**, *27*, 11375-11381.

[432] (Garbarino, 2010) Garbarino, S., & Burke, L. D., *The Surface Active Site Model for Formic Acid Electrooxidation at Palladium in Aqueous Acid Solution*, Int. J. Electrochem. Sci., 2010, **5**, *6*, 828-851.

[433] Pauwels, D., Ching, H. Y. V., Samanipour, M., Neukermans, S., Hereijgers, J., Doorslaer, S. V., Wael, K. D., & Breugelmans, T., *Identifying Intermediates in the Reductive Intramolecular Cyclisation of Allyl 2-bromobenzyl Ether by an Improved Electron Paramagnetic Resonance Spectroelectrochemical Electrode Design Combined with Density Functional Theory Calculations*, Electrochim. Acta, 2018, **271**,10-18.

---

[434] Neukermans, S., Samanipour, M., Ching, H. Y. V., Hereijgers, J., Doorslaer, S. V., Hubin, A., & Breugelmans, T., *A Versatile In-Situ Electron Paramagnetic Resonance Spectroelectrochemical Approach for Electrocatalyst Research*, ChemElectroChem, 2020, **7**, *22*, 4578-4586.

[435] Tamski, M. A., Macpherson, J. V., Unwin, P. R., & Newton, P. R., *Electrochemical Electron Paramagnetic Resonance Utilizing Loop Gap Resonators and Micro-Electrochemical Cells*, Phys. Chem. Chem. Phys., 2015, **17**, 23438-23447.

[436] Tamski, M. A., Dale, M. W., Breeze, B. G., Macpherson, J. V., Unwin, P. R., & Newton, P. R., *Quantitative Measurements in Electrochemical Electron Paramagnetic Resonance*, Electrochim. Acta, 2016, **213**, 802-810.

[437] Morsy, M. A., & Kawde, A. N. M., *Electron Paramagnetic Resonance Monitoring for On-Demand Electrochemically-Generated Radicals*, Electrochim. Acta, 2015, **160**, 22-27.

[438] Aoki, K., *Theory of Ultramicroelectrodes*, Electroanalysis, 1993, **5**, 627-639.

[439] Wang, B., Fielding, A. J., & Dryfe, R. A., *Electron Paramagnetic Resonance Investigation of the Structure of Graphene Oxide: pH-Dependence of the Spectroscopic Response*, ACS Appl. Nano Mater., 2018, **2**, *1*, 19-27.

[440] Wang, B., Fielding, A. J., & Dryfe, R. A., *Electron Paramagnetic Resonance as a Structural Tool to Study Graphene Oxide: Potential Dependence of the EPR Response*, J. Phys. Chem. C, 2019, **123**, *36*, 22556-22563.

[441] Goldberg, I. B., & McKinney, T. M., *Principles and Technqiues of Electrochemical-Electron Paramagnetic Resonance Experiments*, In: *Laboratory Techniques in Electroanalytical Chemistry*, Kissinger, P. T., & Heineman, W. R., New York: Dekker, 1984, 675-728.

[442] Goldberg, I. B., Bard, A. J., & Feldberg, S, W., *Resistive Effects in Thin Electrochemical Cells. Digital Simulations of Electrochemistry in Electron Spin Resonance Cells,* J. Phys. Chem., 1972, **76**, *18*, 2550-2559.

[443] Adams, R. N., *Application of Electron Paramagnetic Resonance Techniques in Electrochemistry*, J. Electroanal. Chem., 1964, **8**, *2*, 151-162.

[444] Coles, B. A., & Compton, R. G., *Photoelectrochemical ESR: Part I. Experimental*, J. Electroanal. Chem., 1983, **144**, *1-2*, 87-98.

[445] Dmitrieva, E., Harima, Y., & Dunsch, L., *Influence of Phenazine Structure on Polaron Formation in Polyaniline: In Situ Electron Spin Resonance-Ultraviolet/Visible-Near-Infrared Spectroelectrochemical Study*, J. Phys. Chem. B, 2009, **113**, *50*, 16131-16141.

[446] Compton, R. G., Daly, P. J., Unwin, P. R., & Waller, A. M., *In-situ Electrochemical ESR: ECE versus Dispi.*, J. Electroanal. Chem., 1985, **191**, *1*, 15-29.

[447] Park, H. W., Won, M. S., Cheong, C., & Shim, Y. B., *In-Situ ESR Detection of Radical Species of p-Benzoquinone in Aqueous Media*, Electroanalysis, 2002, **14**, *21*, 1501-1507.

---

[448] González, J. R., Alcántara, R., Tirado, J. L., Fielding, A. J., & Dryfe, R. A., *Electrochemical Interaction of Few-Layer Molybdenum Disulfide Composites vs Sodium: New Insights on the Reaction Mechanism*, Chem. Mater., 2017, **29**, *14*, 5886-5895.

[449] Wang, B., Fielding, A. J., & Dryfe, R. A., *In Situ Electrochemical Electron Paramagnetic Resonance Spectroscopy as a Tool to Probe Electrical Double Layer Capacitance*, Chem. Commun., 2018, **54**, *31*, 3827-3830.

[450] Piette, L. H., Ludwig, P., & Adams, R. N., *Electron Paramagnetic Resonance and Electrochemistry. Studies of Electrochemically Generated Radical Ions in Aqueous Solution*, Anal. Chem., 1962, **34**, *8*, 916-921.

[451] Murray, P. R., Collison, D., Daff, S., Austin, N., Edge, R., Flynn, B. W., Jack, L., Leroux, F., McInnes, E. J. L., Murray, A. F., Sells, D., Stevenson, T., Wolowska, J., & Yellowlees, L. J., *An In situ Electrochemical Cell for Q- and W-Band EPR Spectroscopy*, J. Mag. Resonance, 2011, **213**, *1*, 206-209.

[452] Froncisz, W., & Hyde, J. S., *The Loop-Gap Resonator: A New Microwave Lumped Circuit ESR Sample Structure*, J. Mag. Resonance, 1982, **47**, 515-521.

[453] Allendoerfer, R. D., Froncisz, W., Felix, C. C., & Hyde, J. S., *Electrochemical Generation of Free Radicals in an EPR Loop-Gap Resonator*, J. Mag. Resonance, 1988, **76**, 100-105.

[454] Hyde, J. S., & Froncisz, W., In: *Advanced EPR: Applications in Biology and Biochemistry*, Edited by Hoff, A. J., Elsevier, 1989, 1-29.

[455] (Li W. L., 2019) Li, W., Li, F., Yang, H., Wu, X., Zhang, P., Shan, Y., & Sun, L., *A Bio-Inspired Coordination Polymer as Outstanding Water Oxidation Catalyst via Second Coordination Sphere Engineering*, Nat. Commun., 2019, **10**, 5074.

[456] (Greeley, 2009) Greeley, J., Stephens, I. E., Bondarenko, A. S., Johansson, T. P., Hansen, H. A., Jaramillo, T. F., Rossmeisl, J., Chorkendorff, I., & Nørskov, J. K., *Alloys of Platinum and Early Transition Metals as Oxygen Reduction Electrocatalysts*, Nat. Chem., 2009, **7**, 552-556.

[457] (Monteiro, 2021) Monteiro, M. C. O., Goyal, A., Moerland, P., & Koper, M. T. M., *Understanding Cation Trends for Hydrogen Evolution on Platinum and Gold Electrodes in Alkaline Media*, ACS Catal., 2021, **11**, *23*, 14328-14335.

[458] (Athanasiou, 2018) Athanasiou, M., Hasa, B., Vakros, J., Sygelloub, L., & Katsaounis, A., *Electrochemical Promotion of Carbon-Supported Pt, Rh and Pd Catalysts for* H_2 *Oxidation in Aqueous Alkaline Media*, J. Chem. Tech. Biotech., 2018, **93**, *6*, 1542-1548.

[459] (Štrbac, 1988) Štrbac, S., Adžć, R. R., & Hamelin, A., *Oxide Formation on Gold Single Crystal Stepped Surfaces*, J. Electroanal. Chem. Interfacial Electrochem., 1988, **249**, *1-2*, 291-310.

[460] (Chen J. H., 1996) Chen, J. H., Nie, L. H., & Yao, S. Z., *A New Method for Rapid Determination of the Potential of Zero Charge for Gold*, J. Electroanal. Chem., 1996, **414**, *1*, 53-59.

---

[461] (Tang, 2023) Tang, B. Y., Bisbey, R. P., Lodaya, K. M., Toh, W. L., & Surendranath, Y., *Reaction Environment Impacts Charge Transfer but not Chemical Reaction Steps in Hydrogen Evolution Catalysis*, Nat. Catal*.,* 2023, **6**, 339-350.

[462] (Wilson, 2023) Wilson, J. C., Caratzoulas, S., Vlachos, D. G., & Yan, Y., *Insights into Solvent and Surface Charge Effects on Volmer Step Kinetics on Pt (111)*, Nat. Commun., 2023, **14**, 2384.

[463] (Cabello, 2014) Cabello, G., Leiva, E. P. M., Gutiérrez, C., & Cuesta, A., *Non-Covalent Interactions at Electrochemical Interfaces: One Model Fits All?*, Phys. Chem. Chem. Phys., 2014, **16**, 14281-14286.

[464] (Garlyyev B. X., 2018) Garlyyev, B., Xue, S., Pohl, M. D., Reinisch, D., & Bandarenka, A. S., *Oxygen Electroreduction at High-Index Pt Electrodes in Alkaline Electrolytes: A Decisive Role of the Alkali Metal Cations*, ACS Omega, 2018, **3**, *11*, 15325-15331.

[465] (Gao, 2015) Gao, Q., Ranjan, C., Pavlovic, Z., Blume, R., & Schlögl, R., *Enhancement of Stability and Activity of MnOx/Au Electrocatalysts for Oxygen Evolution through Adequate Electrolyte Composition*, ACS Catal., 2015, **5**, *12*, 7265-7275.

[466] (Garlyyev B. X., 2018) Garlyyev, B., Xue, S., Watzele, S., Scieszka, D., & Bandarenka, A. S., *Influence of the Nature of the Alkali Metal Cations on the Electrical Double-Layer Capacitance of Model Pt(111) and Au(111) Electrodes*, J. Phys. Chem. Lett., 2018, **9**, *8*, 1927-1930.

[467] (Xue S. B.-L., 2020) Xue, S., Garlyyev, B., Auer, A., Kunze-Liebhäuser, J., & Bandarenka, A. S., *How the Nature of the Alkali Metal Cations Influences the Double-Layer Capacitance of Cu, Au, and Pt Single-Crystal Electrodes*, J. Phys. Chem. C, 2020, **124**, *23*, 12442-12447.

[468] (Guo, 2023) Guo, Y., Tong, X., & Yang, N., *Photocatalytic and Electrocatalytic Generation of Hydrogen Peroxide: Principles, Catalyst Design and Performance*, Nanomicro. Lett., 2023, **15**, *1*, 77.

[469] (Mayet, 2020) Mayet, N., Servat, K., Kokoh, K. B. B., & Napporn, T., *Electrochemical Oxidation of Carbon Monoxide on Unsupported Gold Nanospheres in Alkaline Medium*, Electrocatalysis, 2020.

[470] (Rodriguez, 2010) Rodriguez, P., Garcia-Araez, N., & Koper, M. T. M., *Self-Promotion Mechanism for CO Electrooxidation on Gold*, Phys. Chem. Chem. Phys., 2010,**12**, *32*, 9373-9380.

[471] (Garcia-Araez N. C., 2009) Garcia-Araez, N., Climent, V., & Feliu, J. M., *Potential-Dependent Water Orientation on Pt(111), Pt(100), and Pt(110), As Inferred from Laser-Pulsed Experiments. Electrostatic and Chemical Effects*, J. Phys. Chem. C, 2009, **113**, *21*, 9290-9304.

[472] (Tymoczko J., 2015) Tymoczko, J., Colic, V., Bandarenka, A. S., & Schuhmann, W., *Detection of 2D Phase Transitions at the Electrode/Electrolyte Interface Using Electrochemical Impedance Spectroscopy*, Surf. Sci., 2015, **631**, 81-87.

[473] (Li W. L., 2019) Li, W., Li, F., Yang, H., Wu, X., Zhang, P., Shan, Y., & Sun, L., *A Bio-Inspired Coordination Polymer as Outstanding Water Oxidation Catalyst via Second Coordination Sphere Engineering*, Nat. Commun., 2019, **10**, *1*, 5074.

---

[474] (Shcherbakov, 2021) Shcherbakov, V. V., Artemkina, Y. M., Akimova, I, A., & Artemkina, I. M., *Dielectric Characteristics, Electrical Conductivity and Solvation of Ions in Electrolyte Solutions*, Materials, 2021, **14**, *19*, 5617.

[475] (Hasted, 1948) Hasted, J., Ritson, D., & Collie, C., *Dielectric Properties of Aqueous Ionic Solutions. Parts I and II*, J. Phys. Chem., 1948, **16**, *1*, 1-21.

[476] (Li W. L.-Y., 2022) Li, W., Li, J., Duong, T. D., Sapchenko, S. A., Han, X., Humby, J. D., Whitehead, G. F. S., Victórica-Yrezábal, I. J., da Silva, I., Manuel, P., Frogley, M. D., Cinque, G., Schröder, M., & Yang, S., *Adsorption of Sulfur Dioxide in Cu(II)-Carboxylate Framework Materials: The Role of Ligand Functionalization and Open Metal Sites*, J. Am. Chem. Soc., 2022, **144**, *29*, 13196-13204.

[477] (Fan, 2020) Fan, Z., Wang, J., Wang, W., Burger, S., Wang, Z., Wang, Y., Wöll, C., Cokoja, M., & Fischer, R. A., *Defect Engineering of Copper Paddlewheel-Based Metal–Organic Frameworks of Type NOTT-100: Implementing Truncated Linkers and Its Effect on Catalytic Properties*, ACS Appl. Mater. Interfaces, 2020, **12**, *34*, 37993-38002.

[478] (Bennett, 2018) Bennett, T. D., & Horike, S., *Liquid, Glass and Amorphous Solid States of Coordination Polymers and Metal-Organic Frameworks*, Nat. Rev. Mater., 2018, **3**, 431-440.

[479] (Ma, 2023) Ma, D., Huang, X., Zhang, Y., Wang, L., & Wang, B., *Metal-Organic Frameworks: Synthetic Methods for Industrial Production*, Nano Research, 2023, **16**, *5*, 7906-7925.

[480] (Jiao, 2018) Jiao, L., Wang, Y., Jiang, H. L., & Xu, Q., *Metal-Organic Frameworks as Platforms for Catalytic Applications*, Adv. Mater., 2018, **30**, *37*, e1703663.

[481] (Farha, 2011) Farha, O. K., Shultz, A. M., Sarjeant, A. A., Nguyen, S. T. A., & Hupp, J. T., *Active-Site-Accessible, Porphyrinic Metal-Organic Framework Materials*, J. Am. Chem. Soc., 2011, **133**, *15*, 5652- 5655.

[482] (Shultz, 2009) Shultz, A. M., Farha, O. K., Hupp, J. T., & Nguyen, S. T. A., *Catalytically Active, Permanently Microporous MOF with Metalloporphyrin Struts*, J. Am. Chem. Soc., 2009, **131**, *12*, 4204-4205.

[483] (Corma, 2010) Corma, A., García, H., Llabrés, F. X., & Xamena, I., *Engineering Metal-Organic Frameworks for Heterogeneous Catalysis*, Chem. Rev., 2010, **110**, *8*, 4606-4655.

[484] (Farrusseng, 2009) Farrusseng, D., Aguado, S., & Pinel, C., *Metal-Organic Frameworks: Opportunities for Catalysis*, Angew. Chem. Int. Ed., 2009, **48**, *41*, 7502-7513.

[485] (Sun) Sun, C. -Y., Qin, C., Wang, X. -L., & Su, Z. -M., *Metal-Organic Frameworks as Potential Drug Delivery Systems*, Expert Opin. Drug Deliv., 2013, **10**, *1*, 89-101.

[486] (Horcajada, 2010) Horcajada, P., Chalati, T., Serre, C., Gillet, B., Sebrie, C., Baati, T., Eubank, J. F., Heurtaux, D., Clayette, P., Kreuz, C., Chang, J. S., Hwang, Y. K., Marsaud, V., Bories, P. N., Cynober, L., Gil, S., Férey, G., Couvreur, P., & Gref, R., *Porous Metal-Organic-Framework Nanoscale Carriers as a Potential Platform for Drug Delivery and Imaging*, Nat. Mater., 2010, **9**, *2*, 172-178.

[487] (Li D. C.-Y.-F.-G., 2021) Li, D., Chen, L., Liu, G., Yuan, Z. -Y., Li, B. -F., Zhang, X., & Wei, J. -G., *Porous Metal-Organic Frameworks for Methane Storage and Capture: Status and Challenges*, Carbon, 2021, **182**, 858.

---

[488] (Li H. L.-B., 2019) Li, H., Li, L., Lin, R. -B., Zhou, W., Zhang, Z., Xiang, S., & Chen, B., *Porous Metal-Organic Frameworks for Gas Storage and Separation: Status and Challenges*, EnergyChem, 2019, **1**, 100006.

[489] (He, 2014) He, Y., Zhou, W., Qian, G., & Chen, B., *Methane Storage in Metal-Organic Frameworks*, Chem. Soc. Rev., 2014, **43**, 5657-5678.

[490] (Han, 2019) Han, X., Yang, S., & Schröder, M., *Porous Metal-Organic Frameworks as Emerging Sorbents for Clean Air*, Nat. Rev. Chem., 2019, **3**, *2*, 108-118.

[491] (Rocca, 2011) Rocca, J. D., Liu, D., & Lin, W., *Nanoscale Metal-Organic Frameworks for Biomedical Imaging and Drug Delivery*, Acc. Chem. Res., 2011, **44**, *10*, 957-968.

[492] (Stassen, 2017) Stassen, I., Burtch, N., Talin, A., Falcaro, P., Allendorf, M., & Ameloot, R., *An Updated Roadmap for the Integration of Metal-Organic Frameworks with Electronic Devices and Chemical Sensors*, Chem. Soc. Rev., 2017, **46**, *11*, 3185-3241.

[493] (Li W. X., 2020) Li, W., Xue, S., Watzele, S., Hou, S., Fichtner, J., Semrau, A. L., Zhou, L., Welle, A., Bandarenka, A. S., & Fischer, R. A., *Advanced Bifunctional Oxygen Reduction and Evolution Electrocatalyst Derived from Surface-Mounted Metal-Organic Frameworks*, Angew. Chem., Int. Ed., 2020, **59**, *14*, 5837- 5843.

[494] (Li W. W.-S., 2019) Li, W., Watzele, S., El-Sayed, H. A., Liang, Y., Kieslich, G., Bandarenka, A. S., Rodewald, K., Rieger, B., & Fischer, R. A., *Unprecedented High Oxygen Evolution Activity of Electrocatalysts Derived from Surface-Mounted Metal–Organic Frameworks*, J. Am. Chem. Soc., 2019, **141**, *14*, 5926- 5933.

[495] (Gao, Enhancement of Stability and Activity of MnOx/Au Electrocatalysts for Oxygen Evolution through Adequate Electrolyte Composition, 2015) Gao, Q., Ranjan, C., Pavlovic, Z., Blume, R., & Schlögl, R., *Enhancement of Stability and Activity of MnOx/Au Electrocatalysts for Oxygen Evolution through Adequate Electrolyte Composition*, ACS Catal., 2015, **5**, *12*, 7265-7275.

[496] (Goikolea, 2020) Goikolea, E., Palomares, V., Wang, S., Larramendi, I. R., Guo, X., Wang, G., & Rojo, T., *Na-Ion Batteries - Approaching Old and New Challenges*, Adv. Energy Mater., 2020, **10**, *44*, 2002055.

[497] (Pasta, 2014) Pasta, M., Wessells, C. D., Liu, N., Nelson, J., McDowell, M. T., Huggins, R. A., Toney, M. F., & Cui, Y., *Full Open-Framework Batteries for Stationary Energy Storage*, Nat. Commun., 2014, **5**, 3007.

[498] (Pan Z. L., 2021) Pan, Z., Liu, X., Yang, J., Li, X., Liu, Z., Loh, X. J., & Wang, J., *Aqueous Rechargeable Multivalent Metal-Ion Batteries: Advances and Challenges*, Adv. Energy Mater., 2021, **11**, *24*, 2100608.

[499] (Qiu, 2022) Qiu, S., Xu, Y., Wu, X., & Ji, X., *Prussian Blue Analogues as Electrodes for Aqueous Monovalent Ion Batteries*, Electrochem. Energy Rev., 2022, **5**, 242-262.

[500] (Lamprecht, 2023) Lamprecht, X., Evazzade, I., Ungerer, I., Hromadko, L., Macak, J. M., Bandarenka, A. S., & Alexandrov, V., *Mechanisms of Degradation of* $Na_2Ni[Fe(CN)_6]$ *Functional Electrodes in Aqueous Media: A Combined Theoretical and Experimental Study*, J. Phys. Chem. C, 2023, **127**, *5*, 2204-2214.

[501] (Emets, 2009) Emets, V. V., & Damaskin, B. B., *The Relation between the Potential of Zero Charge and Work Function for sp-Metals*, Russ. J. Electrochem., 2009, **45**, 45-57.

---

[502] (Gubanova, 2022) Gubanova, E., Schmidt, T. O., Watzele, S., Alexandrov, V., & Bandarenka, A. S., *Structure-Dependent Electrical Double Layer Capacitances of the Basal Plane Pd(hkl) Electrodes in* $HClO_4$, J. Phys. Chem. C, 2022, **126**, *27*, 11414-11420.

[503] Bagchi, R. N., Bond, A. M., & Scholz, F., *ESR-Electrochemical Cells and their Performance in Studies of Redox Processes*, Electroanalysis, 1989, **1**, 1-11.

[504] Bulak, E., Varnali, T., Schwederski, B., Bubrin, D., Fiedler, J., & Kaim, W., *Separation of Metal Binding and Electron Transfer Sites as a Strategy to Stabilize the Ligand-Reduced and Metal-Oxidized Form of* $[Mo(CO)_4L]$, Organometallics, 2011, **30**, *23*, 6441-6445.

[505] Dürr, M., Klein, J., Kahnt, A., Becker, S., Puchta, R., Sarkar, B., & Ivanović-Burmazović, I., *Redox Behavior of a Dinuclear Ruthenium(II) Complex Bearing an Uncommon Bridging Ligand: Insights from High-Pressure Electrochemistry*, Inorg. Chem., 2017, **56**, *24*, 14912-14925.